SURFACE INITIATED ROLLING/SLIDING CONTACT FATIGUE IN PEARLITIC AND LOW/MEDIUM CARBON BAINITIC STEELS

Xiaoyan Su
M.S., Institute of Aeronautical Materials, Beijing China, 1984

A dissertation submitted to the faculty of the
Oregon Graduate Institute of Science & Technology
in partial fulfillment of the
requirements for the degree
Doctor of Philosophy
in
Materials Science and Engineering

July 1996

This dissertation " Surface initiated rolling/sliding contact fatigue in pearlitic and low/medium carbon bainitic steels' by Xiaoyan Su has been examined and approved by the following Examination Committee:

Paul Clayton, Thesis Advisor
Professor

Oscar Orringer
Lecturer, Mechanical Engineering Department
Tufts University

David Atteridge
Professor

Lemmy Meekisho
Associate Professor

ACKNOWLEDGMENTS

First, I would like to express my gratitude to my thesis advisor Dr. Paul Clayton for his help, encouragement, and above all, insightful guidance. Thanks to my thesis committee, Drs. Oscar Orringer, David Atteridge and Lemmy Meekisho for their advice in the completion of the thesis.

This program has been funded by the Federal Railroad Administration monitored by W. H. Paxton and J. Deiley. Thanks to Drs. Roger Steele, Oscar Orringer, Milt Scholl and William Paxton for the valuable discussions throughout the program. Burlington Northern Railroad supplied the test materials.

Special thanks to my fellow "Surface Engineering (Wear group)" members for their help and support, and to Dr. Nong Jin for providing valuable information on the experimental bainitic steels. Gratitude to the faculty of the Department of Materials Science and Engineering for their intellectual input, particularly to my SPC Chairman Dr. Margaret Ziomek-Moroz, and appreciation for assistance from all the technicians at the Department.

Deep gratitude to my parents, my sisters and brothers for their understanding and support across continent and ocean. Thanks to my long time friends for their constant encouragement. Thanks for my son Paul P. Wang for believing in me. Finally, thanks to my best friend, colleague, and husband Dr. Don Mc Murchie for his continuous support, understanding, and love.

With love:

For Qianyi Su and Qimin Guo

For Don Mc Murchie

and

For Paul P. Wang

TABLE OF CONTENTS

LIST OF TABLES

LIST OF FIGURES

ABSTRACT

Surface Initiated Rolling/sliding Contact Fatigue of Pearlitic and Low/medium Carbon bainitic Steels

Xiaoyan Su, M.S.
Supervising Professor: Paul Clayton

A study of surface initiated rolling/sliding contact fatigue (RCF) behavior of two pearlitic and four low/medium carbon bainitic steels has focused on three aspects; RCF performance as a function of contact pressure, failure mechanisms, and ratchetting strain behavior including the effect of slide/roll ratio.

A contact pressure range of 850 to 2300 MPa, water lubrication and a slide/roll ratio of 10% were used to establish RCF life. The relationship between rolling contact fatigue life and contact pressure is non-linear. The relative performance of the steels is consistent with their mechanical properties, with longer RCF life being associated with higher strength irrespective of microstructure. The six steels tested exhibited very similar RCF resistance as a function of normalized contact pressure, P_0/k.

Two distinct crack growth modes have been identified. The shear band cracking mode, which is associated with the severely deformed surface layer, predominates above the theoretical shakedown limit of $P_0/k = 4$. The branched cracking mode predominates at lower P_0/k values where subsurface material is relatively undeformed. Failure mechanisms have been suggested respective to the two crack growth modes. The effect of both oil and water lubrication on crack growth has been investigated.

Ratchetting strain data of a pearlitic steel are a non-linear function of both contact pressure and the number of contact cycles. The most important feature of the non-linearity is its asymptotic strain rate behavior. A critical strain concept for crack initiation has been proposed. The variation in ratchetting strain consistently reflected the variation in tangential to normal traction ratios (T/N) at different slide/roll ratios, with a higher strain for higher T/N and convergence in strain rate corresponding to convergence in T/N ratios as contact cycles increased. The variation in T/N values is partially attributed to the influence of sliding distance on the coefficient of friction through building up a stable contact interface, and a stick–slip phenomenon involved at slide/roll ratios ≤ 1%.

INTRODUCTION

In the railroad industry, increasing axle loads for freight trains and increasing speed for passenger trains has been an ever-present endeavor to meet the demands of the growing market.[1,2,3] In North America, freight transportation is the major task. About 30% of the total freight transportation in the US is accomplished by railroads, and the percentage has been gradually increasing.[4] In the last two decades, the railroad industry of North America has experienced significant increase in average wheel loads. The standard axle load since the late 1970's has steadily increased from 22 tons, to 25, 30, and to 33 ton in the1990s, with 39 tons being introduced recently.[5,6,7] The heavy loads plus increased track utility impose severe working conditions for rails. Increased rail failure, as a consequence, causes the railroad industry millions of dollars of economic loss due to rail replacement and extensive maintenance, off-setting the benefit from increased transportation capacity.

As service conditions have changed, rolling contact fatigue (RCF) has become the predominant failure mode on railroads with relatively high axle loads of 25 tons.[4,8,9,10,11] The changes have involved an axle load increase, an application of wide scale lubrication, and the use of hard and more wear resistant rail materials. Both wear and RCF have been the primary causes for rail failure. The improvements in materials and lubrication have significantly suppressed wear, but provide a favorable environment for RCF to take place. The combination of high axle loads and good lubrication of wheels and rails during curving is of particular relevance. At the Facility for Accelerated Service Testing (FAST), when rail wear rate decreased substantially because of generous lubrication, appreciable lengths of rail section had to be replaced due to surface fatigue failure.[3,8] Premium head hardened rails, which had replaced standard plain carbon rails to cope with wear problems in Canadian railroads, only survived 40 to 50 million tons of traffic due to spalling,[9] while an average rail service life was about 150 million tons in curved track and 600 million tons in tangential track for standard rail steels.[10]

RCF is divided into two categories — surface RCF and sub-surface RCF. Sub-surface initiated fatigue commonly refers to shells which lead to transverse defects. The initiation sites of shells are often in the vicinity of the boundary between plastically deformed and non-deformed material.[8,12] There is strong evidence that inclusions play a significant role in the initiation of shells.[5]

Surface RCF, on the other hand, is related to high contact stresses on the surface layer of rails, which often results in a progressive shear strain accumulation, giving rise to a highly sheared surface plastic deformation layer. During RCF processes, multiple cracks are usually initiated within the surface layer, then propagate and coalesce forming crack networks, eventually causing failure by spalling or deep head checking, as shown in Figure 1 and Figure 2.[8,13] These are the most common surface RCF failures that destroy the load carrying capacity in heavy haul rails.[5] "Squat" type failures, as shown in Figure 3, are likely caused by dynamic impact and have occurred in Europe and Japan in rails carrying high speed passenger trains at 200 km/h or greater.[5]

Rail/wheel contact is a complex phenomenon in which multiple factors, such as contact pressure and contact interfaces, slide/roll ratios and the coefficient of friction, lubrication and environmental conditions, as well as metallurgical and mechanical properties of the materials, all come into play and interact to determine the outcome of rail performance. To improve rail surface RCF resistance, it is crucial to understand failure mechanisms, particularly those factors relevant to a prevailing service trend — high contact pressure with liquid lubrication.

The current research is sponsored by the Federal Railroad Association (FRA), and focuses on three aspects:

1 Evaluating RCF performance of two pearlitic and four low/medium carbon bainitic potential rail steels, emphasizing high contact pressure performance.

2 Developing a better understanding of surface initiated RCF failure mechanism under a wide contact pressure range, and the effect of water and oil lubrication.

3 Investigating ratchetting strain behavior.

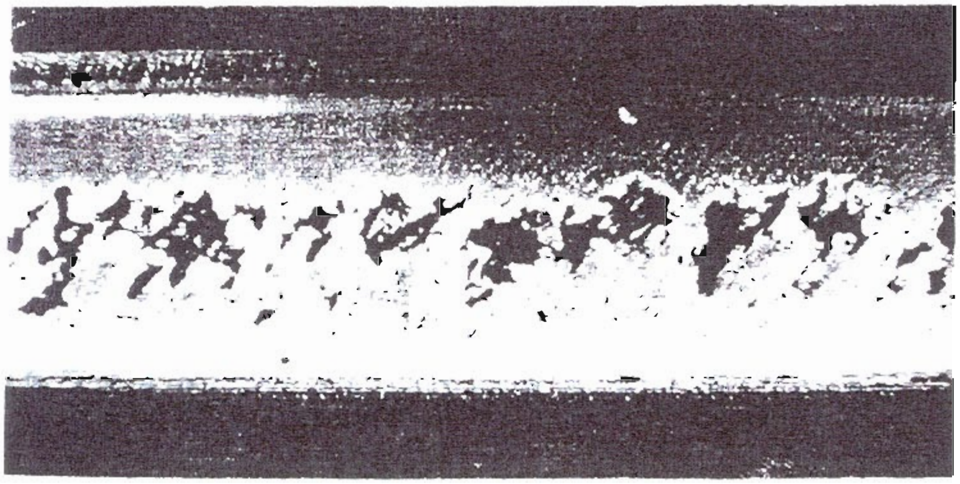

Fig. 1. Spalling in head hardened rails in Burlington Northern Railroad track.

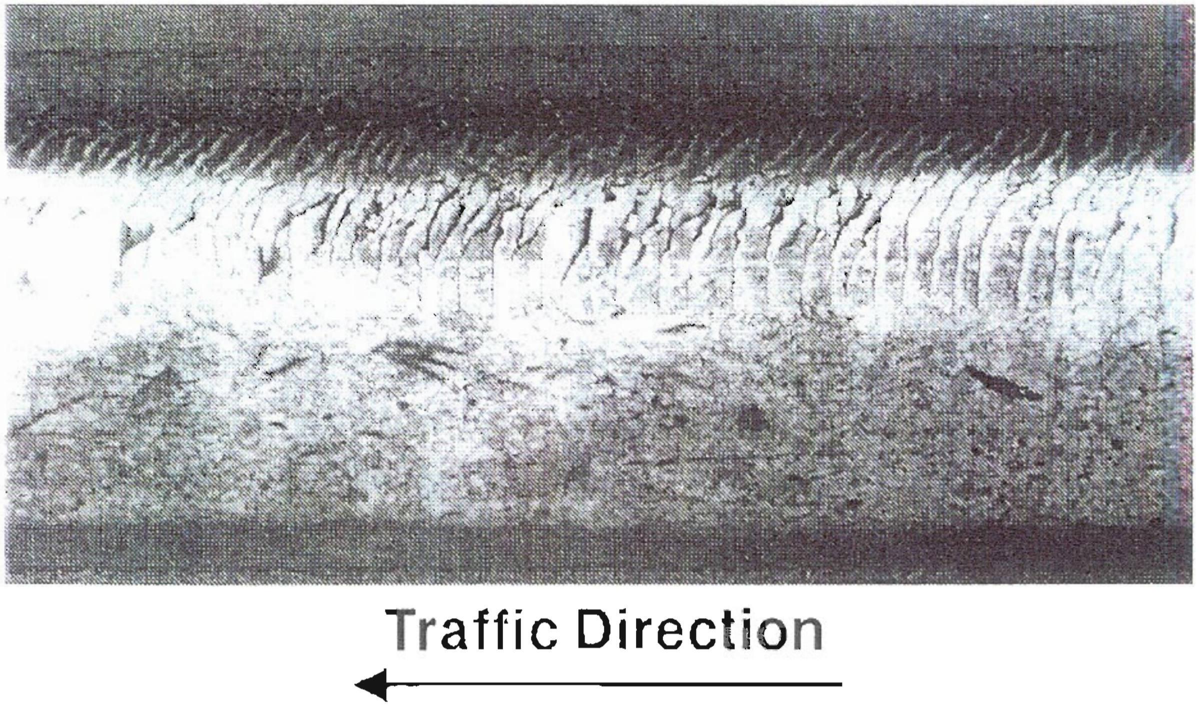

Fig. 2. Head checking.[5]

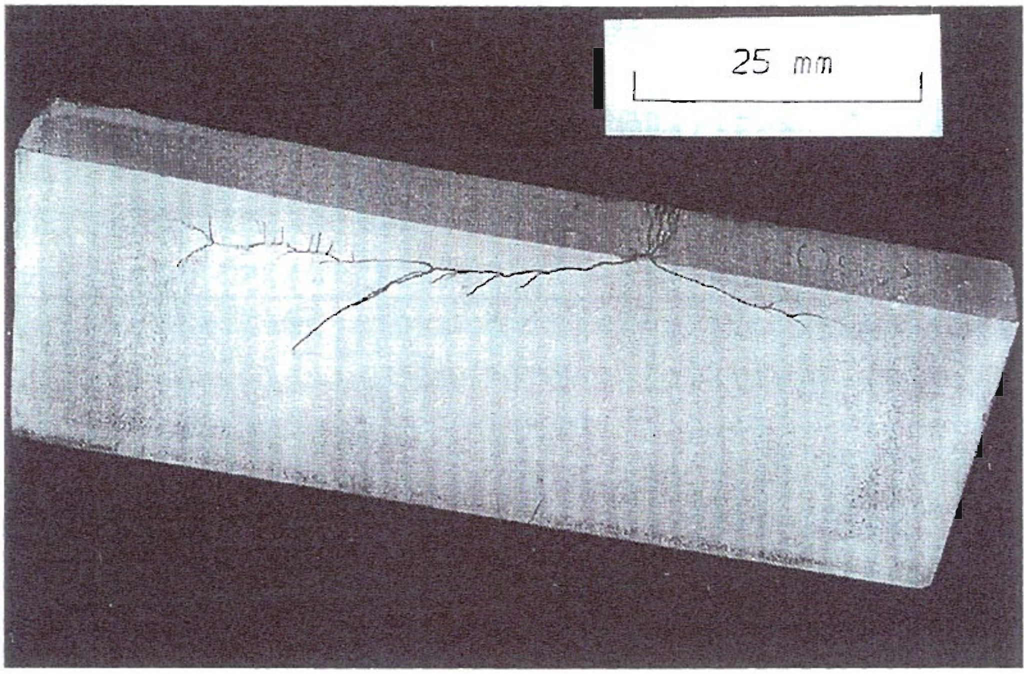

Fig. 3. Longitudinal section through a squat type surface RCF defect.[5]

CHAPTER 1

LITERATURE REVIEW

1.1 MECHANICS OF RCF

Surface RCF failure occurs mostly at high contact pressure areas. In an early AREA (American Railway Engineering Association) survey, 60% of a total of 8,703 rail failures were associated with high contact stresses.[14] To analyze the RCF problem, the stress distribution in contacting bodies needs to be understood.

1.1.1 Contact Area and Pressure Distribution

For contact stress analysis, the starting point is to determine the size and shape of the contact patch, and the pressure distribution on it. In reality, rail/wheel contact is a complex 3-dimensional system, varying with surface profiles, driving actions, non-flanging or flanging dynamics, and creepage conditions. For material strength and RCF research, however, the Hertz solution is simple, yet provides essential characteristics of the contact pressure and stress distribution satisfactory for the purpose. To date, most important contact stress analyses[15,16] are based on the ingenious Hertzian solution, in which rail/wheel contact is simplified as two-dimensional line contact (plane strain).

The Hertzian contact patch size and pressure distribution for two elastic cylinders in line contact with axes parallel and pressed by a normal force P is illustrated in Figure 1.1, and expressed in equations (1.1) through (1.4):

$$a = 1.13\sqrt{(P\Delta R_1R_2)/(L(R_1+R_2))} \quad (1.1)$$

$$P(x) = P_0\sqrt{(1-x^2/a^2)} \quad (1.2)$$

$$P_0 = 0.564\sqrt{P(R_1+R_2)/(L\Delta R_1R_2)} \quad (1.3)$$

$$\Delta = (1-\nu_1^2)/E_1+(1-\nu_2^2)/E_2 \quad (1.4)$$

where E_1 and E_2 are elastic moduli, ν_1 and ν_2 are Poisson's ratios, and R_1 and R_2 are the radii of the two cylinders, respectively. The contact takes place over a narrow rectangular strip, where a is the half width of the contact strip, and L is the contact length. The contact area is very small relative to the radii of curvature of the undeformed surfaces, and the pressure transmitted through the area is highly concentrated. The contact pressure distribution, P(x), is semi-elliptical, with maximum contact pressure, P_0, at the center of the contact patch.

Strictly speaking, Hertzian solutions are limited to linear elastic bodies, and the interface must be frictionless and ideally smooth. It has been shown that the apparent width of the contact for rough surfaces is nearly 20% larger than that of smooth surfaces.[119] The maximum averaged pressure generated at the contact of rough surfaces is smaller than that predicted for smooth surfaces by the Hertzian equations.[119, 127] The trend is consistent with results of Greenwood[16] which show that surface roughness reduces the maximum effective contact pressure and distributes the load over a greater radius. In a case where plastic area is present, the elastic region lying beneath the plastic zone appears to have a major influence on the peak contact pressure and the tangential compliance of the contacting bodies.[136] Although small relative tangential displacements only have a slight influence on the pressure distribution, the influence on the extent of the plastic area is significant. [136] A study on sliding contact between dissimilar elastic cylinders indicated that the stresses well within the body do not change greatly from classic Hertzian analysis with presence of shear traction, but there is a first order modification of surface tensile stress by ±11% of the value calculated by Hertz solution for a coefficient of friction of 0.8.[137]

Despite these differences, various contact theories have shown that Hertzian solutions can be extended beyond the theoretical limitations into the plastic regime,[14,17,136] frictional surfaces,[16] and real surfaces under relatively higher contact pressure[18] without large errors.

1.1.2 Tangential Force and Slide/roll Ratio

Tangential traction is transmitted through the contact interface due to surface friction. According to Coulomb's friction law, the magnitude of the tangential force, T, at a given point of contact cannot exceed the product of coefficient of friction and normal pressure at the same point when two elastic bodies are under contact.

It has been revealed that the coefficient of friction is not an intrinsic material property. It is dependent on multiple factors including physical, chemical and mechanical properties of the materials, contact surface and environmental conditions.[100,121] The friction action is considered to ba a thermodynamically irreversible dissipation process, the behavior of which is defined by the synergism of strain, mass transfer and heat processes.[138] The theoretical coefficient of friction was found to be a function of the sharpness of the hard asperities, the interface conditions and the shape of the plastic zone.[130] It is a function of sliding distance.[103] Tangential force is also a function of other variables, such as slide/roll ratio, contact shape, surface contamination and wheel dynamics, with slide/roll ratio being a major variable.[17]

The slide/roll ratio, also called creepage, is defined as the difference between the two contact surface velocities divided by the mean of the two velocities.[17,19,20] Creepage is inevitable in practice due to accelerating or braking actions, variations in travel distance during curving, and the difference in material properties of the two contact bodies.

For two cylinders under rolling/sliding contact the mean surface velocity V_m, and slide/roll ratio, ξ, are expressed as

$$V_m = (D_b N_b + D_t N_t)/2 \tag{1.5}$$

$$\xi = 2(D_b N_b - D_t N_t)/(D_b N_b + D_t N_t) \tag{1.6}$$

where D_b and D_t are the diameters of the bottom and top cylinders, N_b and N_t are the respective cylinder revolutions per minute.

The typical relation between tangential force and slide/roll ratio, as shown in Figure 1.2, is non-linear with two distinguishable regimes: partial slip and full slip. During partial slip, the contact patch is divided into two regions, stick and slip, and the T/P ratio is less than the coefficient of friction, μ. As the slide/roll ratio increases to saturation, incipient slip occurs and followed by prevailing full slip, thus we have [17,21,22,23]

$$T(x) = \pm\mu P(x) = \pm\mu P_0\sqrt{(1-x^2/a^2)} \qquad (1.7)$$

where T(x) is the tangential force distribution. The negative sign of $T/P<0$ denotes driven condition (for rails) with tangential traction in rails opposite to traffic direction, and $T/P>0$ corresponds to the driving condition. Both experimental and analytical results show that a component under $T/P<0$ (driven) experiences greater plastic deformation compared to a component under $T/P > 0$ (driving), leading to the earlier fatigue failure of the driven component.[25,26,27, 126,147]

1.1.3 Stress Distribution Under Normal and Tangential Forces

Surface initiated RCF is a complex phenomenon due largely to the distinctive characteristics of stress distribution. The focal point of this section is to address the importance of the contact stresses in causing RCF failure, emphasizing stress cycles and maximum shear stresses.

When two cylinders are loaded under static normal pressure only, the stress distribution and contours of maximum shear stress are illustrated in Figure 1.3.[16] The important features of the stress distribution are that the stress field is completely in compression, and the maximum shear stress is located beneath the surface, at $x = 0$, $z = 0.78a$. The maximum shear stress, τ_{max}, is calculated as

$$\tau_{max}=1/2(\sigma_1-\sigma_2) \qquad (1.8)$$

in which σ_1 and σ_2 are the maximum and minimum values of the principal stresses. Under pure rolling $\tau_{max} = 0.30\ P_0$, thus the onset of plasticity occurs first underneath the surface when $\tau_{max} = k$ (k is the yield stress in shear), and this condition corresponds to

$P_0 = 3k$. The location of the maximum shear stress in theory agrees with observations in pure rolling, in which the undeformed top layer of material is sheared relative to the bulk core material due to the subsurface plastic flow.[28]

Tangential force has a significant effect on the contact stress distribution. The most important effects are:

- to aggravate contact conditions by increasing the magnitude of both principal and shear stresses. With coefficient of friction $\mu = 1/3$, τ_{max} increases to $0.42P_0$ instead of $0.30\ P_0$ as in pure rolling.[15]
- to move the severest stress state to the surface, Figure 1.4.[16] For example, when $\mu = 1/3$, the maximum shear occurs at the surface instead of beneath the surface, and the onset of plasticity occurs when P_0 is only 2.4 k.[15]
- to introduce tensile stresses, σ_{xx}, at the trailing edge of a contact interface, although stresses are predominantly compressive with shear just below the surface. This may have a significant effect on RCF, since tensile stresses promote fatigue cracks. The surface tensile stresses (at z=0) for plane strain condition are illustrated in Figure 1.5,[15] and are expressed through Equations. (2.9) to (2.13).[16]

$$\sigma_{xx} = -P_0(1-x^2/a^2)^{1/2} - 2\mu P_0 x/a \tag{1.9}$$

$$\sigma_{zz} = -P_0(1-x^2/a^2)^{1/2} \tag{1.10}$$

$$\sigma_{yy} = \nu(\sigma_{xx}+\sigma_{zz}) \tag{1.11}$$

$$\tau_{zx} = -\mu P_0(1-x^2/a^2)^{1/2} \tag{1.12}$$

$$\tau_{xy} = \tau_{yz} = 0 \tag{1.13}$$

1.1.4 Stress Cycles Under RCF

The RCF stress cycle is multiaxial and non-proportional, as the contact load moves toward and passes over the surface element, it repeats from tension to shear to compression under wheel driving condition (traction force is acting in the rail rolling direction). The load sequence is reversed from compression to shear then to tension for braking conditions, Figure 1.6. With each load passage, the axes of the two principle stresses in the X-Z plane rotate 90 degrees.[15, 16, 24]

In the fatigue process, the stress or strain amplitude, rather than the maximum stress, is the controlling parameter. Figure 1.7 demonstrates the normal stress range experienced at the point O as the surface element approaches and passes under the load. During each contact, the normal stress σ_{xx} acting parallel to the surface, changes from a maximum tension of $0.67P_0$ at the entry of the contact to a maximum compression of $-1.20\ P_0$ at the exit of the contact, resulting in a stress range of $1.87\ P_0$ ($\mu = 1/3$). The range of maximum shear stress is $0.53P_0$ and the maximum octahedral shear stress range is $0.63\ P_0$. Without the tangential load, these values reduce to $1.0\ P_0$ for normal stress σ_{xx}, $0.3\ P_0$ for the maximum shear stress range, and $0.27\ P_0$ for the octahedral maximum shearing stress range.[15]

1.2 MECHANISMS OF SURFACE RCF PROCESS

1.2.1 Mechanisms of Surface RCF Crack Initiation

Surface rolling contact fatigue, like other fatigue processes, involves crack initiation and propagation. The initiation mechanisms can be roughly divided into two categories:

- initiation induced by repeated local plastic deformation due to concentrated contact fatigue stresses at defects; and
- initiation due to ductile fracture induced by incremental shear plastic strain within the whole plastically deformed surface layer.

1.2.1.1 Initiation Due to Local Plasticity at Surface Defects

This mechanism emphases the very local nature of the RCF crack initiation process which is generally associated with small regions of damage, a few thousandths of an inch across, caused by asperities or possibly by foreign particles.[32, 33] Surface defects such as indentations of a harder structure into softer pearlite, were reported as main initiation sites in a field survey.[11,34] Surface intrusions,[35,75] near surface inclusions,[36] and discrete hard white etching layers also served as initiation sites.[9,34,74,134] The white layers were observed to form at low MGT in a Burlington Northern rail study, causing surface cracks to initiate early on in rail service life, as early as 5% of total life.[74,134]

An experiment has shown that the surface RCF life is not sensitive to the size of the defects, but is dependent strongly on the contact pressure. Changing the width of the EDM manufactured transverse furrows by an order of magnitude, and depth from 5 to 25 micron, P_{max} only varied by 6%, thus the resulting P_{max} can be estimated from the Hertzian contact pressure P_0.[122]

The function of defects is to concentrate contact fatigue stress, either causing high localized normal stresses or shear stresses. The concentrated contact stresses may be high enough for the localized generation of dislocations and dislocation pile-ups, leading to local plasticity. Void formation was found primarily to be caused by plastic flow of the matrix around hard particles. The voids further coalesced to form microcracks by growth or by shearing of the metal.[36] The localized plastic flow is a primary cause for crack initiation.

1.2.1.2 Initiation Due To Surface Layer Plastic Deformation

The second mechanism differs from the local plasticity theory, in that plastic flow within the bulk surface layer caused by high contact stresses leads to crack initiation. Cracks, in this case, may initiate without defects,[11,24] and may have a quasi-static cracking fashion due to the exhaustion of ductility of a surface work-hardened layer.[35,40]

Severe plastic deformation in the surface layer of rails which are sheared relative to the bulk materials have been observed in both field and laboratory investigations, Figure 1.8. In a field observation, shear plastic deformation was present in all the rail surfaces investigated (30 sites, 50 defective rails) irrespective of composition, age, or traffic patterns with maximum shear at the surface.[11] Spalling was initiated in the bright polished surface paths directly related to the surface plastic deformed layer.[9] The magnitude of the plastic flow increased with increasing tonnage or axle load, and in curved track was 5 to 10 times that in tangent track, and coincides with increased RCF damage in curved track.[38]

The plastic flow is progressive resulting from accumulation of minute increments of permanent deformation over thousands of RCF cycles.[28] The cumulative nature of the plastic flow is attributed to strain ratchetting behavior – a strain response of materials under rolling and rolling/sliding contact conditions. [24, 26, 28, 38]

The plastically deformed microstructure of pearlitic rail steels has been characterized by a realignment of the ferrite and cementite lamellae towards the rolling direction,[39] as shown in Figure 1.9. Microhardness measurements have shown the increase of hardness in the plastic deformed layer. The hardness increase is attributed to a structure change, namely narrower interlamellar spacing and higher area fraction of hard cementite phase near the surface as a result of realignment.

The mechanism suggests that cracks may initiate by ductile fracture of the surface work-hardened layer. As the cumulative shear strain reaches a critical value over passages of contacts, ductility reserve (energy absorption ability) is gradually exhausted, leading to crack initiation.[10] Crack initiation has been observed on the surface of a test roller when the plastic flow reached saturation.[40] Stress concentration (substantial tensile stresses) due to discontinuity at the plane of the interface between the work-hardened layer and non-hardened layer also promotes fatigue crack initiation.[10] In supporting this mechanism, the fracture surface of a rail material under biaxial loading of compression and shear showed plastic de-cohesion lips indicating that failure was dominated by the ductile fracture mode, and the cracking, which occurred in quasi-static fashion, appeared quite suddenly.[35] The critical strain concept for crack initiation has been also suggested for 52100 through hardened steel and carburized 4118 steel under lubricated rolling/sliding contact,[145] for a pearlitic rail steel under dry rolling/sliding,[96] and for various ductile materials involving cumulative strains. [98]

1.2.2 Mechanisms for Surface RCF Crack Growth

The mechanisms for RCF crack growth, parallel to conventional fatigue theory, fall into stress fatigue and strain fatigue regimes. In the stress fatigue regime, a crack is driven by cyclic contact stresses. Fracture mechanics concepts can be applied in this case, in which mixed mode stress intensity factors of mode I (opening) and mode II (shear) act at a crack tip. In the strain fatigue regime, surface RCF crack growth is suggested to be controlled by plastic strains rather than stresses analogous to a low cycle fatigue concept. The strain type, however, is more complicated for RCF, and includes either a closed loop cyclic strain or a non-fully-reversed incremental plastic strain , i. e. ratchetting.

1.2.2.1 Stress Fatigue—Fracture Mechanics Concept

The linear elastic fracture mechanics (LEFM) concept for RCF crack growth is composed of three essential elements: applied contact stresses and crack face friction, crack length, shape and orientation, and the function of lubricants. [30,41,78,79]

In most analyses, Hertzian contact stress distribution is assumed, and it has been reported that only minor deviation exists even in the presence of a crack. The contact stress cycle is predominantly in compression and shear, except at a very near surface layer where some tensile stresses are present. Once a surface crack breaks downward into the sub-surface, it is assumed that only the mode II stress intensity factor predominates. In addition, cracks are partially closed due to compression, and are thus capable of transmitting frictional force. An analysis has shown that mode I branching crack growth is possible even though the stress field is largely compressive.[129] Nevertheless, mode II crack growth is likely to be dominant.[129] For mode II growth, it is found that the crack face friction is more significant than frictional force on the contact interface in influencing stress intensity factor K_{II}.[45] Increasing crack face friction reduces the shear stress intensity factor range considerably.[41]

Some analyses have suggested that RCF crack growth is mainly attributed to shear stresses, since tangential force increases the mode II intensity factor, causing a crack to open as it leaves the contact area.[30,79] However, so far, no fatigue crack propagation in a plane of the maximum shear has been generated successfully in laboratory experiments under biaxial loading of compression and shear, suggesting that purely shear mode crack growth is unlikely.[42] However, crack growth in a plane of maximum shear was achieved when a non-proportional loading of tension and shear was applied.[78]

In order for a RCF crack to grow downwards into the subsurface, mode I stress intensity has to act at the crack tip. In this hypothesis, the function of fluid is indispensable, because not only may it reduce the crack face friction, but most importantly provides a source for creating mode I crack growth.

The fact that the presence of a fluid is necessary for RCF cracks to grow was first observed by Way in 1935.[33] Cracks in dry RCF tended to develop parallel to the surface,[32,36] and the depth of crack networks was confined within the plastic deformed layer.[44] During the subsequent contacts, cracks were likely be worn away. With lubrication, cracks extended well beyond the plastic deformed layer, and instead of growing parallel to the surface, grew inward with an increased angle to the surface,[44] varying from 10 to 50 degrees in the direction of the motion of the load.[43,72] For various lubricants tested, including water, water with an inhibitor, and silicone oil, RCF crack behavior, in terms of the same crack network depth, was similar, showing no distinguishable corrosion effect.[44]

Two hypotheses have been proposed to explain the function of fluid, one is the hydraulic pressure mechanism,[33] the other is fluid entrapment theory.[42] Both explain that RCF crack growth is promoted by mode I stress intensity resulting from pressurizing of crack faces by fluids. However, the second theory attempts to explain the phenomenon of crack orientation. It states that a fluid can only get into a crack when tangential traction is to open the crack, which is always true in a driven component, and thus predicts a bigger fluid effect in a driven component than in a driving component consistent with experiments.[42]

The effect of lubrication may be more complicated than we think. It varies with viscosity.[7,13] In the case of a glycerol lubricated roller, a crack network originated from a single site to produce a pit, in contrast to the multiple crack initiations observed for water lubricated rollers.[20] Lubricants also affected the morphology of the RCF cracks, with clean oil producing pits with sharply defined edges, and sloping steeply inward, while under water lubrication, shallow flakes were produced.[46]

Although LEFM describes a driving mechanism for surface RCF crack growth, the concept is not widely applied in practice due to many obstacles. The RCF loading condition is complex, contact stresses plus crack face friction and the function of fluid need to be accounted for. A great number of surface RCF cracks are developed beyond the elastic regime, violating the LEFM criterion. Surface RCF cracks often occur as extensive multiple cracks, the interaction between cracks also makes the LEFM concept difficult to apply. It has been shown for multiple cracks that the load transfer between cracks can cause either significant increases or drops in stress intensity factors of both mode I and mode II. The interaction depends on the distance between cracks, their relative position with respect to the loading zone, and the interfacial coefficient of friction. [123,124] In addition, the baseline material crack growth data simulating the RCF condition is minimal.

1.2.2.2 Strain Fatigue—Crack Growth Driven By Plastic Strain

For ductile metals under high rolling/sliding contact loads, surface RCF cracks often grow on the planes which carry the maximum compressive stresses or along the line of shear flow. It is believed these cracks are shear cracks with a ductile nature, driven by plastic strain rather than elastic stress intensity.[149] The plastic strain may be either cyclic or incremental, i. e. ratchetting. In this sense, the RCF strain behavior, in terms of strain amplitude and strain rate, controls the crack growth.

Surface plastic deformation plays an important role in RCF crack growth. Crack growth along shear plastic flow bands has been observed in both laboratory and field observations. The realignment of the ferrite and cementite lamellae towards the rolling direction may provide a favorable orientation for cracks to propagate.[39] Plastic deformation from the dry rolling/sliding stage prepared the material for extensive cracking during subsequent operation with lubricants.[42] There may be a correlation between the depth of surface layer deformation and the depth of crack networks. It was evident that under dry rolling/sliding cracks stopped within the work-hardened layer.[42] The thicker the work-hardened layer, the deeper the spalling.[10,72]

In general, RCF processes are governed by the integral system of contact loads, environment, and material properties. For ductile materials under high contact loads, plastic flow may be responsible for both RCF crack initiation and growth. Under low and moderate contact loads, local plasticity at defects, and cyclic contact stress may play a more important role. It is quite likely in practice that the various mechanisms may interact.

Lubrication proves to be one of the most important factors in the surface initiated RCF process. Dry RCF promotes faster crack initiation over lubricated conditions. Dry initiation followed by liquid lubricated conditions has been found to be the worst combination to cause RCF failure. Wear of rails may have an advantageous role in eliminating cracks already initiated and delaying crack growth.[47]

1.3 MODEL DEVELOPMENT

This section introduces two groups of models: models which predict RCF strain responses of rails; and models which predict RCF life, in terms of the number of load passages (cycles) to surface crack initiation and final failure as a function of operating variables, such as maximum contact pressure, friction force, slide/roll ratio, and lubrication conditions.

1.3.1 Modeling of RCF Strain Responses

Understanding strain response is essential for evaluating RCF resistance and predicting rail performance. A strain fatigue concept is only significant when plasticity is involved. Analytical and empirical modeling on strain responses focuses on:

- evaluating the shakedown limit, i. e. a contact load level, under which materials primarily strain elastically, and
- modeling ratchetting strain behavior (the prevailing strain response under rolling/sliding contact), predicting the ratchetting strain rate and the magnitude at a given contact conditions.

To model these problems, some assumptions have been made to simplify the rail/wheel contact. In most models, two-dimensional line contact with complete slip and Hertzian pressure and contact stress distribution is assumed,[25,26,29,30] neglecting the effect of plasticity. This is believed to be a close approximation to the true stress field since the plastic layer is very thin compared to the bulk materials, and the assumption has been confirmed by a FEM analysis.[31]

1.3.1.1 Shakedown Limit

In the theory of plasticity, the shakedown theorem was developed to define elastic and elastic-plastic regimes for repeated loading. Either ratchetting or closed loop plastic strain cycles occur only when a material continuously deforms plastically, i. e. above the shakedown limit.

Plastic flow may not continue to occur after initial yielding, because:

- the residual stresses generated after the first few contacts oppose the applied contact stresses to prevent further yielding. As a result, a higher contact pressure has to be applied to force the material to yield subsequently.
- most rail materials will work-harden leading to an increased yield strength.
- the contact area may change through the deformation, thus attenuating the contact stresses. In most analyses, however, this consideration is ignored.

To determine the shakedown limit, residual stresses have to be evaluated first. Residual stress analysis is one of the major endeavors in RCF research. Comparisons of residual stress calculations in 2-D line contact[27,126] have shown that two aspects are in common in residual stress analyses. The first is that only a very small number of cycles, about 2 to 10 load passages, is required for residual stress to reach steady-state, and this agrees with experimental results. The second is that the sizes of the residual stress zones are similar in most analyses.[30,126] However, the magnitude and location of the maximum residual stresses differ considerably due to different assumptions on material hardening laws used in these residual stress predictions.[25,27,31,48,51,53] The higher the plastic modulus, the smaller the residual stresses.[126] The peak residual stress in the rolling direction calculated by Merwin and Johnson[25] is only 0.25 to 0.4 of the FEM predictions.[31,53] The location of the peak residual stress was found around 0.32 to 0.6a in a study,[25] and 0.9 to 1.2a in other studies,[27,53,126] where a is the half width of the contact area. It has been found that the normal load basically determines the subsurface residual stresses and the plastic zone size.[126] The influence of tangential force penetrates to a depth of 0.3a, and has diminishing influence on the residual stress beyond this thin layer. [126]

For shakedown limit calculation, all the models [29,31,51] predicted similar values, which varied from P_0/k of 3.5 to 4.0 for pure rolling regardless of the material work-hardening behavior because initial cyclic yield strength in all cases were about the same. Figure 1.10 shows a shakedown map for 2-D line contact and complete slip. The map divides the sub-surface and surface flow regimes and defines a shakedown limit, which is a function of normalized contact pressure, P_0/k, tangential traction, as well as material work-hardening behavior. The shakedown limit decreases considerably as the contact condition deviates from pure rolling. The materials with kinematic hardening have the highest shakedown limit. The contact pressure in rails usually ranges from 1200 to 2500 MPa.[5] The higher end of this range well surpasses the shakedown limit of about 4.0, even for work-hardened materials with a coefficient of friction of less than 0.25. According to the map, surface flow will occur when the coefficient of friction is equal to or greater than 0.25. This implies that surface flow is a common situation in practice, since typical values of the coefficient of friction vary from 0.17 for rails lubricated by grease/sand to 0.5 for dry rail in curves.[16,19,49.148]

Case hardening and heat treatment are often used in surface engineering to improve the strength of the surfaces. A study extended the shakedown analysis to a half -space whose surface has been heat-treated or case hardened so that hardness and yield strength vary with depth.[143] The results show that the shakedown limit is a function of the surface or case hardness, the core or bulk hardness, and the depth of the hardened layer. Shakedown limit increases as the case hardness increases. A change in the coefficient of friction from a low value characteristic of lubricated condition ($\mu < 0.1$) to high friction ($\mu \sim 0.5$) can decrease the shakedown limit by as much as 50%.[143] The change in surface topography during interaction of hard on soft contact surfaces also influences the shakedown limit.[144] It is shown that the shakedown limit is dependent on the roughness characteristics of the hard surface, the hardness of the soft surface, the contact modulus and the coefficient of friction[144] Increasing the magnitude of the shear yield strength of the material or decreasing the local value of the coefficient of friction raises this limit. Decreasing the contact modulus, which is the term expressed in Equation 1.4, has the same effect.[144]

1.3.1.2 Strain Responses Above Shakedown Limit

When loaded above the shakedown limit, the questions are: what types of strain responses will occur, ratchetting or fully reversed between two strain limits? If ratchetting occurs, then how much and how fast does the shear strain accumulate over contact cycles? What is the correlation between ratchetting strain and RCF performance?

During conventional strain fatigue cycles, materials are strained cyclically between two limits, forming a closed hysterisis loop. Different from the closed strain loop, the prevailing strain behavior observed in rail materials is — ratchetting, an open stress-strain curve. The plastic strain rate is higher in the primary loading direction than the unloading due to a mean stress effect, giving rise to a non-fully reversed strain cycle, as shown in Figure 1.11. In rails, ratchetting strain accumulates cycle by cycle in the direction of tangential force, causing the prevailing shear plastic flow observed in rail surfaces. [24,25,26,28]

The principle features of ratchetting strain include the following:

- The magnitude of the ratchetting deformation is cumulative in nature, increasing with RCF cycles,[24,25,28] Figure 1.11. The behavior is asymptotic with the cumulative process being sustained over a large number of cycles, rather than transient, with which strain accumulation occurs only in the initial cycles.[94]

- The ratchetting strain rate is a function of contact pressure, tangential traction, and slide/roll ratio. It increases with increasing contact pressure and tangential load,[28, 54] and increases with slide/roll ratios.[40] Increasing either mean stress while keeping stress amplitude constant, or visa versa, leads to a faster rate of strain accumulation, but the dependence is non-linear.[93,94]

- Under rolling/sliding contact, the magnitude and the rate of ratchetting is strongly dependent on material hardening behavior. For copper, the rate is fairly constant, as shown in Figure 1.12(a), [28] while the rate is non-linear for rail steels, Figure 1.12(b).[24] At a given load, the ratchetting rate is higher during the initial cycles and the main amount of plastic flow is developed at an early stage. The rate decreases as the number of cycles increases, finally approaching zero, causing the forward flow to saturate, as shown in Figure 1.11.[38]

- Ratchetting strain is also dependent of the type of loading. A change from uniaxial to multiaxial loading alters the hysterisis loops and ratchetting strain behavior for 1020 and 1026 carbon steels,[108] and 316 L stainless steel. [94]

- An important difference in ratchetting behavior between rail steels and reported pressure vessel steels[93,94,108] is that the former ratchet over considerably longer cycles, for example 50,000 or more[24] compared to the latter, which ratchet typically less than a few thousand cycles.

1.3.1.3 Constitutive Modeling for Ratchetting Strain

The objective of any constitutive model for ratchetting strain is to establish the relation between stress and strain increment. The single most important factor for the strain analysis is material hardening. Three basic material hardening laws have been incorporated in the models: elastic-perfectly plastic, linear kinematic hardening (LK), and non-linear kinematic (NLK) hardening.

The early analyses assume elastic-perfectly plastic behavior which is only suitable for certain materials, such as copper. It can only predict the rate under pure rolling, since this kind of model will predict infinite deformation when a top layer of material approaching zero thickness under rolling/sliding contact. The predicted ratchetting strain per cycle for copper was 5 times[29] and even 23 times[51] larger than the experimental data.[28] Obviously, this model is not applicable for rail materials. [25,29,50]

An alternative model is based on linear kinematic hardening. The constitutive model was developed from the experimental results of cyclic stress-strain data of a rail steel under torsion and tension with mean stresses. The experiment showed that the rail material approached a fully reversed hysterisis loop after a small number of cycles for a range of mean stress to cyclic yield stress ratio of 0.3 to 1.1.[51,52] For example, only two cycles were required for the material to approach a closed loop under rolling/sliding with T/P=0.2 and P_0/k_k= 4.5 (k_k was the kinematic yield strength in shear).[52] This behavior fits the category of so-called transient ratchetting. The cyclic stress-strain response was represented by a closed bi-linear hysterisis loop, Figure 1.13a. A FEM analysis was incorporated in the model and the results showed that a material with linear kinematic hardening did not develop cumulative shear deformation under pure rolling or rolling/sliding.[48,51,52,53] The prediction agreed with the experimental measurement for a 0.80% carbon rail steel under pure rolling, showing virtually no forward flow (less than 0.04 mm on the surface) after 10^4 cycles under P_0/k_e=8 (k_e was the cyclic yield strength in shear).[51]

The result seems controversial, given the experimental results showing forward plastic flow under these conditions. However, whether incremental shear flow occurs or just fully reversed cycles may well be determined by the nature of a specific material, its strain hardening properties under contact loading, and the loading conditions. In general, models based on kinematic hardening may describe specific cases, but they do not have the ability to predict ratchetting behavior of rails in practice.

The third group of models is based on a non-linear kinematic hardening (NLK) law,[24,26,27,50,54,111,126] and the stress-strain curves can be schematically represented by Figure 1.13b. For kinematic hardening, it is assumed that the yield surface retains its shape and size, but moves freely in stress space. Assuming a von Mises material, the yield surface can be described by

$$f = J(\sigma\text{-}X)-k = [3/2(\sigma'-X'):(\sigma'-X')]^{1/2}-k \leq 0 \qquad (1.14)$$

where σ and X are the stress and back stress tensors, σ' and X' the deviators of σ and X. The back stress X defines the center of the yield surface, and the hardening rule describes how the yield center translates in the stress space. The kinematic hardening modulus, K_x, relates to the hardening rule by defining the magnitude of the increment of the yield surface center, dX, for a given stress increment, $d\sigma$.

In linear kinematic hardening, the hardening rate is constant and not a function of the loading direction, thus, only closed hysterisis loop will result, and no ratchetting can be predicted. In non-linear hardening, the hardening characteristics of the material depend on plastic strain and the loading direction. However, early non-linear kinematic models were not capable of describing ratchetting, since the hardening rate was the same for loading and unloading even though the rate varied with current plastic strain. This difficulty was overcome by Hassan et al,[93,108] and Chaboche et al [94,109] for treating pressure vessel materials, and by Bower and Johnson,[24,54] McDowell and Moyar[26,55,111] and Sehitoglu and Jiang[27,126] particularly in dealing with rail steels. Most of these NLK hardening models are based on the original idea introduced by Armstrong–Frederick which allows the K_X to vary along the loading surface, thus the hardening rate is also established as a function of loading direction.

The basic form proposed by Armstrong– Frederick is: [116]

$$\mathbf{dX} = 2/3c_1 d\varepsilon_p - c_2\mathbf{X}dp \qquad (1.15)$$

where c_1 and c_2 are constant and functions of dp in general, and $d\varepsilon_p$ and dp are the plastic strain and the equivalent total plastic strain increment, respectively. The important point about the equation is that it introduces a recall term ($c_2\mathbf{X}dp$) associated with an evanescent strain memory effect. Substituting the equation into the general kinematic hardening equation[92] yields

$$K_x = 2/3c_1 - (2/3)^{1/2}c_2\mathbf{Xn} \qquad (1.16)$$

indicating that K_X depends on the inner product **Xn**, i. e. the direction of the current applied stress point on the loading surface. The essence of Equation 1.15 is that it removes the back stress X upon reverse loading faster (higher rate) than it builds up due to the variations in K_x, resulting in a different hardening rate between loading and unloading. This point is schematically illustrated in Figure 1.14 [92] for uniaxial $\sigma - \varepsilon^p$ response. If isotropic hardening is absent, the plastic modulus, K_p, will be equal to the hardening modulus, i. e. $K_p = K_x$, according to the consistency condition.[92] Plastic strain is directly linked to plastic modulus by applying the flow law as

$$d\varepsilon_p = d\sigma/K_p \qquad (1.17)$$

where $d\varepsilon_p$ and $d\sigma$ are the plastic strain and stress increment, respectively. Because of the difference in plastic modulus associated with the loading direction, an open hysterisis loop will result.

Equation 1.15 is the basic theme on which most NLK models have developed. The recovery term has been taken for various forms usually in accordance with experimental data. In one model the coefficient of the dynamic recall term is a function of both instantaneous and accumulated inelastic strain, and the coefficients are adjusted phenomenologically according to experimental data for austenitic stainless steel 17-12 SPH tubular specimens subjected to cyclic torsion loading under constant tensile stress at 600° C.[117] Another model emphasizes the plastic modulus, and allows the yield surface to translate at the rate of the experimental ratchetting strain, and as a result, the simulation of uniaxial ratchetting strain for 1020 and 1026 carbon steels is improved.[93] For carbon steel 1026 tube specimens under constant internal pressure and bi-axial loading, a model has been developed by selecting suitable parameters for Armstrong – Frederick type equation, and reasonably good predictions were achieved[108] A modified non-linear kinematic rule employed a threshold in the dynamic recovery term, and the model led to a fairly good agreement with a known experimental trend for ratchetting in stainless steel 316 L.[113]

A problem with using these models for rail steels is that they have been developed for predicting ratchetting strain in pressure vessel applications, and the total cycles to failure is small (ranging from less than 100 to a few thousand cycles) compared to RCF life. Furthermore, the original Armstrong-Frederick type hardening law only predicts a constant ratchetting strain rate. So far, a constant strain rate behavior under rolling/sliding has been only observed for copper.

Two kinds of models have been specifically developed for rail steels subject to rolling/sliding contact. One assumes strain rate is a decreasing function of contact cycles, [19,24,54] the other assumes a steady state strain rate after a small number of contact passages.[26,27,111,126]

By introducing an additional kinematic variable Y in the recall term, Bower and Johnson [19,24,54] developed a NLK model, which can predict gradually reduced ratchetting rate with increasing contact cycles as observed with rail materials. The hardening rule was expressed as:

$$dX_{ij}=2/3c d\varepsilon_{ij}-\gamma_1(X_{ij}-Y_{ij})d\lambda \qquad (1.18)$$

$$dY_{ij}=\gamma_2(X_{ij}-Y_{ij})d\lambda \qquad (1.19)$$

where $d\varepsilon_{ij}$ is an increment in plastic strain and $d\lambda$ is the modulus of the plastic strain increment.

If $\gamma_1 = \gamma_2 = 0$, the model reduces to linear kinematic hardening; if $\gamma_1 > 0$ and $\gamma_2 = 0$, the material accumulates strain at a steady rate, if $\gamma_2 > 0$, the strain rate will decrease over continued cycles.

To construct the constitutive model, four material constants are used: the initial yield strength k_e; the initial hardening rate c; the first feedback rate γ_1 which governs the ratchetting rate; and the second feedback rate γ_2 which governs the reduction in ratchetting rate with repeated cycles. The four parameters are obtained from a uniaxial cyclic stress-strain test with a mean stress in tension.

This model is encouraging because it predicts the initial hardening rate of rail material under rolling/sliding contact which agrees with experimental measurements, the decreased strain rate as load cycle increases, and final saturation, representative of rail material ratchetting behavior. Compared to experimental results this model showed a good estimation for ratchetting rate in copper and good agreement for rail steels under multiaxial non-proportional loading of tension-shear-compression.[24,54] A problem arouse when the model was used to predict the forward flow in rail head materials. The significant discrepancy was in the difference between the number of total cycles in the two cases.

The model can only predict the first 600 cycles of forward flow, while rail material accumulated deformation over 50,000 cycles. The cause for the discrepancy is that the prediction was based on material hardening parameters derived from a cyclic tension-compression test of only about 600 cycles to failure, and they do not fully agree with the true behavior experienced by rail steels under RCF. The large strains and long RCF cycles to failure sustainable in rails compared to small cycles to failure in uniaxial push-pull tests are presumably due to the enhancement of ductility attributed to the hydrostatic pressure in wheel/rail contact.[24]

An alternative non-linear kinematic hardening model for rolling/sliding line contact accounts for ratchetting behavior by predicting a very small but constant strain rate without consideration of the cessation of ratchetting.[26,27,55,111] The material properties in one model were obtained from uniaxial cyclic data over a few hundred cycles.[55] The material constants in an improved model were obtained from both uniaxial and bi-axial loading conditions.[111] These are versatile models which provide solutions for a wide range of loading conditions for both high and low strength alloys. A feature of the models is that a constant strain rate is predicted after a relatively small number of cycles, only sixteen [111] or twenty [126] load passages, compared to the total contact fatigue life. It is believed that a reasonable extrapolation of the early life ratchetting rate data seems appropriate, therefore predictions for ratchetting strain can be extended for thousands or hundreds of thousands of cycles. However, the predicted constant strain rate behavior deviates from the non-linear strain rate in rail steels observed experimentally.

Indeed, surface RCF strain analysis is very sensitive to the material hardening properties used. A material which displays elastic-perfectly plastic behavior would always ratchet with a constant strain rate; and a material which displays continuous linear kinematic hardening would not ratchet, but gives rise to a closed-loop cyclic plastic strains; only non-linear kinematic hardening materials would ratchet and very often with a non-linear strain rate.

A task for improving model predictions is two fold: (1) to obtain material properties which give accurate representation of the strain hardening behavior of the thin surface layer of rail steels under rolling/sliding contact. This is a real challenge for the experimentalist, because the surface material behavior is determined by both the constraint of surrounding materials and inherent material properties. (2) to measure RCF strain directly in contacting bodies to aid model validation and development.

In previous research, a correlation between ratchetting behavior and surface RCF failure processes has been seldom addressed, the attention has focused mainly on the strain behavior itself. An understanding of how the ratchetting strain quantitatively relates to RCF crack development, including both initiation and propagation, is lacking. To identify controlling factors in surface RCF and to develop a valuable RCF life prediction, the correlation between plastic strain and RCF behavior need to be investigated. This research is significant, since it may eventually lead to a realistic RCF life prediction model to link small scale laboratory tests to large scale in-service rail life prediction based on, say, an equivalent RCF strain concept.

1.3.2 Experimental Measurement of Ratchetting Strain

Strain responses measured directly from rolling components provide valuable information both for mechanism study and for model development. Experimental measurement of RCF strain is difficult since the contact components are constantly rotating, and the strains of interest are often the interior strains on the symmetry plane of a rolling part.

In general, two methods have been developed. One uses markers, such as wires, metal inserts,[24,28] or the microstructure itself. [95,96] The main problem with this method is that measurements can only be made by final destructive sectioning of the specimens, periodic measurements at cycle intervals cannot be readily obtained, thus making a quantitative correlation between RCF crack development and strain cycles difficult. Furthermore, inserts are relatively large, from 0.2 mm,[24] to 0.4 mm,[28] and thus affect the accuracy. Besides markers, scratches directly engraved on the rolling surface have been applied to allow the continued measurement as contact cycles repeat.[40,55] But only surface information can be obtained by this method, and another serious disadvantage is that the scratches often became blurred as the plastic deformation progressed.

A grid method[56,57,58,142] is an extension of the scratch method, and has been used extensively for a variety of measurements, such as in cold-drawing, explosion, and other studies interested in measuring deformation. As advances in micro machining and photo resistance technology have been made, fine grids as small as 50-100 lines/mm can be cut on the surface of a specimen to measure the strain field. It is particularly applicable for surface strain measurement, especially at high strain gradient such as notches, crack tips,[58] and subsurface deformation under sliding contact. [99,142]

The idea of using split specimens to avoid final sectioning and at the same time to satisfy a plain strain condition has been employed in several investigations.[56,99,142,147] Grids or markers were put on the inner faces of the split specimens to record shear strain in samples subjected to cutting,[56] a hard wedge sliding over,[99,142] and rolling contact with a tangential traction to normal load ratio of 0.015.[147]

1.3.3 Modeling of Surface RCF Life

With progress in understanding of RCF mechanisms, models to predict surface RCF life as a function of operating variables and material properties have been developed. The first group of variables is mainly the operating parameters, which include contact pressure, tangential traction, coefficient of friction, effect of defects, lubrication, and environment conditions. The second group is the material properties. Obviously, to include all the variables in a single model is a difficult task, if not impossible. Most models focus on selected major parameters.

Many models have been developed to predict surface crack initiation life of rolling bearings. Although these models do not directly address rail/wheel contact problems, they may provide some insights. A paper reviewed eleven published models, and identified consensus parameters and relationships.[131] The author then incorporated major life-modifying variables, which include Hertz contact pressure, EHD film ratio, asperity traction coefficient, asperity height, slope and spectrum width, fatigue stress, and stress concentration factor to predict spalling life for rough Hertz line contact. The model predicts strong effects of interface friction on the spalling life.[132,133]

A model has quantitatively estimated the effect of defects on the crack initiation life under rolling contact.[118] The model indicates that near surface voids are more detrimental than stiff defects (inclusions), and predicts that a near surface spherical void of given size and depth reduces the maximum allowable fatigue limit design pressure by 75% while a stiff inclusion of the same size, shape and location reduces it only by 25%. It is shown that a void has a greater near field effect on the stress distribution, while the effect of a stiff inclusion applies over a larger distance, and the critical points are always located at the interface of the defects and matrix.[118]

Using dislocation pile-up theory, crack initiation originating at the surface and subsurface are treated as extreme cases. Surface initiation life is predicted to be shorter than the subsurface cracks under the same stress conditions since a lower dislocation density is needed for surface crack initiation. Factors such as residual stress, hardness, temperature, are taken into consideration. The higher the hardness, the longer the crack initiation life.[125] A critical strain concept is proposed in a model, which assumes that cracking is to occur when the accumulated strain energy of the dislocation reaches a critical value.[135]

Some models are directly applicable to rail/wheel contact problems. It is a general trend that RCF life increases as normal contact pressure decreases. At a given P_0, RCF life shortens as the T/P ratio increases. Creepage, i. e. slide/roll ratio, also has a significant effect.[20,37] In tests including creepages of 0, 0.3, 0.5, 0.7, 1, 2, 3, 5, and 10% at a constant normal pressure, surface RCF life was drastically decreased as creepage increased from 0 to 0.3%, while RCF life was extended when the ratio increased further,[20] showing the complexity of the effect, Figure 1.15.

Empirical models have been developed based on small scale laboratory tests on rail materials. A model incorporating maximum contact pressure and creepage has a form as:

$$N = fP_0\,\phi(\xi) \qquad (1.20)$$

where N is surface RCF life, P_0 is the maximum contact pressure, and ξ, a slide/roll ratio. Based on experiments on pearlitic rail steels with different hardness and interlamellar spacing, a model incorporating contact pressure, and hardness has been developed.[13,73]

RCF life in the model holds a linear relation with P_0 over the maximum contact pressure range of 900 to 1400 MPa, and is expressed as:

$$N = 0.045P_0-0.00022P_0H+0.33H-67 \tag{1.21}$$

where P_0 in MPa, and H is Knoop hardness (@ 500 g load)

The only material property incorporated in the models, so far, is hardness, which is one of the most important parameters in RCF life prediction, although other material properties, such as strain hardening behavior, cyclic stress-strain responses may play a very important role. The constants in the model are derived from linear regression using the data from RCF tests.[11] The model is empirical and is limited to the materials it is based upon. The model did not predict the RCF life of bainitic steels very well.

An attempt was also made to include a lubrication effect by using RCF life under water lubrication as a baseline.[13,73] The RCF life under other lubricants can be obtained from an empirical model expressed as:

$$N_{lub}=(\mu_{water}/\mu_{lub})^k x N_{water} \tag{1.22}$$

where μ is the coefficient of friction, and k is a constant obtained from the experiment.

The main concern is that the models are based on small scale specimen laboratory tests. It is valuable for predicting the trend of RCF performance and assessing RCF resistance of various materials. However, using these models to predict surface RCF life of rails requires a lot of work to bridge small scale laboratory test data to rail service life in practice.

1.4 RELATION BETWEEN MECHANICAL PROPERTIES AND RCF

1.4.1 Strength and Hardness

The majority of rail materials are plain carbon, silicon and manganese eutectoid pearlitic steels (STD), with 0.4 to 0.8 % C and 0.6 -1.4% Mn,[3,4] and a hardness range of 280 to 360 HB. Different "premium-alloy" rails have been developed by increasing the alloy content or adding other alloy elements such as chromium, molybdenum and vanadium.[3] Surface RCF resistance of pearlitic rail steels has been investigated and linked with some of the material properties, mainly strength and hardness.

High strength materials are found to be superior, since plastic deformation will be reduced.[62] Hardness is one of the most important mechanical properties in dictating RCF performance. Numerous experiments have shown that the RCF resistance increases as hardness increases. High strength head-hardened rail steel of fine pearlitic structure exhibited increased RCF life compared to conventional plain carbon rail steels.[59,62]

The strength of pearlitic steels is determined by the pearlite interlamellar spacing, the pearlite colony size, and the strength of the matrix. The smaller the colony size and the finer the spacing, the higher the RCF resistance. As the interlamellar spacing decreases, the hardness increases, and so does the RCF resistance[13,44,59,62] The improvement in strength of pearlitic steels generally has been achieved through two approaches, by alloying additions of silicon, manganese, and chromium; and by heat-treating to achieve fine pearlite spacing.[62,64,72,76,78]

However, RCF resistance does not always increase with increasing equivalent carbon content and hardness. A test of various pearlitic steels showed that as hardness increases, the resistance to RCF increases and peaks at Brinell hardness of 380, but did not increase with further increasing the hardness.[64] An experiment at FAST showed that under improved lubrication, the dominant mechanism of gage face failure appeared to be RCF spalling rather than wear, and STD rail steels benefited much more than head hardened (HH) and other alloyed premium steels (CrMo, CrV, SiCr...) with the lubrication.[12] This finding indicates that increased hardness in premium rail steels may not necessarily achieve the expected performance under surface RCF conditions. It has been pointed out that hardness varies with position and time.[140] It can depend on temperature, sliding speed and the chemical environment. Transfer of materials and subsequent mechanical mixing strongly influence local hardness.[140] The relative hardness, i. e. a ratio of rail to wheel hardness, rather than rail hardness alone, proves to be a more relevant parameter in evaluating a rail/wheel system wear,[148] and the parameter may be important in RCF performance as well.

A pearlitic microstructure was demonstrated to be superior to tempered martensitic and bainitic structure with the same hardness in wear[62,72,81,83] and in some cases of RCF.[62,72,77] The advantage of a pearlitic microstructure is that the cementite lamella are able to line up parallel to the surface under rolling/sliding, rotating during shear plastic deformation, thus producing alternating hard and soft regions with decreased interlamellar spacing. The realignment was facilitated by both fracture and the plastic deformation of lamellae, as shown in Figure 1.9. The soft ferrite matrix was severely deformed, allowing a reduction in the interlamellar spacing on approaching the contact surface and most of the lamellae were broken into small particles.[44] The effect of this realignment is to produce an increased area fraction of hard cementite plates on planes parallel to the surface, and thus increase the worn surface hardness since the hardness of cementite is 1000 to 1500 Hv, while martensite is only 500 Hv. This provides better wear resistance than martensite and bainite microstructures, which do not modify and enhance their microstructures in such a way.[39]

But, the structure realignment may have different effects in RCF. The hard particles and narrow hard barriers that benefit wear resistance may not be necessarily effective in RCF. Since under RCF, shear flow bands often provide a favorable path for cracks to grow, material properties dictating the crack growth resistance is in the weakest orientation, where toughness may be very important. In practice, HH steels are often reported to spall prematurely, raising a concern for ductility and toughness.

To meet the demand of ever-increasing axle loads, in addition to improving the existing materials, other materials may need to be explored, since pearlitic steels developed over the past 60 years may soon approach the limit of their capacity.[61] Recent investigations have reported a superior wear resistance in low carbon bainitic steels compared to a premium HH rail steel.[82] Contrary to the previous finding that increasing hardness beyond 38 to 40 HRC for a pearlitic steel gained nothing in terms of wear resistance,[81] increasing hardness of the lower bainite and mixtures of upper and lower bainite to hardness of 54 and 49 HRC achieved much greater resistance to type III wear than pearlite of 39 HRC.[146] An investigation on surface RCF performance of potential rail materials, particularly those low carbon bainitic steels,[82] would be beneficial.

1.4.2 Cyclic Stress-Strain Properties

The cyclic stress-strain behavior of pearlitic eutectoid steels is strongly dependent on the interlamellar spacing and strain amplitude, with cyclic softening in fine pearlite, cyclic hardening in coarse pearlite, and both cyclic softening and hardening in medium pearlite at low and high strain amplitudes, respectively.[65] Cyclic hardening is generally concurrent with dislocation cell formation. As the interlamellar spacing or plastic strain amplitude increases, the dislocation cell formation occurs more readily, and the cell size decreases with increasing strain amplitude. The fine spacing and high hardness pearlitic steels have a benefit of high strength, but also result in cyclic softening.[80]

In a test on rail materials of STD, HH and Cr-Mo and Cr-V alloys, all four materials were cyclically softened at a low strain level then cyclic hardened at high strain levels.[66] However, the strain range covered in this study only reached about 1.5%, and the cyclic hardening was only obvious in the STD steels. The results of cyclic stress-strain properties of a 0.82 C, 0.87 Mn eutectoid pearlitic steel showed cyclic softening over the strain range of 0.15-0.3% and cyclic hardening when the strain was greater than 0.6%.[67]

A laboratory test showed that HH and Cr-Mo had longer strain life compared to STD and Cr-V steels, and FAST test results supported that data showing that the HH and Cr-Mo had superior fatigue resistance.[66] However, a low cycle fatigue test showed that a conventional STD steel had a higher fatigue resistance than a high alloy steel at a high strain level.[69]

With all these data available, the question remains as to how uniaxial cyclic stress-strain data can be used for RCF resistance assessment where the stress-strain state differs considerably for rolling/sliding contact. The research on the correlation between RCF performance and uniaxial cyclic stress-strain behavior should be conducted before any meaningful conclusions can be drawn.

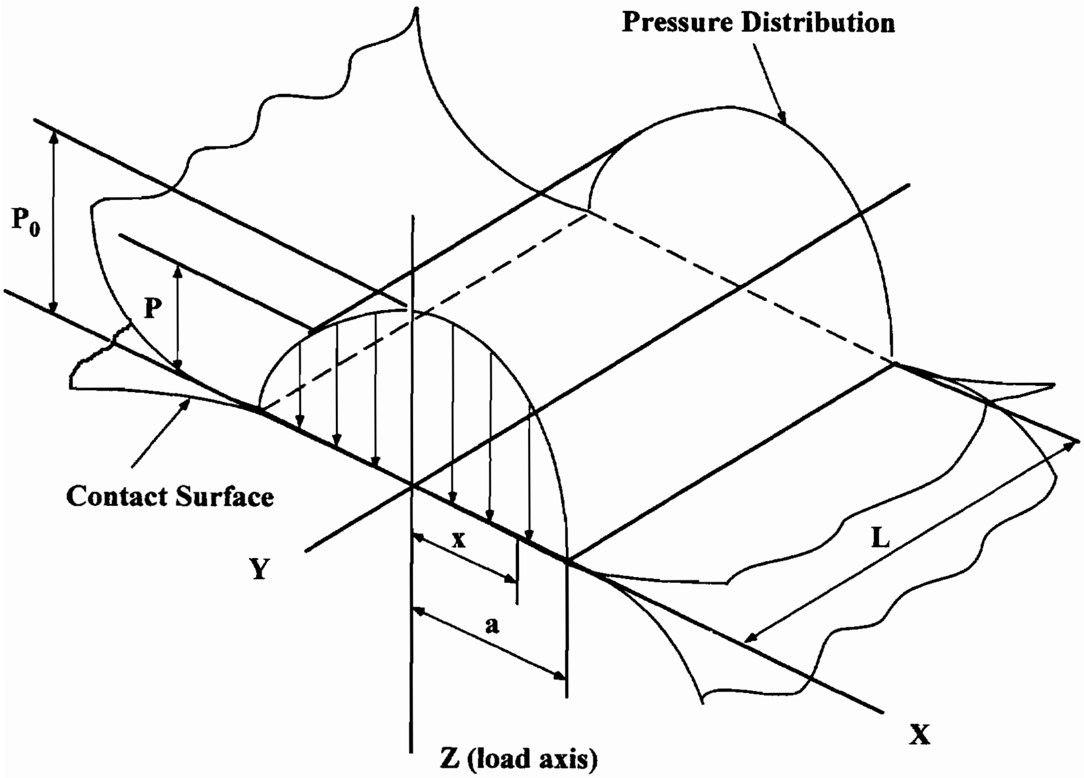

Fig. 1.1. Contact patch and pressure distribution for two elastic cylinders in two-D line contact.

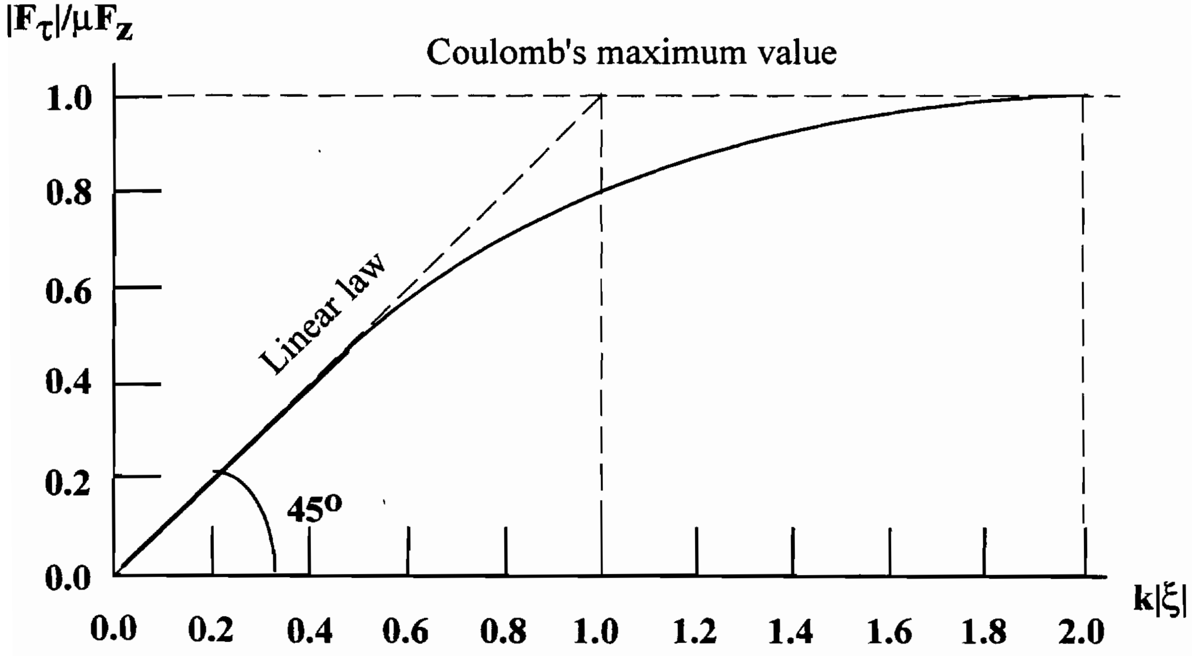

Fig. 1.2. Relationship between tangential force, F_τ, and slide/roll ratio, ξ.[17]

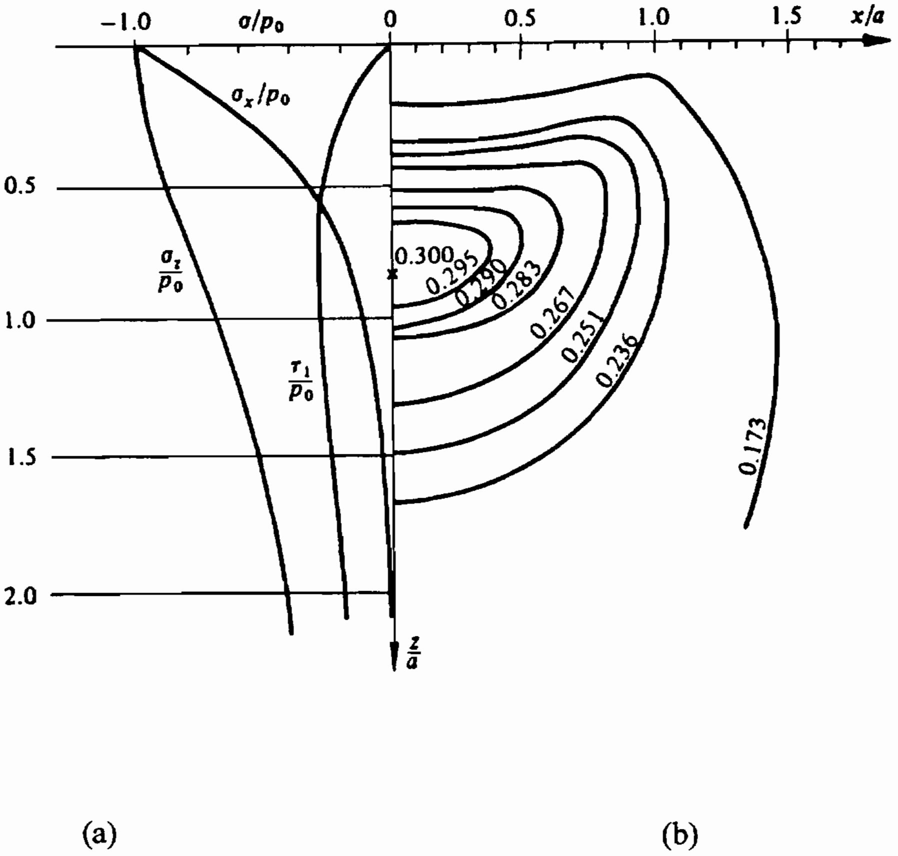

Fig. 1.3. Contact of cylinders under pure rolling (a) subsurface stresses along the axis of symmetry (b) contours of principal shear stress. [16]

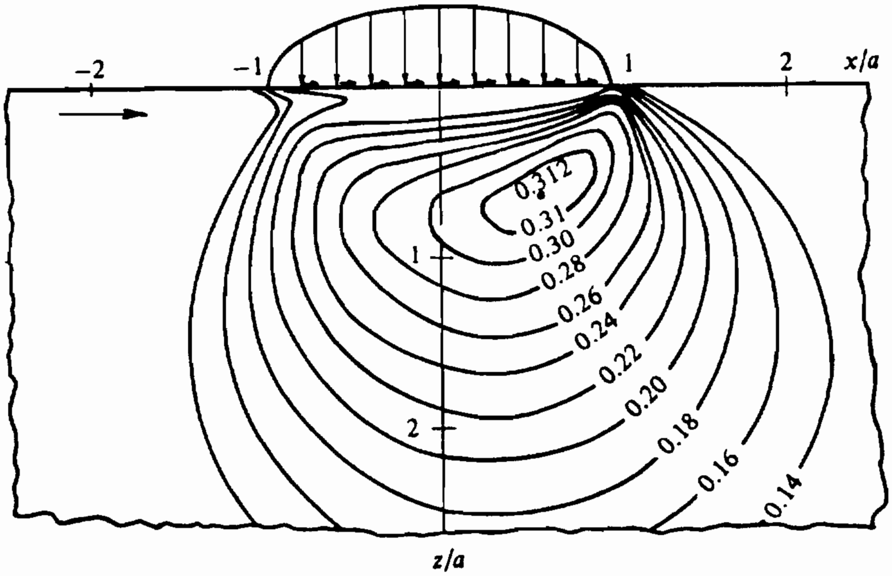

Fig. 1.4. Contours of the principal shear stress with tangential traction (T = 0.2 P).[16]

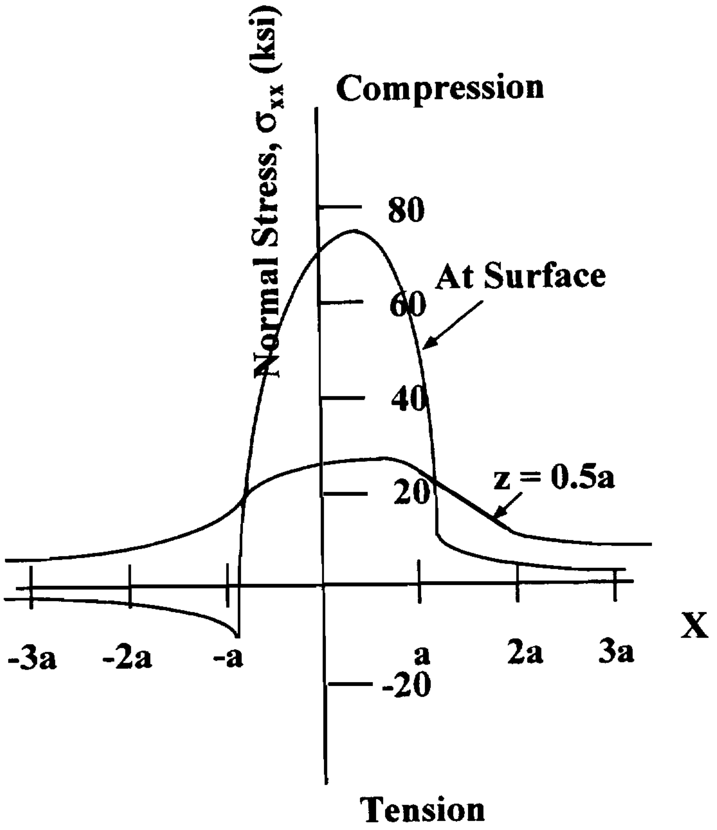

Fig. 1.5. Tensile stress at an edge of the rolling/sliding contact interface. [15]

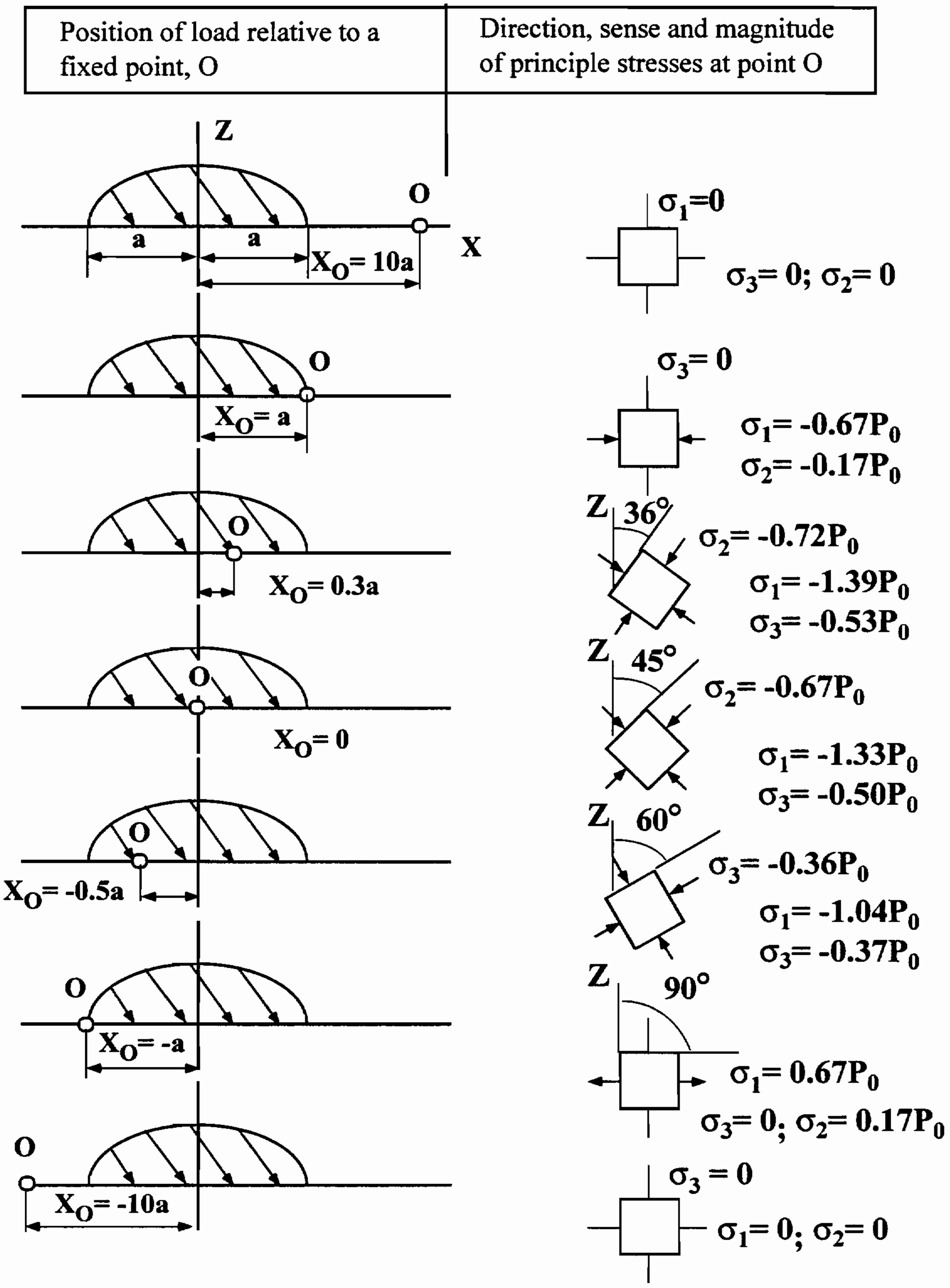

Fig. 1. 6. Changes in magnitude , sense and direction of principal stresses at a fixed point O at the surface, as a load moves past it. [15]

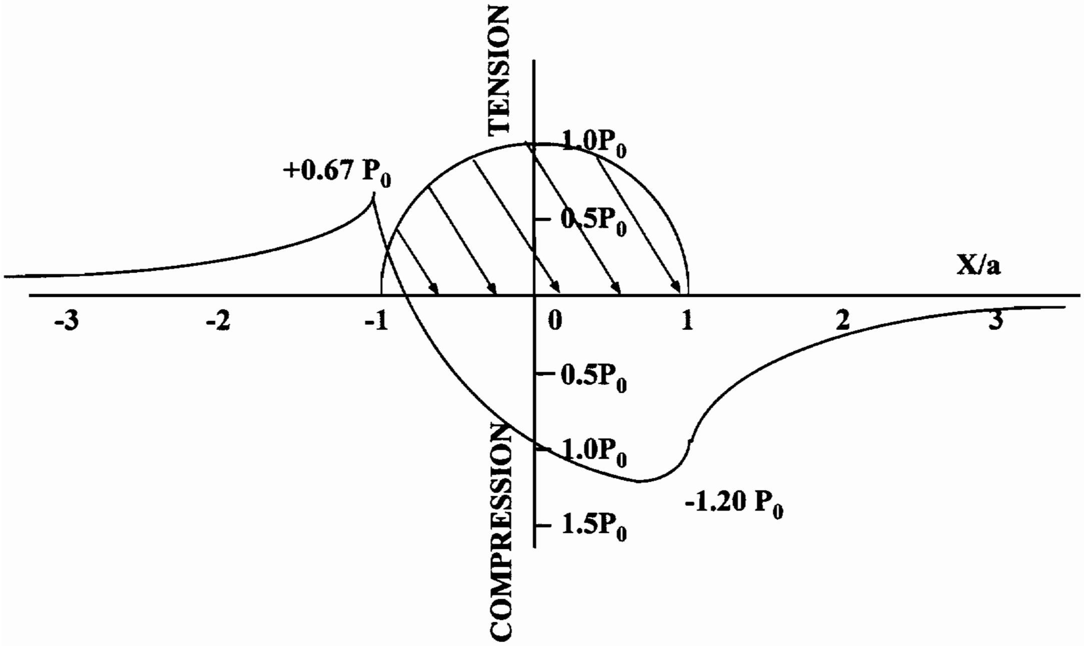

Fig. 1.7. Stress range of σ_{xx} at point O during one contact cycles. [15]

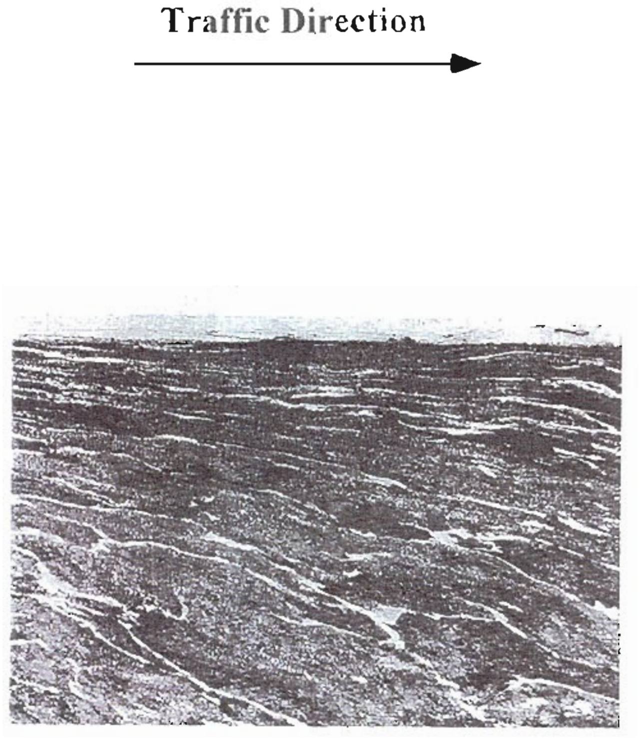

Fig. 1.8. Longitudinal/vertical section through bright running band showing plastic flow in the opposite direction to traffic. [11]

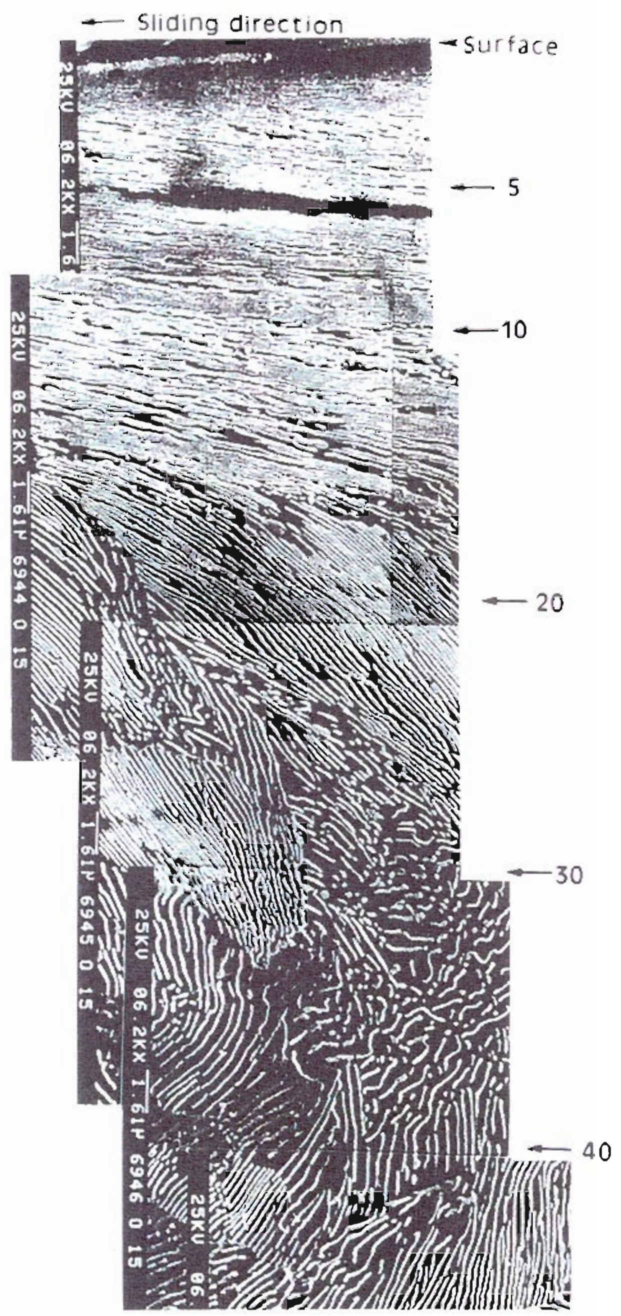

Fig. 1.9. Plastic deformation of pearlitic microstructure, lamellae have been blended, broken and plastically deformed.[39]

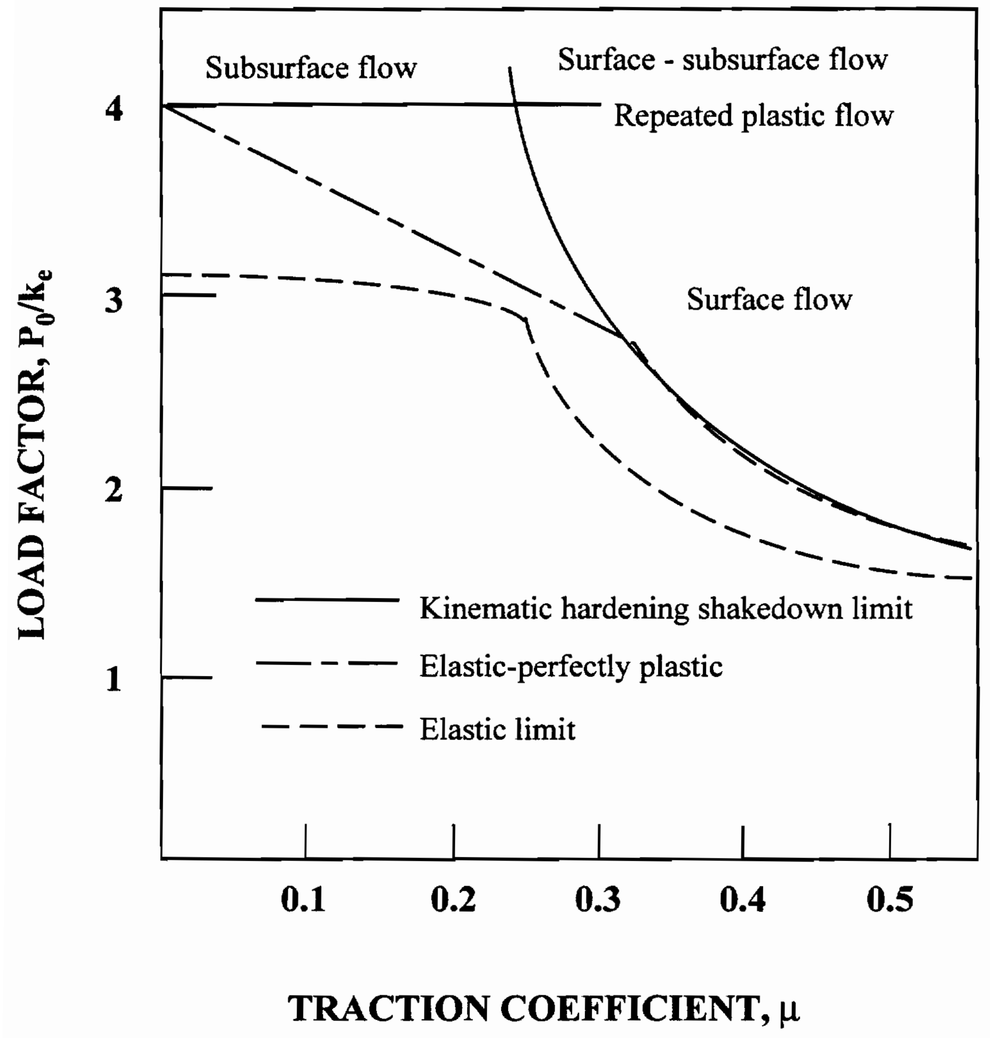

Fig. 1.10. Shakedown map. [24]

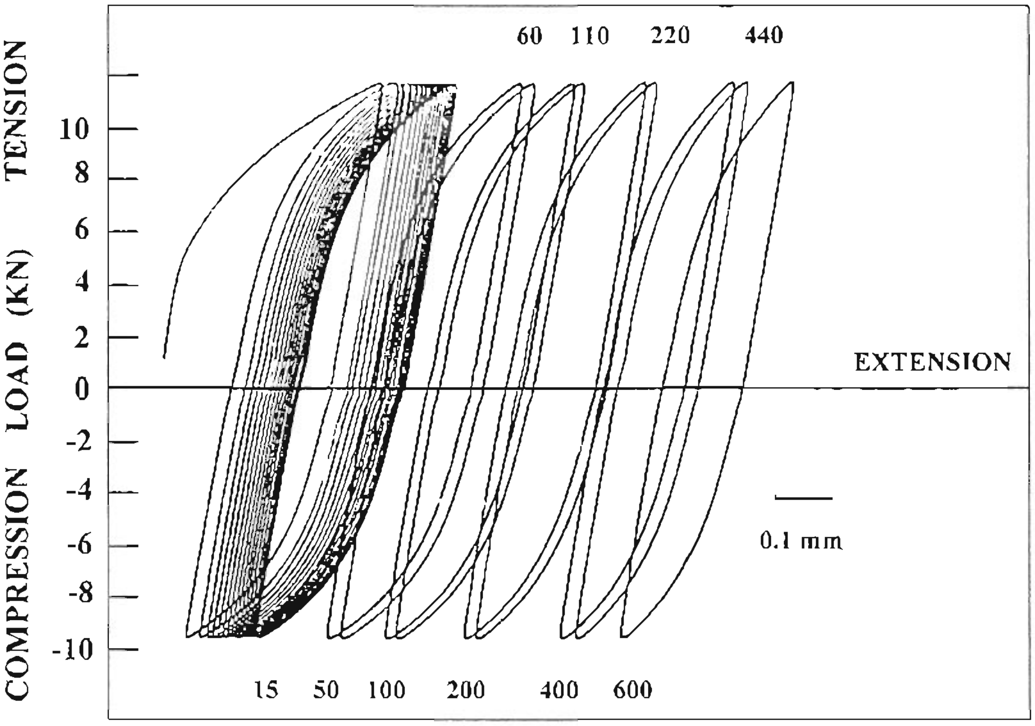

Fig. 1.11. Ratchetting behavior of a rail steel under cyclic load-controlled tension-compression test with a mean load. [24]

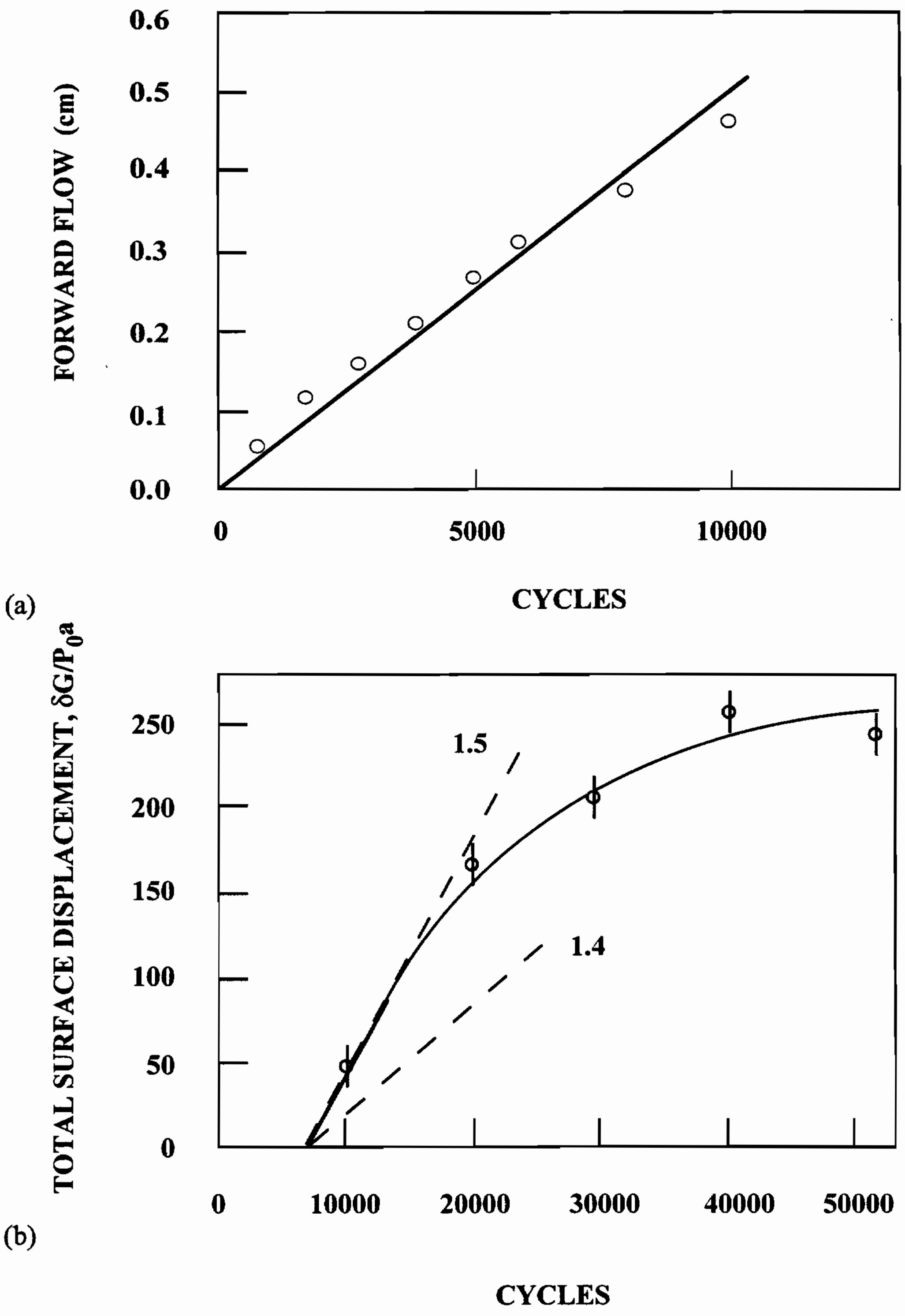

Fig. 1.12. Cumulative surface forward displacement (a) for copper[28] (b) for rail steel.[24]

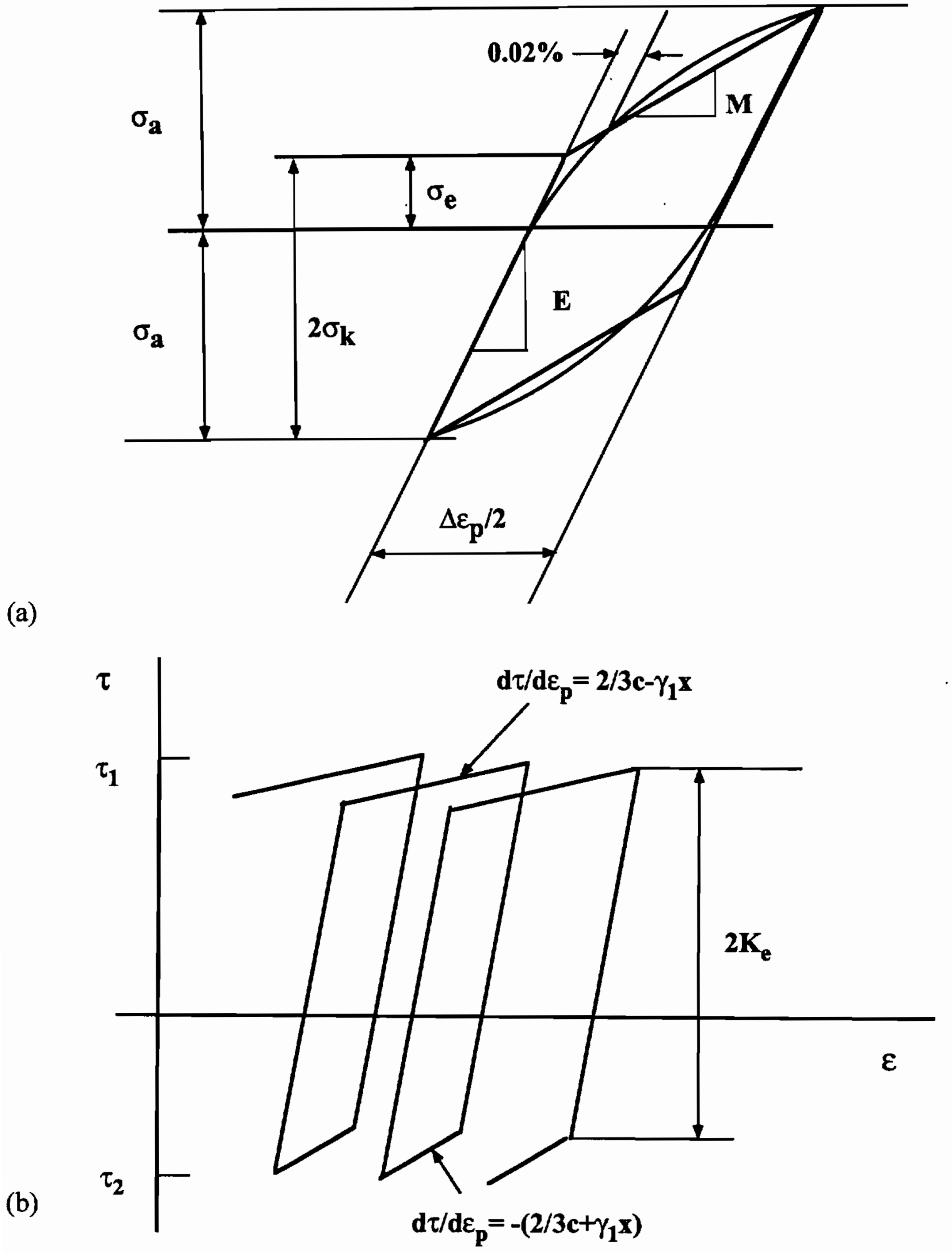

Fig. 1.13. (a) Elastic-linear-kinematic plastic representation of stress-strain hysterisis loop for a rail steel, [48](b) Non-linear kinematic hardening under proportional cyclic loading. [54]

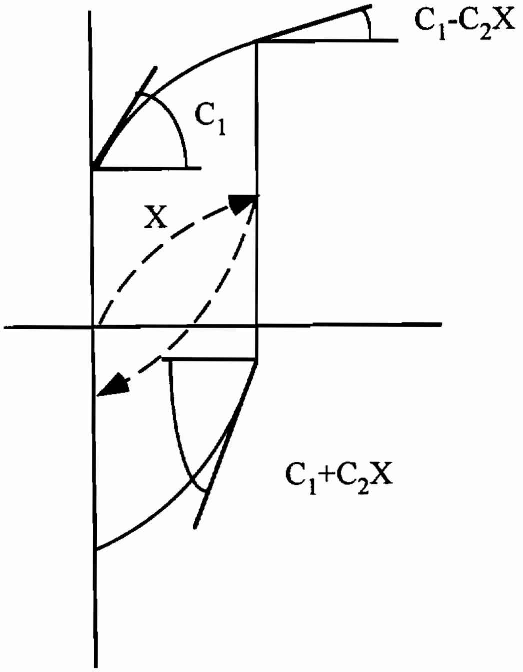

Fig. 1.14. Schematic illustration of non-linear kinematic hardening by a uniaxial stress-strain curve. [92]

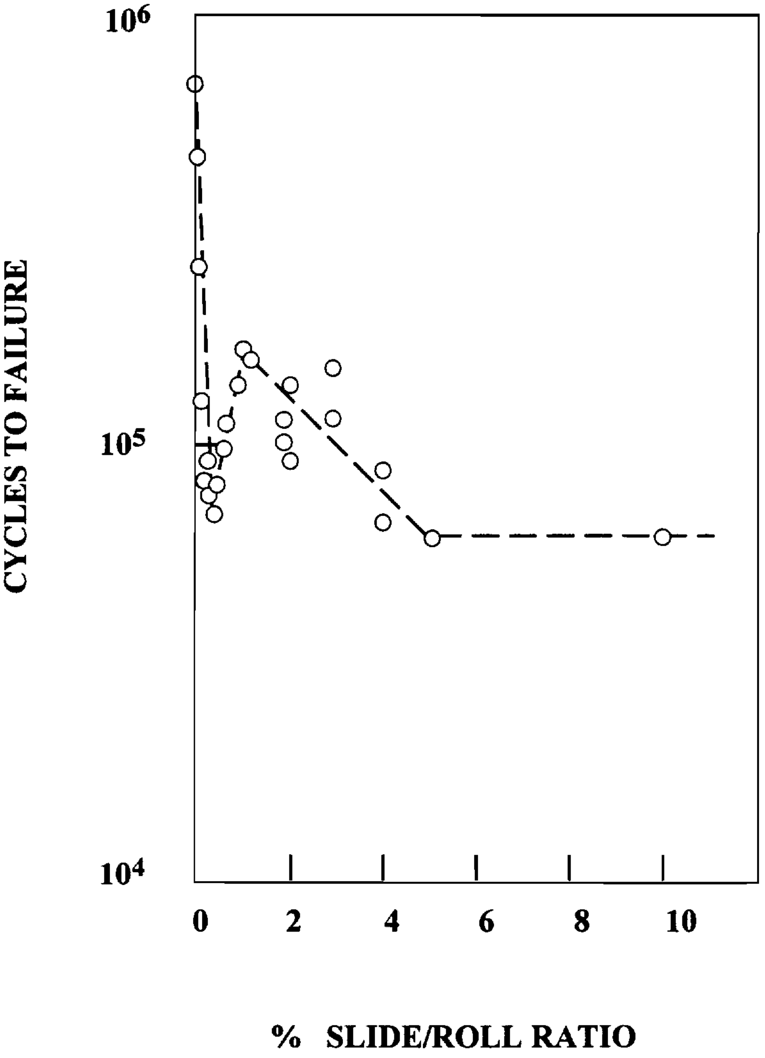

Fig. 1.15. Rolling contact life as a function of slide/roll ratio (water lubrication, $P_0 =$ 1500 MPa).[20]

CHAPTER 2

EXPERIMENTAL PROCEDURES

The experimental work includes three parts: RCF performance tests, ratchetting strain measurements, and a mechanism study through SEM, optical microscopy (OM) and microhardness profile measurements. The effect of liquid lubrication was investigated as a part of the mechanism study, in using oil and water as lubricants.

2.1 MATERIALS

Two pearlitic rail steels, STD (standard carbon) and HH (head hardened), and four low/medium carbon bainitic steels J1, J2, J4 and J6 have been investigated. The chemical composition and mechanical properties are listed in Tables 2.1 and 2.2. Microstructure of the materials are shown in Figure 2.1a through Figure 2.1f. Compared to the STD steel, the interlamellar spacing and the prior austenite grain size of the HH are finer. The fine interlamellar spacing gives rise to increased hardness and strength in this steel.[13,44,59,62] Wrought microstructures of the bainitic steels are summarized in Table 2.3. The bainitic microstructures were all produced by continuous cooling in air. These steels have been developed to test wear performance for potential applications in rails at OGI.[70] Results of wear performance tests have indicated that water quenched J1 and as-received air cooled J6 are superior in wear resistance compared to a pearlitic HH steel.[70] Detailed information on heat treatment, chemistry, microstructure, and wear performance can be found elsewhere.[70]

2.2 SURFACE RCF PERFORMANCE TESTS

RCF tests were carried out with an Amsler twin-disc rolling/sliding test machine. The test rollers are mounted on two parallel rotating shafts and the load is applied by a compressed spring. Figure 2.2 shows the Amsler test fixture. Contact loads were within the range of 700 to 5000 N, producing maximum contact pressures of 850 to 2300 MPa. The highest maximum contact pressure in previous tests conducted at Oregon Graduate Institute was 1440 MPa.[13,59] The contact pressure in current research is much higher than that in previous investigations, because an attempt in current research is to simulate the increased axle load conditions in practice.

Specimen geometries are shown in Figure 2.3. The truncated cone-on-flat geometry was used for the top roller to enable high contact stresses to be achieved while providing sufficient support for the running track. The materials for pearlitic steel specimens were cut from rail heads. The orientation of the test rollers is illustrated in Figure 2.4 (a), with the running track of the test rollers perpendicular to the longitudinal direction of the rail. The effect of specimen orientation on RCF performance was investigated in previous research[13] for the same STD steel, and no effect was discovered. Bainitic steel specimens were all cut from the 3"x3" rolled square bars, and the orientation is shown in Figure 2.4.(b).

For the case of two contacting cylinders with their axes parallel, the maximum hertzian contact pressure can be calculated from[63]

$$P_0 = 0.418\,[NE(R_T+R_B)/LR_TR_B]^{1/2} \qquad (2.1)$$

where R_T and R_B are the upper and lower roller radii respectively, E is Young's modulus, L is the width of a contact track and N is the applied normal load. The load is transmitted through a narrow interface contact patch, which is a rectangle with area of 2a by L. A half contact patch width, a, is calculated by

$$a=1.13[(P\Delta R_1R_2)/(L(R_1+R_2)]^{1/2} \qquad (2.2)$$

$$\Delta=(1-\mu_1^2)/E_1+(1-\mu_2^2)/E_2 \qquad (2.3)$$

Both top and bottom rollers were made from the same material for all the materials tested but the upper roller normally fails because it is the driven or slower moving roller. The roller dimensions were selected to provide a slide/roll ratio of 10%, as calculated by :

$$\text{Slide/Roll Ratio} = 2(1.104D_B-D_T)/(1.104D_B+D_T) \qquad (2.4)$$

where, D_T and D_B are the top and bottom roller diameters respectively. The bottom shaft rotates 1.104 times faster than the upper shaft.

The coefficient of friction, μ, is a crucial parameter in rolling/sliding contact, and it was calculated according to moment readings as:

$$\mu = 2.75M/(PR) \qquad (2.5)$$

where 2.75 is a constant adjusted for this specific machine; M is the moment; P, an applied load; and R, a radius of the driving roller. Tangential traction, T, is related to normal contact pressure through the coefficient of friction as:

$$T = \mu P \qquad (2.6)$$

At all times throughout a test both rollers were covered by a water film maintained by a constant feed of 40 drops per minute adjusted manually. The water was tap water, and was cut off automatically by an electronically controlled valve as soon as a test was stopped.

A counter on the bottom shaft recorded the number of revolutions during a test. The criterion of failure used to determine RCF life involves either the loss of surface material as spalling or a collapse of the fatigue damaged surface. These events lead to an increase in the vibration level which is detected by an accelerometer mounted on the machine. When the vibration reaches the preset value the accelerometer activates a cut-off switch and the test is stopped. The contact cycles to failure thus included both crack initiation and crack growth.

2.3 MECHANISM STUDY

A study of the used rollers of RCF performance tests was carried out by optical (a Nikon Epiphot microscope) and SEM (a Zeiss Model) observations and microhardness measurements (a LECO M–400 hardness tester) to obtain information on crack morphology, surface layer deformation patterns and microhardness profiles. The metallographic samples were cut through the longitudinal cross section plane parallel to running tracks of the tested rollers, then polished and etched with 2% nital. The microhardness data were measured on the subsurface of the same plane, traversing from the near surface down to about 1.2 mm in depth. Two to three traverses were repeated on each sample. The load used was 300 and 500 grams.

A preliminary study on the effect of liquid lubrication was initiated in this study. Liquid lubrication plays a significant role in surface RCF, such as modifying coefficient of friction, varying contact conditions and failure modes, and as well as bringing about possible environmentally assisted cracking. However, the focus of this research is the effect of water and oil lubrication upon RCF crack growth, in terms of crack length, depth, surface damage characteristics, and on the crack growth mode.

Experiments for this purpose were conducted with STD steel only, using the same specimen geometries as in RCF performance tests. The maximum contact pressures (P_0) were 1874, 1448, and 1295 MPa, yielding P_0/k ratios of 6.03, 4.66 and 4.16, respectively. An initial dry running period was applied at the beginning of each test, 1000 cycles for P_0 = 1874, and 2000 cycles for P_0 = 1448 and 1295 MPa. The initial dry period was intended to initiate cracks with similar density, depth and length distributions. A simple mineral oil and water with pH of 6 were then applied after the dry running, covering the rolling tracks at all times. The total contact cycles used for both oil and water were identical, 5,000 cycles for P_0 = 1874 MPa, 23,600 cycles for 1448 MPa, and 100,000 cycles for 1295 MPa. Crack morphology, in terms of depth, length, surface damage, and the crack depth with respect to deformation layer, were examined by microscopy.

2.4 RATCHETTING STRAIN MEASUREMENT

2.4.1 Split Rollers and Strain Derivation

Two materials, STD and J2, were used for ratchetting strain measurements, with the focus on the STD steel. Split rollers were used for the experiments, Figure 2.5, with the two halves bolted tightly together during a test. Prior to testing, the interior faces of the two half rollers were polished to 1 μm, and then machined to the final diameter to avoid any edge rounding due to polishing.

Grids and indentations were engraved on the inner faces of the split rollers to serve as markers. Two methods were employed to make grids, one was by a scratch tester, the other by micro machining. Grids of 40 lines per mm were cut by a diamond tip scratch cutter under a 50-gram load. The spacing between grids and the travel distance of the diamond tip were manually controlled by operating a X-Y stage. This method was time consuming, approximately two hours for a net of grids of 1.2 mm by 1.2 mm square. Micro machined grids were 50 lines/mm, and the spacing was precise, but the method was much more expensive. Photographs of these grids are shown in Figure 2.6. A set of indentations spaced 0.1 mm apart were produced by a LECO M-400 Vicker's hardness tester loaded at 500 to 1000 grams. A typical length of the indentation lines was about 1 mm down into the subsurface to guarantee that a portion of the line would remain undeformed, and thus serving as a baseline. Each inner face of the split rollers contained at least three groups of indentations distributed along the periphery. Figure 2.7 shows a group of indentations before and after deformation.

Indentations were much easier to make than grids. Most importantly, due to severe shear deformation, shallow grids were blurred making measurements impossible, while deeper indentations proved more durable. The strain data were all obtained through measuring displacement of lines of indentations.

The greatest advantages of the split roller design is that it enables periodic measurements of shear displacement without sectioning of rollers. However, two free surfaces are created on the symmetry plane modifying the stress state experienced by a solid roller. To compare the deformation for the two cases, scratches perpendicular to the longitudinal rolling direction were engraved on the running surface of samples of both. Four tests were conducted with solid and split rollers to compare displacement of the scratches at identical loads and cycle intervals. Additionally, a profilometer (a Mitutoyo surface roughness tester) was used to assess the out-of-plane deformation on an interior face of a split roller.

Tests were conducted at contact loads ranging from 2250 to 4150 N producing P_0/k values of 4.94 to 6.71. Measurements were made at six contact pressure levels, P_0 = 1536, 1635, 1759, 1818, 1879 and 2086 MPa, intending to obtain systematic data. Water lubrication was applied and the slide/roll ratio was 10%. The coefficient of friction, μ, ranged from 0.22 to 0.24.

In RCF performance tests, an accelerometer was used to determine the total RCF life, but it was not used for split roller tests. The number of cycles to end a test was pre-decided as the average number of cycles determined for RCF life in tests for solid rollers using the same contact conditions. The solid rollers were made from the same heats of steels. The appearance and crack densities of the split rollers were comparable with those observed for solid rollers tested under the same conditions.

Subsurface displacements were measured from between 3 and 5 groups of indentations located on different sites around the edge of split rollers. The measurements were made at a magnification of 400 times using a LECO M-400 microhardness tester with a resolution of 5 µm. A rotational x-y stage made it easy to align the undeformed baseline indentations with the measurement scale.

The data derivation is schematically illustrated in Figure 2.8. The displacement versus depth results were curve fitted by polynomials with powers of 4 or 6, whichever suited the data best. The maximum displacement, u_{max} which occurred on the contact surface, z=0, was determined from the fitted curve. Ratchetting strain was derived from the displacement versus depth curve, i. e. u–z curve. Under rolling/sliding contact, the cumulative shear strain, γ_{xz}, in a cylindrical coordinate with the origin located in the center of the specimen, is approximately given by

$$\gamma_{xz} = \partial u/\partial r + 1/r\ \partial v/\partial \vartheta - u/r \qquad (2.7)$$

where u and v are displacements in x ($x = r\vartheta$) and z ($z = r$) directions. The second order derivatives are omitted in Equation. 2.7. The maximum displacement, u, can reach around 400 μm, resulting in shear strain as high as 140%, whereas deformation in compression was much lower, with strains of only 1% to 2%. In addition, compressive deformation, v, occurred only during initial cycles and did not accumulate. The contribution to shear strain from compressive displacement, $1/r\partial v/\partial\vartheta$, was, therefore, neglected. The third term, u/r, at any given measurements was only about 1% to 2% of the $\partial u/\partial r$ term, thus the third term was also neglected. As the first degree approximation, the ratchetting strain at any given contact cycles was determined, as shown in Fig. 2. 8, from the maximum slope of the u — z curve, as $\gamma = du/dz_{max}$.

2.4.2 Effect of Slide/roll Ratio Tests

The effect of slide/roll ratio on ratchetting strain was investigated under a constant contact pressure of 1759 MPa. Different slide/roll ratios were produced by varying bottom roller diameters while keeping top split roller diameters constant. Slide/roll ratios employed were 0.3%, 0.4%, 1%, 5%, 10%, and 25%. Two tests were repeated at both 1% and 5% slide/roll ratios. Water covered the running surface throughout the tests. Displacement and shear strain data were obtained in the way described above.

Table 2.1. Chemical Composition of the Materials (wt%)

	C	Mn	Si	S	P	Ni	Cr	Mo	B	Ti	Al
STD	.73	.93	.28	.03	.01		.17		.001		
HH	.79	.91	.66	.01	.02		.47				
J1	.18	2.01	1.13	.01	.01		1.94	.48	.003	.03	.03
J2	.12	3.97	.27	.01	.01		.02	.47	.003	.04	.03
J4	.02	2.02	.27	.01	.01	1.93	1.96	.48	.003	.02	.03
J6	.26	2.00	1.81	.01	.01		1.93	.49	.003	.04	.04

Table 2.2. Mechanical Properties of the Materials

Material	Yield (MPa)	UTS (MPa)	RA (%)	EL (%)	K_e (MPa)	HRC
STD	538	1034	20	12	311	27
HH	790	1320	40	13	456	37
J1	846	1360	39	14	488	40
J2	830	1151	55	16	479	37
J4	721	945	69	18	416	28
J6	1002	1530	7	4	578	45

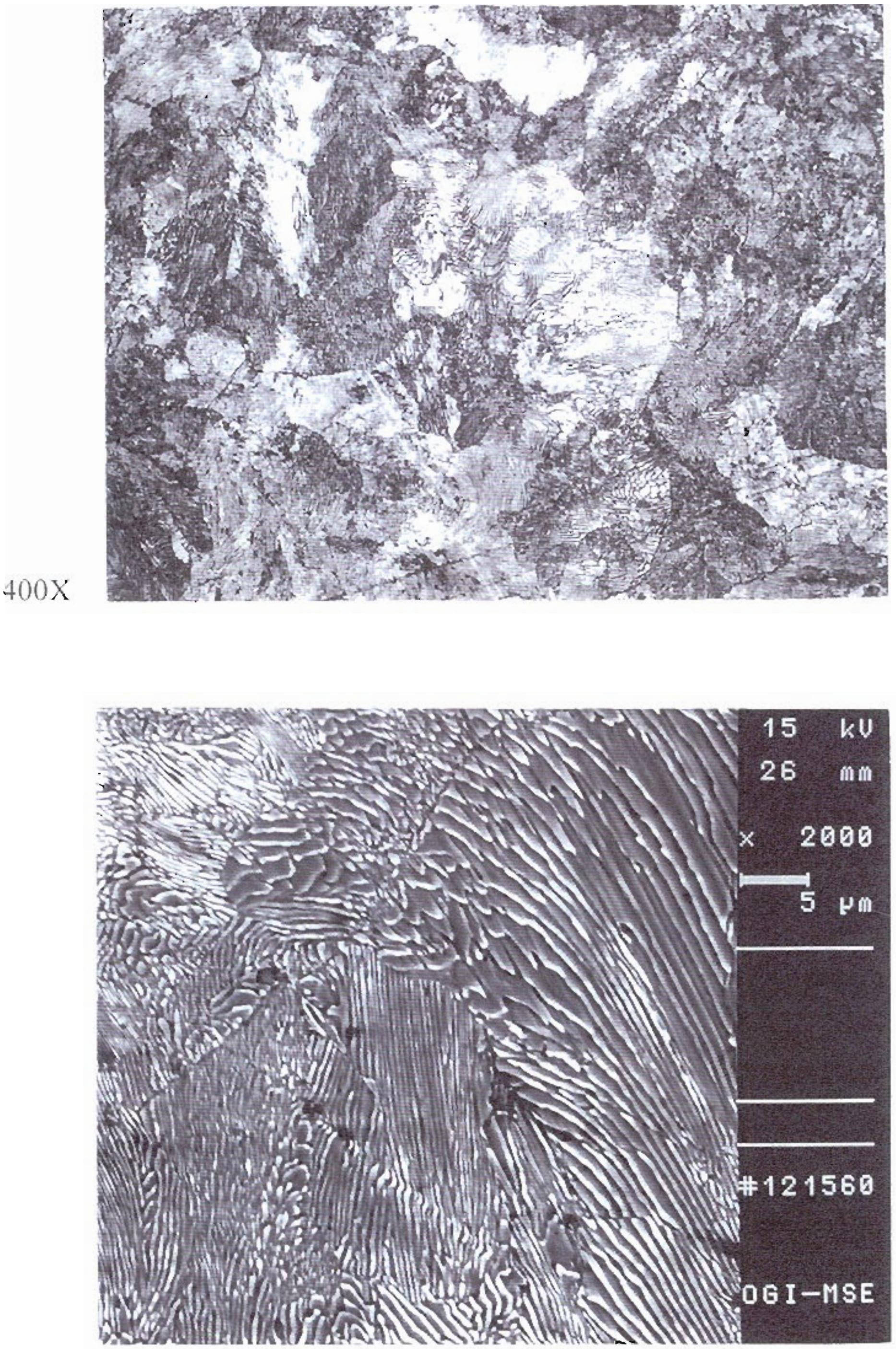

Fig. 2.1a. Metallographic photographs of pearlitic steel STD.

400 X

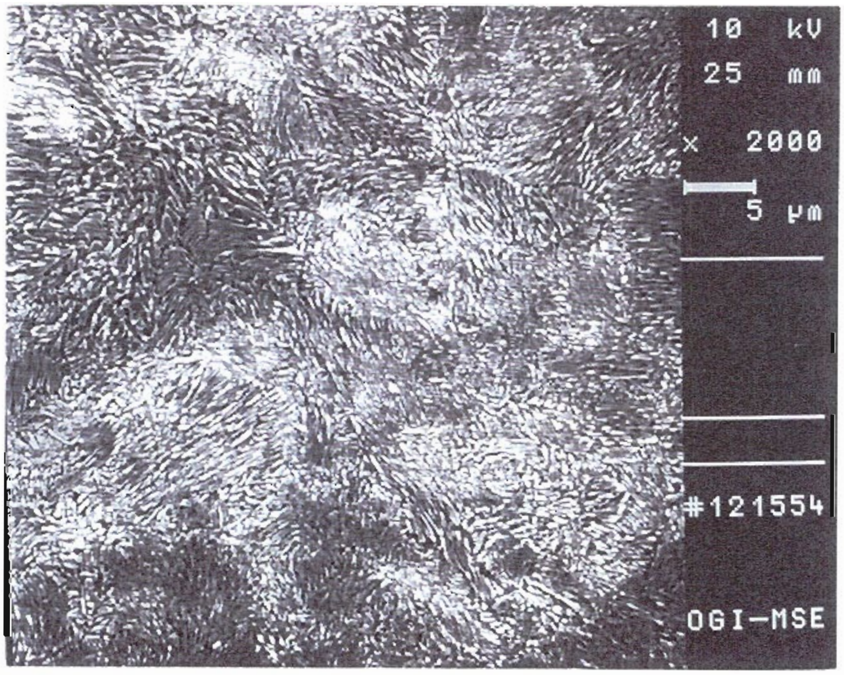

Fig. 2.1b. Metallographic photographs of pearlitic steel HH.

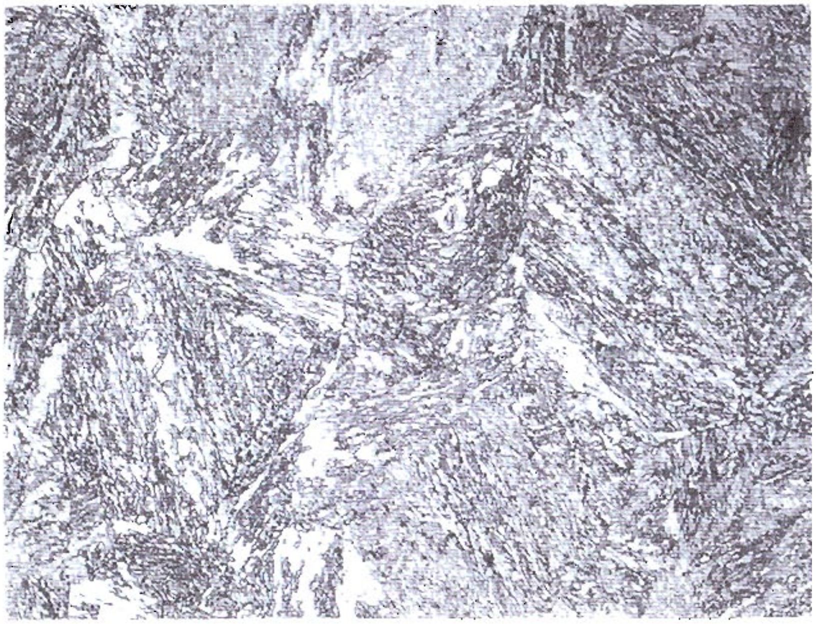

400 X

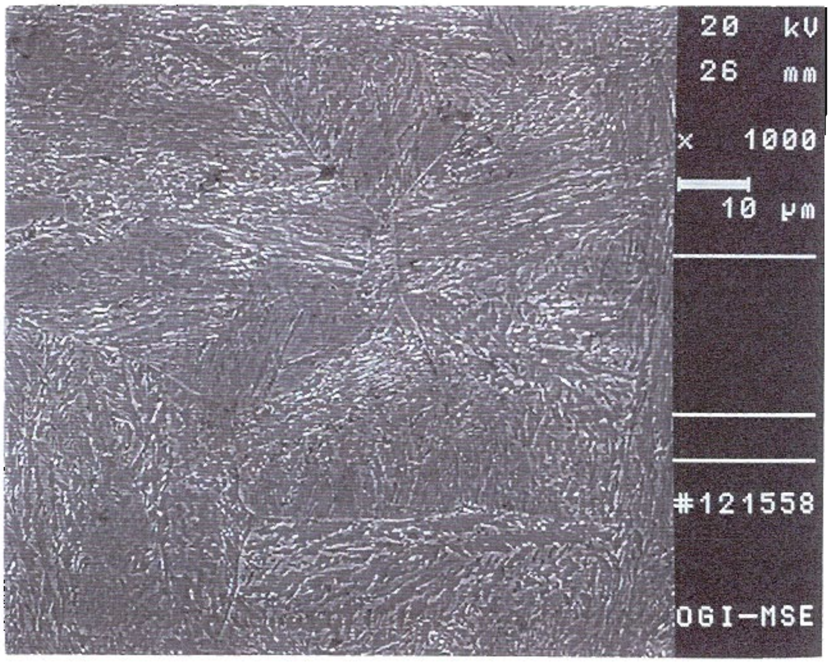

Fig. 2.1c. Metallographic photographs of bainitic steel J1.

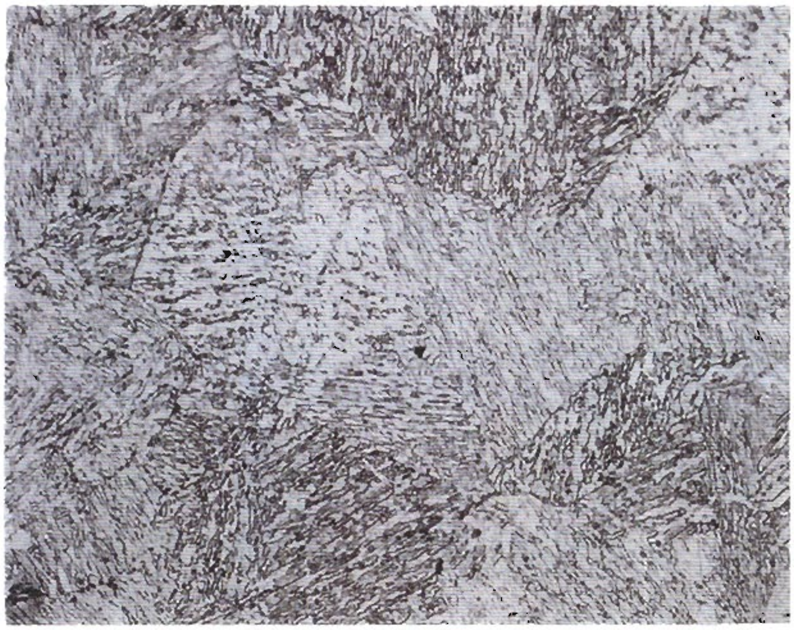

400 X

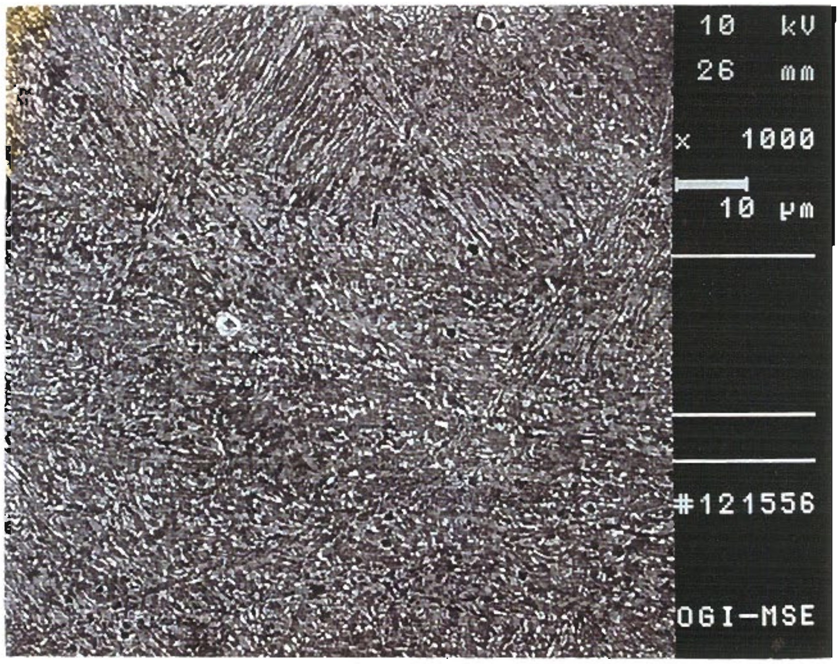

Fig. 2.1d. Metallographic photographs of bainitic steel J2.

400 X

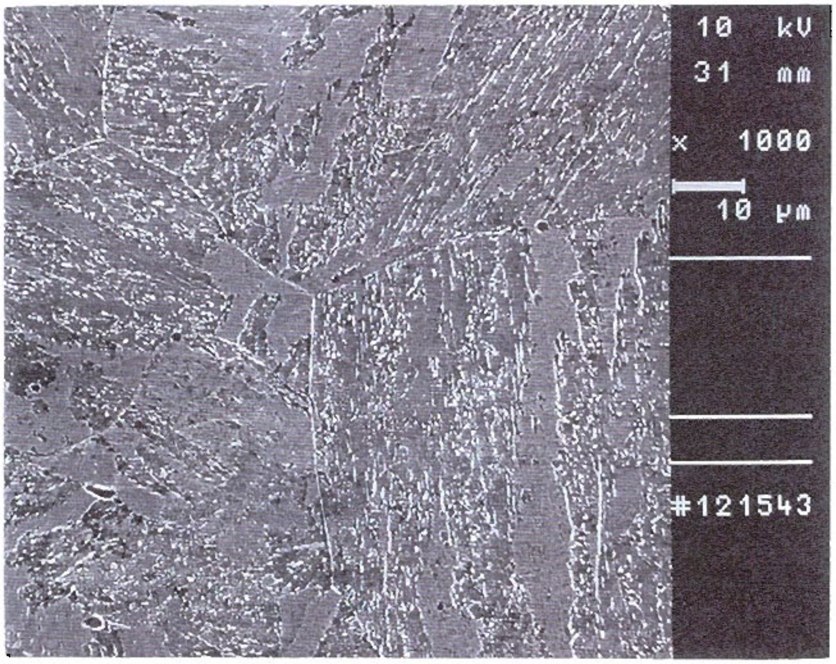

Fig. 2.1e. Metallographic photographs of bainitic steel J4.

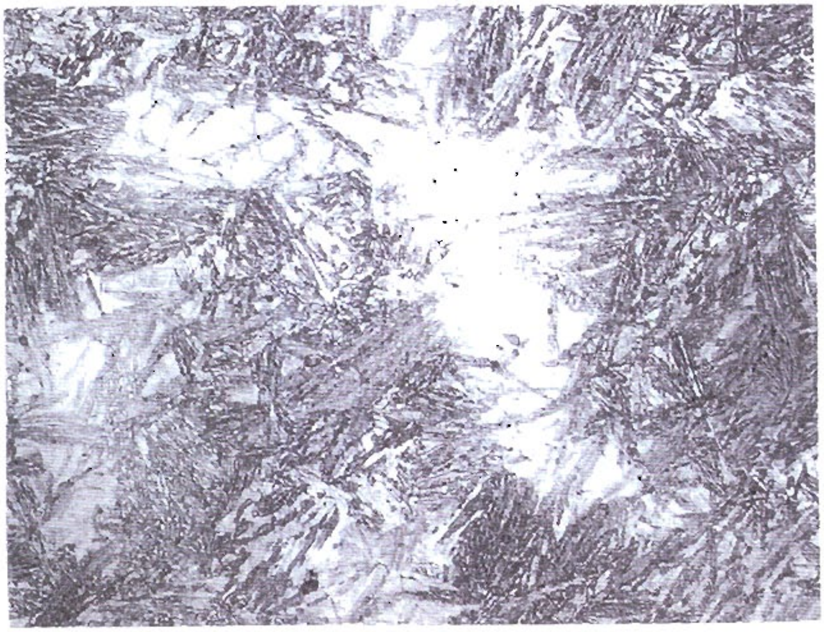

400 X

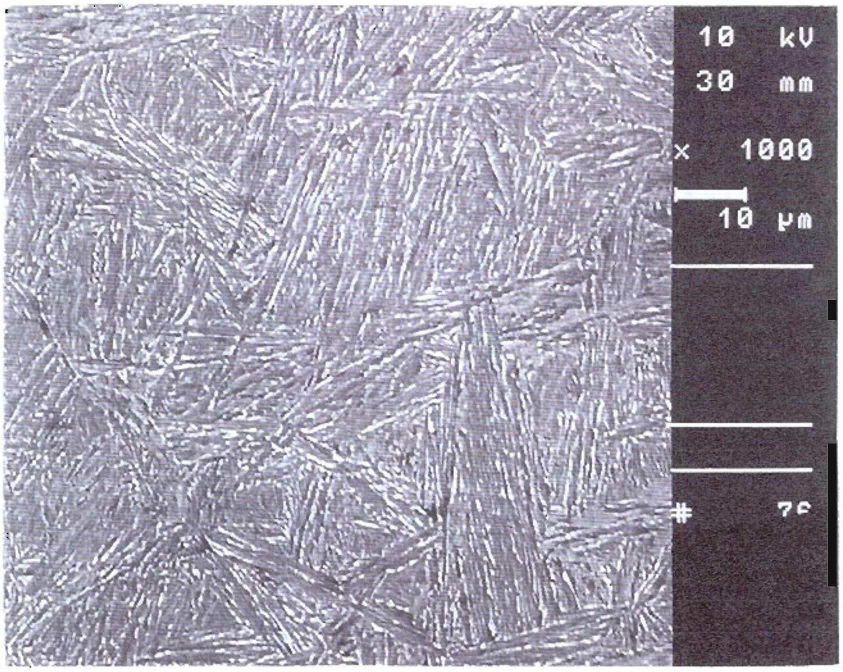

Fig. 2.1f. Metallographic photographs of bainitic steel J6.

Table 2.3. Microstructures of the Bainitic Steels

J1	J2	J4	J6
Predominantly carbide-free bainite (lath ferrite and interlath retained austenite) with some granular bainite (massive ferrite and M-A islands)	Predominantly lower bainite (lath ferrite with intralath carbides) with areas more typical of carbide-free and granular bainite	Predominantly granular bainite	Predominantly carbide-free bainite

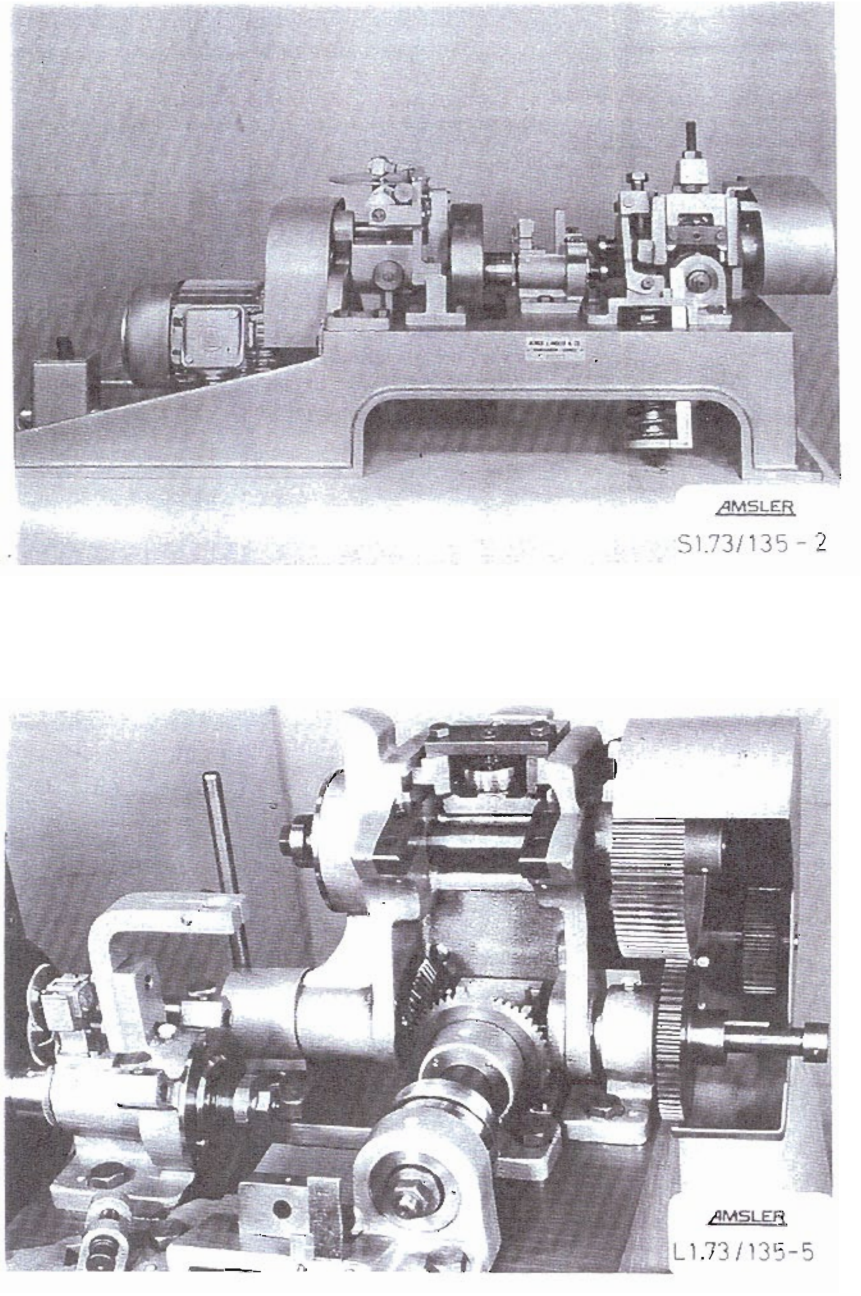

Fig. 2.2. Amsler twin-disc rolling sliding test machine.

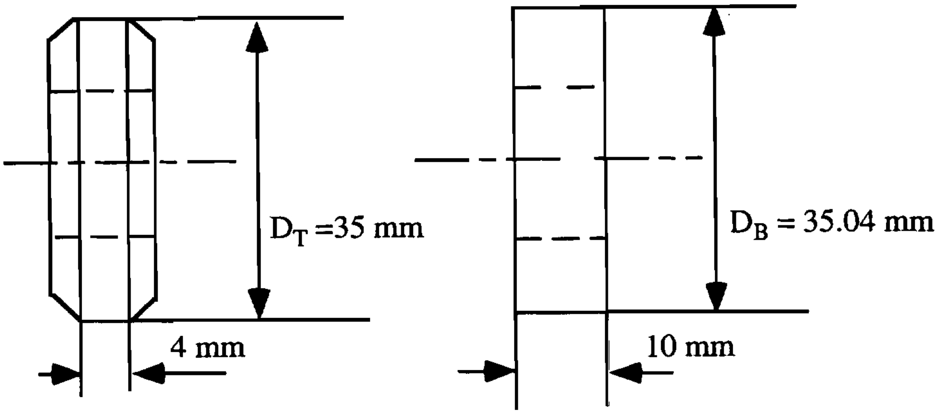

Fig. 2.3. Surface RCF specimen geometry.

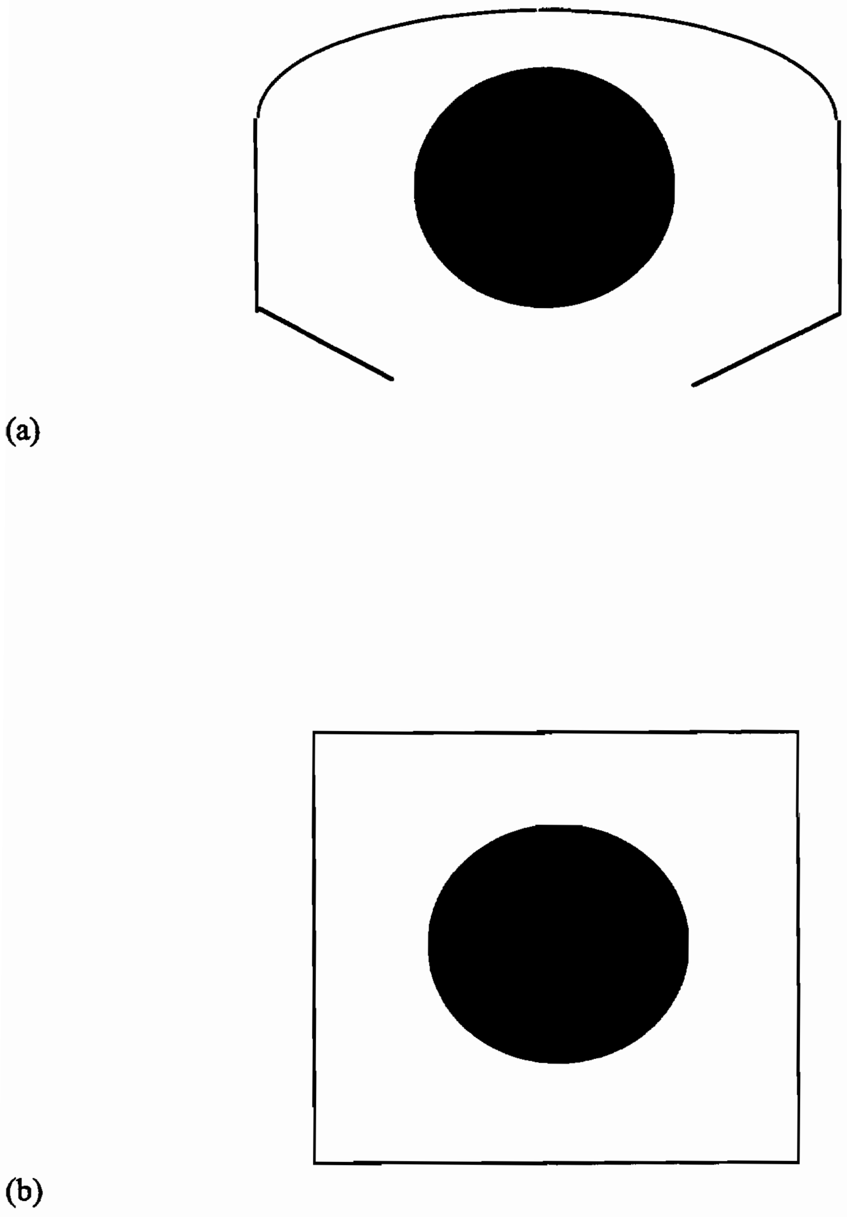

Fig. 2.4. Specimen orientation (a) for pearlitic steels (b) for bainitic steels.

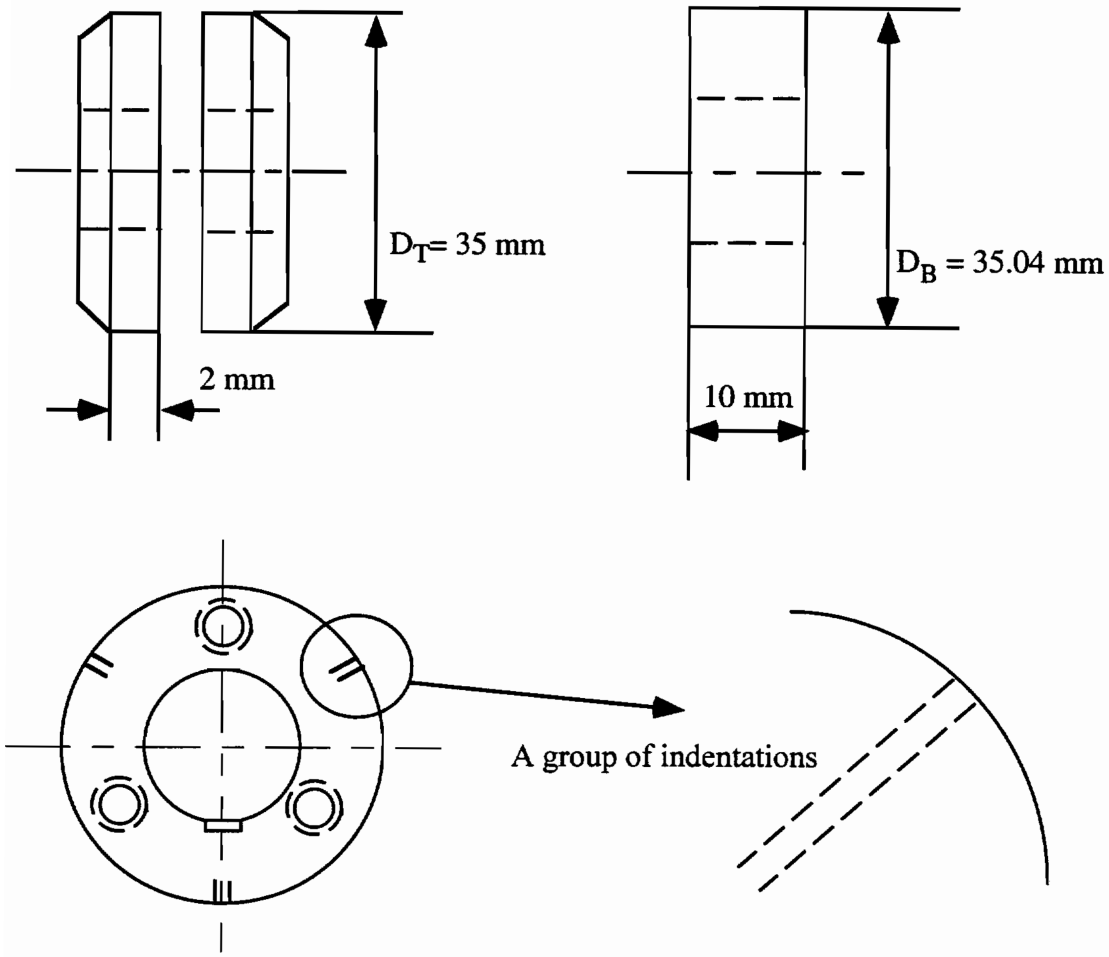

Fig. 2.5. Split rollers and indentation locations.

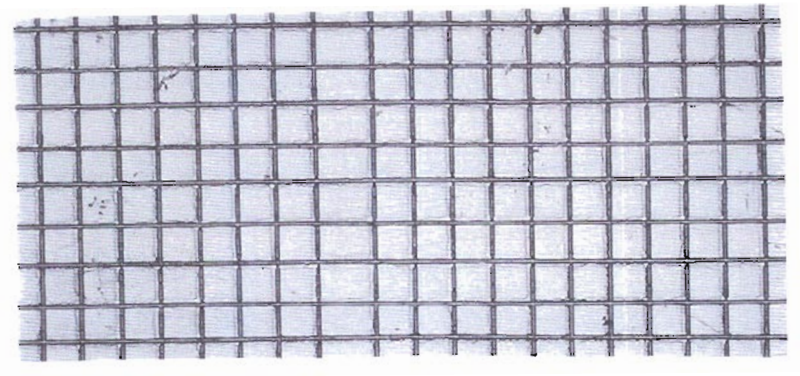

(a) 200 X

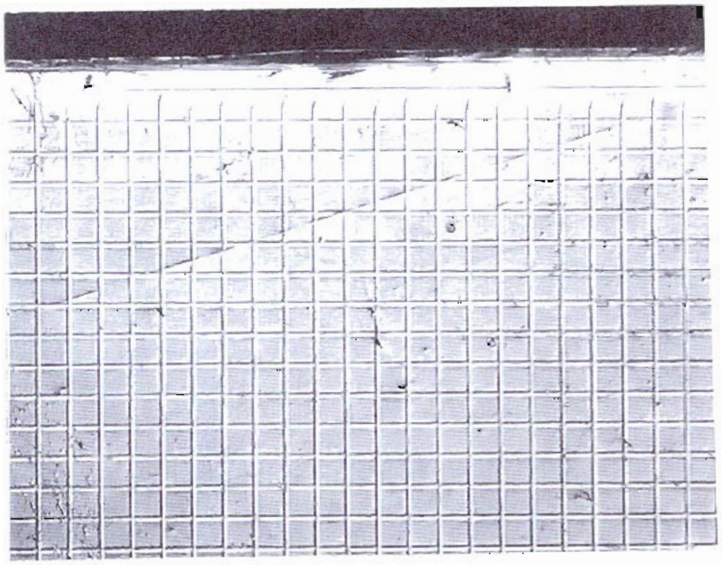

(b) 200 X

Fig. 2.6. Grids (a) made by scratch tester (b) made by micro machining.

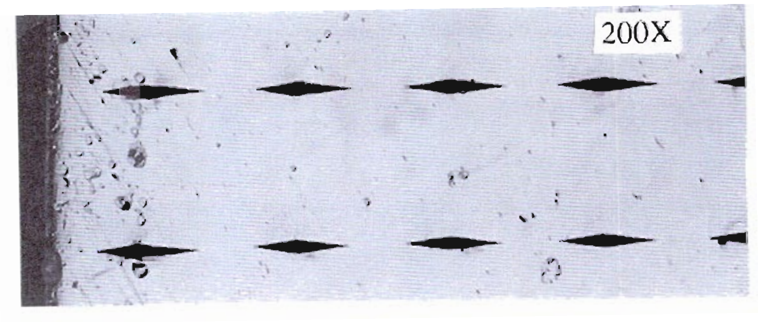

(a)
N = 0

(b)
N = 2000

Fig. 2.7. A group of indentations tested at $P_0 = 1759$ MPa (a) N = 0 (b) N = 2000 cycles.

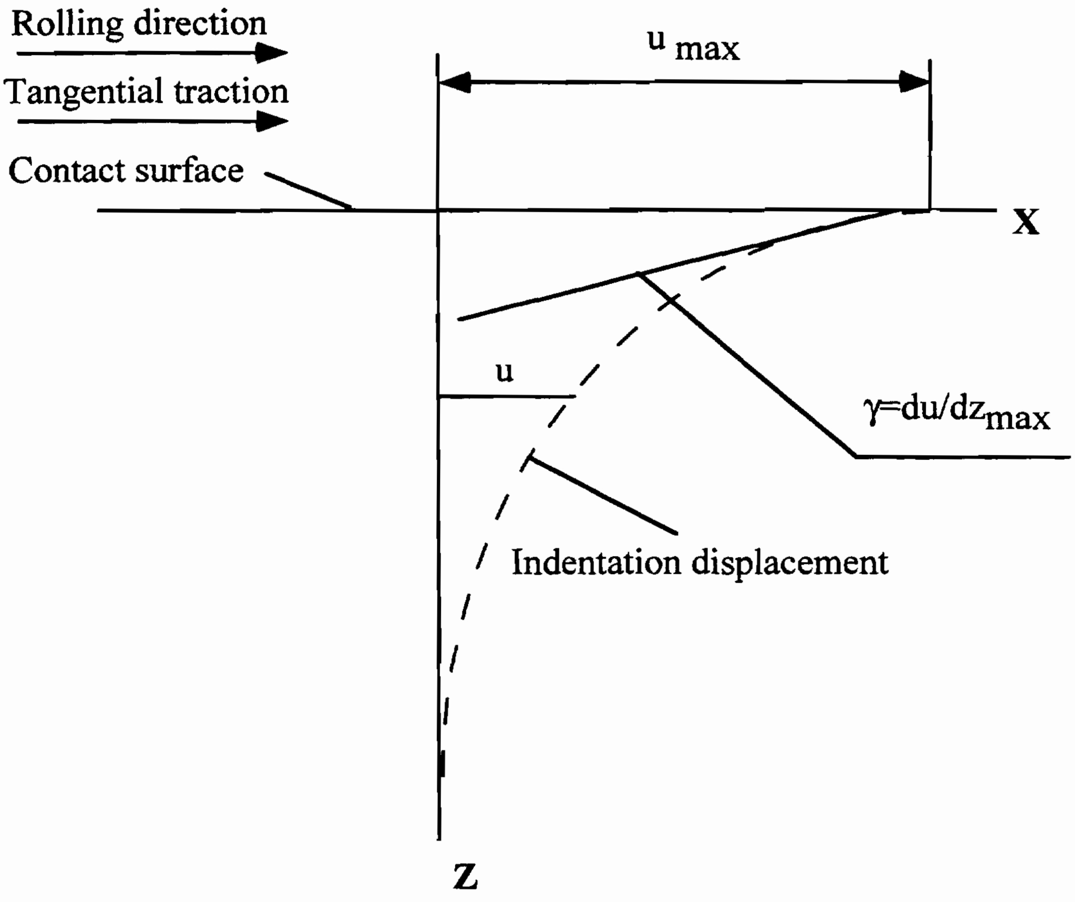

Fig. 2.8. Schematic illustration of determination of ratchetting strain.

CHAPTER 3
EXPERIMENTAL RESULTS

3.1 SURFACE RCF PERFORMANCE

3.1.1 Coefficient of Friction

The coefficient of friction fluctuated during experiments, being, in general, lower at the start of a test, and gradually increasing to a steady stable level, reaching the highest value near the end of a test. The stable period usually lasted about 70% of total test duration. The coefficients of friction for all materials tested ranged from 0.19 to 0.28 during the stable period.

Coefficients of friction varied slightly with materials. The average value for the bainitic steel J6 was 0.21, and for J1 and J2 it was 0.22. An average value for pearlitic steel HH and bainitic steel J4 was 0.23, while it was around 0.24 for STD steel. Since tangential traction is proportional to the coefficient of friction, the STD steel was subjected to about 4 to 14% higher tangential traction than the other materials for a given normal contact pressure. Given the variation of the coefficients, however, the difference is not significant.

For a given material, coefficients of friction also varied with contact pressure. It was interesting to observe that coefficients of friction were approximately 15% lower at the high end of the contact pressure range compared with the low end. This trend is consistent with experimental data presented by Clayton and Hill.[19] Table 3.1. summarizes the results of coefficients of friction.

3.1.2 Surface RCF Performance Data

Figure 3.1. shows the results of surface RCF life as a function of maximum contact pressure, P_0. Life decreases with increasing contact pressure, in a non-linear fashion. Test results are listed in Table 3.2.

Bainitic steel J6 exhibits the best RCF resistance in terms of RCF life at a given contact pressure, but the data also show a relatively large scatter band. Pearlitic steel STD and bainitic steel J4 show a similarly low resistance. As shown in Figure 3.2, the RCF life of J6 was about 5 to 6 times that of STD steel. The results of the other materials are clustered within a band formed between data of J6 and STD. The relative ranking of performance of the rest steels is bainitic steel J1, followed by J2 and HH.

The results of STD and J4 steels are shown in Figure 3.3. The total RCF cycles to failure of these two steels overlap. Only two typical contact load levels, 4150 and 1600 N, were applied to J4 tests due to the limited availability of the material. The strength of STD steel, in terms of yield stress and hardness, is the lowest among all the materials tested. Although J4 has the lowest strength among all the bainitic steels, its strength is higher than STD.

When these data are plotted on a log-log scale, Figure 3.4, it is apparent that the relationship between RCF life and contact pressure can be well described by a power law function as:

$$\text{RCF Life} = A(P_0)^b \qquad (3.1)$$

An alternative interpretation of the relationship is suggested by Figure 3.5, in which life is plotted as function of the normalized contact pressure, P_0/k, where k is the yield strength in shear and given by $\sigma_{0.2}/\sqrt{3}$. The possibility of bi-linear behavior with a transition at around P_0/k of 4.0, presents itself. The significance of the value of 4.0 is that it is close to the theoretical shakedown limit reported in the literature for work-hardened materials under rolling/sliding contact.[16,24,51] According to a theoretical analysis, cumulative surface plastic flow occurs at values above the limit with a tangential to normal load ratio of 0.25 or greater. [24] Current test conditions with normalized contact pressure levels above 4.0 and tangential to normal load ratios of 0.22 to 0.24 satisfy the criterion for the occurrence of surface cumulative flow. For the hardest material J6, the P_0/k values at all times were below 4.0, and no obvious transition behavior was observed.

The second feature of Figure 3.5 is that the data have been compressed into what could be interpreted as a single relation with a narrow scatter band.

Reproducibility of surface RCF data was investigated during previous investigations at OGI.[11,59] The same testing equipment and specimens, and as well as the same failure criterion were adopted in both the previous and the present tests. Variability results from the two previous tests were about ± 15%,[13] and ±6% (6 tests at 1302 MPa) and ± 26% (3 tests at 1413 MPa),[59] respectively. Current data reveal a variability of ±30% about the mean value for RCF life data obtained at 1635 MPa. The current result in combination with the previous values, gives the average variability of ±20% for the test system.

3.2 MECHANISM STUDY

3.2.1 Microscopy of Damaged Rollers

3.2.1.1 Characterization of Surface RCF Crack

Observations of the fatigued rollers were focused on two of the steels, STD and J4, and the possibility of two different deterioration mechanisms associated with the shakedown limit.

Cracks on the STD roller surfaces, viewed from above, are shown in Figure 3.6. At high contact pressure levels ($P_0 = 2086$ MPa, $P_0/k = 6.71$), the crack lines are coarse with shear lips (material rolled over on crack mouths), while cracks at low contact pressure ($P_0 = 857$ MPa, $P_0/k = 2.76$), are well defined fine lines without shear lips. At high contact pressure ($P_0 = 2086$, $P_0/k = 5.01$), the J4 bainitic steel, Figure 3.7, also showed the shear lip feature while at lower contact pressure ($P_0 = 1295$, $P_0/k = 3.11$) the cracks are fine lines.

A distinct difference between crack morphology at high and low contact pressures for both materials is further revealed from the longitudinal cross sections of the rollers. Above the shakedown limit ($P_0/k \approx 4.0$), cracks seldom branch, Figure 3.8, being roughly parallel to each other. They are severely sheared when approaching the surface, resulting in the shear lips. Below the shakedown limit multiple branched cracks prevail, Figure 3.9, with a main crack oriented at approximately 40 degrees to the contact surface.

Figure 3.10a shows the surface layer deformation of STD steel after testing at $P_0/k=6.71$. A significant depth of surface material, about 500μm, is sheared in the rolling direction. The microstructure is significantly changed in the deformed zone, Figure 3.10b. The changes are clearly contrasted in Figure 3. 11, which shows a largely undeformed surface layer (Figure 3.11a) and a shallow deformed zone of about 15 μm above the undeformed pearlite for a test at $P_0/k = 2.76$, Figure 3.11b.

It is evident that crack orientation at the surface is dictated by the shear flow pattern. The cracks shown in Figure 3.8 would all be within the severely deformed region. Even at the lower contact pressure, while the crack is within the shallow severely deformed layer, the crack follows the flow pattern. Beneath this region, however, it tends to branch easily.

For bainitic steels J1, J2, and J6 shear flow is not as obvious as for pearlitic steels, consistent with the higher yield strengths. For the softest bainitic steel J4, however, at the highest normalized contact pressure applied, $P_0/k = 5.01$, a heavily sheared zone, Figure 3.12a, is observed. The change of microstructure within the heavily sheared region is shown in Figure 3.12b. Figure 3.13a shows the largely undeformed surface material and branched cracks generally observed in the bainitic steels at lower contact pressures. Figure 3.13b reveals that at the test condition of $P_0/k = 3.11$ there is a surface shear zone of about 5 μm.

3.2.1.2 Some Phenomena Observed at the Low Contact Pressures

Longitudinal grooves and surface spalling are the two additional phenomena worth mentioning. At low contact pressures, usually well below the normalized contact pressure level of $P_0/k = 4$, longitudinal grooves were often observed on the surface of rollers in STD, HH and J6. This phenomenon was most pronounced in J6, with a significant amount of grooves found in five out of a total of seven specimens tested. The longitudinal grooves are shallow and parallel to the rolling direction. Figure 3.14a shows the longitudinal grooves in a J6 roller. This kind of groove can also be found in Figure 3.6b for STD and Figures. 3.15a and 3.15c for HH steel. The density of the grooves varied from specimen to specimen, but the orientation and appearance were similar.

This kind of groove was absent at high contact pressures. It is reasonable to speculate that the longitudinal grooves are mainly low contact pressure phenomenon. The high frequency occurrence in J6 may be due partly to the high strength of the material, which allows it operate within the elastic regime even under the highest contact pressure applied. A possible reason for the grooves may be attributed to the residue of machining grooves at low contact pressures. Figure 3.14b shows the machined grooves prior to testing. However, the post-rolling grooves differ from the machining grooves in that they lack uniformity. Machined grooves typically have identical spacing and appearance. Therefore, the feature is a form of deformation cannot be absolutely excluded.

The grooves are unlikely crack initiation sites, since virtually no cracks were found developing from them. It is possible that the grooves contributed to the higher coefficients of friction at the lower end of contact pressure range.

The second phenomenon, spalling, is also observed frequently for rollers tested under relatively low normalized contact pressures. These spalls appeared as holes of different size and density, and accompanied with fine cracks, as shown in Figure 3.15a for HH steel. The subtle difference of these spalls compared to the form of material loss under high normalized contact pressure seems to be that the former have better defined edges with less tearing. Figure 3.15b shows appearance of a HH roller tested at the normalized contact pressure of $P_0/k = 5.10$ ($P_0 = 2324$ MPa), cracks are generally coarser shear cracks with much fewer spalls compared to the damaged surface in Figure 3.15a for $P_0/k = 2.46$ ($P_0 = 1121$ MPa).

During the experiment with HH steel, there was a tendency for tests to be cut off after an unexpectedly short time. Observations of the rollers revealed spalls in the form of holes, as shown in Figure 3.16. The overall surface damage when the spalling was observed was often much lighter, in terms of crack length and density, compared to the surface appearance of damaged rollers tested for a normal test length. Sometimes no obvious cracks were observed in the adjacent area of the spalls. Although similar spalls with fine cracks were also observed in other materials, as demonstrated in Figure 3.6b for STD and Figure 3.14a for J6, the spall phenomenon in HH was most pronounced.

3.2.2 Microhardness Data

Figure 3.17 shows microhardness measurements from STD rollers tested under different contact conditions. Even at the lowest contact pressure, a slight increase in hardness is present, consistent with the observed shallow shear flow near the surface. The magnitude of the hardness and the depth of the work-hardened layer increase with increasing contact pressure. At the highest contact pressure, the depth of the work-hardened layer is about 0.8 mm and the maximum hardness is about 1.4 times the initial hardness. Results of HH steel are shown in Figure 3.18. An increase in hardness nearing the contact surface presents a similar trend to the STD steel.

Work-hardening is not as obvious for the bainitic steels because of higher initial hardness. Nevertheless, an increase in hardness is measured at the highest P_0/k levels. Microhardness data for J1 through J6 are shown in Figures. 3.19 through 3.22.

For both pearlitic and bainitic steels, the depth of measured hardness increases are always greater than the observed depth of the heavily sheared zone using optical microscopy. Nonetheless, in both cases there is qualitative agreement in that the depth of hardening increases with contact pressure.

3.2.3 Microscopy of Rollers Tested for Lubrication Effect

Dry rolling/sliding followed by lubrication significantly reduced surface RCF life. The total contact cycles to obvious surface failure was reduced to 20% of the original RCF life data obtained during RCF performance tests for the same contact pressure conditions with water throughout. The damaged surfaces were covered by massive large particles, or flakes, produced by crack networks, and appeared more severe than that tested without a dry running period. The coefficient of friction during dry rolling/sliding varied with sliding distance. The peak coefficient of friction probably corresponded with the roughest surface due to formation of incipient cracks. A reduction of coefficient of friction often followed the peak value, and was possibly related to the removal of the rough surface layer through a wear process. A relatively stable coefficient of friction was usually approached by the end of a dry test. The coefficients of friction for dry condition ranged from 0.39 to 0.71, the values were 0.06 to 0.08 for oil and 0.17 to 0.25 for water. The coefficient of friction data are listed in Table 3.3.

Figure 3.23a shows the initial cracks produced during the dry period. They are shallow cracks roughly parallel to the surface. Figure 3.23b shows the deformation layer produced during the dry running. The depth of the deformed layer is approximately 3 to 5 times deeper than the cracks. The shallow cracks in combination with a relatively deep surface deformation layer were the starting conditions for subsequent lubrication effect tests.

Figure 3.24 is the top view of crack morphology under oil lubrication following the dry period. The surface of the rollers was covered with large flakes. The qualitative severity, in terms of the size of flakes, increased with the contact pressure. Large flakes were also present on the roller surfaces under water lubrication, and the severity obviously increased with contact pressure, Figure 3.25.

Crack morphology on the longitudinal cross sections are shown in Figures 3.26 and 3.27 for oil and for water lubrication, respectively. The severity of the damage, in terms of the length and the depth of the cracks, increased with contact pressure for both lubrication conditions.

Comparison of the crack morphology between oil and water lubricated rollers revealed two major differences:

- The particle or flake size for oil lubrication was generally larger, but the flakes appeared thinner than for water lubrication. The larger particle size makes the damage for oil lubrication appear more severe. This is particularly evident when qualitatively comparing the damage of both oil and water lubricated surfaces under a low contact pressure of 1295 MPa.

- The crack lengths under oil were generally longer than under water for the same loading conditions. However, the depth of cracks under water was greater than under oil. Cracks tend to turn down to grow deep into the material under water lubrication, and the turning of the crack path can be observed in Figure 3.27.

Figures 3.28 and 3.29 show how the crack morphology related to deformation patterns. At relatively high contact pressure (P_0 = 1874 MPa, P_0/k = 6.03), a significant deformation layer was produced, approximately 400 μm. Cracks under oil seem to follow the shear flow pattern, but are confined within the deformation layer, forming long but comparatively shallow cracks, Figure 3.28a. This feature is consistent with the large but relatively thin flakes or particles observed on the top view of the surface. Figure 3.28b shows that a large particle with the thickness comparable to the depth of the deformation layer was formed, and about to detach from the surface. A close-up view of the crack tip (a crack in Figure 3.28a) shows that the crack path evidently followed the dividing line between the deformed and undeformed regions. A zig-zag pattern was present at the crack tip, and the crack was apparently trapped within the deformation layer, Figure 3.28c. The zig-zag crack tip feature is also shown in Figure 3.28b for another crack.

A typical crack under water lubrication is shown in Figure 3. 29. This crack also seemed to follow the shear flow band when propagating within the deformation layer. However, it was not confined within the deformed layer, the crack path turned inwards and the crack is obviously deeper than the one under oil for the same contact pressure. The inclined angle of the main crack (not counting the near surface region) to the surface was about 40°, approximately 20° greater than that of oil lubricated cracks, Figure 3.29a.

A close-up view of the crack tip in Figure 3.29b shows that the crack passed through the deformation layer and advanced into the basically undeformed region for about 200 μm.

3.3 RATCHETTING STRAIN DATA

3.3.1 Comparison Between Solid and Split Rollers

The out-of-plane deformation was measured for split rollers tested at the maximum contact pressure P_0 of 1759 MPa. Theoretically, the out-of-plane strain should be zero on the symmetry plane of a solid roller with a plane strain condition. However, due to the split inner faces some out-of-plane deformation was present. The out-of-plane deformation was measured by a profilometer (Surfanalysis 401), and the profiles are shown in Figure 3.30. The magnitude of the deformation, which is represented by the absolute values of the peaks and valleys, increased with contact cycles, and reached maximum of 4 μm at 50,000 cycles. The increment of deformation reduced with contact cycles, with about 50% of the deformation being accumulated during the first 10% of the cycles.

Comparisons of surface scratch displacement between solid and split rollers were made at the maximum contact pressures P_0 = 1874 and 1759 MPa. For each contact interval, 3 to 5 scratches along the periphery of both types of rollers were measured, and average displacement data obtained. The results are shown schematically in Figure 3.31. The shape of the scratches are schematic, but the values were measured. The maximum displacement in the solid roller was at the center of the running track, while the maximum displacement in split rollers was about 0.6 to 0.7 mm offset from the center. The difference between the maximum displacement, point B, and the displacement on the symmetry plane, point A, ranged from 20 to 70 μm. Since the subsequent indentation displacements were measured on the plane of symmetry, the symmetry plane displacements, i. e. point A, in both spilt and solid rollers are compared. The center displacements of split rollers ranged from 71 to 86% of those of the solid rollers, with 6 out of 9 measurements between 81 to 86%.

The result indicates that the trend of the displacement in both types of rollers was the same, with a large initial increment gradually decreasing with increasing numbers of contact cycles. The center displacement of the split rollers averaged 80% of that in the solid rollers.

3.3.2 Subsurface Displacement

Deformation results are presented by two types of curves, curves of indentation displacement versus depth form the surface, i. e. U–Z curves, and curves of maximum displacement, the surface displacement, versus contact cycles, i. e. a U_{max}–N curve.

A typical set of experimental data of indentation displacement as a function of depth from the surface for STD steel is shown in Figure 3.32. This test was run at P_0 = 1759 MPa (P_0/k = 5.65) with measurements at seven different numbers of cycles. Figure 3.33 shows an example of the original data for bainitic steel J2. Periodic measurements were made for each specimen, so that a large quantity of data were obtained. The depth of deformation layer for the STD specimen shown in Figure 3.32 is about 0.65 mm, which is consistent with the hardness profile measured at the same maximum contact pressure.

Plotting the maximum displacements, U_{max}, against the number of contact cycles creates the relation shown in Figure 3.34 for several values of P_0/k. The surface displacement reached more than 400 µm at contact pressure levels of P_0/k greater than 5.66. The maximum displacements were about 200 µm for lower contact pressures.

The reproducibility of the results can be judged from the repeated tests carried out at P_0/k values of 6.03 and 5.66. In the latter set of tests the difference in displacement at a given number of contact cycles was approximately 25 µm. This yields a variation about the mean value of ±15% for the initially small displacement of less than 100 µm and ±5% for the relatively large displacements greater than 250 µm.

3.3.3 Ratchetting Strain

As shown in Figure 3.35, maximum ratchetting strain is a non linear function of contact cycles, with the slope of the curves decreasing with an increasing number of contact cycles. A large amount of strain was accumulated during the initial cycles, then the strain increment continuously decreased with cycles.

Re-plotting the data on a log-log scale, as shown in Figure 3.36 for STD steel, reveals that a power law relationship appears to describe the data satisfactorily. At a given contact pressure, the ratchetting strain can be expressed as

$$\gamma = AN^{b} \tag{3.1}$$

where γ is strain, N the number of cycles, and A and b are fitting parameters that are dependent on the contact conditions. Figure 3.37 shows ratchetting strain data for bainitic steel J2. Although there are fewer data points than for STD, the same power function is apparent.

At a comparable maximum contact pressure level, $P_0/k = 5.05$ for J2, and $P_0/k = 5.25$ for STD, the strain for J2 is obviously higher than for STD as shown in Figure 3.38, even though STD was subjected to 4% higher contact pressure than J2. The ratchetting strain in J2 was up to 3 times of that in STD.

Figure 3.39 reveals the effect of contact pressure on the ratchetting strain for a given number of contact cycles. These relations are also non-linear and can be satisfactorily fitted by either power or exponential functions. The power indices are greater than unity, indicating that ratchetting strains increase with contact pressure at an accelerating rate. Displacement and ratchetting strain data are included in Table 3.4.

3.3.4 Ratchetting Strain at Various Slide/roll Ratios

3.3.4.1 Tangential to Normal Traction Ratio

Tangential to normal traction ratio (T/N) is measured from a moment reading just as for the coefficient of friction. As mentioned in the literature review section, the T/N ratio equals the coefficient of friction when full slip is achieved, and it is generally lower than the coefficient of friction if partial slip, which usually occurs at low slide/roll ratios, is involved. Therefore, the more generalized term, T/N ratio, instead of the coefficient of friction, is used in the following section.

Figure 3.40 shows the variations of T/N during the entire test duration for a range of slide/roll ratios. The greatest variation occurred during the initial 5000 cycles, ranging from 0 to 0.29. This big gap was reduced as the number of contact cycles increased, the ratio ranged from 0.12 to 0.29 at 30000 cycles, and from 0.12 to 0.23 at 50000 cycles, showing a trend of convergence. During the period approximately from N = 5,000 to 40,000 cycles, a relatively steady state was achieved. The steady state results of T/N ratios are plotted in Figure 3.41, showing two important features:

- big variations at lower slide/roll ratios of 0.3%, 0.4%, and 1%, and
- an increasing trend with increasing slide/roll ratio.

The T/N ratios during the initial 5000 cycles are shown in Figure 3.42. The fluctuation is most pronounced for lower slide/roll ratios of 0.3, 0.4 and 1%. Two tests were repeated for 1% slide/roll ratio, and the difference between these was as high as a factor of 3. In addition, an oscillation in the T/N ratios occurred for both the 1% slide/roll ratio specimens, one oscillated between 0.23 to 0.29, and the other between 0.16 to 0.20. The lesser degree of oscillations, typically 0.01 between the peak and the valley, were also observed at slide/rolls of 0.3 and 0.4%. Generally speaking, all the data fall into an envelope enclosed by the values at the lowest (0.3 and 0.4%) and the highest (25%) slide/roll ratios. An "anomalous" phenomenon, which shows that the T/N ratio at 1% slide/roll ratio was actually higher than that at 5%, and even exceeded that of 10%, disturbed what would otherwise have been a neat trend of higher T/N ratios for higher slide/roll ratios. The highest T/P ratio, around 0.29, was achieved at slide/roll ratio of 25%.

As contact cycles increased, the T/N ratios at low slide/roll ratios of 0.3 and 0.4% increased, and the exceptionally high T/N values of a specimen tested at 1% slide/roll ratio decreased. The oscillation still remained but gradually reduced to a less noticeable amplitude. Overall, the data tended to stabilize and converge after the first 10000 cycles.

A drop and a subsequent recovery was often observed during the tests. A typical data set showing this behavior is plotted in Figure 3.43. This phenomenon may be in part attributed to start up from static to dynamic motion, and to cleaning of the surfaces after each interval. The cleaning procedure was necessary for periodical indentation displacement measurement, but, it may alter the surface condition by wiping off debris. However this is a transient phenomenon, thus no significant influence on ratchetting strain is assumed.

3.3.4.2 Displacement and Ratchetting Strain Data at Various Slide/roll Ratios

Subsurface displacement versus depth from the surface were measured at identical contact cyclic intervals, 5000, 15,000, 30,000 and 50,000 for 5 specimens, and at 10,000, 20,000, 35,000, 50000 for additional 3 specimens. Tests at 25% slide/roll ratio had to stop sooner at 42,000 cycles due to earlier RCF failure.

Results of the surface displacement versus the number of contact cycles at the same maximum contact pressure of 1759 MPa are shown in Figure 3.44. The general trend is that the displacement is higher at higher slide/roll ratios. However, exceptions exist within the initial 5000 cycles, where displacements for rollers tested at 1% slide/roll ratio were higher than one tested at 5% slide/roll ratio. In fact, a data point at 1% slide/roll ratio was as high as that obtained at 10% slide/roll ratio. Two specimens tested at 5% showed a bigger difference among themselves, about 70 μm, compared to specimens tested at other slide/roll ratios.

Ratchetting strain data are plotted in Figure 3.45 on linear and logarithm scales, respectively. In general, the strains were higher at higher slide/roll ratios. However, some anomalous data were present during initial cycles, where strains at 1% are higher than 5%, which is consistent with the displacement data shown in Figure 3.44. Data during the 5000 initial contact cycles demonstrate the biggest scatter band, and the highest strain value is about 12 times that of the lowest value. As contact cycles increased, the difference gradually reduced to about 1.5 times, showing a trend of convergence. On a logarithm scale, the trend of convergence is quite evident, as shown in Figure 3.46. The displacement and ratchetting strain data are listed in Table 3.5.

Table 3.1a. The Coefficient of Friction of Pearlitic Steels

No.	P (N)	P_0 (MPa)	f (Initial)	f (Stable)	f (Final)
STD-12	4150	2086	.21	.22	.24
STD-9	3350	1874		.23	
STD-28	3350	1874		.22	.23
STD-29	2950	1759		.20	.22
STD-5	2950	1759		.26	
STD-18	2950	1759	.21	.24	.24
STD-45	2950	1759	.22	.23	.21
STD-8	2550	1634		.24	.24
STD-25	2550	1634	.19	.24	
STD-47	2550	1634		.23	.24
STD-2	2000	1448		.23	.24
STD-13	1600	1295		.26	.27
STD-16	1000	1024		.28	.28
STD-15	700	857		.27	.28
HH-10	5150	2324		.24	
HH-8	4150	2086	.20	.21	.22
HH-5	4150	2086	.21	.20	.23
HH-6	2550	1634	.22	.23	.25
HH-2	2000	1448		.25	
HH-9	1600	1295		.25	
HH-4	1200	1121		.26	.28

Table 3.1b. Coefficient of Friction of Bainitic Steels

No.	P (N)	P_0 (MPa)	f (Initial)	f (Stable)	f (Final)
J1-13	5150	2324	.18	.20	.22
J1-5	4150	2086	.19	.20	.22
J1-7	4150	2086	.19	.21	.22
J1-10	2950	1759	.20	.20	.23
J1-4	2950	1759	.19	.21	.23
J1-6	2550	1634	.19	.22	.24
J1-3	2000	1448		.24	.28
J1-1	1600	1295	.18	.22	.24
J1-8	1600	1295		.22	.24
J1-2	1200	1121	.21	.24	
J2-9	5150	2432		.19	
J2-8	4150	2086	.18	.19	
J2-4	2950	1759	.20	.21	
J2-7	2550	1634	.15	.20	.21
J2-3	2000	1448		.20	
J2-2	1600	1295		.24	.25
J2-6	1600	1295		.24	
J2-1	1200	1121	.24	.26	.24
J4-1	4150	2086		.21	
J4-4	4150	2086		.21	.22
J4-2	1600	1295	.19	.24	.26
J4-3	1600	1295	.21	.25	.26
J6-8	4150	2086	.18	.19	.20
J6-6	3350	1874	.18	.19	.20
J6-5	2550	1634	.20	.22	.22
J6-9	2000	1448		.21	.23
J6-7	2000	1448	.20	.23	.24
J6-10	1600	1295		.22	.24
J6-4	1600	1295		.22	.24
J6-3	1200	1121		.23	.26

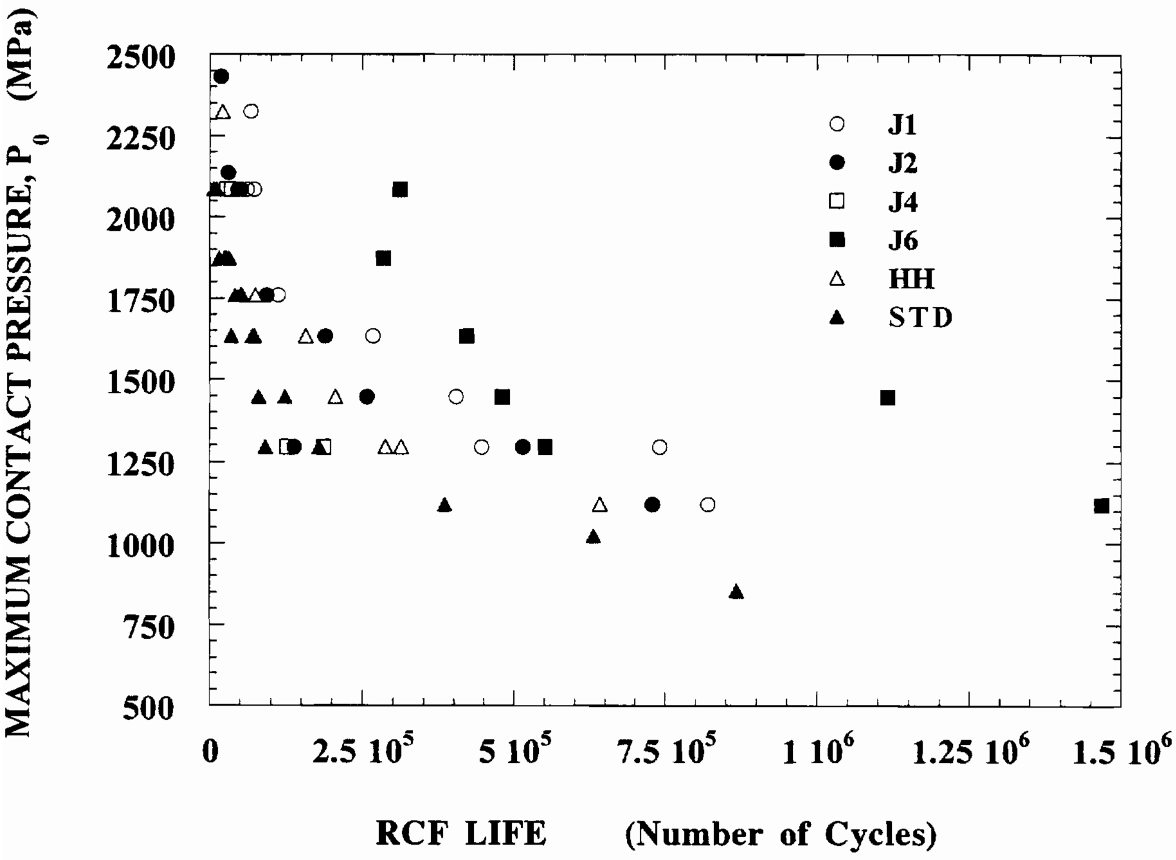

Fig. 3.1. Results of surface RCF performance test, showing RCF life is a non-linear function of the maximum contact pressure, P_0.

Table 3.2a. RCF Test Results of Pearlitic Rail Steels STD and HH

STD			HH		
No.	P_0 (MPa)	RCF	No.	P_0 (MPa)	RCF
x95-03	2086	1.12e+04	x136-10	2324	2.23e+04
x95-12	2086	6.97e+03	x136-08	2086	4.55e+04
x95-09	1874	2.86e+04	x136-05	2086	4.70e+04
x95-07	1874	1.61e+04	x136-01	1759	7.50e+04
x95-28	1874	2.50e+04	x136-06	1634	1.57e+05
x95-05	1759	4.19e+04	x136-02	1448	2.05e+05
x95-29	1759	5.20e+04	x136-03	1295	2.88e+05
x95-08	1634	7.24e+04	x136-09	1295	3.13e+05
x95-04	1634	3.57e+04	x136-04	1121	6.42e+05
x95-10	1634	3.57e+04			
x95-25	1634	6.94e+04			
x95-02	1448	8.02e+04			
x95-01	1448	1.23e+05			
x95-13	1295	1.79e+05			
x95-14	1295	9.12e+04			
x95-11	1121	3.84e+05			
x95-16	1024	6.31e+05			
x95-15	857	8.67e+05			

Table 3. 2b. RCF Test Results of Bainitic Rail Steels

J1			J2			J4			J6		
No.	P_0	RCF	No.	P_0	RCF	No.	P_0	RCF	No.	P_0	RCF
J1-13	2324	6.74e04	J2-9	2432	1.80e04	J4-1	2086	2.85e04	J6-8	2086	3.12e05
J1-7	2086	6.12e04	J2-10	2137	3.00e04	J4-4	2086	3.55e04	J6-6	1974	2.84e05
J1-5	2086	7.27e04	J2-8	2086	4.59e04	J4-2	1295	1.87e05	J6-5	1634	4.20e05
J1-4	1759	1.12e05	J2-5	2086	5.00e04	J4-3	1295	1.26e05	J6-9	1448	1.12e06
J1-6	1634	2.67e05	J2-4	1759	9.30e04				J6-7	1448	4.80e05
J1-3	1448	4.03e05	J2-7	1634	1.88e05				J6-10	1295	5.52e05
J1-1	1295	4.46e05	J2-3	1448	2.57e05				J6-3	1121	1.47e06
J1-8	1295	7.41e05	J2-2	1295	1.37e05						
J1-2	1121	8.21e05	J2-6	1295	5.14e05						
			J2-1	1121	7.28e05						

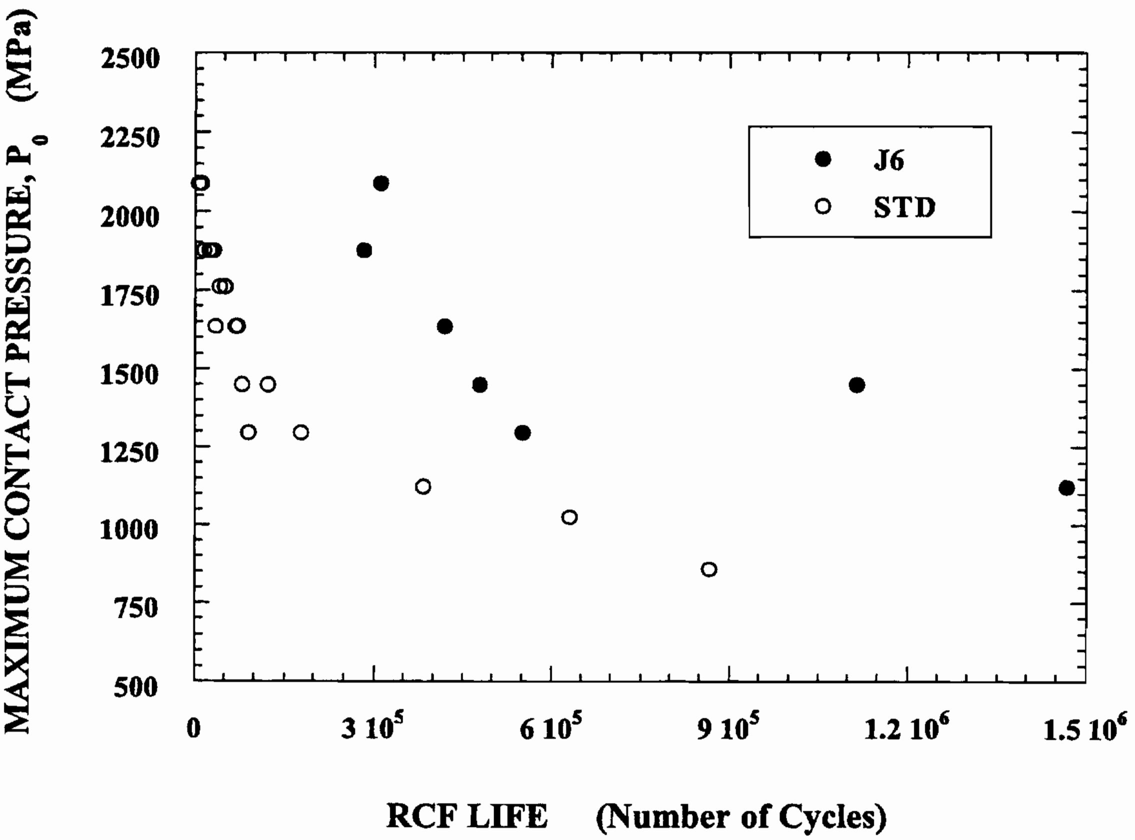

Fig.. 3.2. Surface RCF performance data of bainitic steel J6 and pearlitic steel STD.

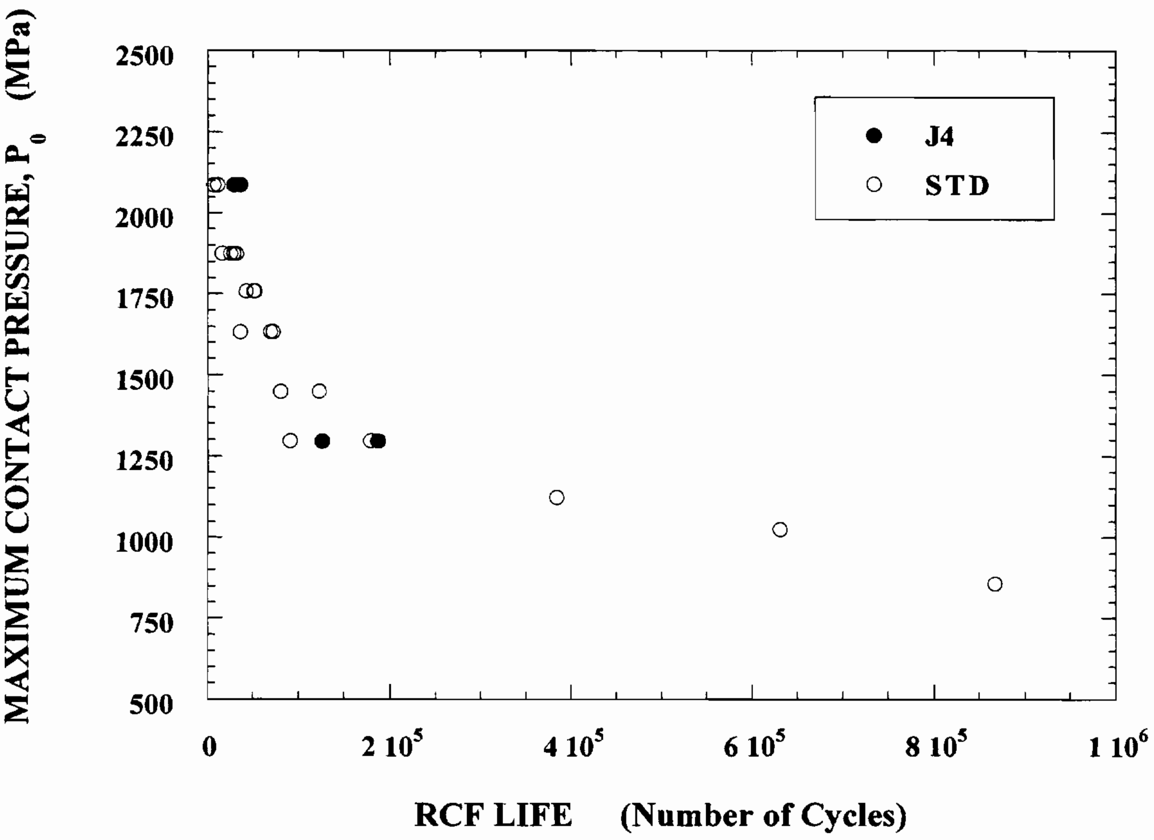

Fig. 3.3. Surface RCF performance data of bainitic steel J4 and pearlitic steel STD.

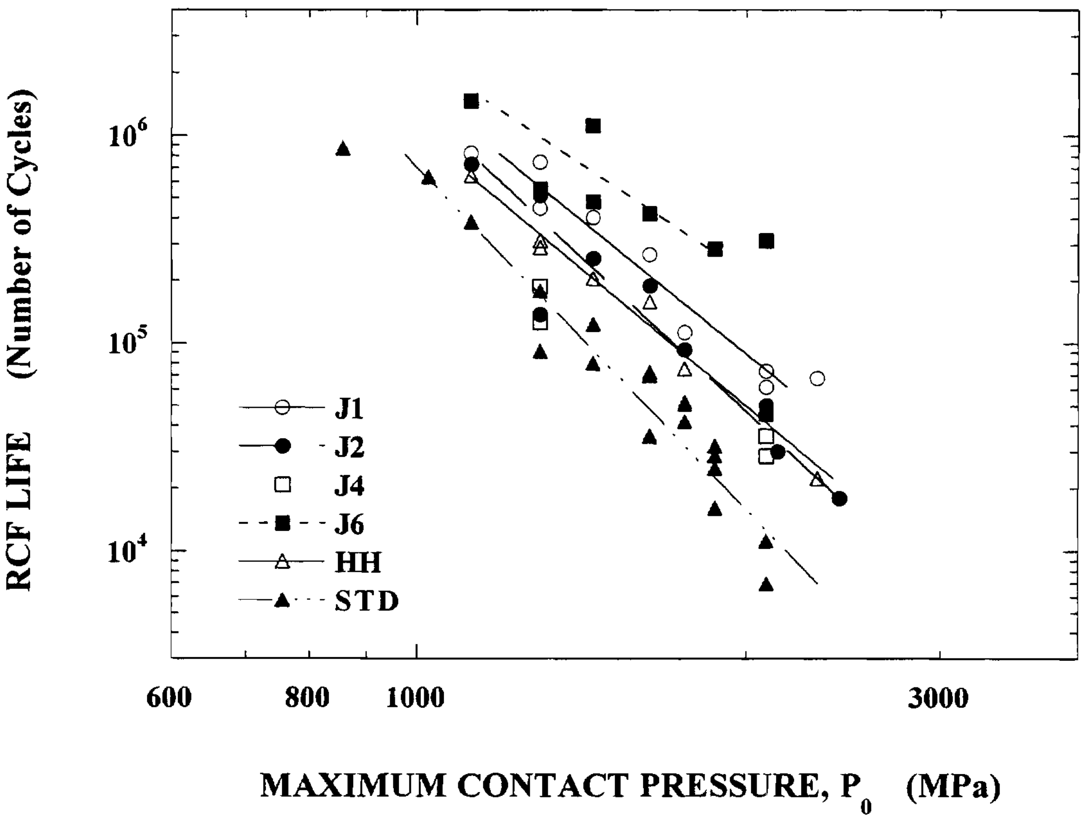

Fig. 3.4. RCF performance data plotted on a log-log scale, showing a power law function between surface RCF life and the maximum contact pressure.

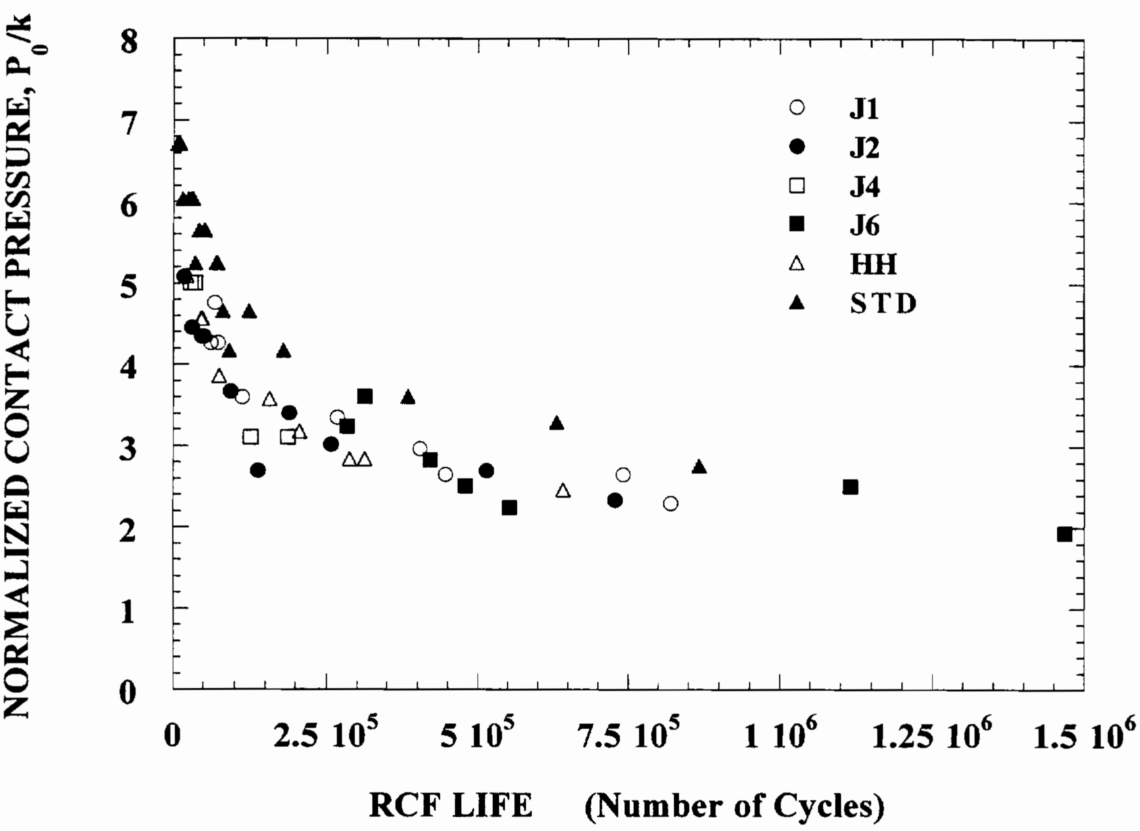

Fig. 3.5. Surface RCF life versus normalized contact pressure, P_0/k.

(a)

(b)

Fig. 3.6. Top view of cracks on pearlitic STD roller surfaces (a) at P_0 = 6.71 (b) at P_0/k = 2.76.

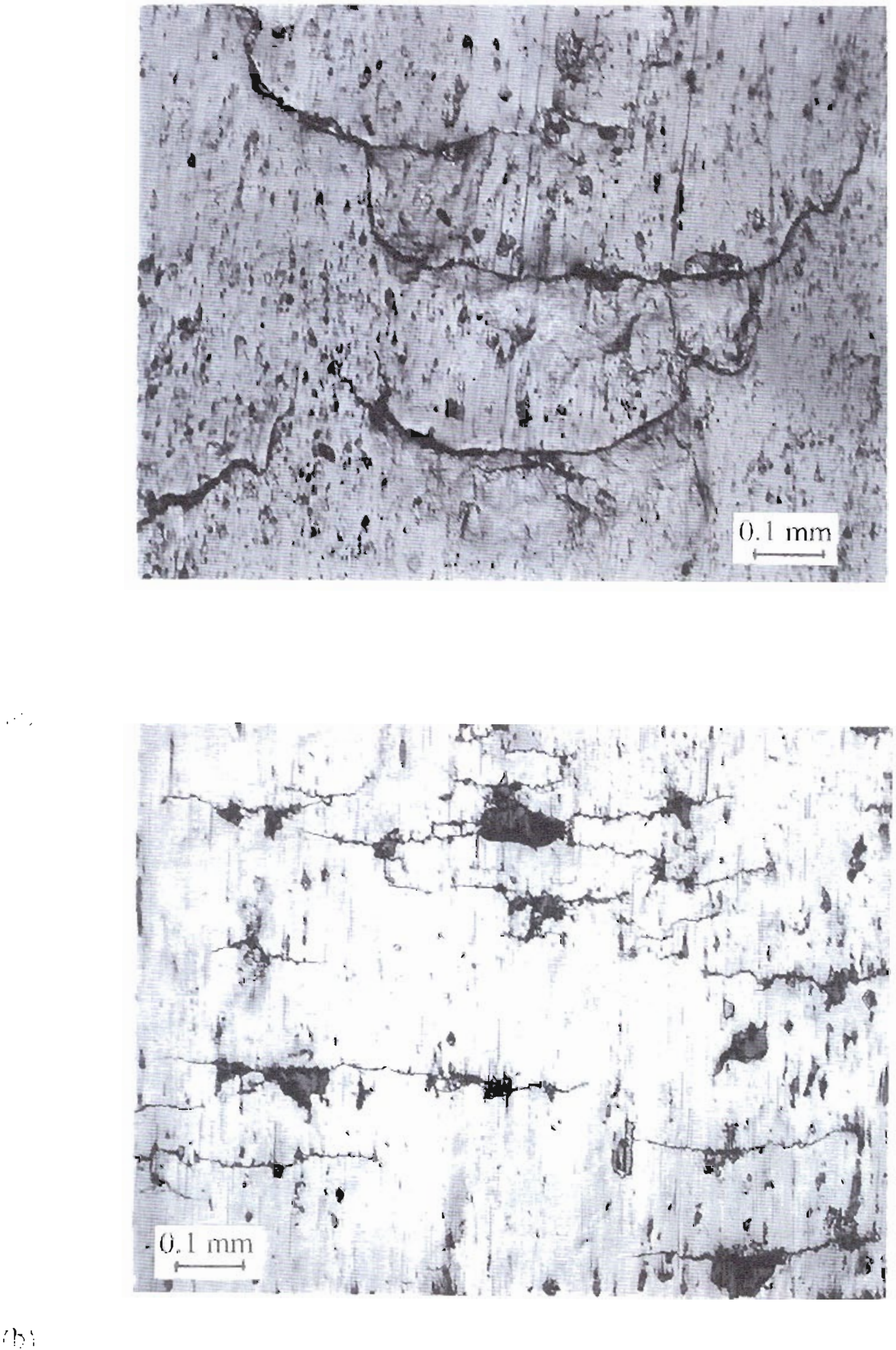

Fig. 3.7. Top view of cracks on bainitic steel J4 roller surfaces (a) P_0/k = 5.01 (b) P_0/k = 2.96.

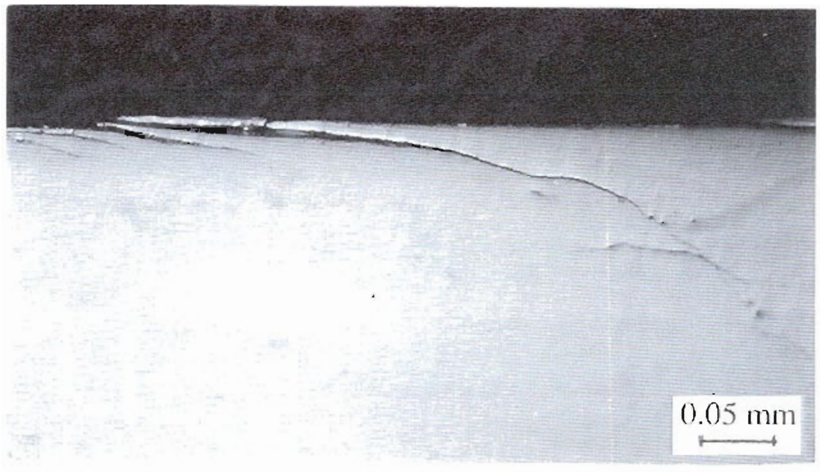

$P_0/k = 6.71$

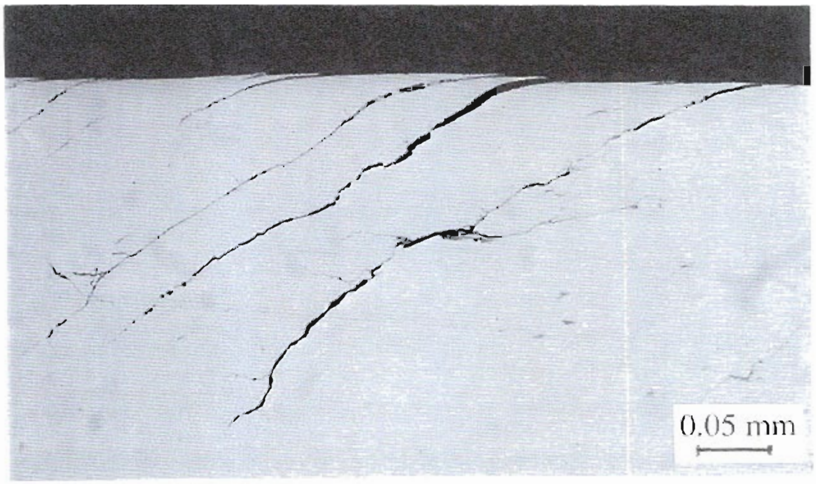

$P_0/k = 6.03$

(a) STD

Fig. 3.8 Longitudinal cross-section of rollers tested at high contact pressures, showing predominately shear band cracks (a) STD, $P_0/k = 6.71$ and 6.03 (b) J4, $P_0/k = 5.01$.

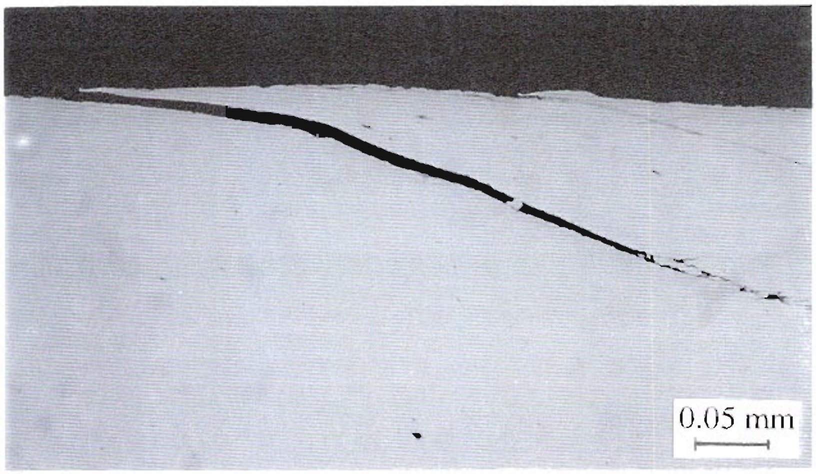

(b) J4, $P_0/k = 5.01$

Fig. 3.8 Longitudinal cross-section of rollers tested at high contact pressures, showing predominately shear band cracks (a) STD, $P_0/k = 6.71$ and 6.03 (b) J4, $P_0/k = 5.01$.

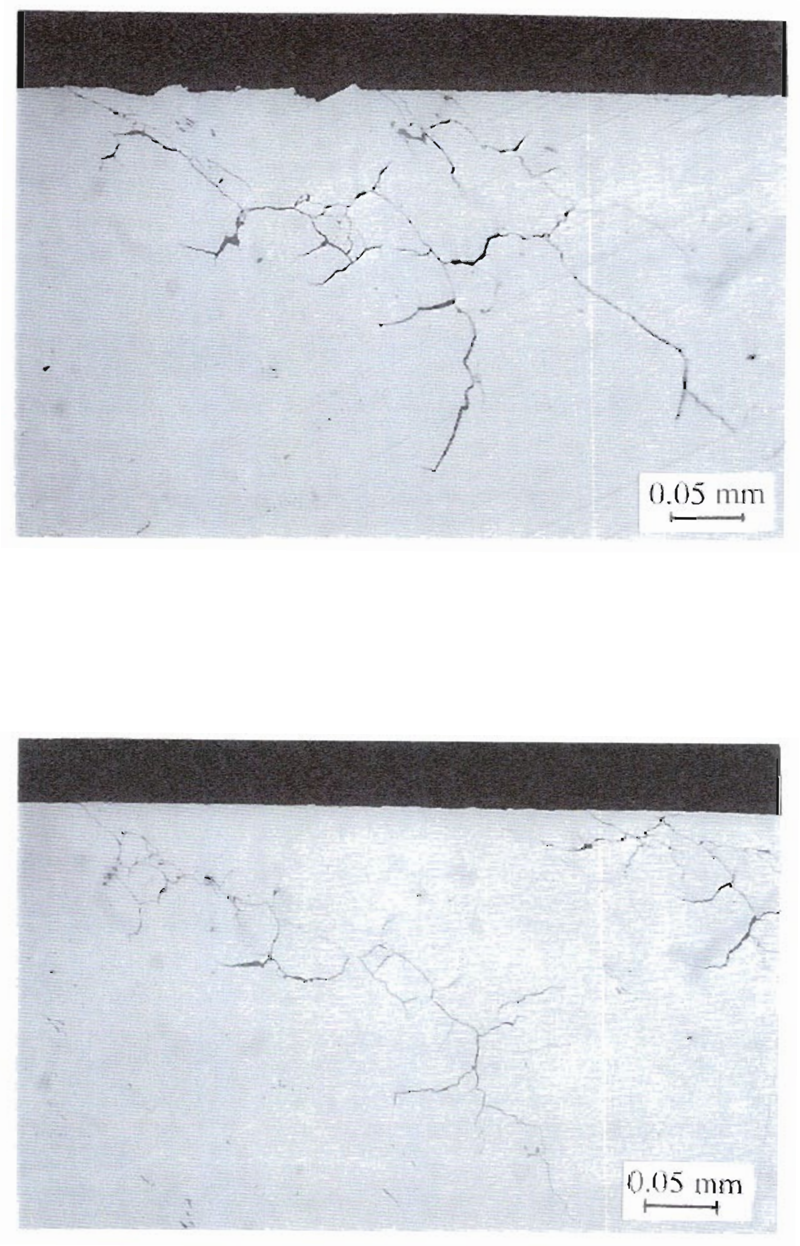

(a) STD, P_0/ k= 2.76

Fig. 3.9. Longitudinal cross-section of rollers tested at low contact pressures, showing predominately branched cracks (a) STD, $P_0/k = 2.76$ (b) J4, $P_0/k = 3.11$.

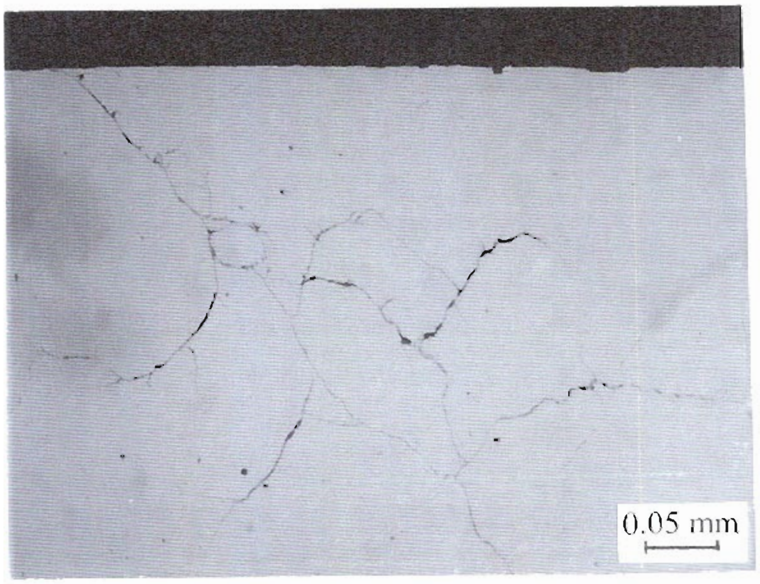

(b) J4, $P_0/k = 3.11$

Fig. 3.9. Longitudinal cross-section of rollers tested at low contact pressures, showing predominately branched cracks (a) STD, $P_0/k = 2.76$ (b) J4, $P_0/k = 3.11$.

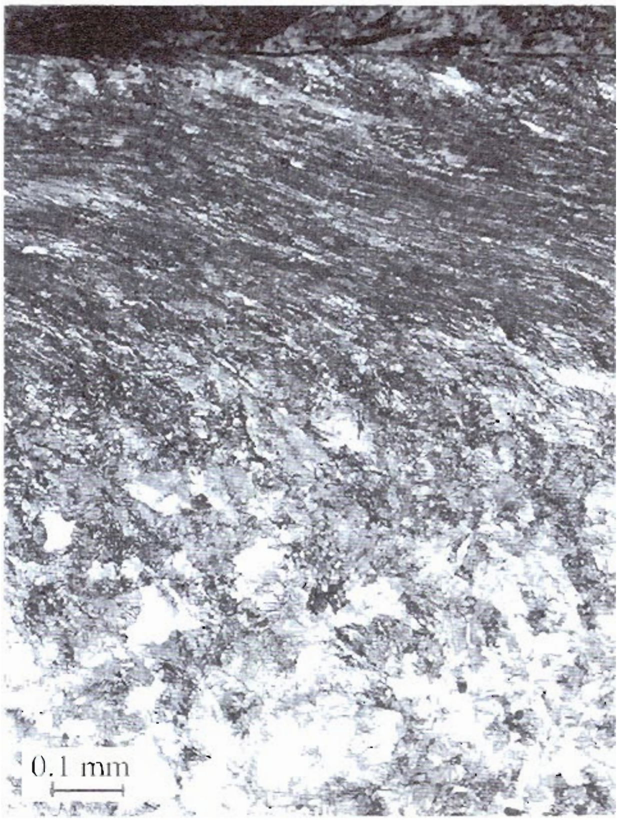

(a)

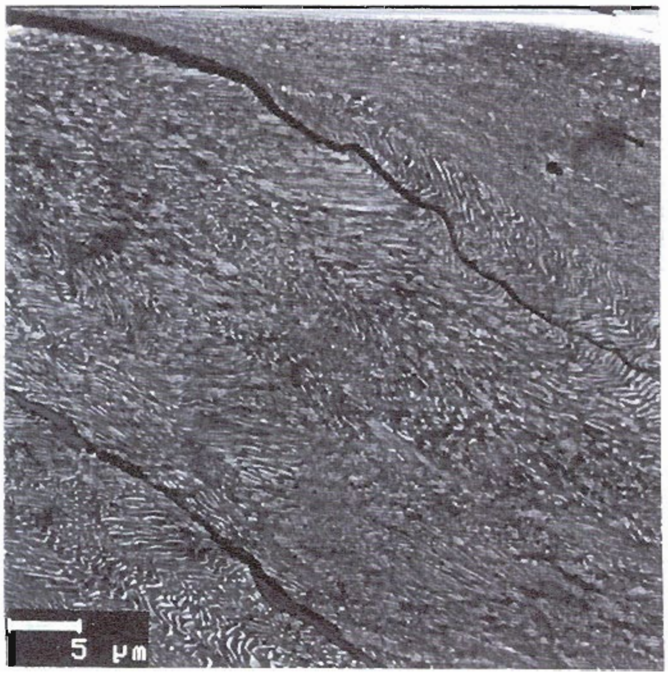

(b)

Fig. 3.10. Shear deformation of STD steel (a) a significant shear flow zone, P_0/k = 6.71(b) modified microstructure with cracks following the shear flow band. P_0/k = 6.03.

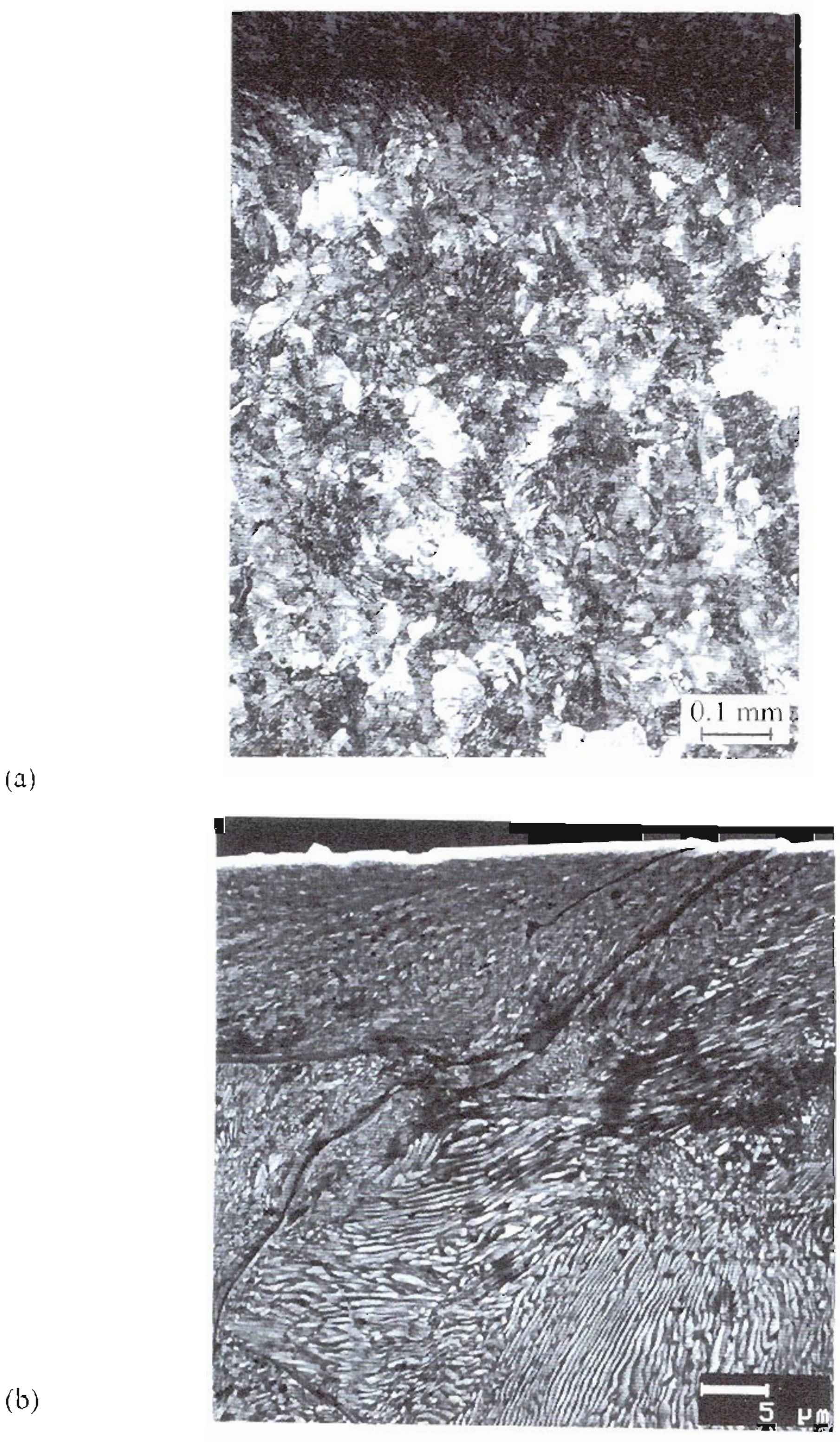

Fig. 3.11. Largely undeformed subsurface at low contact pressure $P_0/k = 2.76$ in STD steel (a) a significant undeformed subsurface (b) shallow shear layer on the surface and largely undeformed microstructure.

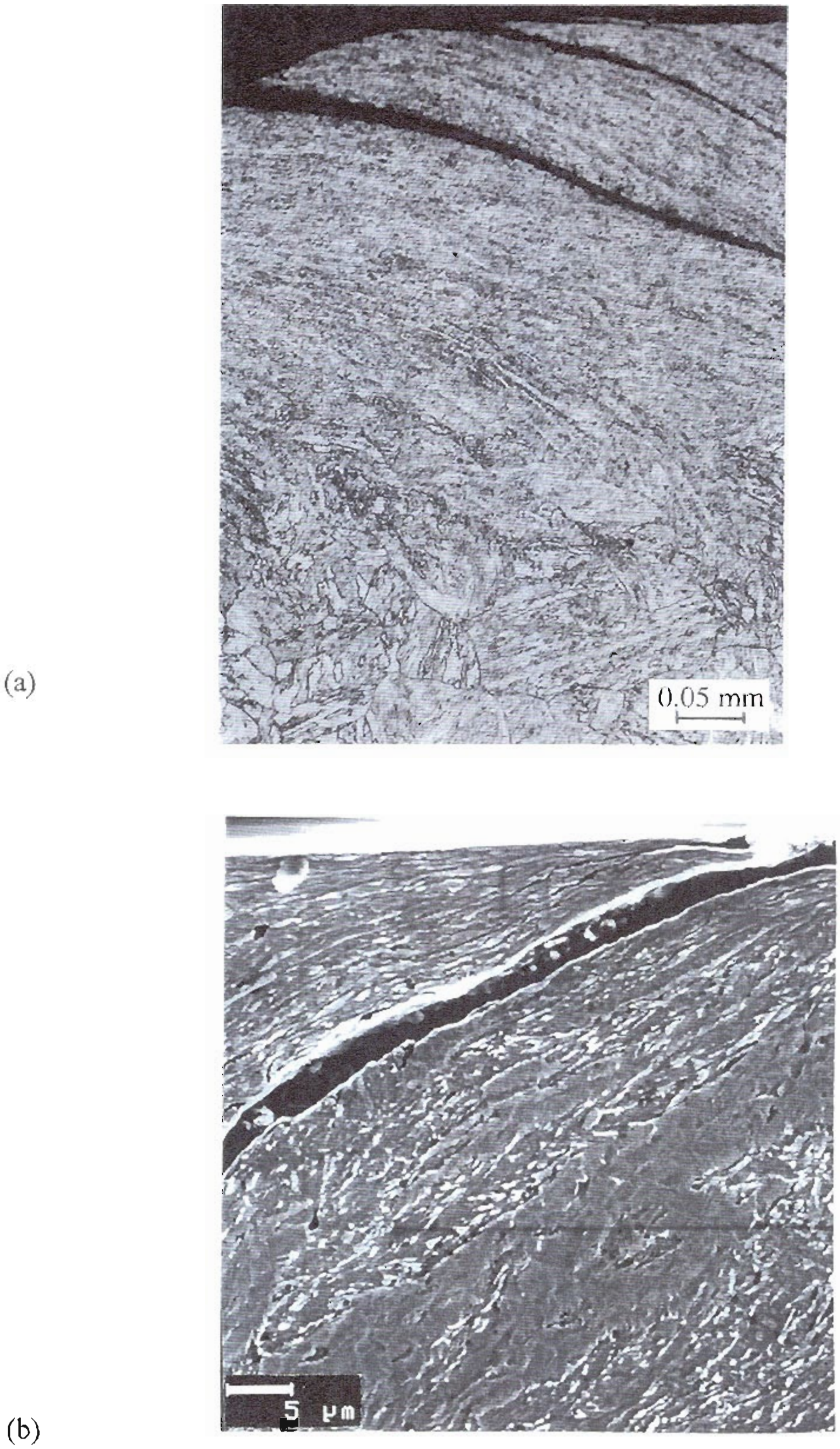

Fig. 3.12. Shear flow zone of J4 at $P_0/k = 5.01$(a) Shear flow layer and shear band cracks (b) severely sheared microstructure.

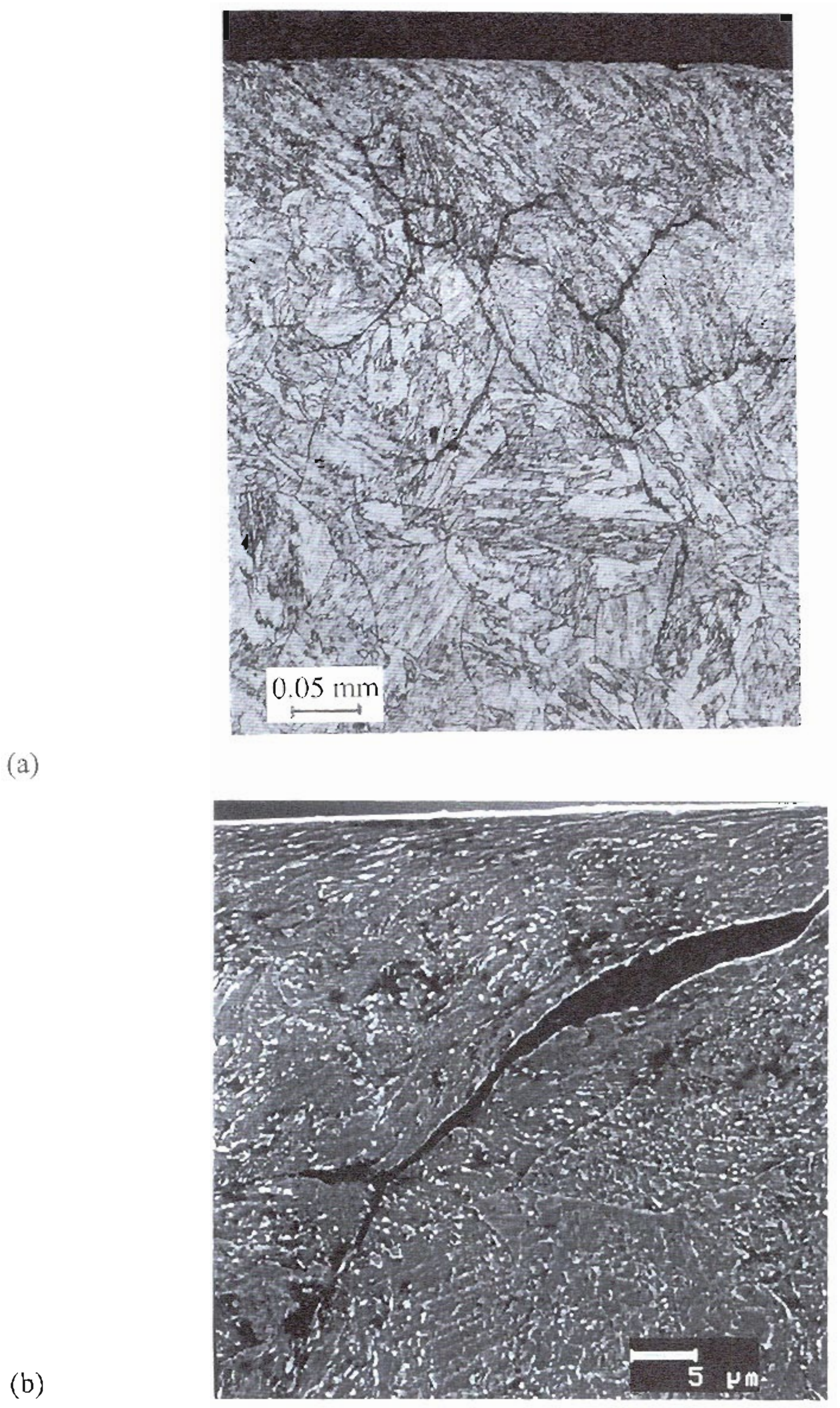

Fig. 3.13. Largely undeformed subsurface zone and branched cracks in J4 at P_0/k = 3.11(a) a branched crack in a largely undeformed subsurface zone (b) a photo showing the microstructure in this zone.

(a)

100 X

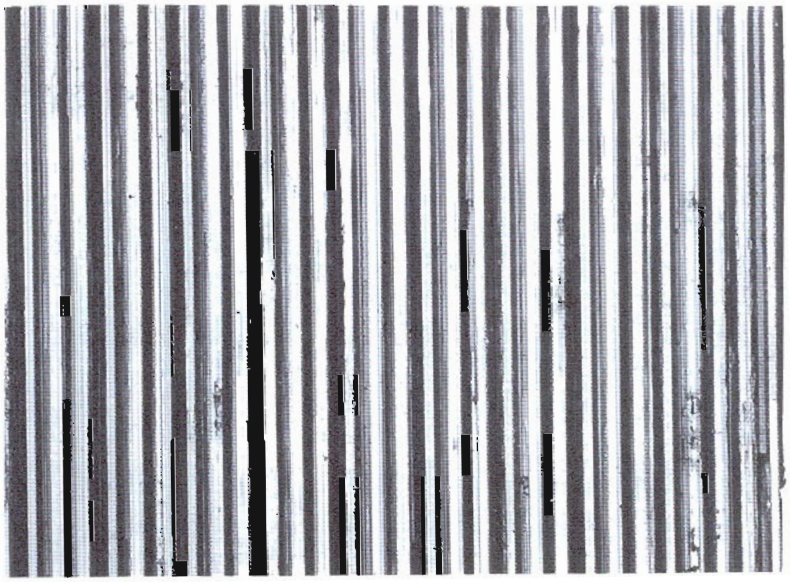

(b)

100 X

Fig. 3.14. Longitudinal groves on the surface of J6 rollers (a) after a test (b) machine marks prior to testing.

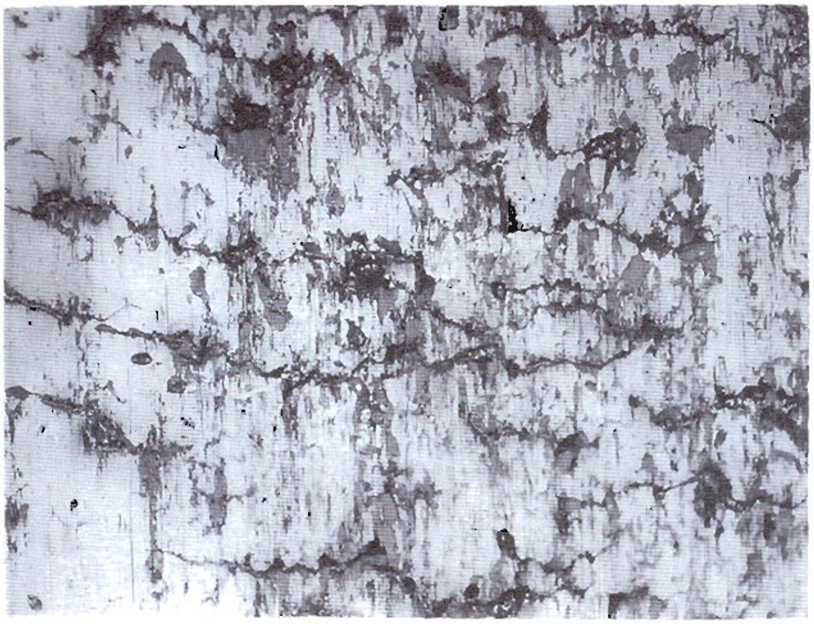

(a)
100 X
P_0 = 1211 MPa
P_0/k = 2.66

(b)
100 X
P_0 = 2324 MPa
P_0/k = 5.10

Fig. 3.15. Top view of tested rollers of HH steel (a) spalls, groves and fine cracks at low contact pressure (b) coarser shear cracks at a high contact pressure.

100 X

Fig. 3. 16. Spalls on the surface of a HH roller at N = 51,240, 25% of the average RCF life at P_0 = 1448 MPa, Po/k = 3.18 for this material.

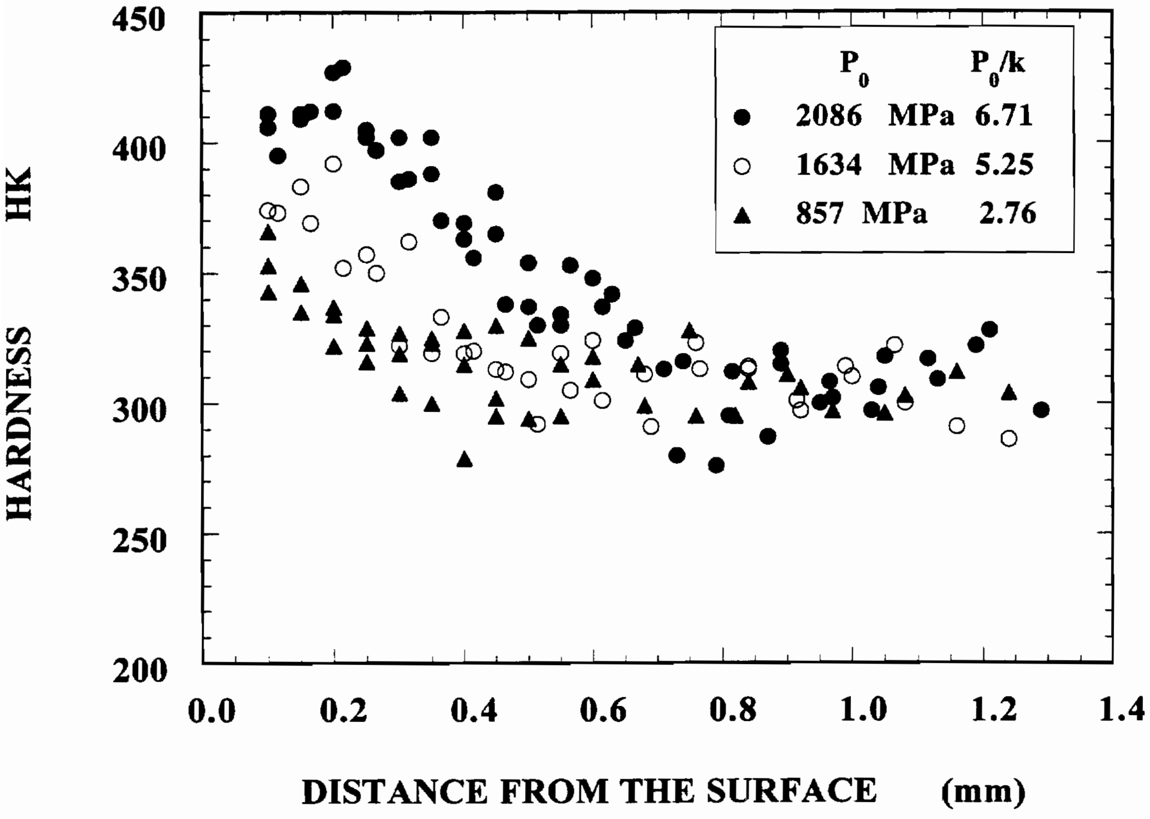

Fig. 3.17. Microhardness data of STD rollers.

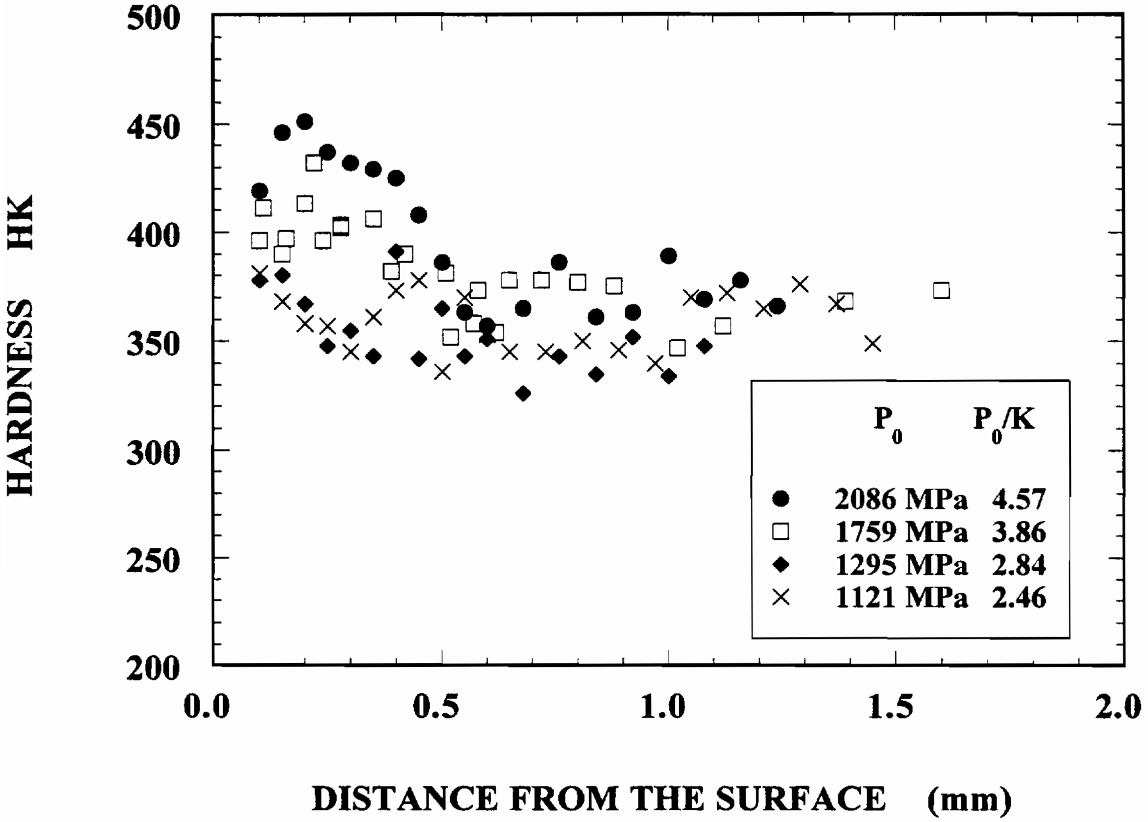

Fig. 3.18. Microhardness data of HH rollers.

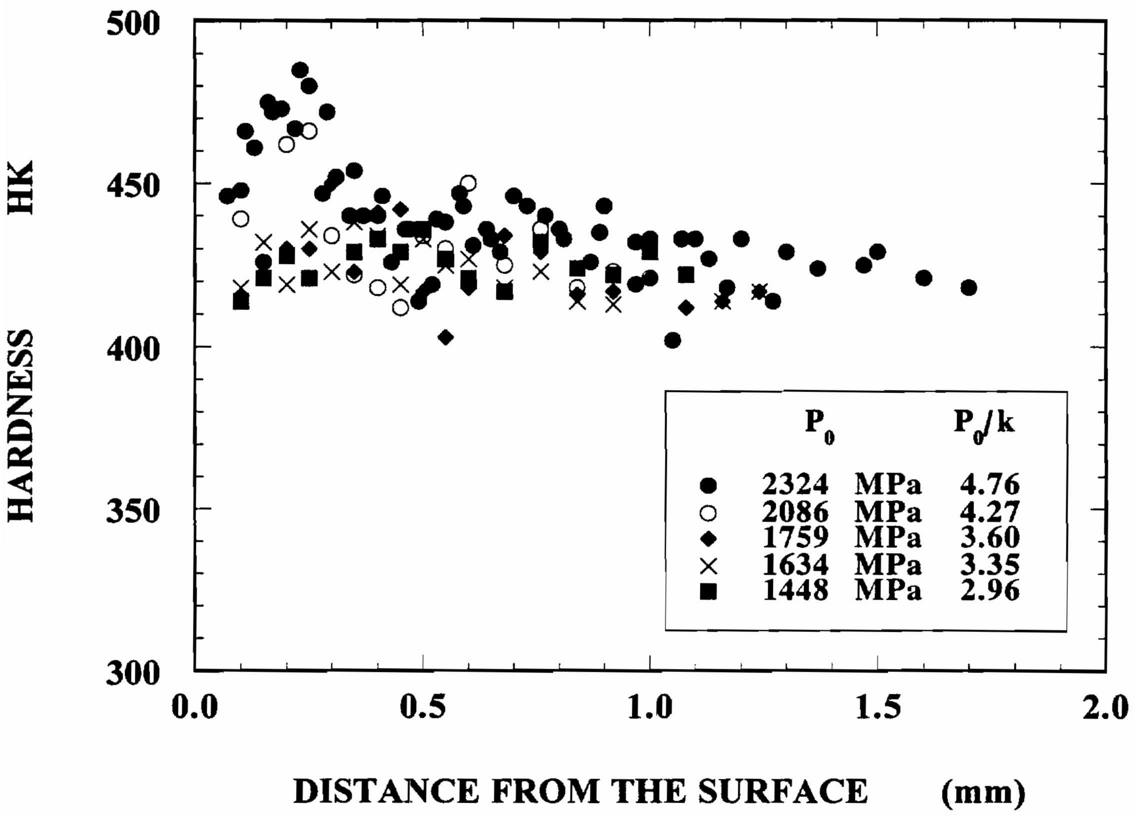

Fig. 3.19. Microhardness data of bainitic steel J1 rollers.

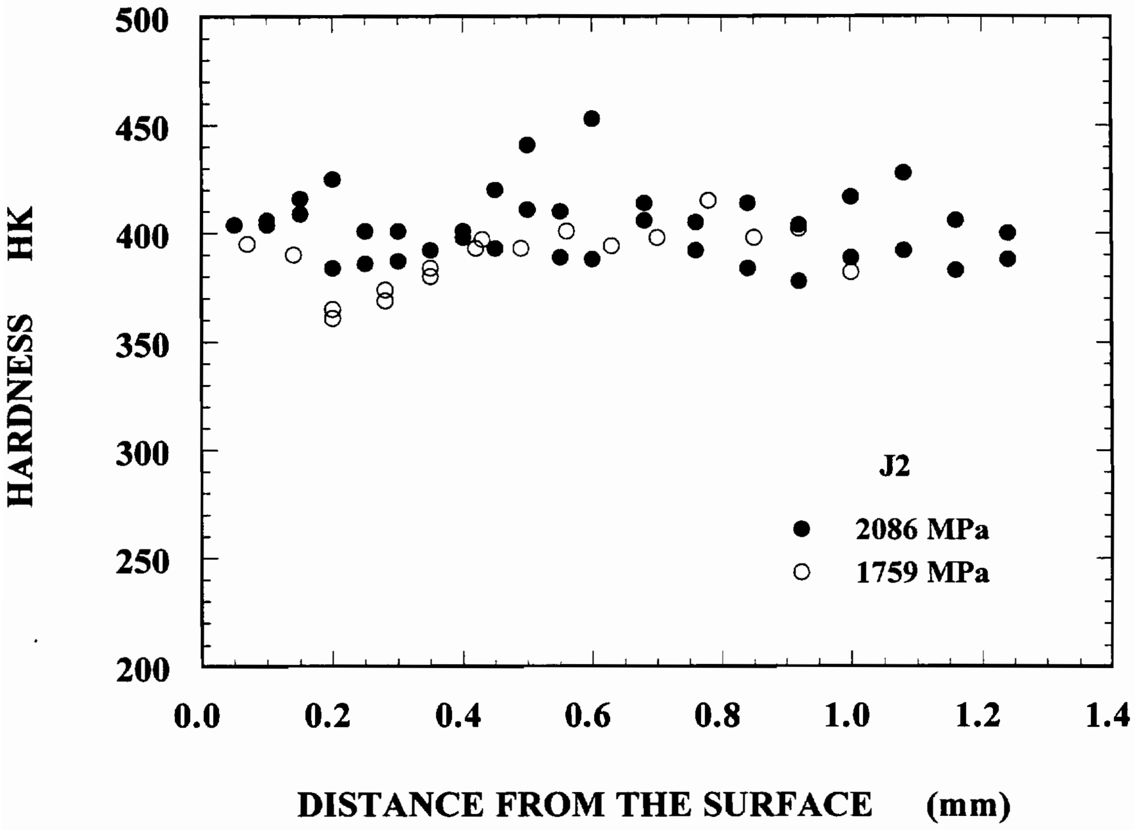

Fig. 3.20. Microhardness data of bainitic steel J2 rollers.

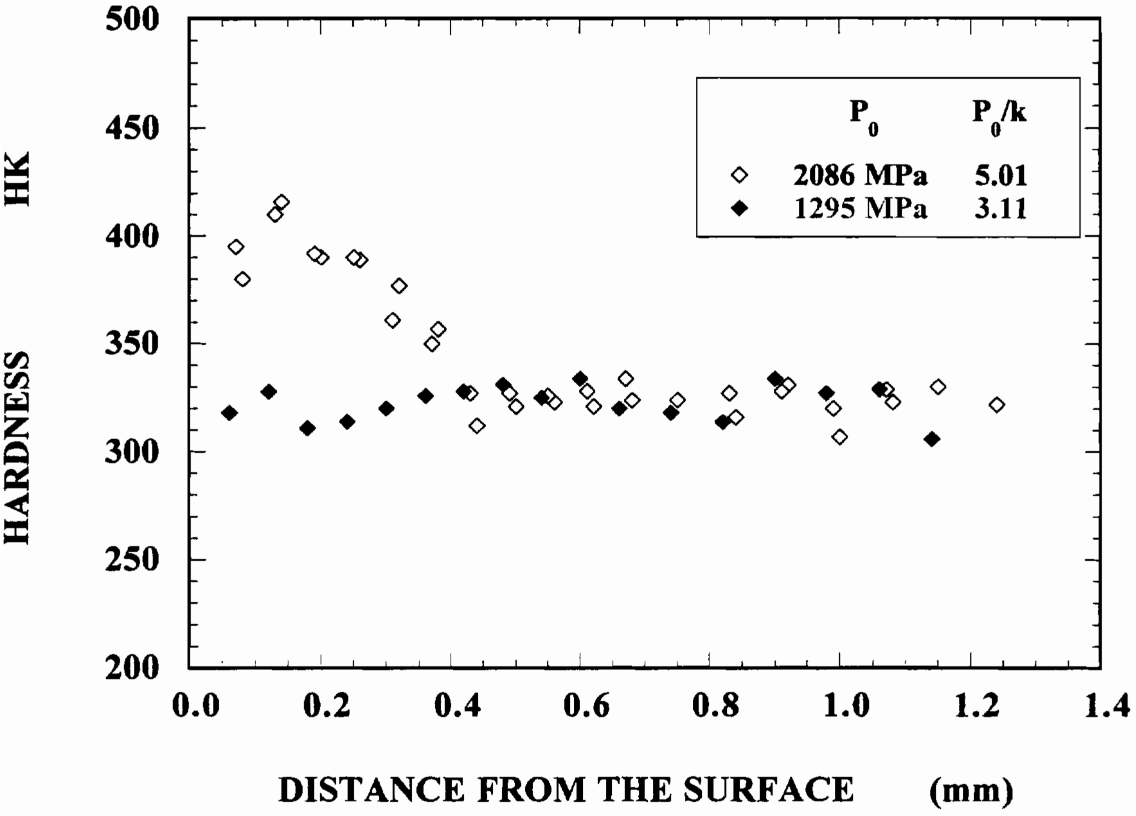

Fig. 3.21. Microhardness data of bainitic steel J4 rollers.

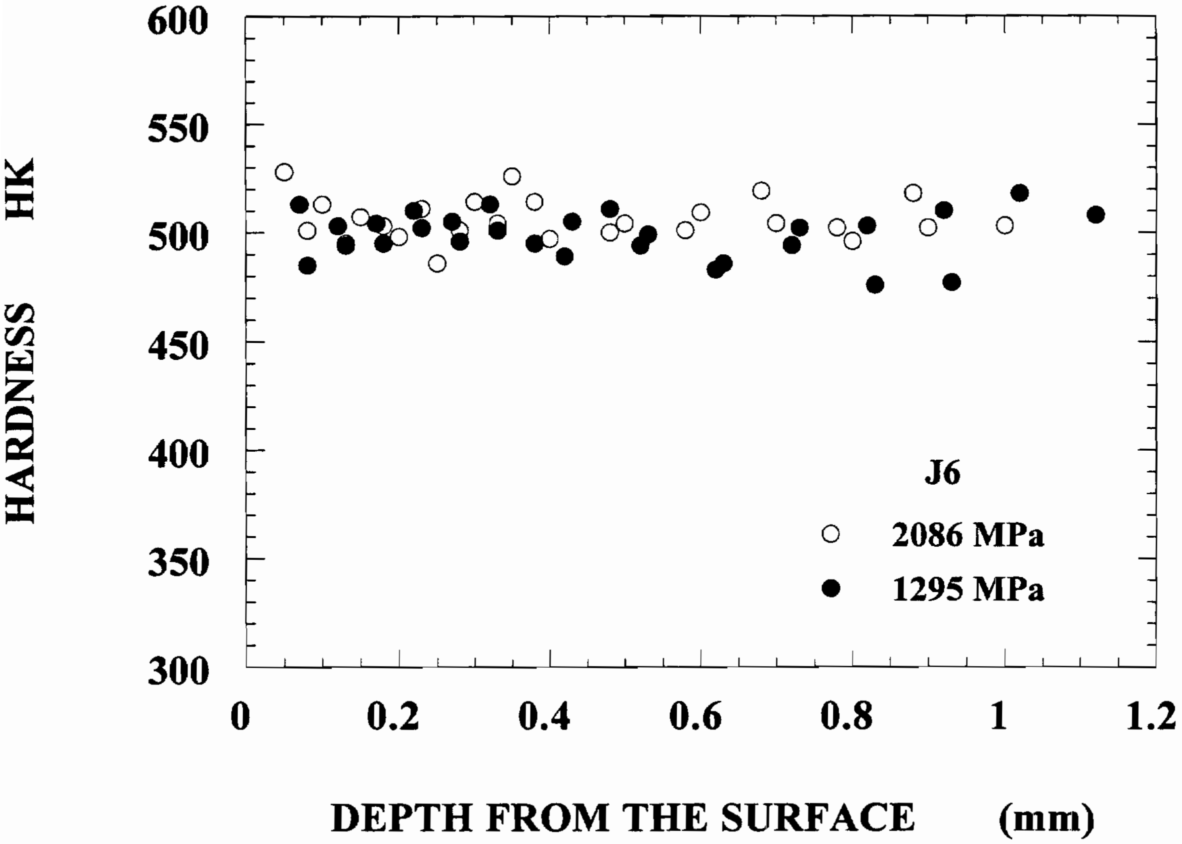

Fig. 3.22. Microhardness data of bainitic steel J6 rollers.

Table 3.3. Coefficients of friction for lubrication effect tests.

	P_0= 1295 MPa P = 1600 N	P_0 = 1448 MPa P = 2000 N	P_0 = 1874 MPa P = 3350 N
Dry	0.39 - 0.45	0.59 – 0.71	> 0.5*
Oil	0.06 – 0.07	0.08	0.08
Water	0.17	0.25	0 .24 – 0.21

* Moment reading exceeded the scale.

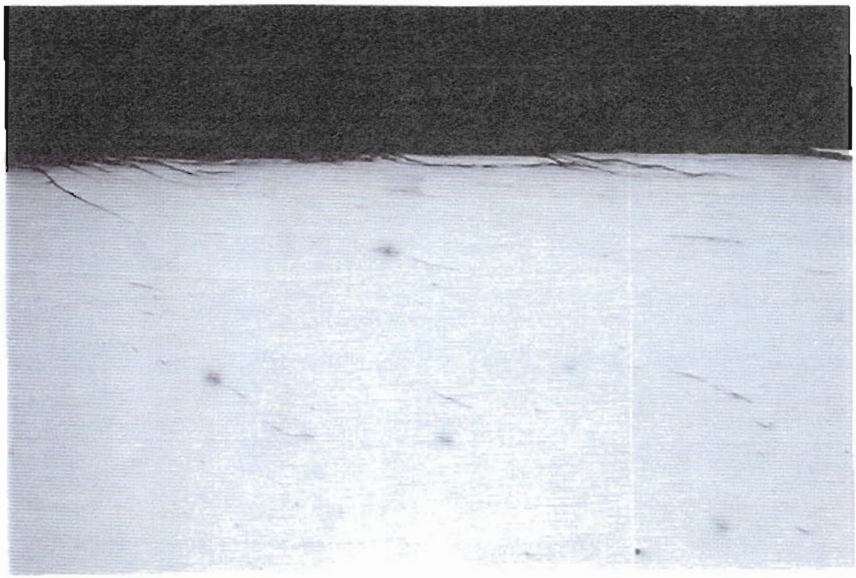

200 X

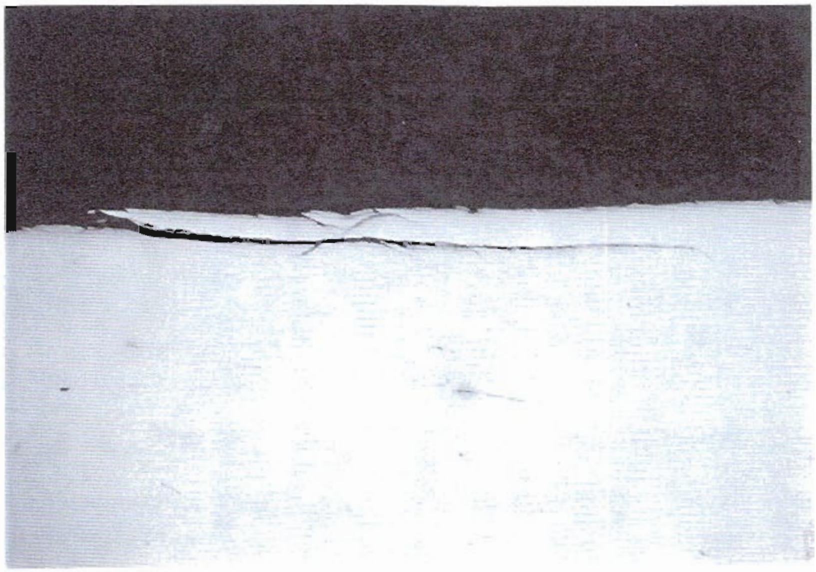

200 X

Fig. 3. 23a. Shallow cracks initiated during the dry period at P_0 = 1448 MPa, P_0/k = 4.66.

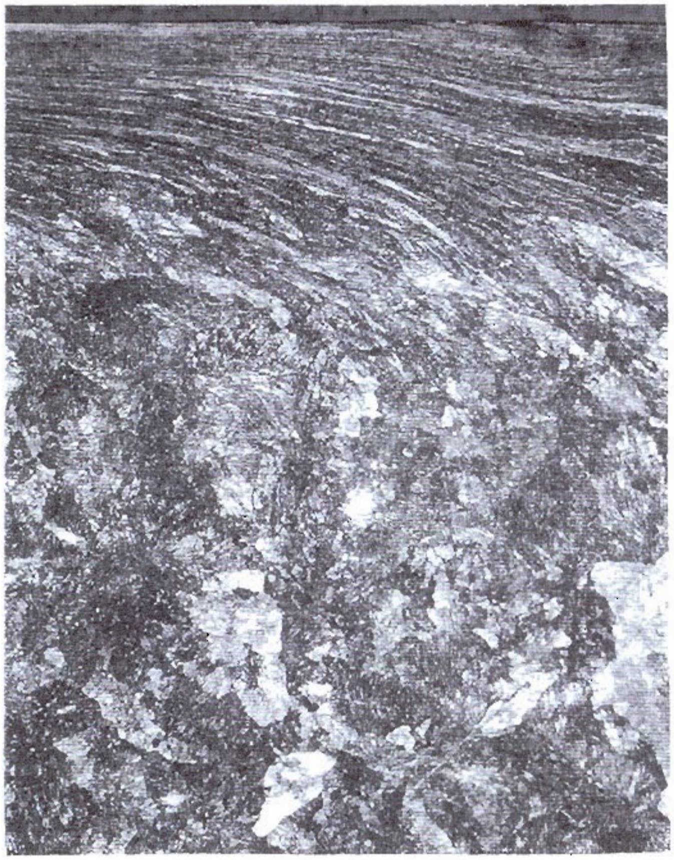

Fig. 3.23b. A shear zone produced during the dry period, showing the shear zone is obviously deeper than the cracks in Fig. 3.23a.

100 X $P_0 = 1295$ MPa, $P_0/k = 4.17$

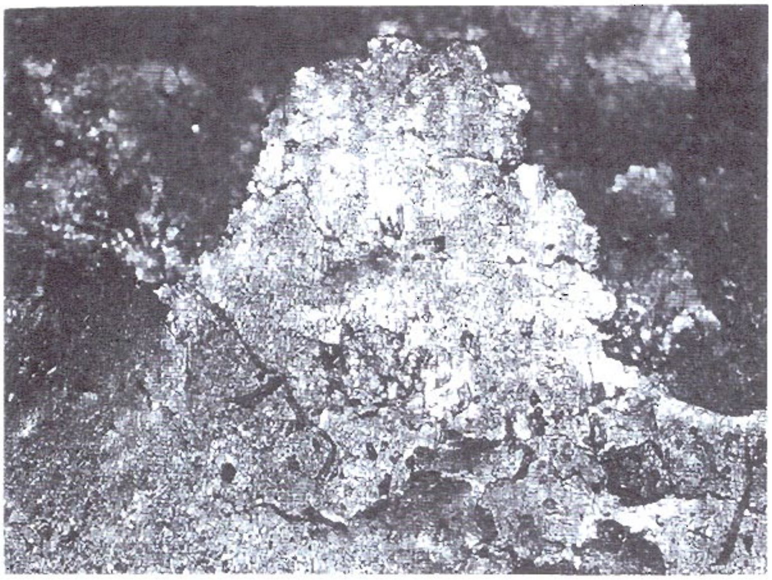

50 X $P_0 = 1874$ MPa, $P_0/k = 6.03$

Fig. 3.24. Top views of crack morphology for rollers subjected to oil lubrication.

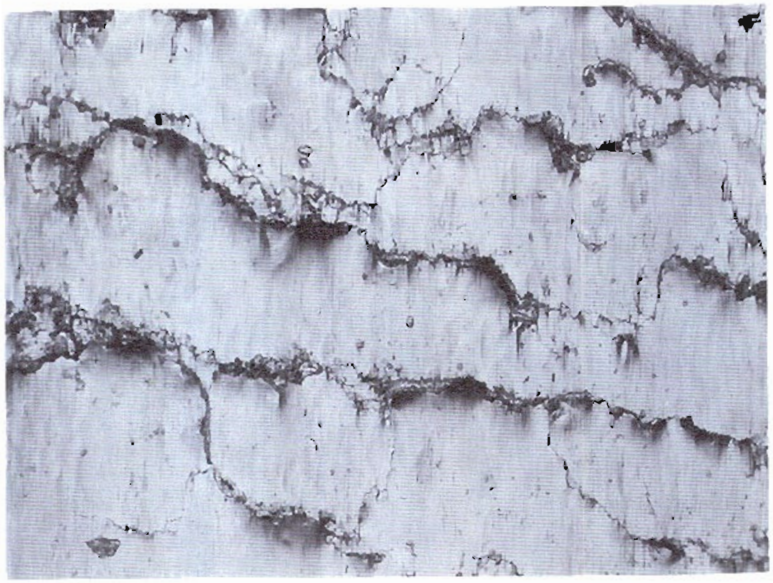

100 X P$_0$ = 1295 MPa, P$_0$/k = 4.17

100 X P$_0$ = 1874 MPa, P$_0$/k = 6.03

Fig. 3.25. Top views of crack morphology for rollers subjected to water lubrication.

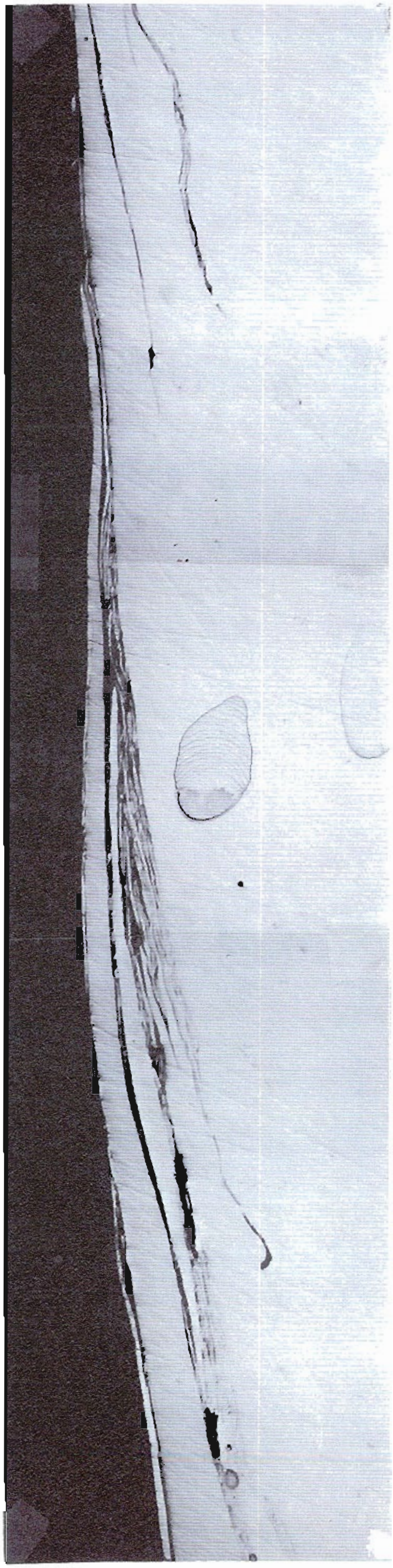

200 X $P_0 = 1448$ MPa, $P_0/k = 4.66$

Fig. 3.26. Longitudinal cross section of rollers tested under oil lubrication.

50 X P_0 = 1874 MPa, Po/k = 6.03

Fig. 3.26 (continued). Longitudinal cross section of rollers tested under oil lubrication.

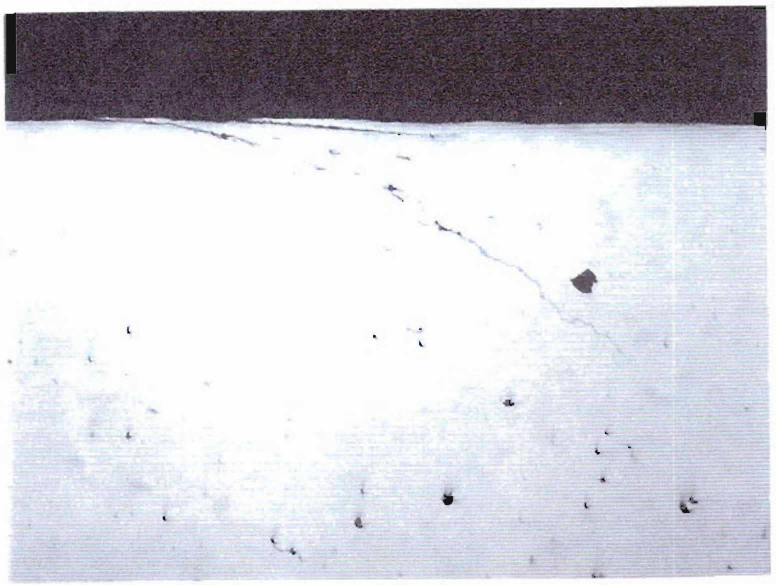

200 X $P_0 = 1295$ MPa, $P_0/k = 4.17$

Fig. 3.27. Longitudinal cross section of rollers tested under water lubrication.

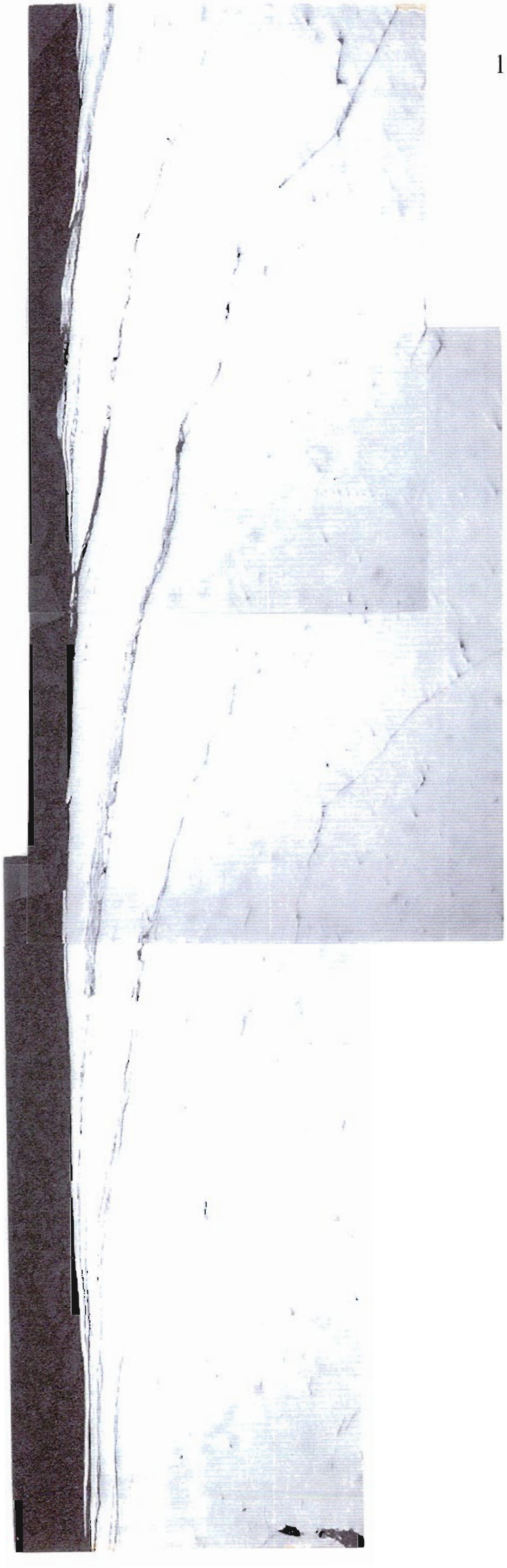

200 X P_0 = 1874 MPa, P_0/k = 6.03

Fig. 3.27(continued). Longitudinal cross section of rollers tested under water lubrication.

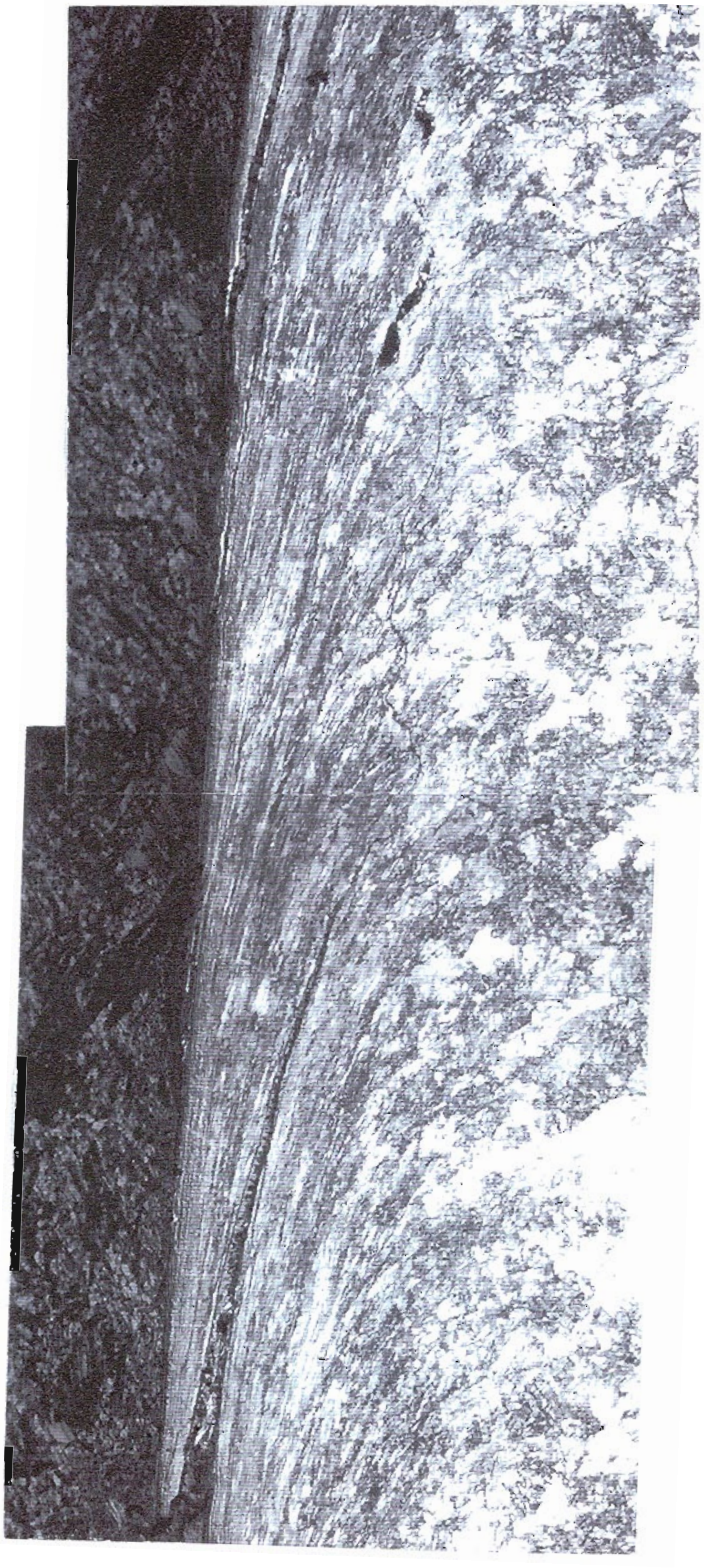

100 X $P_0 = 1874$ MPa, $P_0/k = 6.03$

Fig. 3.28a. Cracks under oil lubrication follow the shear flow line.

100 X $P_0 = 1874$ MPa, $P_0/k = 6.03$

Fig. 3.28b. Cracks are confined within the shear flow zone, the crack tips following the dividing line between deformed and relatively undeformed regions.

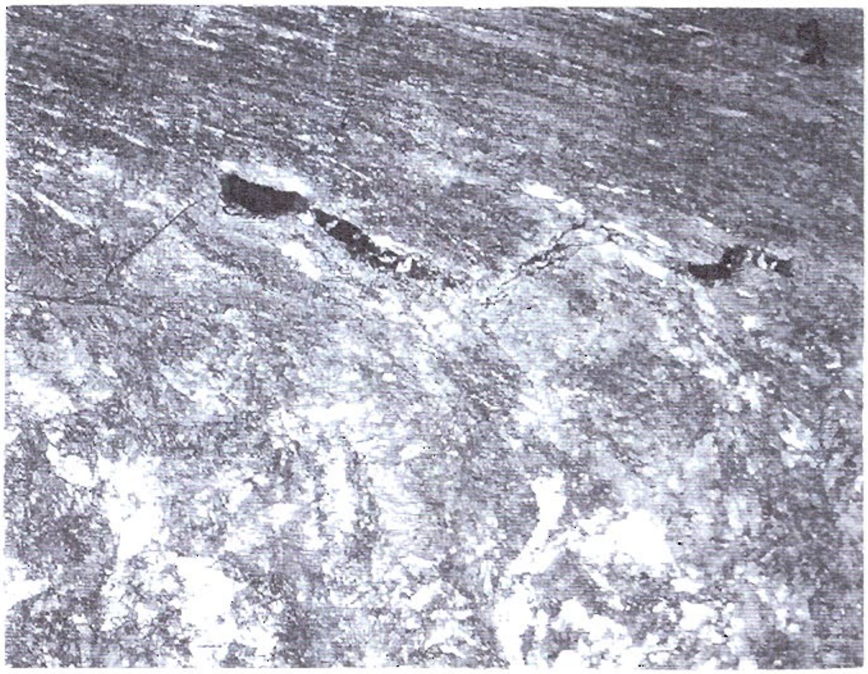

200 X $P_0 = 1874$ MPa, $P_0/k = 6.03$

Fig. 3.28c. A zig-zag pattern at a crack tip. Apparently the crack tip follows the dividing line between deformed and relatively undeformed regions.

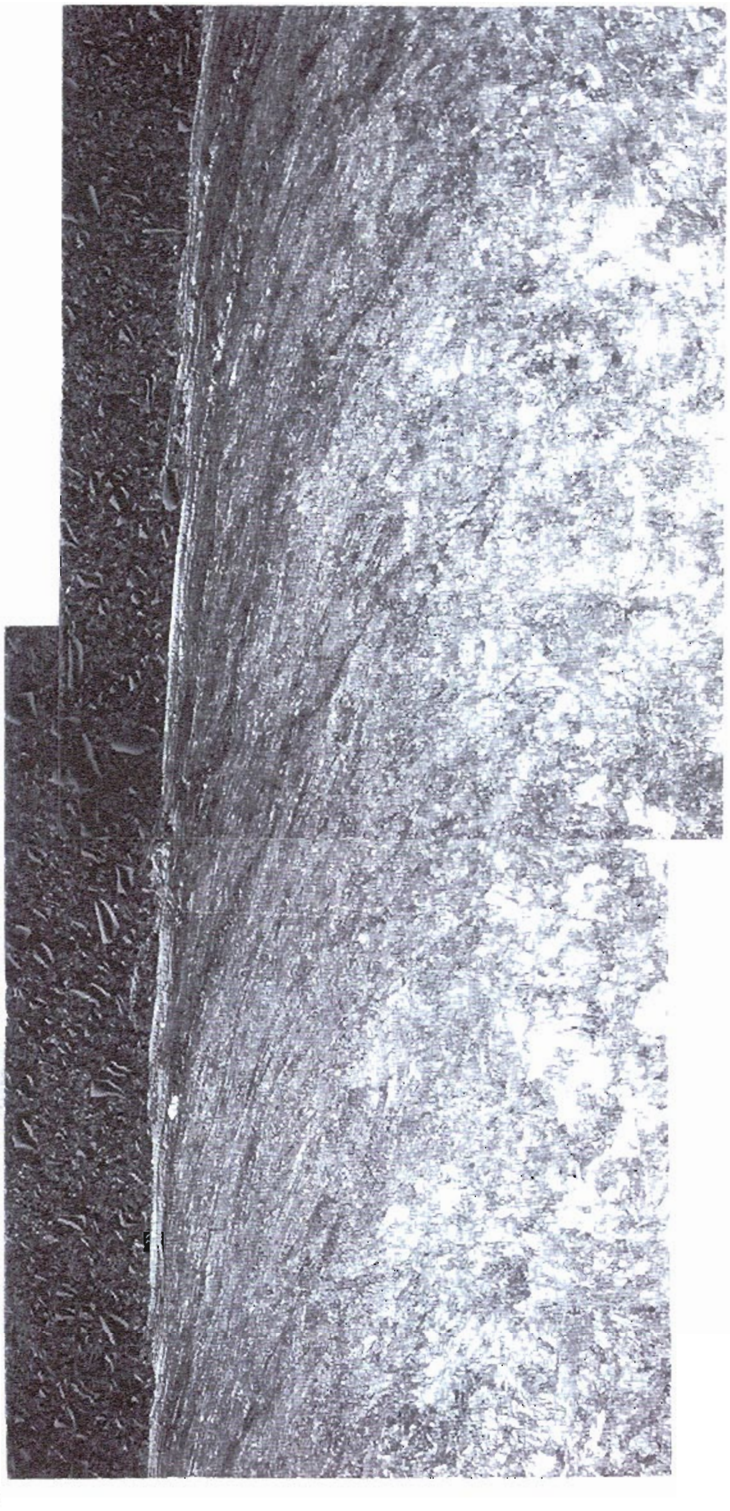

100 X P_0 = 1874 MPa, P_0/k = 6.03

Fig. 3.29a. A typical crack under water lubrication, showing cracks growing into the relatively undeformed zone with an increased angle to the contact surface.

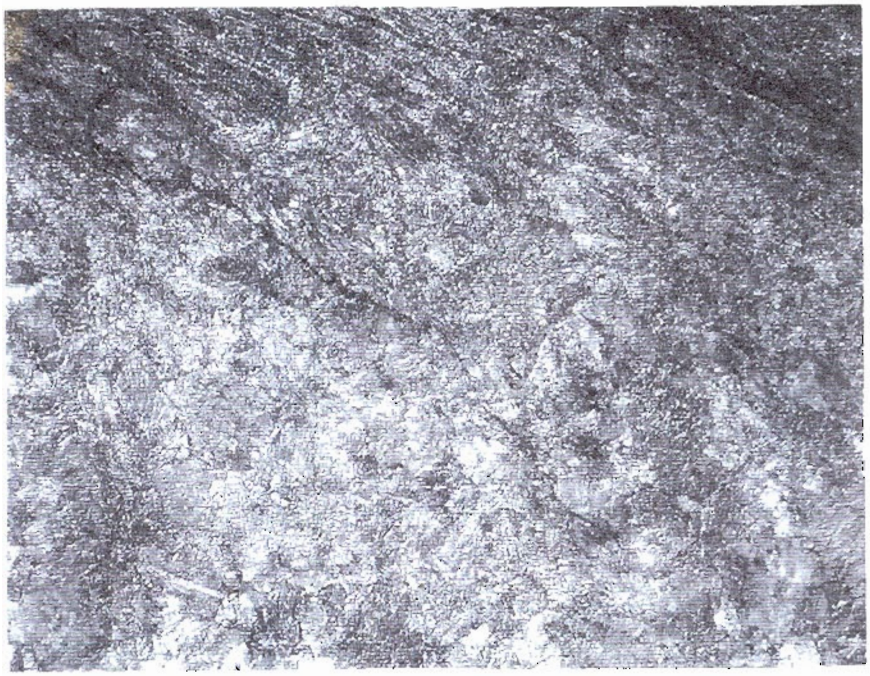

200 X P_0 = 1874 MPa, P_0/k = 6.03

Fig. 3.29b. A close-up view of a crack tip under water lubrication, showing the tip passing between the dividing line between deformed and relatively undeformed zone.

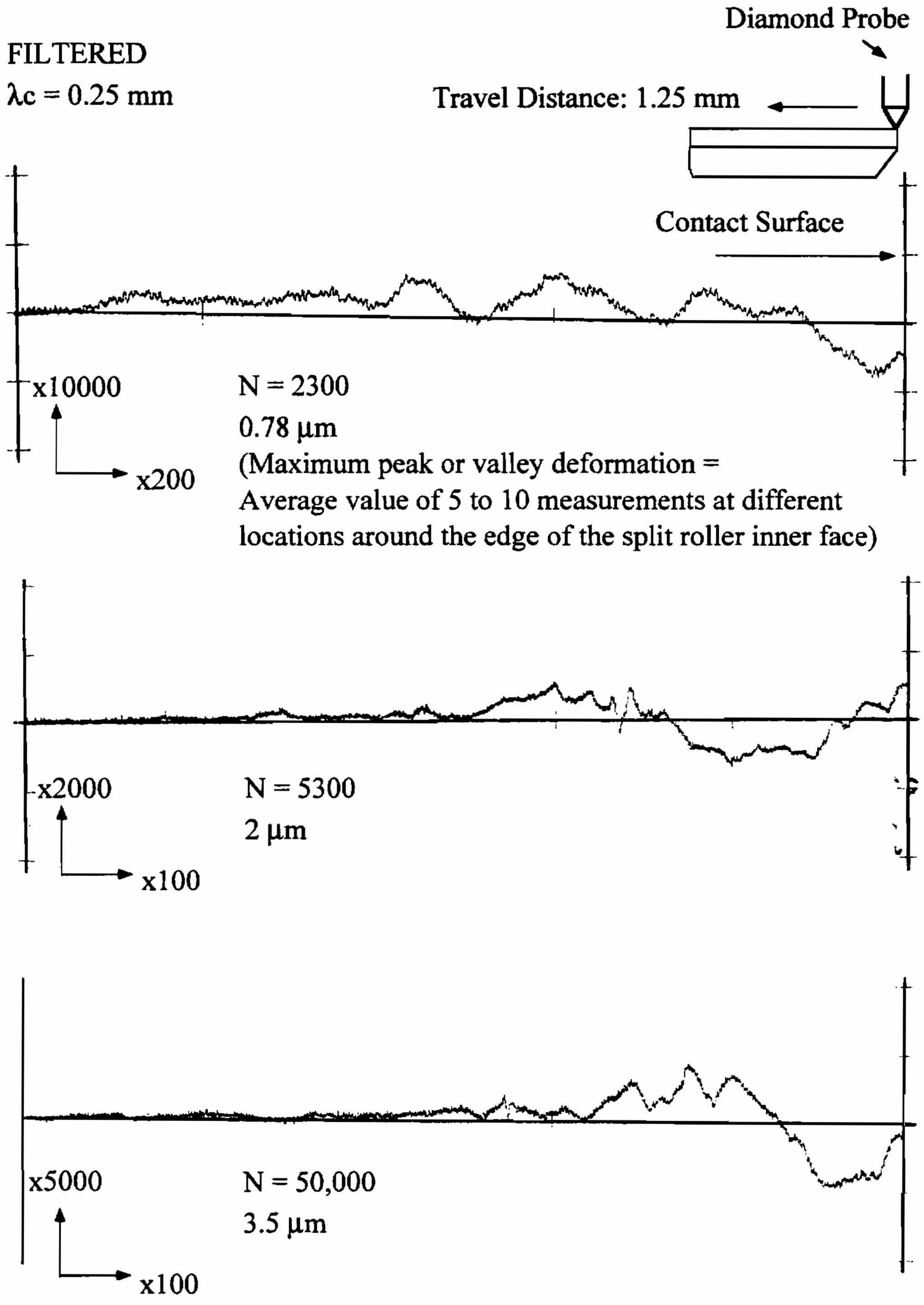

Fig. 3.30. Out-of-plane deformation measured at P_0 = 1759 MPa.

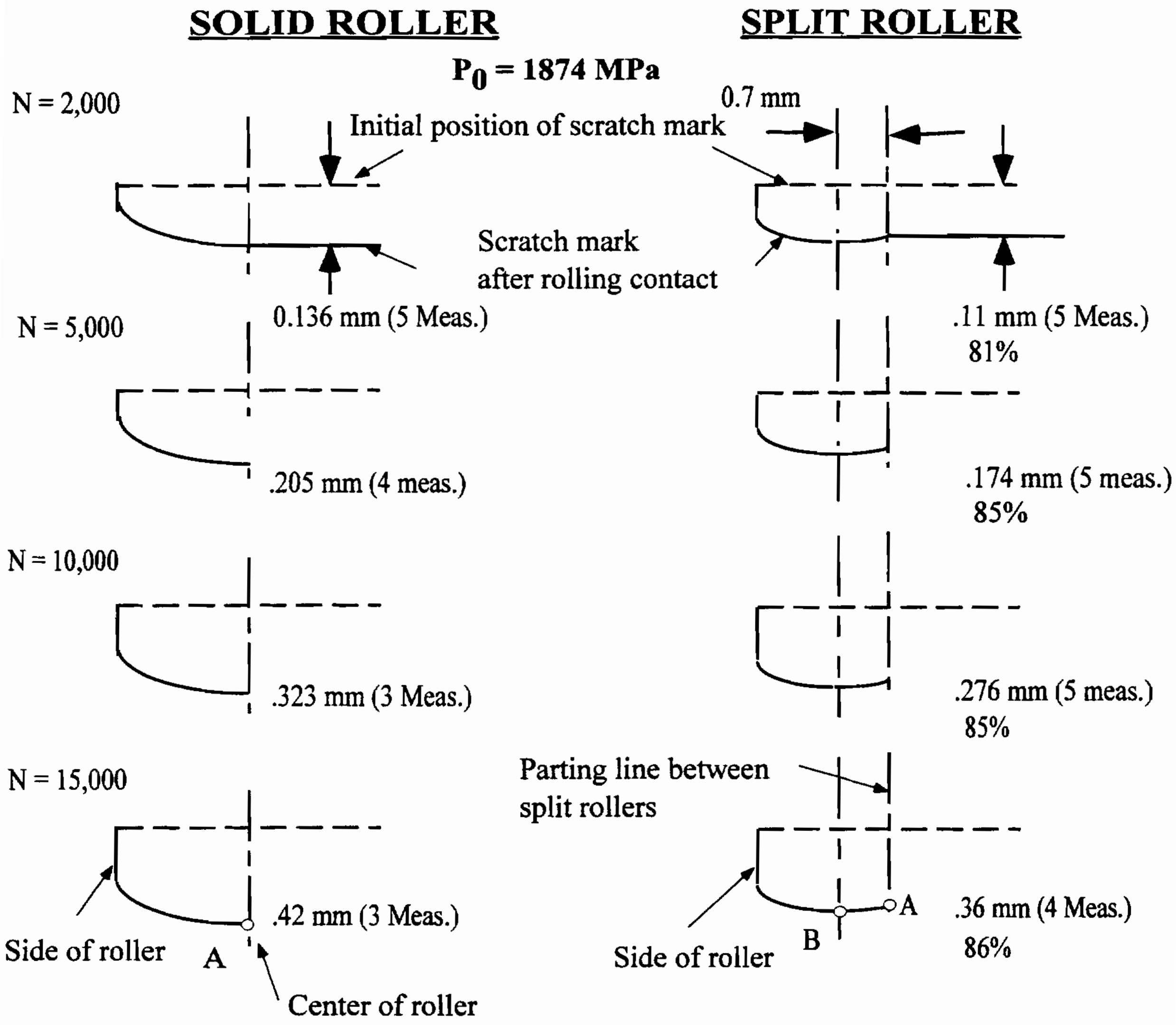

Fig. 3.31a. Comparison of surface scratch displacement between sold and split rollers at P_0 = 1874 MPa.

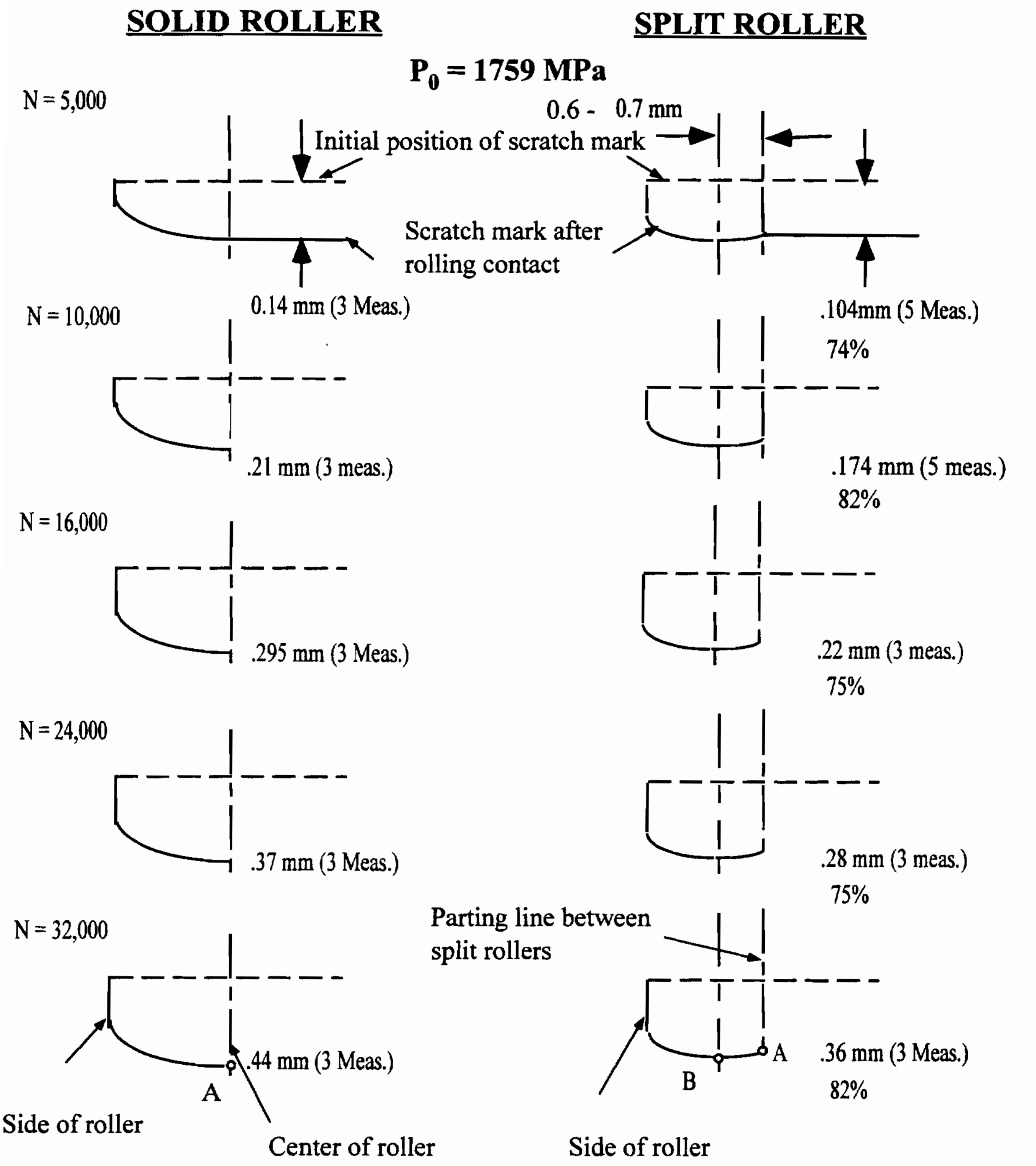

Maximum displacement point: approx. 0.7 mm from the center
Difference between A and B: approx. 20 - 70 μm.

Fig. 3.31b. Comparison of surface scratch displacement between sold and split rollers at P_0 = 1759 MPa.

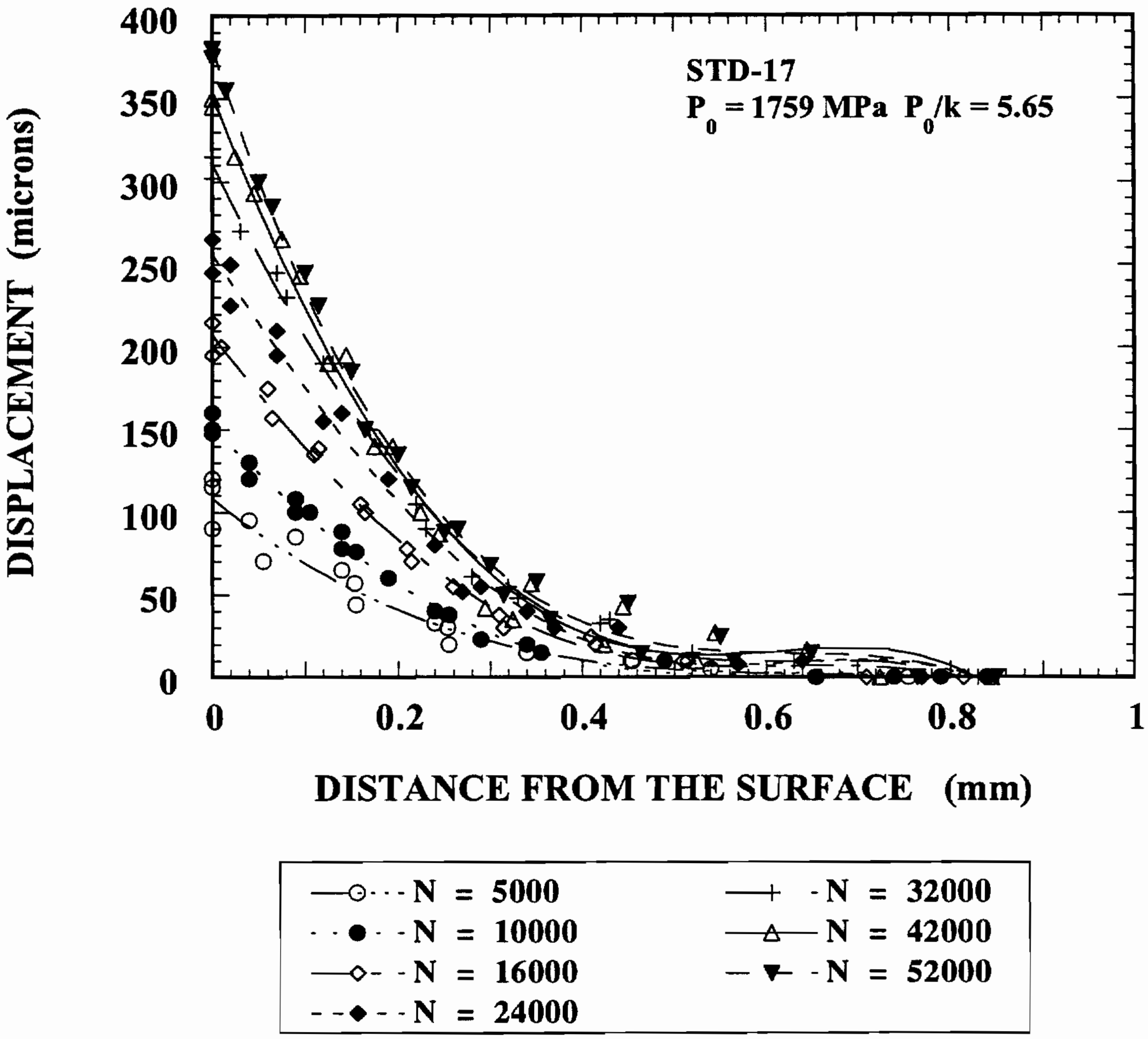

Fig. 3.32. Original data of indentation displacement versus depth from the contact surface for a pair of STD split rollers.

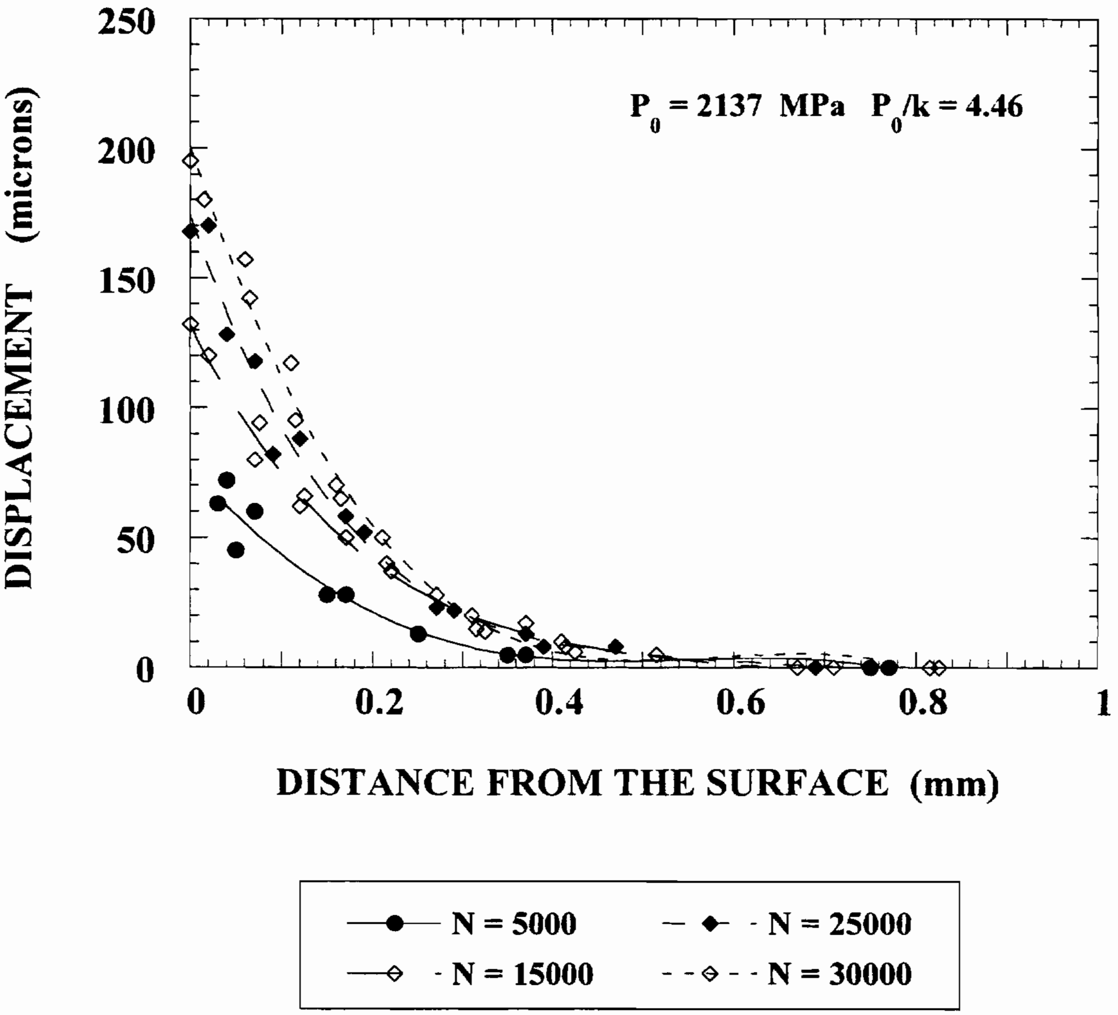

Fig. 3.33. An example of original data of indentation displacement versus depth from the surface for a bainitic steel J2 specimen.

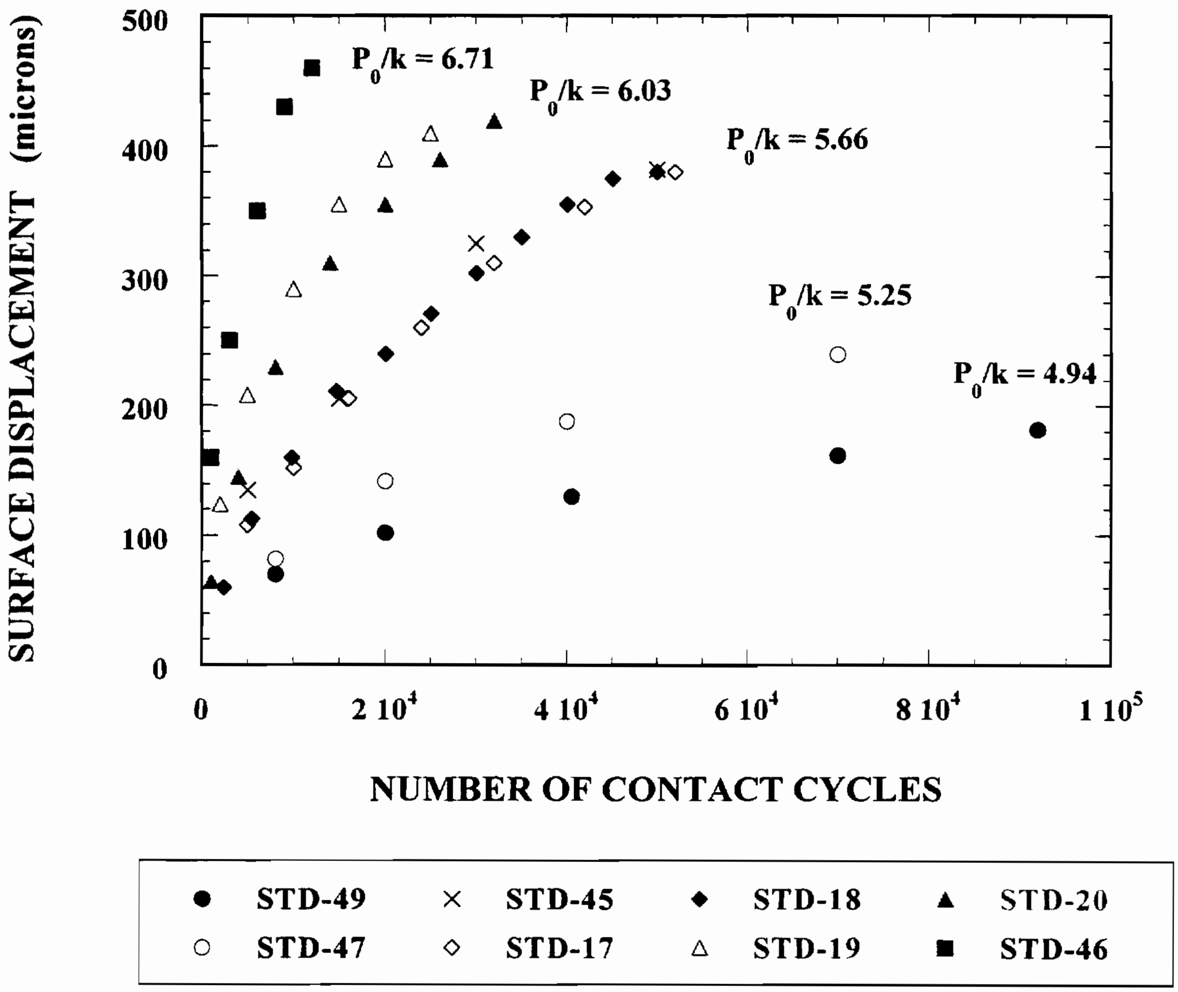

Fig. 3.34. Surface displacement versus the number of contact cycles at various contact pressure levels.

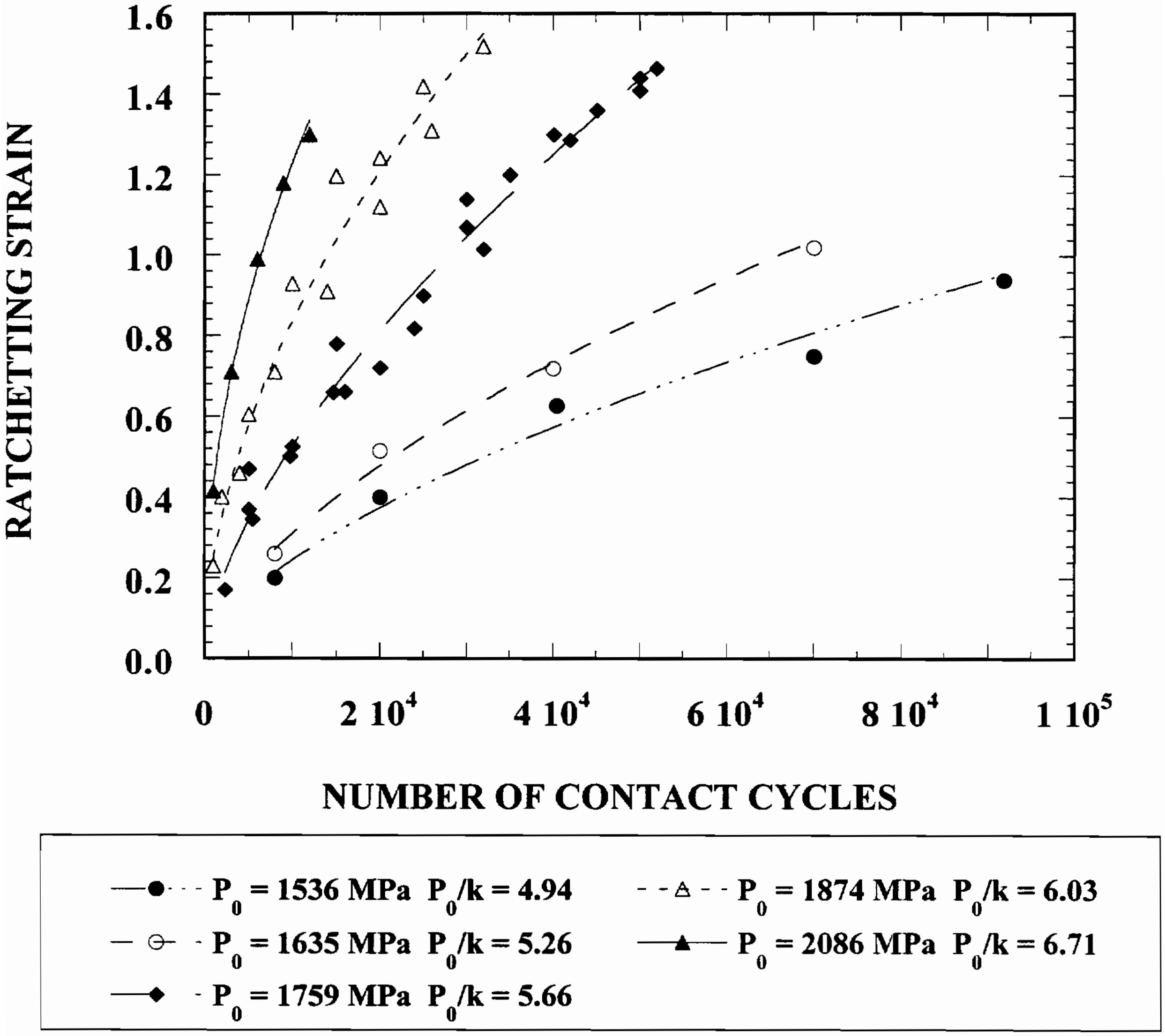

Fig. 3.35. Ratchetting strain plotted against the number of contact cycles, showing a non-linear correlation.

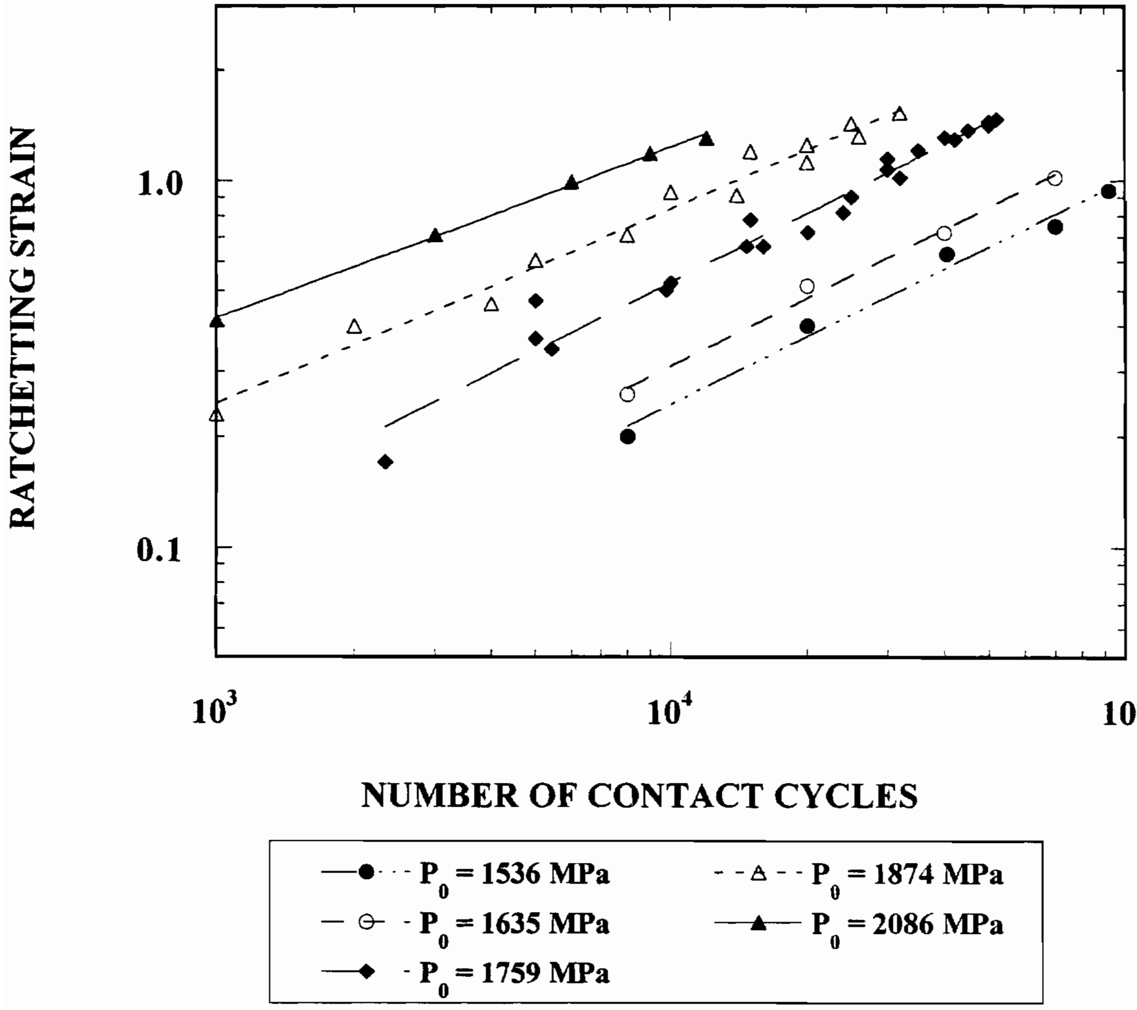

Fig. 3.36. Ratchetting strain versus the number of contact cycles for STD steel on a log-log scale, showing a power function.

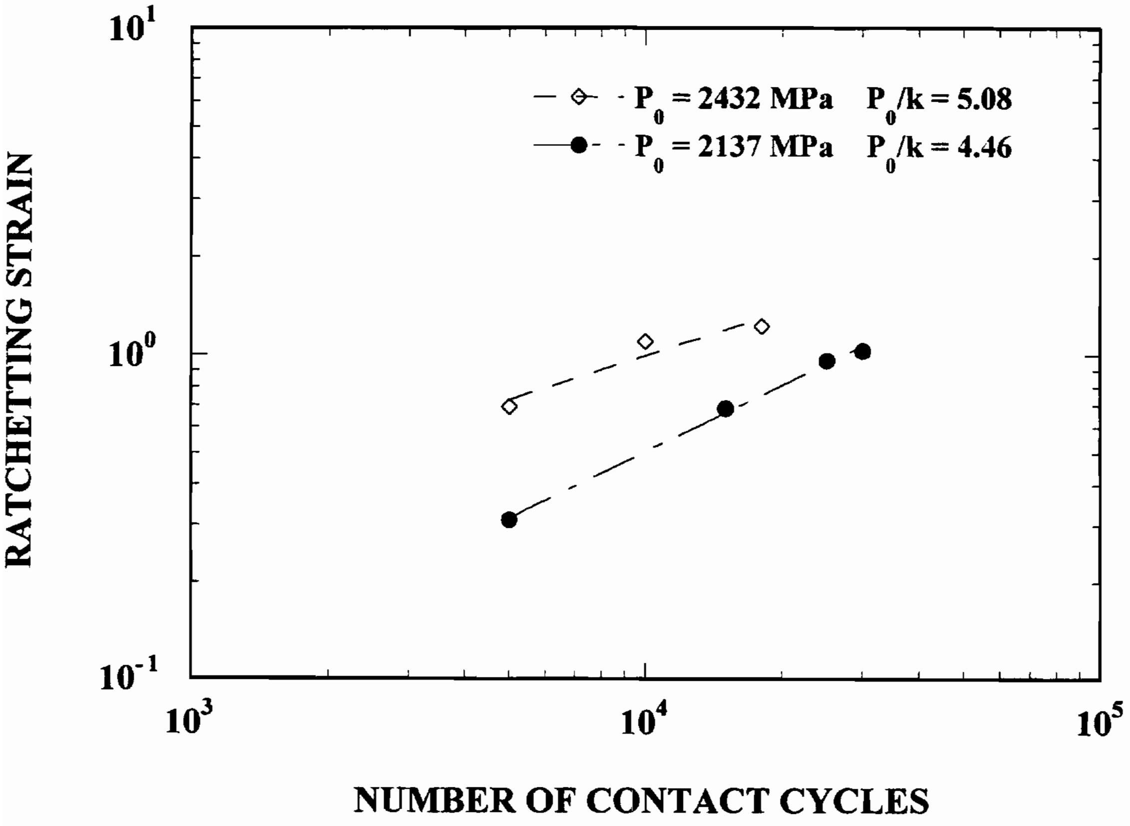

Fig. 3.37. Ratchetting strain versus the number of contact cycles for J2 steel on a log-log scale, showing a power function.

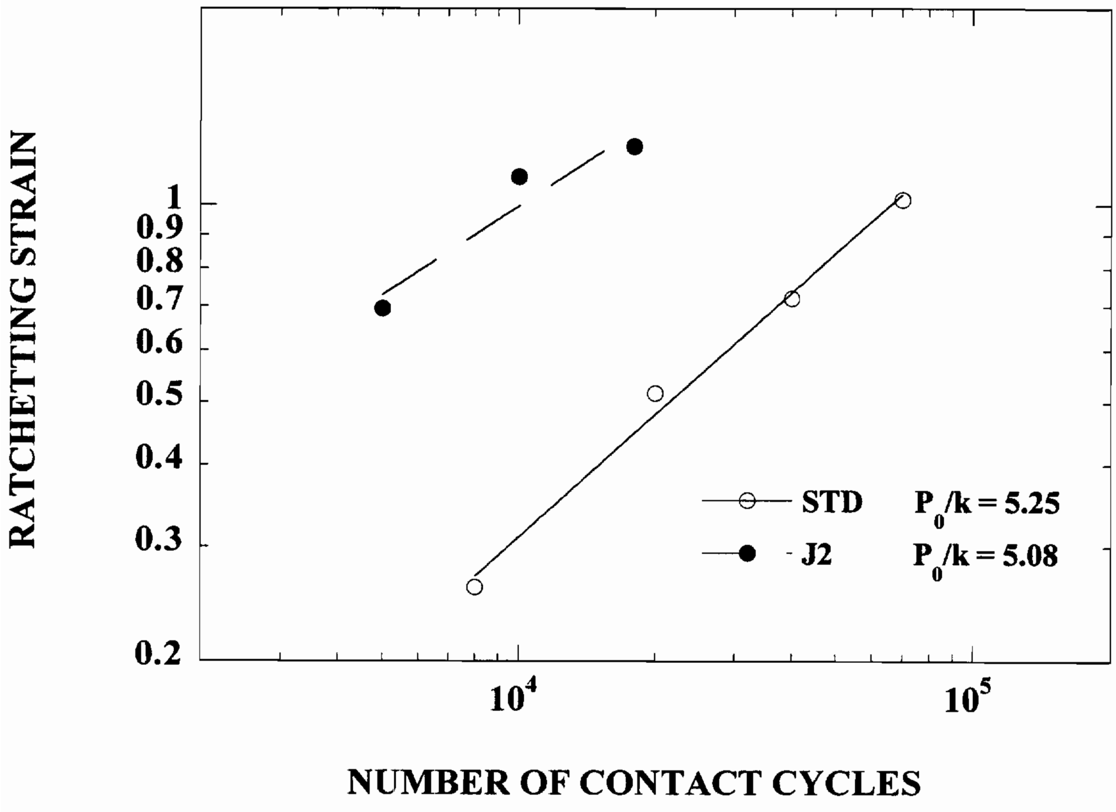

Fig. 3.38. Comparison of ratchetting strain between STD and J2 at a comparable normalized contact pressure level.

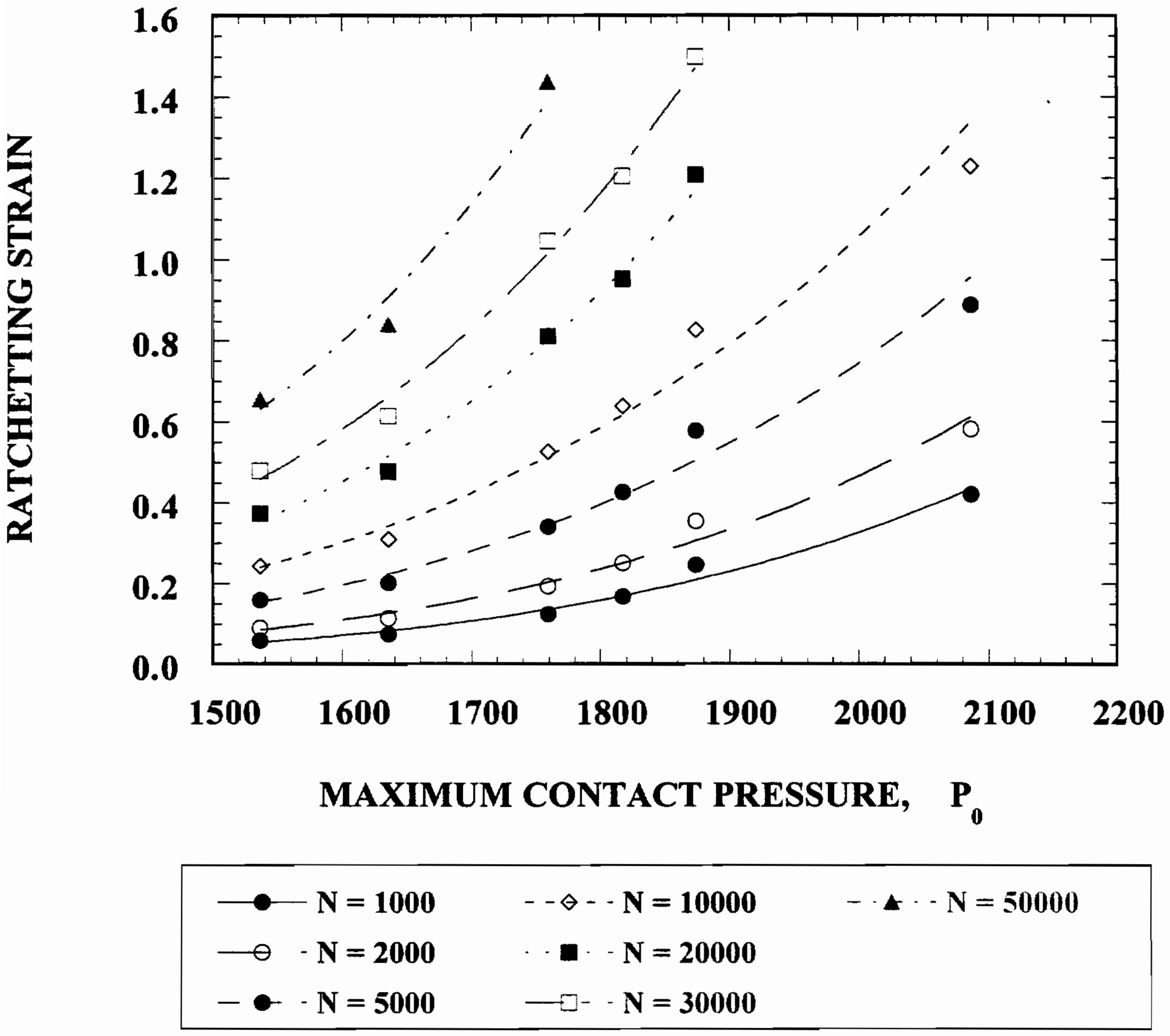

Fig. 3.39. Ratchetting strain as a function of the maximum contact pressure at given numbers of contact cycles.

Table. 3.4a. Ratchetting strain and surface displacement data of STD steel

P_0 = 1536 MPa P_0/k = 4.94			P_0 = 1635 MPa P_0/k = 5.25			P_0 = 1759 MPa P_0/k = 5.66		
N	δ (μm)	ε_r	N	δ (μm)	ε_r	N	δ (μm)	ε_r
8000	70	.200	8000	82	.260	5000	135	.470
20000	102	.400	20000	142	.515	15000	210	.780
40460	130	.628	40000	188	.719	30000	325	1.140
70000	162	.750	70000	240	1.020	50000	382	1.440
91870	182	.940				5000	108	.370
						10000	152	.525
						16000	205	.661
						24000	260	.818
						32000	310	1.016
						42000	353	1.287
						52000	380	1.464
						2330	60	.170
						5430	113	.346
						9770	160	.502
						14700	211	.660
						20040	240	.720
						25040	271	.900
						30040	302	1.070
						35040	330	1.200
						40080	355	1.300
						45100	375	1.360
						50000	380	1.410

N: Number of contact cycles.
δ : Surface displacement.
ε_r: Ratchetting strain.

Table. 3.4a. (Cont.) Ratchetting Strain and Displacement Data of STD Steels

$P_0 = 1818$ MPa $P_0/k = 5.85$			$P_0 = 1874$ MPa $P_0/k = 6.03$			$P_0 = 2086$ MPa $P_0/k = 6.71$		
N	δ (μm)	ε_r	N	δ (μm)	ε_r	N	δ (μm)	ε_r
3000	110	.300	2000	124	.400	1000	160	.415
8000	190	.620	5000	208	.605	3000	250	.710
16000	244	.860	10000	290	.930	6000	350	.990
26400	300	1.050	15000	355	1.197	9000	430	1.180
			20000	390	1.243	12000	460	1.300
			25000	410	1.420			
			1000	65	.230			
			4000	145	.460			
			8000	230	.710			
			14000	310	.910			
			20000	355	1.120			
			26000	390	1.310			
			32000	420	1.520			

Table 3.4b. Ratchetting Strain and Displacement Data of Bainitic Steel J2

$P_0 = 2137$ MPa $P_0/k = 4.46$			$P_0 = 2432$ MPa $P_0/k = 5.08$		
N	δ (μm)	ε_r	N	δ (μm)	ε_r
5000	74	.311	5000	210	.695
15000	135	.684	10000	320	1.104
25000	175	.960	18000	376	1.228
30000	200	1.030			

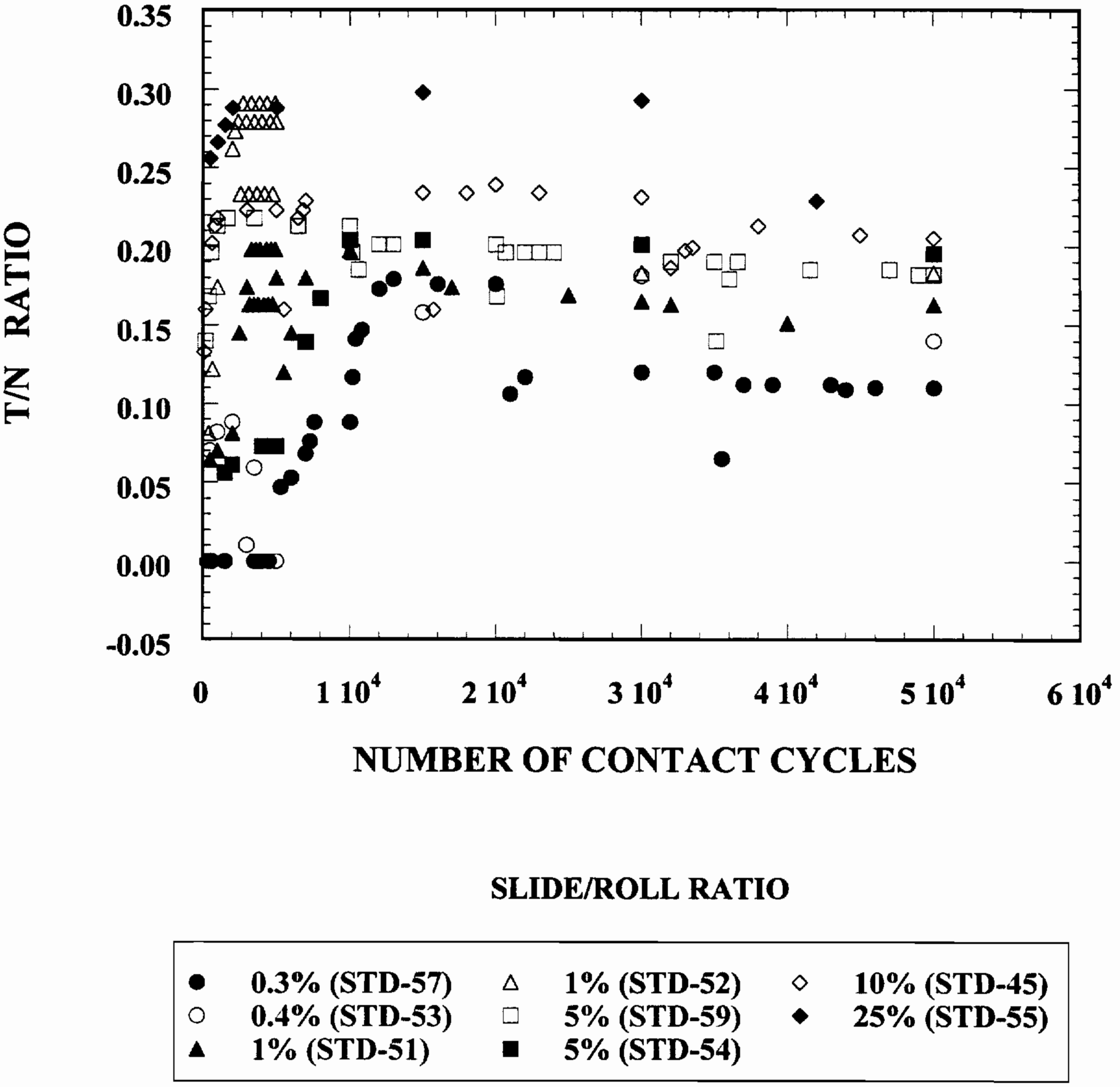

Fig. 3.40. T/N ratios at various slide/roll ratios during the entire test duration.

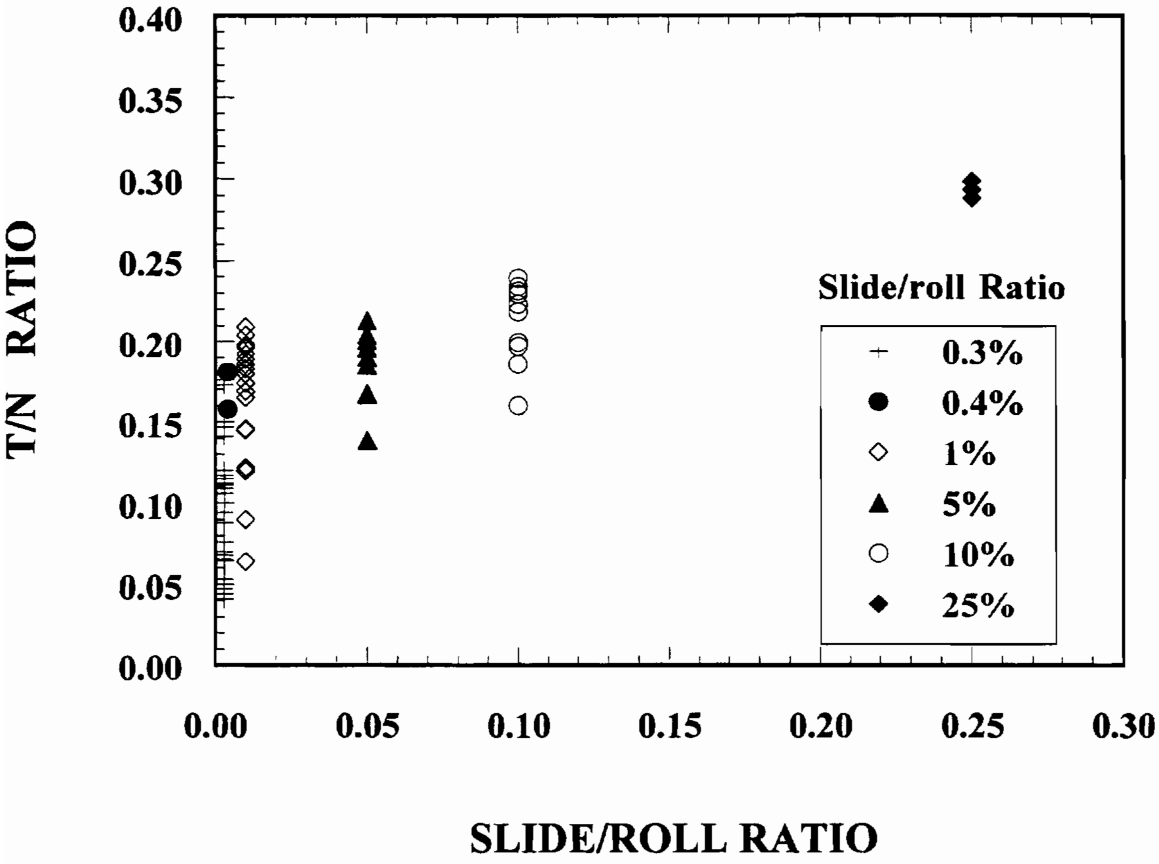

Fig. 3.41. T/N ratio as a function of slide/roll ratio during relatively steady state period (N = 5000 to 35000 cycles).

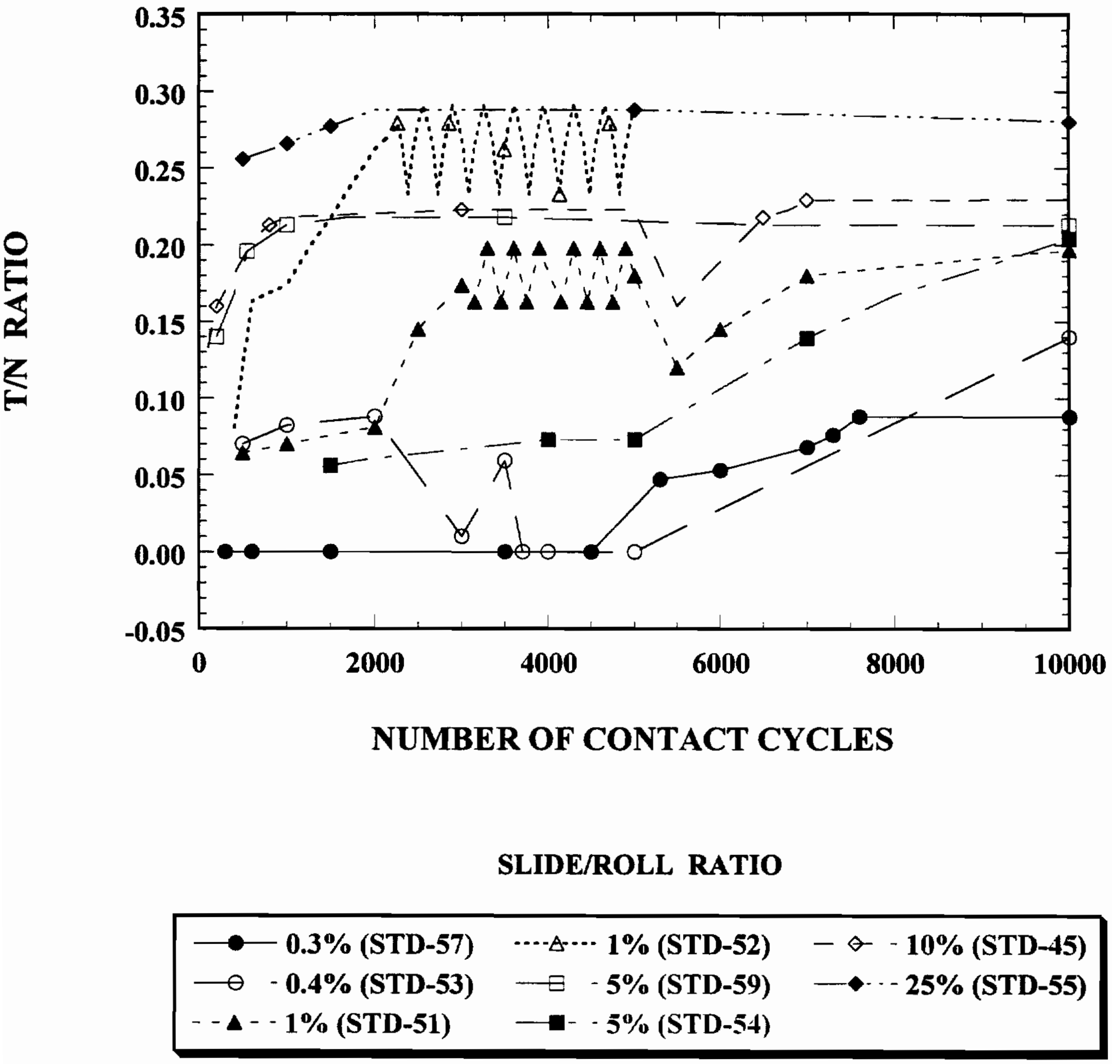

Fig. 3. 42. Variation of T/N ratios during contact cycles of N<10000.

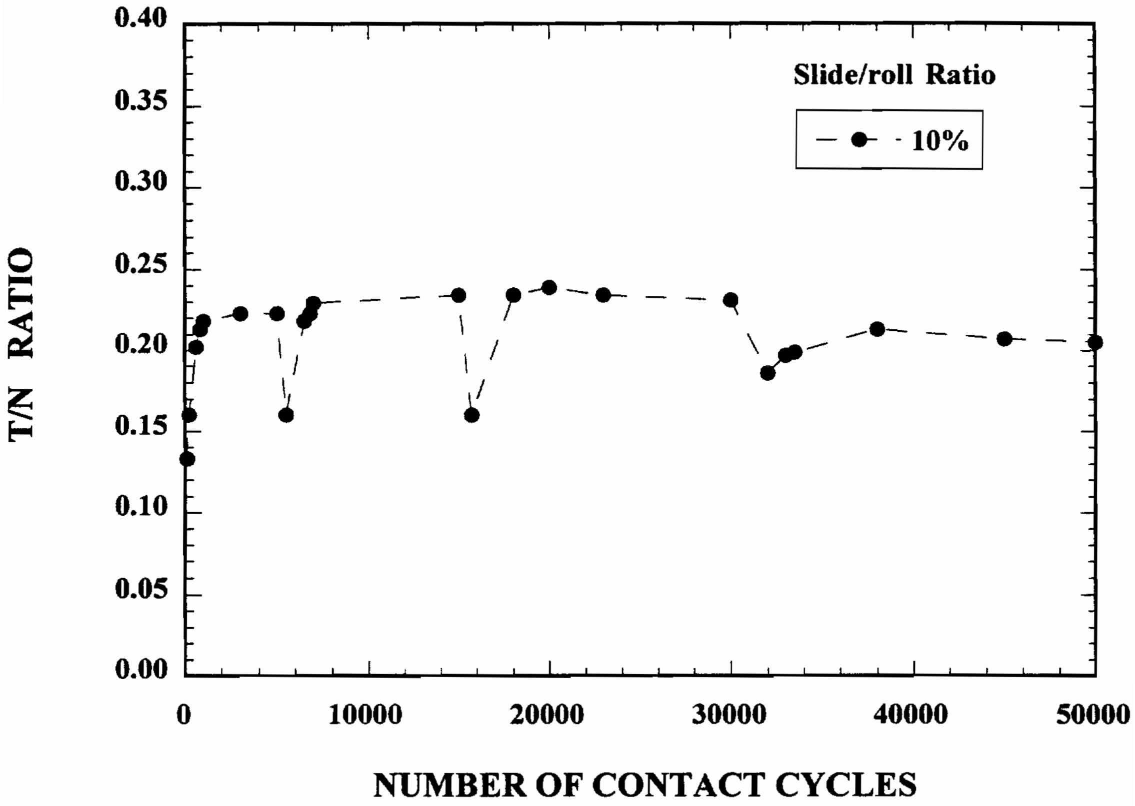

Fig. 3.43. A drop and a recovery of the T/N ratio after each measurement interval at slide/roll ratio = 10%.

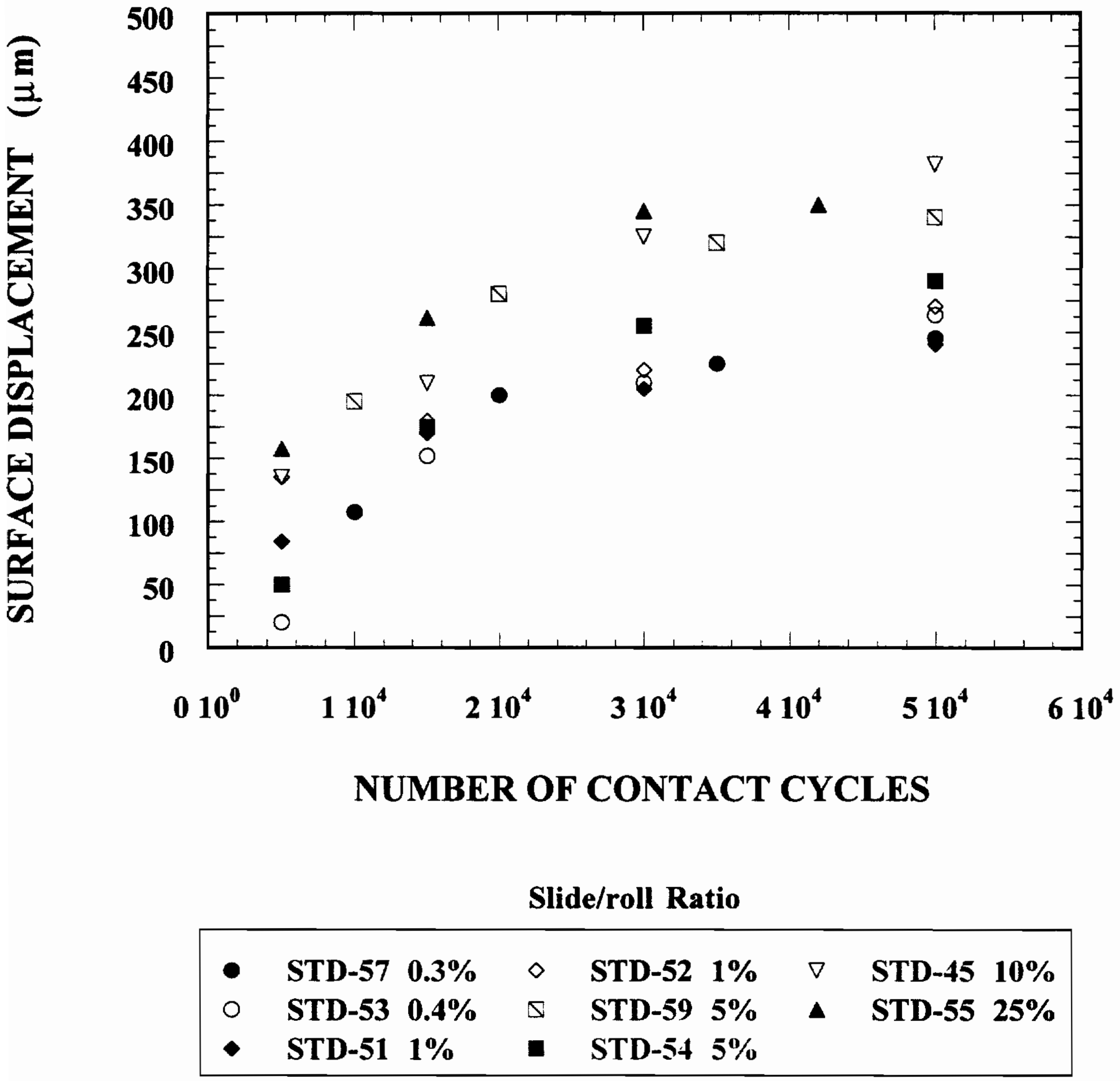

Fig. 3.44. Surface displacement versus the number of contact cycles at various slide/roll ratios.

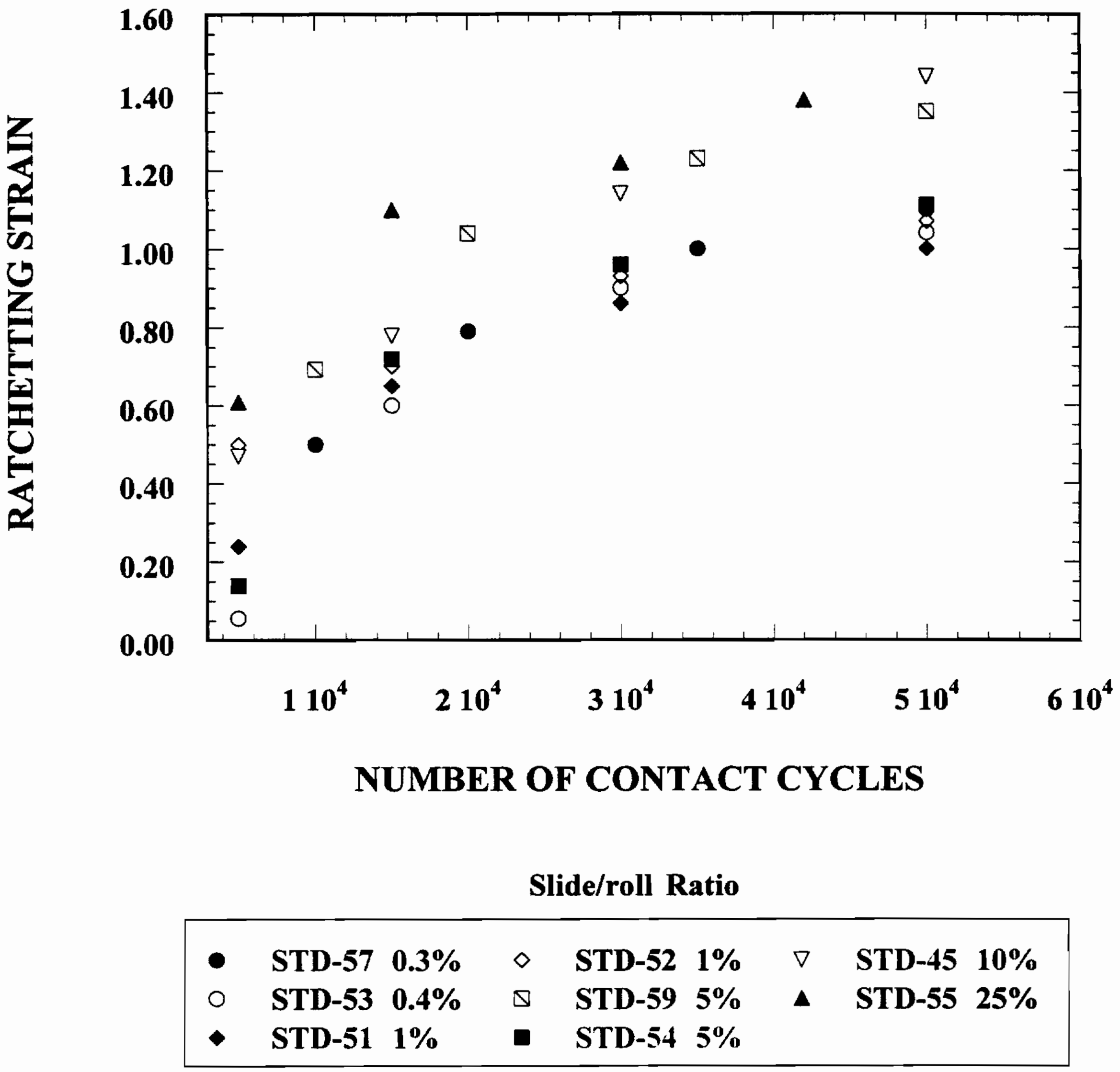

Fig. 3.45. Ratchetting strain versus the number of contact cycles at various slide/roll ratios on a linear scale.

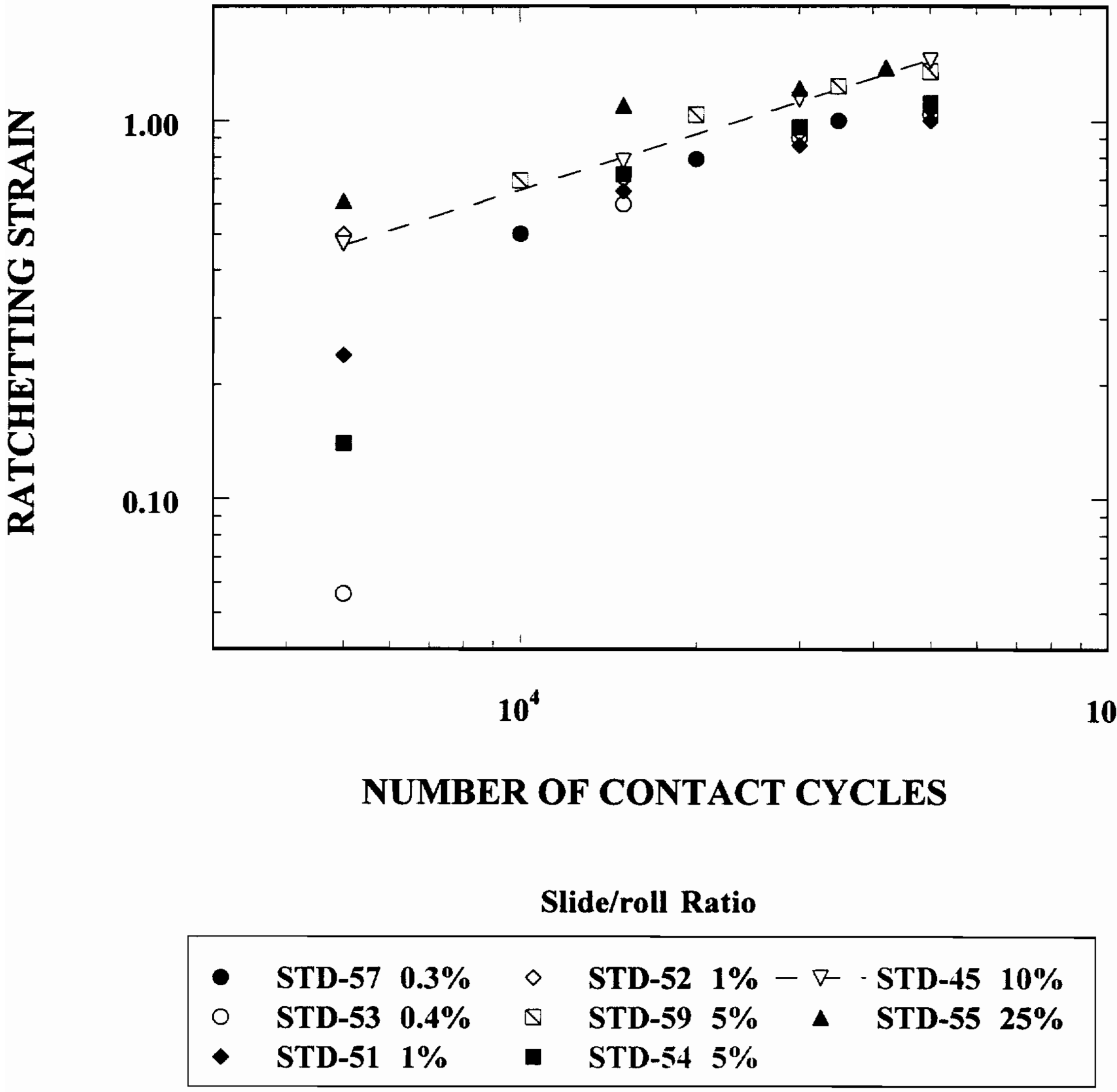

Fig. 3.46. Ratchetting strain versus the number of contact cycles at various slide/roll ratios on a log-log scale.

Table. 3.5. Ratchetting strain and surface displacement data of pearlitic steel STD at various slide/roll ratios.

Specimen No.	**Slide/roll Ratio**	**N**	**δ (μm)**	**γ**
STD-57		10000	107	.501
	0.3%	20000	200	.790
		35000	225	1.000
		50000	245	1.100
STD-53		5000	20	.056
	0.4%	15000	152	.600
		30000	210	.900
		50000	263	1.040
STD-51		5000	84	.240
	1%	15000	170	.650
		30000	205	.860
		50000	240	1.000
STD-52		5000	135	.500
	1%	15000	180	.700
		30000	220	.930
		50000	270	1.070
STD-54		5000	50	.140
	5%	15000	175	.720
		30000	255	.960
		50000	290	1.110
STD-59		10000	195	.693
	5%	20000	280	1.040
		35000	320	1.230
		50000	340	1.350

Table. 3.5 (Cont.). Ratchetting strain and surface displacement data of pearlitic steel STD at various slide/roll ratios.

Specimen No.	Slide/roll Ratio	N	δ (μm)	γ
STD-45	10%	5000	135	.470
		15000	210	.780
		30000	325	1.140
		50000	382	1.440
STD-55	25%	5000	158	0.610
		15000	261	1.100
		30000	345	1.200
		42000	350	1.380

N: Number of contact cycles.

δ: Surface displacement

γ: Ratchetting strain.

CHAPTER 4

DISCUSSION

4.1 SURFACE RCF PERFORMANCE

4.1.1 Non-linear Behavior of RCF Performance data

Surface RCF life increases with decreasing contact pressure in small scale tests with a slide/roll ratio of 10% and an average tangential to normal traction ratio of 0.24 generated under water lubrication. The relationship is non-linear over the contact pressure range of 850 to 2300 MPa. Previous research, in which the same STD material was used, suggested a linear relationship between RCF life and contact pressure[11,59] but the contact pressure range was limited to 900 to 1400 MPa. Under the conditions below P_0 = 1400 MPa, the current data also show the trend of linearity, and fall within a scatter band of a factor of 2 of the equation expressing the correlation between RCF life and the contact pressure derived previously. [13]

The non-linearity is only present when the contact pressure is pushed to higher levels. One way to interpret the results is that RCF life is a power law function of contact pressure. Previous researchers have also used power functions to correlate RCF life with contact pressure. The result of Clayton and Hill[20] revealed that the power index is also a function of the slide/roll ratio, ξ, reaching a constant value at $\xi > 4\%$. The power index in the current research ranges from - 4.01 to - 5.16 (Figure 3.4), consistent with the value of -4.2 at $\xi = 5\%$ and 10% reported previously.[20] Other values reported in the literature are -1, [46] -1.5 for $\xi = 11\%$, [43] -5 for $\xi = 0$ and 20%, [84] and -3.68 to -14.48 for $\xi = 10\%$.[13]

An alternative interpretation for the non-linearity is that there is a bilinear behavior (see Figure 3.5), with a change in mechanism of failure at a normalized contact pressure of $P_0/k \approx 4$. The value of $P_0/k \approx 4$ is close to the theoretical shakedown limit, which has been invoked in explaining the deformation behavior of materials. [14,24] Continued yielding in the form of strain ratchetting is only possible when loaded above the shakedown limit, therefore, the transition behavior of the data may be dictated by the deformation behavior.

If the relationship depicted in Figure 3.5 is relevant to the field, it predicts that modifying P_0/k values either by reducing contact pressure or increasing the strength can significantly increase the RCF life. However, the improvement will be much less above the transition, since the slope of the curves is much steeper than these below it. Modifying P_0/k to move from the steep slope region to the long life region could achieve substantial increases in RCF life. However, reducing P_0/k value by increasing strength could prove difficult to achieve. For example, for standard carbon rail steel, a P_0/k of 5 represents a P_0 of 1560 MPa. In order to withstand this P_0 and bring P_0/k down to 2.5 to achieve a much longer life, a yield strength in shear of 640 MPa would be required. This is a much higher strength than that possessed by any materials tested in the current work.

It is possible, however, that increasing strength is not the only criterion, particularly for the steep region above the transition. If the critical strain to initiate shear band cracking decreases with increasing strength or hardness, the effect of ductility needs to be explored in greater detail.

From a practical point of view, it has to be remembered that the relationships have been derived for small scale laboratory tests at a fixed slide/roll ratio. RCF behavior can be significantly affected by changing the amount of slip. Furthermore, it is very difficult to calculate the contact pressure experienced by wheels and rails between the rail gage corner and the wheel flange/throat region where the contact is non-Hertzian. If deformation depth could be shown to be a consistent function of P_0/k then it might prove possible to use the deformation depth of rails to estimate actual P_0 values in service.

4.2 MECHANISMS OF SURFACE RCF

4.2.1 Two Crack Growth Modes — Shear Band Cracking and Branched Cracking

It is evident that shear flow is almost always present on the running surface, even at the lowest contact pressure employed (Figure 3.11b, $P_0/k = 2.76$ for STD, and Figure 3.13b, $P_0/k = 3.11$ for J4). Crack orientation at the immediate surface is obviously dictated by the flow pattern at both high and low contact pressure levels, although only a very short crack length is within this region at low contact pressure. The plastic deformation may contribute to crack initiation by generating dislocation pile-ups and then voids and microcracks as referred to in the literature review. [35,36]

The microscopy study of the current research has clearly revealed that there are two crack growth modes — shear band cracking and branched cracking. The magnitude of the shear plastic flow determines the crack growth mode. Shear band cracking relates to a significant depth of the heavily sheared zone loaded well above the shakedown limit.

The shear flow leads to work-hardening, thus creating a surface layer with modified microstructure and increased hardness. As a consequence of the generation of the shear flow layer, crack morphology changes from branched cracks to predominately shear band cracks. The shear band cracks are generally parallel and seldom branch, since they tend to follow the shear flow generated path, which possibly is a weaker, realigned microstructure oriented in the direction of overall shear flow. At the crack mouth, the surface material is severely sheared causing the so called shear lips. The severity of shear lips depends on both the normal and tangential contact pressure levels. Surface RCF life, in this case, often ends before cracks can grow into the relatively undeformed material below the shear zone.

Shear flow is progressive, it is the result of strain ratchetting, i. e. a cycle by cycle minute increment of permanent strain in the primary loading direction. For a given material, the rate of strain ratchetting, an increment of strain per cycle, is a function of contact conditions, and increases with normal and tangential traction. [24,26,28,38,87]

For surface RCF processes characterized by shear band cracking, failure is postulated to be due to the exhaustion of ductility reserve within the work-hardened layer. The term, a ductility reserve, has been used in the literature, but has not been clearly defined. In the current research, the author would like to suggest a term — a critical strain, which in a sense is equivalent to the ductility reserve. The critical strain is defined as the maximum shear strain that a material can sustain without cracking. When the ductility reserve can no longer accommodate the progressive shear strain, or in other words, the progressive shear strain reaches the critical strain level, voids and microcracks would initiate to further absorb the strain energy.

The shear band cracking failure may be due to ductile fracture, which has been characterized as involving the coalescence of voids and microcracks.[88] Supporting evidence for the proposed mechanism has been reported,[40] in which crack initiation was observed on a test roller when the plastic flow reached saturation, i. e. no further shear displacement without cracking. Also, a laboratory test showed that the fracture surface of rail steel under biaxial loading of compression and shear, simulating the stress condition under rolling/sliding, produced cracks with plastic de-cohesion lips indicating that failure was dominated by a ductile fracture mode, and the cracking occurred in quasi-static fashion, appearing quite suddenly due to exhaustion of ductility. [35]

A high ratchetting strain rate leads to a faster reduction in ductility reserve. In this sense, surface RCF processes in the shear band cracking dominated regime are ultimately controlled by ratchetting strain behavior.

The point of ductile fracture also brings to mind a point addressed in the previous section, increasing hardness alone may not be productive in this regime. If shear band cracking occurs at a given strain level that is related to surface hardness, the harder the surface the less the strain it may take.

At low contact pressure, the shear zone is very shallow and cracks extended below it and become multiple branched cracks. The main cracks are typically oriented at approximately 40 degrees to the contact surface. Crack networks formed by connection of the branches and main cracks can eventually cause surface spalls, Figures 3.6b, 3.14a, 3.15a and 3.16. Below the shakedown limit, rolling contact fatigue processes are predominately within the bulk elastic regime, and materials are subjected to a combination of compression and shear contact stresses. In addition, a hydrostatic pressure condition is built up in the region adjacent to the contact interface, and crack tip is hydraulically pressurized by water at each passage of load. The branched cracks are the products of this complex stress system.

The author believes that branched cracking is the distinguishing feature of contact fatigue cracks produced under rolling/sliding contact with water lubrication within a predominantly elastic regime. In addition to the photographs presented in previous section for STD and J4, Figures 4.1 and 4.2 demonstrate additional photographs of branched cracks in pearlitic steel HH, and bainitic steels J1, J2, J6. An idea for improving RCF resistance by microstructure modification is suggested in section 4.2.3.

4.2.2 Effect of Water and Oil Lubrication on Crack Growth

The original intent for the study of the effect of liquid lubrication was to answer a much debated issue: what is the predominant surface RCF crack grow mode, mode I (opening) or mode II (shear)? If mode I is dominant, then water would facilitate crack growth by exerting a hydraulic pressurizing function to enhance mode I growth. A pressurizing function through water is the hypothesis suggested first by Way [33] and then supported by many other researchers. [42,44,70] If mode II is dominant, oil would facilitate the growth by reducing crack face friction, which has been suggested as an even more efficient method of increasing the stress intensity factor K_{II} than by increasing the contact interface friction. [41,45] Viscosity and surface tension may bring about a difference in effect of a liquid. Increasing viscosity would tend to limit lubricant seepage into a crack.[79] Naturally, water will penetrate to crack tips more easily than oil owing to its comparatively low surface tension, but oil will reduce the crack face friction much more efficiently than water owing to its lower coefficient of friction.

Under initial dry rolling/sliding, the tangential to normal traction ratio ranged from 0.4 to 0.7, averaging 0.55, inducing a significant shear flow. Cracks under this condition were very shallow and basically parallel to the surface. The depth of the cracks was much less that the depth of the deformation layer. Wear processes followed by contact fatigue in subsequent liquid added tests significantly shortened the surface RCF life to about 20% of what was achieved during the RCF performance tests without any previous dry cycles. One of the reasons for the short life is that the number of contact cycles for crack initiation was substantially reduced due to the high magnitude of plastic deformation during the dry wear process.

The coefficient of friction during the subsequent lubrication tests was 0.06 to 0.08 for oil, and 0.17 to 0.25 for water. The difference in the coefficients made tangential traction under oil only one third that under water, and one thirteenth of that under dry contact. As a result of the low tangential traction, the shear stress was reduced, leading to a reduction in shear stress intensity factor, K_{II}. Despite the reduction in frictional force at the contact interface, oil apparently promoted very long shear band cracks. Without oil, the cracks would remain as short, very shallow cracks as observed in the dry wear processes. The enhanced crack growth indicates that the reduction of crack face friction through oil lubrication actually did take place. Once oil got into cracks, the low coefficient of friction made the relative shearing motion of crack faces easier, and thus promoting mode II crack growth. Furthermore, the phenomenon apparently proves the point that the reduction in crack face friction in enhancing the stress intensity factor, K_{II} outweighs the opposite effect of decreasing the stress intensity factor by a reduction in the contact interface friction.

A revealing point is that the effectiveness of oil to promote shear mode crack growth is highly dependent on the shear flow layer. The severity of cracks, in terms of crack length, depth, and surface damage increased with contact pressure, and more precisely, increased with increasing magnitude of shear flow. It was evident that cracks under oil were confined within the shear flow band. The zig-zag crack tips (Figure 3.28c) at the boundary dividing deformed and relatively undeformed regions seem to show the difficulty of crack growth when there was no further deformation band. The ability of oil to promote crack growth is apparently determined by the existence of a shear flow layer. It is reasonable to assume that without a shear deformation band, oil may not promote RCF crack growth at all, on the contrary, it may impede RCF fatigue initiation. In fact, a RCF test[13] showed a substantial increase in RCF life with oil lubrication throughout. The importance of the shear band was also addressed in a previous investigation,[44] in which it was concluded that the shear deformation layer prepared a favorable condition for crack growth during subsequent lubricated periods, and cracks followed the shear flow band.

Liquid lubrication either by oil or water exacerbated RCF crack growth when a prior deformation layer existed. Within the deformation layer, cracks in both conditions followed the shear flow path, but the mechanism of promoting crack growth may be fundamentally different.

A prior existing deformation band also provides a favored condition for subsequent crack growth under water. This is shown by more serious surface damage in the form of flakes, long cracks following the shear flow path, and much shortened life compared to that without dry running. But, the ability of water to promote RCF crack growth is not limited by the existence of a deformation layer. Deeper cracks beyond the deformation zone with larger inclined angles compared to those under oil lubrication were present. The crack length, however, seems shorter than that with oil. This may be due to less effective reduction of crack face friction with water. The crack morphology indicated mode I crack growth, and the explanation for the phenomenon falls under the original hypothesis[33] that water generates an opening mode crack growth by pressurizing the crack tips.

The higher frictional force under water will contribute to faster crack initiation and a higher magnitude of plastic deformation compared to oil. The low surface tension of water enables it to penetrate into crack tips, voids, or other defects fairly easily, and thus promote crack growth and crack network formation by pressurizing these defects. If no prior plastic deformation layer is present, oil would have much less influence on RCF crack growth, but water would still be effective. Following this line of reasoning, water, overall, is more detrimental to surface RCF resistance than is oil.

In answering the original question of whether mode I or mode II is the predominant RCF crack growth mode, no simple response can be given, since the question overlooks the possibility that adding liquid may actually change the outcome rather than just facilitate or impede a preexisting growth mode. Instead, the question should be re-addressed as under what conditions will either mode I or mode II become predominant? An interesting report[120] describes the FEM calculation of the stress intensity factors for near surface short straight (parallel to the surface), and branched (main crack parallel to the surface but with branches at the tip) cracks. The report revealed that a straight crack under normal Hertzian loading will only be subjected to mode II loading. The stress intensity factor range, ΔK_{II}, decreases as the crack face friction increases, and the crack face friction leads to a series of stick-slip events at the crack interface. The tip of the branched crack is shown to be subjected to both mode I and mode II loading, although the magnitude of the mode I is 25% that of mode II, the mode I strongly affects mode II by nullifying the effect of crack face friction. The findings seem to support the idea that crack shape and orientation manifest certain crack growth modes. Current experimental results apparently indicate that both modes can occur in RCF processes. Mode I was more likely to be predominant under water lubrication, while mode II was predominant under oil. In fact, it is likely that no major mode I crack growth can be generated without the pressurizing function via liquid. Without oil, cracks would stay as wear type cracks, and there would not be much of mode II crack growth involved. A specific crack growth mode may be a result of the interactive participation of a specific liquid with certain contact load conditions.

Another important issue about liquid lubrication is related to corrosion aspects and whether there is any stress corrosion, or corrosion fatigue involved. It is also uncertain how the lubrication effect quantitatively changes with surface tension and viscosity, whether or not oil has any pressurizing function, although to a much lesser degree than water. These topics are quite interesting and have practical significance, but beyond the scope of the current work.

The implications for improving RCF in practice based on the preliminary findings are:

- avoid alternating contact cycles such as a period of dry followed by liquid lubrication,
- reduce the magnitude of plastic deformation,
- apply solid lubricants, or use oil lubrication continuously.

These conditions may reduce the detrimental effect of liquids in promoting RCF crack growth.

4.2.3 Dependence of Surface RCF Resistance on Mechanical Properties and Microstructures

The results show that the surface RCF process is much more dependent on mechanical properties rather than microstructure. First of all, RCF performance data of all the steels show the same non-linear behavior, particularly when they are plotted against P_0/k, and fall very close together. At a given P_0, the RCF resistance is clearly dependent on the material strength, with the highest strength steel, J6, having the greatest resistance. Secondly, when contact pressure is high enough to cross over the shakedown threshold, all the materials show the distinct two crack growth modes and progressive shear deformation, regardless of the differences in pearlitic and bainitic microstructures. The insensitivity to microstructure is particularly true at high contact pressure levels where all the steels behave quite similarly, in terms of the severely deformed microstructure, and shear band cracks, which is consistent with plastic deformation not being microstructure sensitive. Conventional fatigue studies have shown that crack propagation beyond stage I also reveals little influence of microstructure. [85,86]

For branched cracks at low contact pressure, plastic strain is no longer predominant, allowing microstructural factors, such as grain size and structure, as well as inclusions and surface conditions to play a more important role. The connections of the main cracks and branches form crack networks, which eventually cause surface spalls observed on the top of the rollers (Figure 3.15). It has been reported that premature failure, causing an unexpectedly short rail life compared to an average RCF life of standard rails, occurred in premium rails made of HH steel.[9] It is, perhaps, not a coincidence that HH steel showed a tendency to spall more easily in the current work. A hypothesis to explain the reported easy spalling behavior in the HH steel is that the fine prior austenitic grain size compared to STD steel may provide more opportunity for branching to occur. Although branched cracks advanced both transgranularly and intergranularly, a high volume fraction of grain boundaries would provide much more potential paths for branches to form.

The effect of metallurgical factors, such as grain size, interlamellar spacing, and grain orientation, on fatigue crack growth under conventional fatigue conditions such as push-pull and rotational bending has proved to be complex.[85,86,87,88,89,90] This influence is most important in the regime which includes stage I and near threshold crack growth. [85] The interaction between cracks and grain size is most pronounced when both sizes are comparable, and grain boundaries would retard fatigue crack growth by acting as a barrier for generating micro plasticity in a new grain, or by deflecting the crack path to increase crack closure.[85,86] Increasing prior austenitic grain size and, to a lesser extent, interlamellar spacing in pearlitic steels, were found to substantially decrease fatigue crack growth rate at a stress ratio of R = 0.1 for the entire crack growth life from threshold to final fracture.[87] In contrast, one study indicated that a decrease in pearlitic interlamellar spacing increased fatigue crack growth threshold.[88] A reduction in grain size has the beneficial effect of delaying crack nucleation, and thus provides higher fatigue strength, but those microstructural features that improve nucleation resistance, very often, degrade crack propagation resistance.[89,90]

However, these findings can not be directly applied to rolling contact fatigue. Systematic research on the microstructural effect on surface RCF crack growth is rare. This is partly due to the difficulties involved in a controlled test system which can isolate microstructural factors and monitor crack growth. The grain size effect could be fundamentally different for materials subjected to different loading conditions. In conventional fatigue, a final physic failure, is dictated by fracture of a main crack, while failure under rolling/sliding contact in the branched cracking regime is more likely dictated by spalls resulted from massive crack networks rather than by unconnected main cracks. The benefit of having more branches for conventional crack growth is to absorb more energy thus to slow down the main crack growth. The same factor of having more branches may turn out to be detrimental for rolling contact crack growth, since the function of forming crack networks by more branches may override the energy absorption effect.

The effect of microstructure modification in the branched crack prevailing regime on crack growth could be a fruitful avenue of future exploration.

In practice, examining cracks on rail surfaces and comparing them to the morphology of the two modes may aid in identifying failure mechanisms, and improving surface RCF performance through the most effective measure, whether by strength, ductility or contact pressure via design, in accordance with the mechanism.

4.3 RATCHETTING STRAIN UNDER ROLLING/SLIDING CONTACT

4.3.1 Asymptotic Non-linearity of Ratchetting Strain Behavior

The striking feature of the relationship between maximum ratchetting strain and the number of contact cycles in STD rail steel subjected to rolling/sliding contact is its asymptotic nature. The strain rate decreases gradually over thousands of cycles before stabilizing but with no indication that it will reach zero at the end of the tests. This behavior is demonstrated in Figure 4.3a where ratchetting strain rates, $d\gamma/dN$, decrease to an approximately stable strain rates, over 20,000 to 30,000 cycles for contact pressure in the range of 1536 to 2086 MPa. For bainitic steel J2, although less data were available, asymptotic non-linearity was also apparent, as shown in Figure 4.3b.

The term "asymptotic" has been used to describe ratchetting behavior of materials subjected to tension–torsion loads[94] but it means something different from the current context. The same term in the former describes a strain behavior which reaches a constant ratchetting strain rate only after a smaller number of cycles. The asymptotic ratchetting in that context is to oppose a so called transient ratchetting. Transient ratchetting refers to a strain behavior that shows ratchetting only occurs during a small number of initial cycles, then the stress-strain goes back to closed hysterisis loops and no further ratchetting can be observed. The single most important difference between the current and previous context is that the number of contact cycles required before achieving a steady state strain rate is significantly higher in the current context. This may represent a distinct feature of rail steels under rolling/sliding contact conditions. Figure 4.4 schematically distinguishes these three strain behaviors mentioned above.

For models to predict ratchetting strain satisfactorily it is crucial that this asymptotic behavior is incorporated. So far this has not been achieved. As mentioned in the literature review, non-linear kinematic hardening models are promising for describing ratchetting behavior. Two types of non-linear kinematic hardening models have been developed specifically for rail materials under rolling/sliding contact.[24,26,27,111,126] One type of model predicted gradually reducing strain rate with cycles, but the total cycles over which the ratchetting can be calculated is very short, about 600 cycles,[24] for which no measurement data were available for comparison. The smallest number of cycles at which the strain rate and surface displacement were measured was 1000 in the current experiment, and the total test cycles ranged from 25,000 to 90,000. The material constants employed by the model were from uniaxial push-pull tests subjected to a high strain amplitude. Under such conditions the test material could not survive a large number of cycles.

The second type of models[26,27,111,126] is quite versatile, providing a stable strain rate for a wide range of normal and tangential traction combinations. Figure 4.5 shows a comparison of the present measurements with one model.[111] The material properties in the model were similar to that of the STD steel, with a yield strength of 285 MPa (311 MPa for STD). Young's modulus and Poisson's ratio were taken as $E = 207$ GPa and $v = 0.3$, respectively. At low cycles the prediction and experimental results are in agreement but with increasing cycles the model overestimates the cumulative strain. The model predicts a stable strain rate after only 16 cycles. This deviates from the asymptotic ratchetting strain behavior of the rail steel, causing the unrealistically high predictions.

A possible reason for the discrepancy lies in the material constants used. The models are developed based on material data generated from either uniaxial push-pull[24,26] or biaxial tension-torsion tests.[111] These differ from the conditions experienced by rail materials in rolling/sliding contact. The important characteristics of rolling/sliding contact include hydrostatic pressure and non-proportional loading conditions. The hydrostatic pressure enables materials to withstand higher strain without failure compared to uniaxial or biaxial loading. The beneficial effect is possibly contributed by an increase in rupture strain and a decrease in strain rate.[115] The non-proportional loading may induce a difference in material hardening and stress-strain response compared to the proportional loading conditions for the same equivalent strain conditions.[91,115] A database obtained directly from rolling/sliding conditions is desirable both for a better understanding of rolling contact fatigue and model development.

4.3.2 Parameter Development Based on the Experimental Data

The experimental data can be used to develop an empirical model for ratchetting. Ratchetting strain can be described by a power law function as, $\gamma = AN^b$. Let $\gamma_0 = A$ as N approaches 1, then the equation can be written as

$$\gamma = \gamma_0 N^b \tag{4.1}$$

where γ_0 can be viewed as an initial strain increment at a given contact pressure.

Conceptually, two parameters are required to describe the ratchetting strain behavior for a given contact condition: the initial ratchetting strain increment, γ_0, and the strain rate, $d\gamma/dN$, which in turn, is determined by γ_0 and the slope b.

The test conditions used in current experiments are essentially two-dimensional line contact. The normal and tangential pressure distribution is approximately Hertzian, and the surface stresses (at z=0, $-a \leq x \leq a$) under the normal and tangential traction for plane strain condition are expressed through Equations. (4.2) to (4.6).[16]

$$\sigma_{xx} = -P_0(1-x^2/a^2)^{1/2} - 2\mu P_0 x/a \tag{4.2}$$

$$\sigma_{zz} = -P_0(1-x^2/a^2)^{1/2} \tag{4.3}$$

$$\sigma_{yy} = \nu(\sigma_{xx}+\sigma_{zz}) \tag{4.4}$$

$$\tau_{xz} = -\mu P_0[1-(x/a)^2]^{1/2} \qquad |x| \leq a \tag{4.5}$$

$$\tau_{xz} = 0 \qquad |x| \geq a \tag{4.6}$$

$$\tau_{xy} = \tau_{yz} = 0 \tag{4.7}$$

where a is the half width of a contact patch, μ is the tangential traction to normal pressure ratio and taken as the values of the coefficient of friction under full slip, and υ is Poisson's ratio.

The normal stresses give rise to a hydrostatic pressure condition, which does not directly cause shear deformation. The shear stress, τ_{xz}, generated by tangential traction, $T = -\mu P$, therefore, is mainly responsible for the cumulative shear flow. The shear stresses due to tangential traction on the contact surface are illustrated in Figure 4.6, in which the stress amplitude is from zero to μP_0, with primary shear stress in the rolling direction under the driven condition. To simplify the parametric study, the cyclic shear stresses under rolling/sliding contact can be considered as varying between zero and μP_0, although the true stress state is a complex system comprised of non-proportional and hydrostatic stress conditions.

The initial ratchetting strain increment, γ_0, can be expressed as a function of the maximum shear stress, μP_0, by fitting the experimental data. As shown in Figure 4.7, both power and exponential functions can be used to fit the data, with an exponential function giving a slightly better fit. The exponential function is derived as

$$\gamma_0 (\mu P_0) = 8.3275 \text{x} 10^{-8} e^{(.0.024867 \mu P_0)} \qquad (4.8)$$

where μ is equal to 0.235 taken as an average of the coefficients of friction measured experimentally.

The power index, b, varied between 0.47 to 0.66, exhibiting a roughly decreasing trend with increasing contact pressure. A simple linear function is fitted to the data, Figure 4.8, as:

$$b (\mu P_0) = -1.1023 - 0.00128 (\mu P_0) \qquad (4.9)$$

These values can be determined for any given contact pressure and substituted into the general equation:

$$d\gamma/dN = \gamma_0 b N^{b-1} \qquad (4.10)$$

to obtain values of the strain rate at any given number of contact cycles and contact pressure for this particular STD steel, in this type of rolling sliding contact under water lubricated conditions and a slide/roll ratio of 10%.

This equation is considerably simpler than most other models which typically incorporate detailed stress-strain behavior. The simplicity could have practical advantages.

For bainitic steel J2, the difference in ratchetting strain behavior compared to the STD steel can be evaluated by the two parameters, which reflect the difference in material hardening behavior. Since no systematic data are available for J2, no mathematical relationships can be derived at this stage. However, based on the comparison at a comparable contact pressure level for both materials (Figure 3. 36), it can be reasonably estimated that the strain rate and the initial strain increment for the bainitic steel is higher than the pearlitic steel.

4.3.3 Ratchetting Strain Modulus

One goal of this experiment is to contribute to model development by providing some material base line data. This may be achieved by deriving a ratchetting strain modulus.

Fundamentally, the objective of any constitutive model is to establish a relationship between stress and strain increments, i. e. predicting stress-strain curves. But what was measured by the current experiments was not an entire hysterisis stress-strain loop, the experiment data are only the end result — the net strain accumulation after each passage of load. For this reason, direct derivation of a plastic modulus can not readily be made.

Introducing a new parameter, ratchetting strain modulus, K_r, which is directly related to the ratchetting strain increment, $d\Upsilon$, through:

$$d\Upsilon = d\tau / K_r \qquad (4.11)$$

where $d\Upsilon$ and $d\tau$ are ratchetting strain and stress increment during each contact cycle, may enable a linkage to non-linear kinematic hardening models which emphasize the determination of a plastic modulus, K_p.[92]

The non-linear kinematic hardening models fall roughly into two classes, models which emphasize the determination of plastic modulus, K_p, and models which emphasize the determination of the kinematic hardening modulus, K_x.[92,93] The kinematic hardening modulus, K_x, relates to hardening rules by defining the magnitude of the increment of a yield surface center, dX, for a given stress increment, $d\sigma$. The plastic modulus, K_p, is directly related to plastic strain increment through the flow law as:

$$d\varepsilon^p = d\sigma/K_p \tag{4.12}$$

where $d\sigma$ and de^p are the current stress and plastic strain increment in a load cycle. For non-linear kinematic hardening, the hardening rate is a function of the loading direction,[92,94] thus the plastic moduli for loading and unloading are different, resulting in open hysteresis loops and ratchetting. Assuming the plastic modulus for loading is K_{p+} and for unloading is K_{p-}, then the ratchetting strain increment, during one contact cycle will be:

$$d\gamma = d\tau/K_{p+} - d\tau/K_{p-} = d\tau(1/K_{p+} \ -1/K_{p-}) \tag{4.13}$$

where $d\tau$ is a stress increment and has equal value in both the loading and unloading directions.

From equations 4.11 and 4.13:

$$K_r = 1(1/K_{p+} \ - 1/K_{p-}) \tag{4.14}$$

From Equation. 4.10, the strain increment, $d\gamma$, for a given contact cycle (dN = 1) is:

$$d\gamma = \gamma_0 bN^{b-1}dN = \gamma_0 bN^{b-1} \tag{4.15}$$

and therefore

$$K_r = d\tau/d\gamma = d\tau\ /(\gamma_0 bN^{b-1}) = \mu P_0/(\gamma_0 bN^{b-1}) \tag{4.16}$$

where $d\tau$ is equivalent to μP_0.

Substituting from Equation 4.1, the ratchetting strain modulus can also be expressed as a function of current strain:

$$K_r = \mu P_0/(\gamma_0^{1/b}\, b\gamma^{1-1/b}) \tag{4.17}$$

Equations 4.16 and 4.17 indicate that the ratchetting strain modulus is a function of μP_0, and evolves with contact cycles, or with current ratchetting strains. By substituting expressions for γ_0 and b, K_r can be evaluated explicitly for various μP_0 values.

4.3.3 Correlation Between Ratchetting Strain and RCF Life

An important issue is to understand how the ratchetting strain relates to rolling/sliding contact fatigue life. Experimental results have revealed that ratchetting itself is evidently divided into two types, type A and type B.[94] Figure 4.9a demonstrates this point. For type A under uniaxial loading, the inelastic strain is quasi-reversed, which occurs when the primary load is small compared to the secondary one. The plastic strain in loading and unloading are of the same order, and the total strain cycle is composed of both cyclic and ratchetting strain, with ratchetting strain being a small portion of the total plastic strain, i. e. $d\varepsilon_p \ll \Delta\varepsilon_p$. A component of cyclic strain is important in this case. For type B, occurring under high primary stress, the plastic strain in the direction of the primary load is much larger than in the reversed direction. As the primary load further increases, strain behavior approaches the limiting case where the inelastic strain is non reversible, and the ratchetting strain is much greater than the cyclic strain, i. e. $d\varepsilon_p \gg \Delta\varepsilon_p$. Type B ratchetting can be considered as quasi-monotonic, and a contribution from the cyclic strain term may be negligible. Under sliding contact, the total strain is comprised of reversing component $\Delta\varepsilon^p_{xx}$ and ratchetting component $\Delta\varepsilon^p_{zx}$, as shown in Figure 4.9b.[96,98,99] It is reasonable to assume that under high surface traction, the strain type would approach that of type B, with ratchetting strain being a dominant component, since compressive strain component is constrained by hydrostatic pressure conditions.

It has been proposed in previous section that surface initiated RCF is associated with two distinct crack growth modes — shear band cracking and branched cracking. For the shear band cracking mode dominated RCF, failure is assumed to be caused by ductile fracture in shear. To predict RCF life in terms of initiation, it is necessary to invoke a critical ratchetting strain concept. This might take the form of low cycle fatigue law as:

$$N_f = (\gamma_c / \gamma_0)^{1/b} \tag{4.18}$$

where γ_c is the critical ratchetting strain and N_f is the RCF life introduced into Equation 4.1. The concept postulates that for the shear band cracking mode, surface RCF failure occurs when the cumulative strain reaches the critical strain, γ_c, at which the material can no longer deform continually to absorb the strain energy, and as a result, the material would fail in the form of macroscopic surface cracks. In this sense, the critical ratchetting strain can be viewed as a criterion to relate to rolling contact fatigue life just as the rupture strain relates to monotonic loading.

A different relationship for rolling contact fatigue failure involving ratchetting strain has been proposed previously[98] with cycles to failure given by

$$N_f = \varepsilon_c / \Delta\varepsilon_r \tag{4.19}$$

where $\Delta\varepsilon_r$ is ratchetting strain per cycle, and ε_c is the critical strain. Kapoor[98] suggests that the critical strain level is close to the monotonic fracture strain. This suggestion might appear simplistic for rolling/sliding contact given the involvement of hydrostatic pressure and non-proportional loading conditions, however, satisfactory experimental agreement has been found for various ductile materials subjected to uniaxial or biaxial loading conditions.[98]

It is possible that a critical strain under rolling/sliding may be considerably different from that described above. An experiment has shed some light on this issue. From one test of a hard steel wedge sliding over a cold rolled 5083-H321 aluminum–magnesium alloy,[99] a constant strain value to rupture (to cause macroscopic cracking) was about 480% for three attack angles of the hard wedge under a constant load. If this value can be taken as a critical strain, it is obviously higher than monotonic rupture strain for common Al-Mg alloys, which is usually below 100% from tensile testing.

The specific value of the critical strain for the pearlitic steel tested here remains an open question. If it is defined as the strain at which macroscopic cracks initiate, a sophisticated monitoring system to detect an initial crack needs to be used[141] to evaluate it experimentally. If the critical strain can be considered a material property, it should be independent of specimen geometry and loading conditions, thus experimental investigations need to be done to evaluate the effect of these variables and a novel experiment to simulate rolling/sliding contact under more precise control needs to be developed.

4.3.4 Effect of Slide/roll Ratios

Slide/roll ratio has a significant effect on ratchetting strain. The effect is mostly pronounced at cycles less than 10,000, and it is manifested in the following aspects:

- a large scatter band of about a factor of 12 enveloped by the peak at 25% and the valley at 0.3 and 0.4% of slide/roll ratios, and
- an "anomalous" behavior such as a higher strain at 1% than that at 5% slide/roll ratio, and
- a big difference in strains for specimens tested at the same slide/roll ratios, most obviously at the low end of slide/rolls of 0.3, 0.4%, 1% and 5%.

Beyond the initial 5000 cycles, a general trend starts to emerge which shows that ratchetting strain increases with increasing slide/roll ratio. As contact cycles further increase, data at different slide/roll ratios converge, indicating the diminishing effect of slide/roll ratio with an increasing number of contact cycles (figures 3.45 and 3.46).

An explanation for the strain behavior is attributed to the variations in T/N ratios. At a given normal contact pressure, higher tangential traction generates a higher shear stress field, and a correspondingly higher ratchetting strain. Therefore, it comes as no surprise that the large variation in T/N ratios of about 14 times during initial cycles

(Figure 3. 42) brought about a large variation in ratchetting strain. The higher T/N value at a 1% slide/roll ratio consequently resulted in a higher ratchetting strain than that at 5% slide/roll ratio, since a lower T/N was produced under the latter condition. As contact cycles increased, the T/N ratios settled down to a distinct trend — the higher the slide/roll ratio, the higher the T/N value, and the difference reduced from 14 times to about 2 times (Figure 3.40), giving rise to the reduced influence of slide/roll ratio.

In previous discussion, it was pointed out that the strain rate reflects that of asymptotic hardening behavior, and it is a function of the current strain, or the number of contact cycles for a constant slide/roll ratio of 10%. A consistent T/N ratio, averaging 0.235, was achieved under that condition. For various slide/roll ratio tests, the effect of the different T/N ratio on the strain rate is present, in addition to the hardening behavior mentioned above, and the T/N ratio effect is shown in Figure 4. 10. Examples to illustrate the T/N ratio effect are the big variations of strain rate at N < 10,000, and a rate increase from N = 2500 to N = 10000 cycles for two specimens tested at 0.4% and 5% slide/roll ratios, consistent to the increase in T/N during the same contact period for these specimens (Figure 3.42).

In the current experiment, three factors were observed which may play a role in producing the difference in T/N ratio. These factors are:

- the sliding distance,
- a stick-slip phenomenon, possibly at slide/roll ratios of below 1%, and
- the formation and the duration of oxide films on the contact interface.

A direct outcome of varying slide/roll ratio is that the sliding distance over total distance rolled will be different while other conditions are kept the same. The coefficient of friction is not an intrinsic material property, but is dependent on multiple factors including physical, chemical and mechanical properties of the materials, contact surface conditions such as work-hardening, roughness and asperity orientations, debris distribution, as well as environment conditions.[100,101,102,121,145,151] The effect of sliding distance for the same materials slid against each other has been reported, and the results show that the coefficient of friction rose gradually over a certain sliding distance from an initial value of 0.13 to the steady stable value of 0.71 for Armco iron specimens under dry conditions.[103] A study on wear behavior of BS11 rail steel under dry rolling/sliding suggested that the coefficient of friction is significantly affected by rolling distance.[96] The greatest change in friction occurred during initial sliding.[96,103]

An explanation for the effect of sliding distance is that a steady state value of the coefficient of friction requires a build up of a stable interface, in terms of surface asperities, distribution of particles, and surface deformation and work-hardening. It was observed that both the magnitude of the plastic strain gradient and the depth of a highly deformed layer increased with sliding distance.[139] It is, therefore, reasonable to postulate that to build up a stable interface requires a certain sliding distance over which tangential traction can actually be exerted, thus contributing to surface deformation and work-hardening. Keeping this idea in mind, it is quite logical that the greatest variation in T/N ratios occurred during the initial contact cycles, during which the stable interface has yet to be gradually established and the sliding distance had the greatest effect. Once a stable interface condition was achieved, as sufficient contact cycles passed, the difference among the T/N ratio reduced from 14 times down to 2 times, showing a trend of convergence. The general observation during the steady state is that of higher T/N values for higher slide/roll ratios.

A stick– slip phenomenon was very likely involved at low slide/roll ratios of 0.3%, 0.4% and 1%, with the phenomenon being more marked at 1%. Two reasons lead to the realization of existence of a partial slip. One, the oscillation of the frictional force in the current tests as shown in Figure 3. 42 is similar to the features presented in Figure 4.11 from an ASTM standard G115 -93. As indicated in the ASTM standard, the presence of stick-slip is usually manifested by an oscillation of frictional force (decrease and subsequent increase) as sliding proceeds.[104] Two, the oscillation occurred at 0.3, 0.4, and 1% which fits in the low slide/roll ratio range at which a partial slip is likely to be present in accordance with the literature. The influence of stick-slip versus complete slip is a complicated issue. It has been reported that stick-slip causes more fatigue damage than full slip.[128] It is recognized that partial slip would have an added effect on the ratchetting strain behavior, however the specific effect is not clear at the present stage.

A tendency for formation and survivability of oxide films may be an additional contributor to the difference in the T/P ratio. The formation and survivability of an oxide film affects the coefficient of friction, since an increase in surface hardness due to oxide films often leads to a reduction in the coefficient of friction.[100] During the initial 5000 cycles, orange/gold colored oxide films were formed on the surface of rollers tested at slide/roll ratios of 0.3, 0.4 and 1%, with a much weaker presence at 0.3 and 0.4%. The films often occurred in a form of an alternating pattern, as schematically shown in Figure 4.12. The marked alternating pattern of the films occurred repeatedly for two 1% slide/roll specimens, and was also obvious for a specimen tested at 0.3%. The alternating films were likely related to the stick-slip phenomena. Whether the films were a result of a slick-slip phenomenon, or vice versa, is an intriguing question. This type of alternating orange/gold color films was not observed for higher slide/roll ratios. The films basically disappeared after the number of contact cycles was greater than N = 10,000.

An effect of sliding distance partially explains the variation in the coefficient of friction. The stick-slip phenomenon and oxide films might be a cause for the big variation in T/P values at the low slide/roll ratios. However, what the consequences of a stick-slip plus oxide films are on the T/N ratio, and further on the strain behavior, and whether these two are interrelated phenomena, still remains a mystery.

At the present stage, the effect of random test factors, such as specimen, machine or operating variables, can not be completely ruled out. It is not clear whether the big difference in the T/N ratio for specimens tested at the same slide/roll ratio, for example, 1.7 times at 1% and 3.5 times at 5% (Figure 3.42), is a result of experimental incidents. However, the tests at the low end of slide/roll ratios seem more sensitive to random testing variables. Clearly, a more precise control is desired if future tests at the low slide/roll ratios are to be conducted.

It is important to mention that the constant maximum normal contact pressure of P_0 = 1759 MPa was applied during the tests. Changing contact pressure may introduce some variation in slide/roll effect study. In addition, how sliding distance affects the T/N ratio, especially in a quantitative sense, can not be explained from the present data. The effect of slide/roll ratio on ratchetting strain warrants further research.

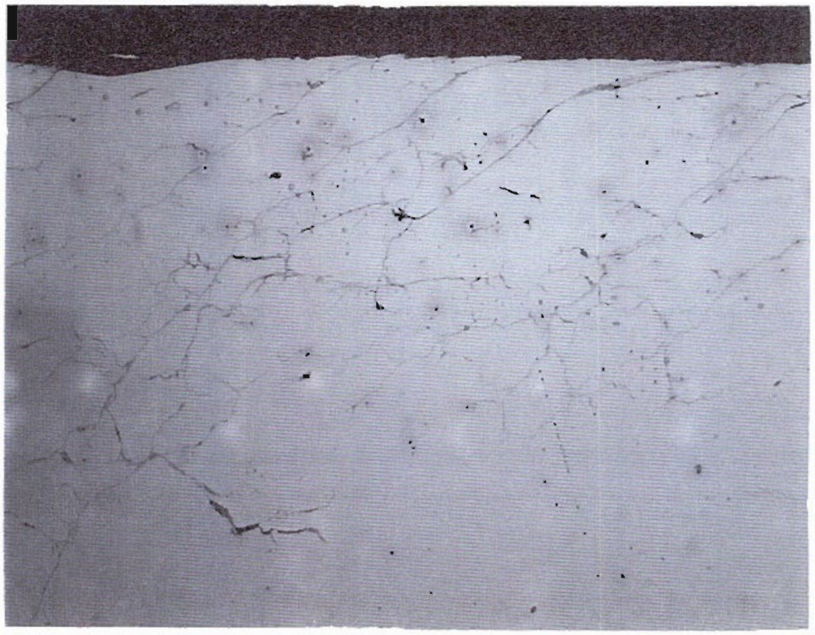

(a) 200 X

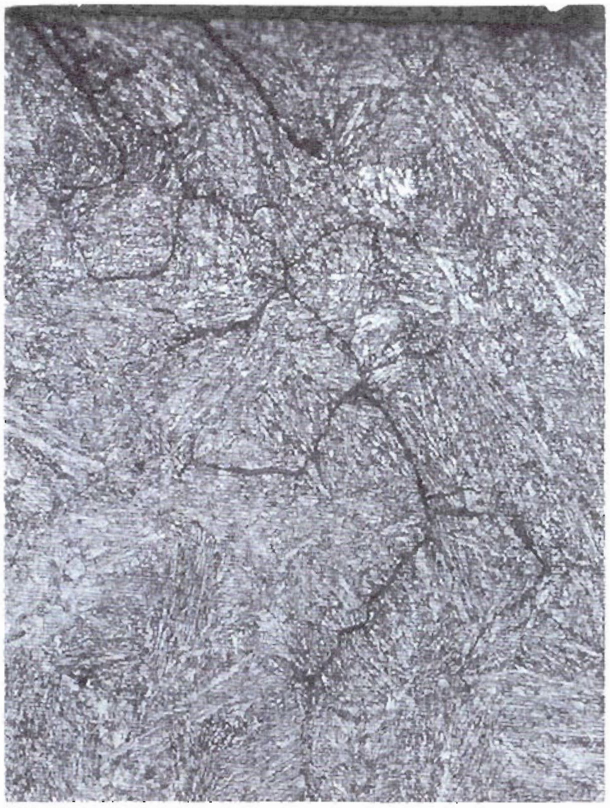

(b) 400 X

Fig. 4.1. Examples of branched cracks in (a) HH steel (b) J1 steel.

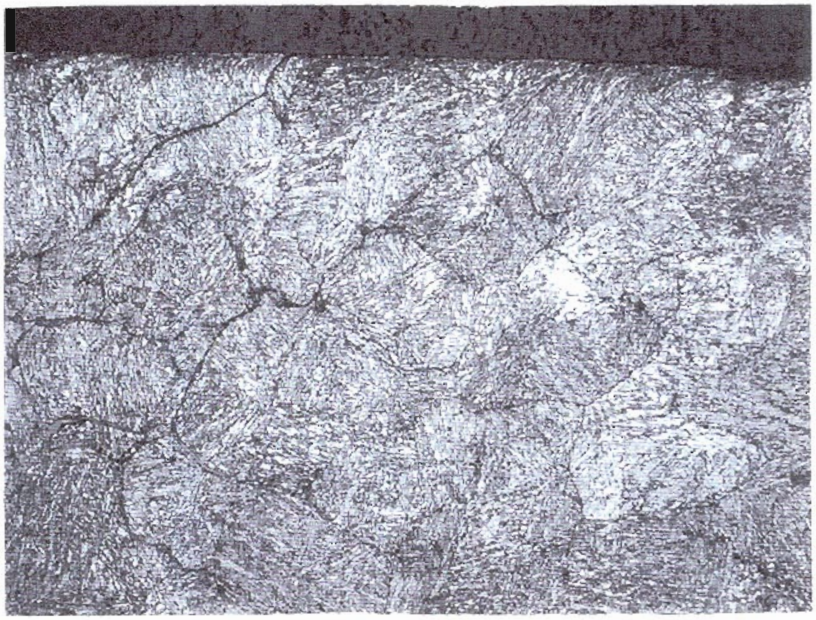

(a) 200 X

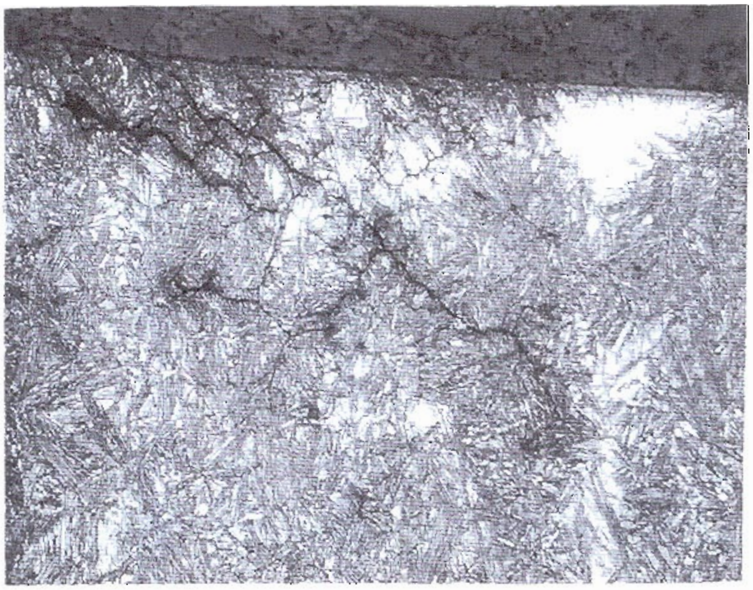

(b) 200 X

Fig. 4 2. Examples of branched cracks in (a) J2 steel (b) J6 steel.

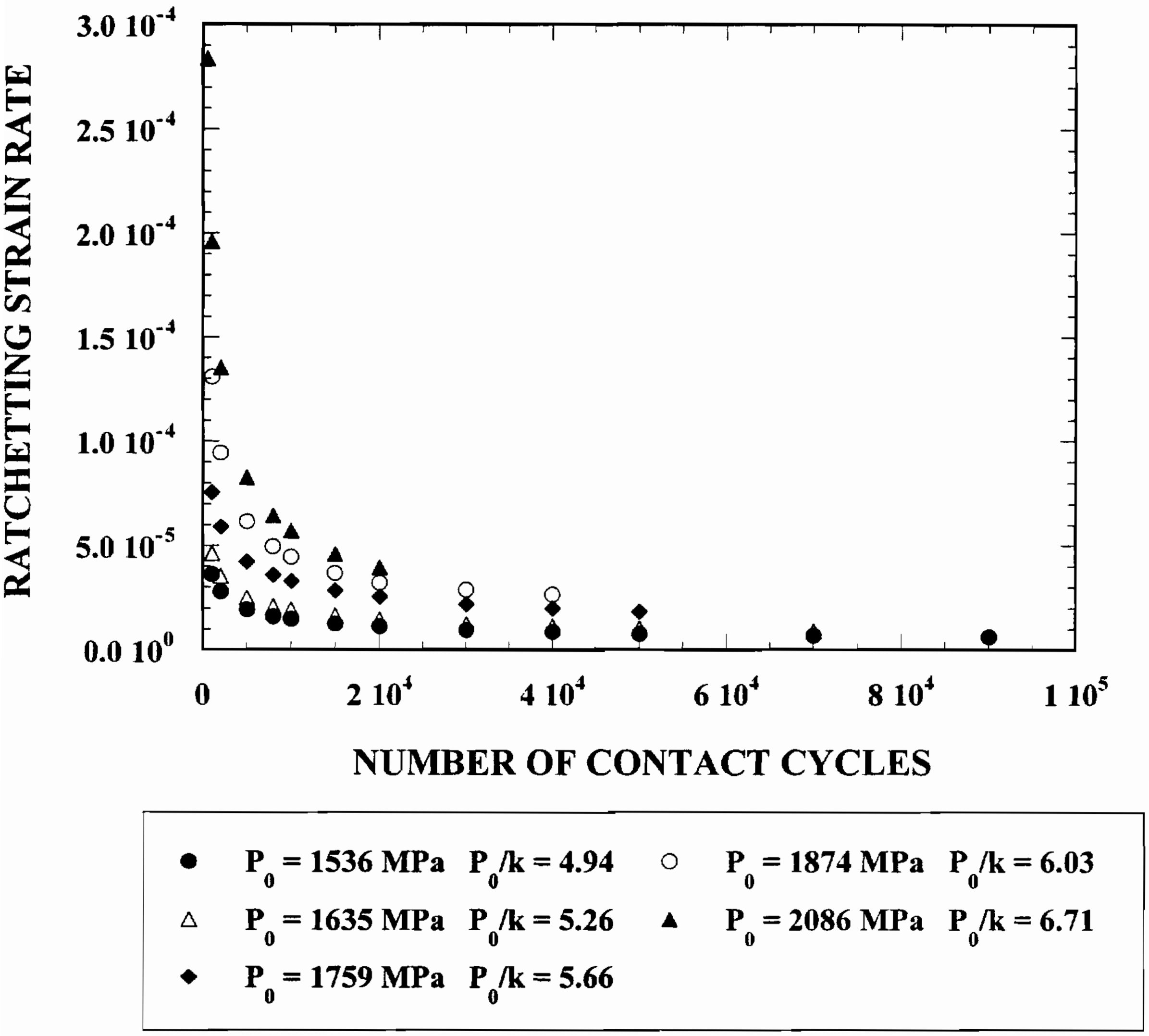

Fig. 4.3a. Ratchetting strain rate as a function of the number of contact cycles for STD steel, showing asymptotic behavior.

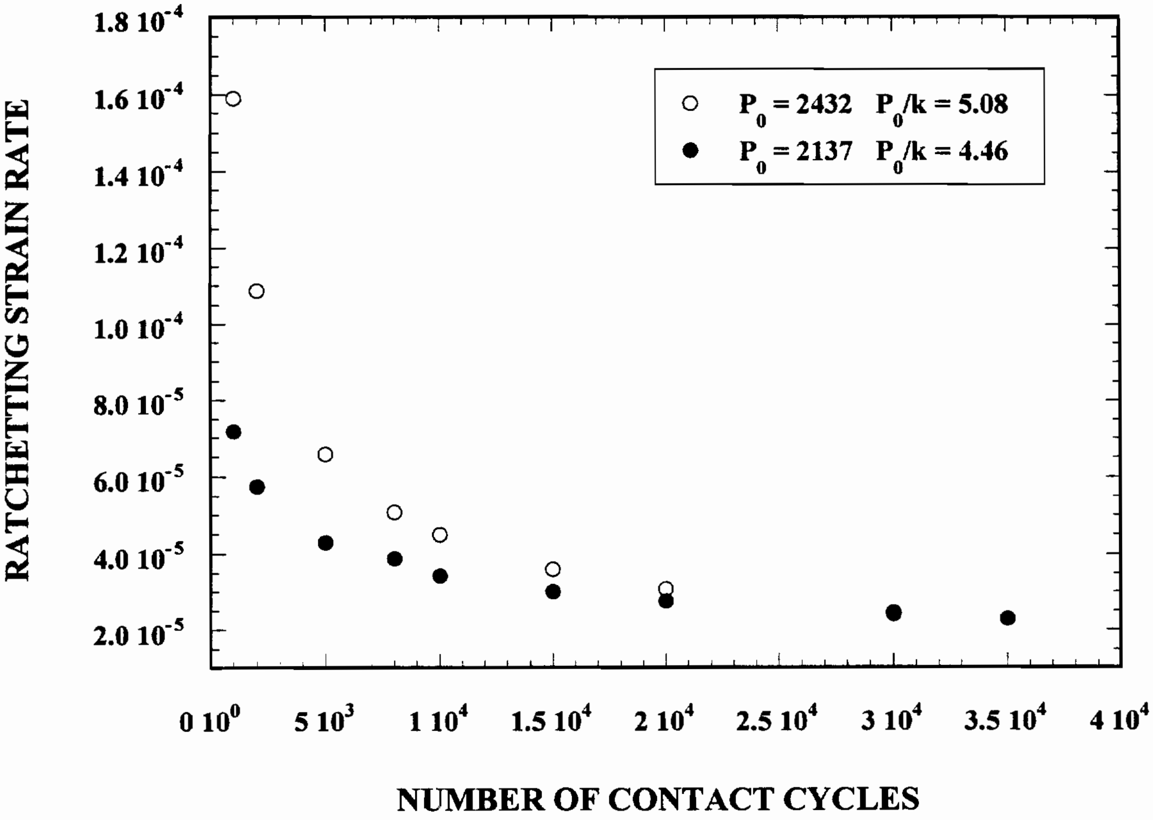

Fig. 4.3b. Ratchetting strain rate as a function of the number of contact cycles for J2 steel, also showing asymptotic behavior.

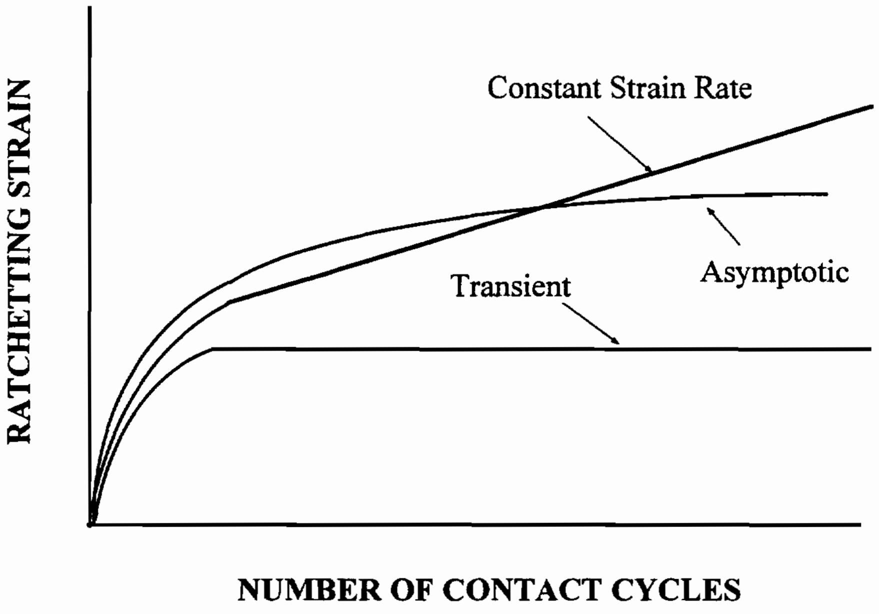

Fig. 4. 4. Three types of ratchetting strain behavior.

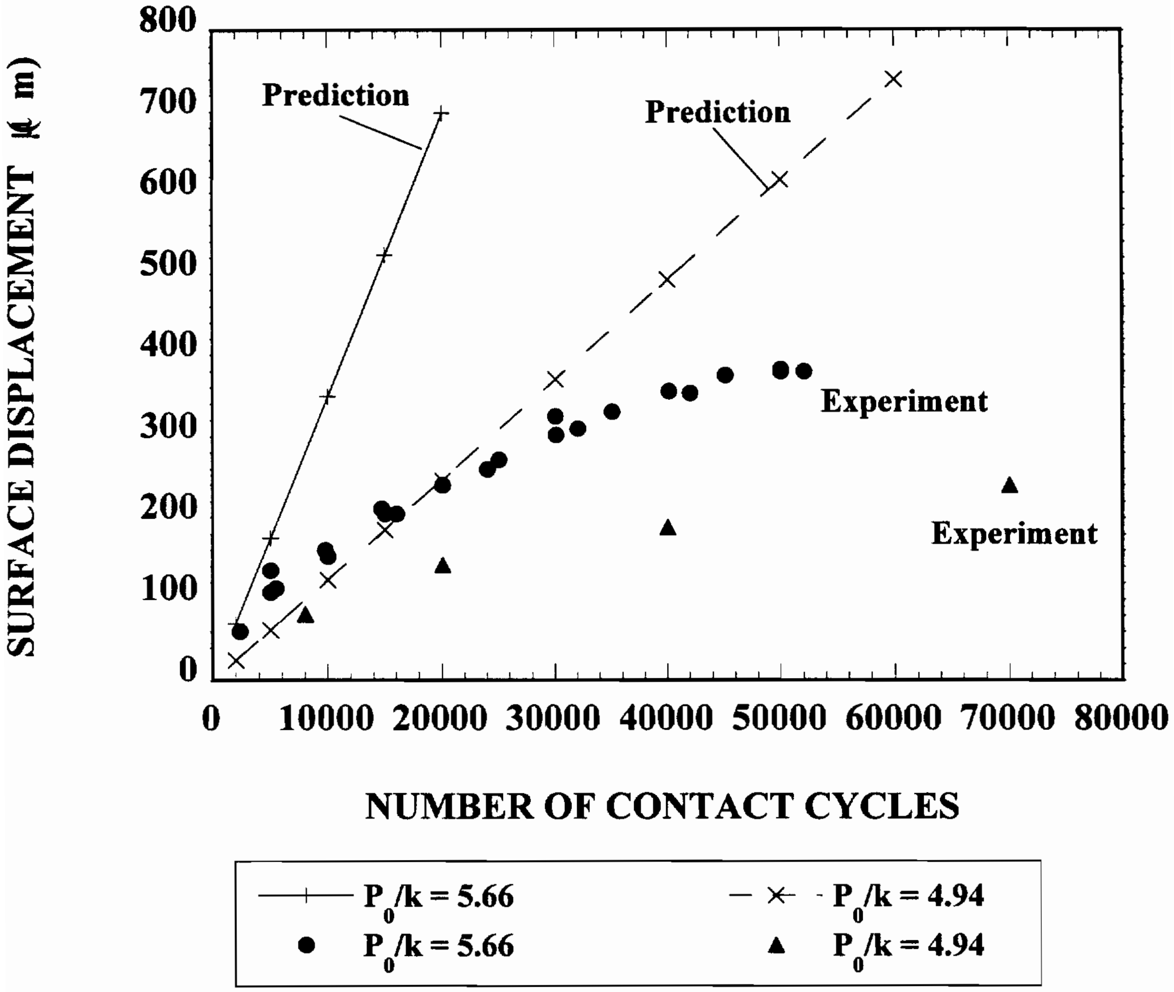

Fig. 4.5. Comparison of experimental data with a model prediction.

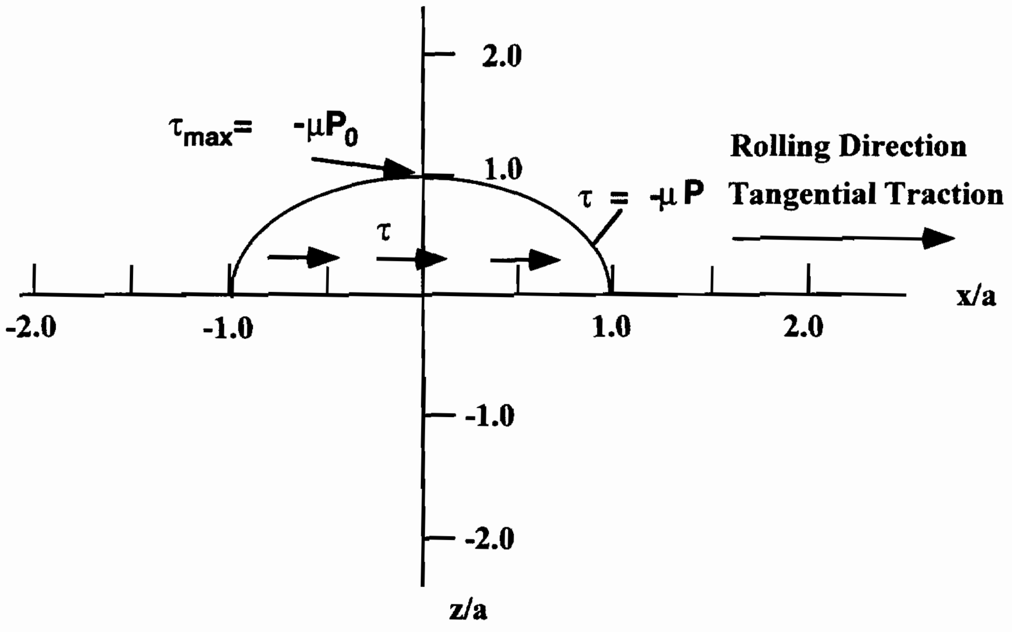

Fig. 4.6. Shear stress on the contact interface generated by tangential traction.

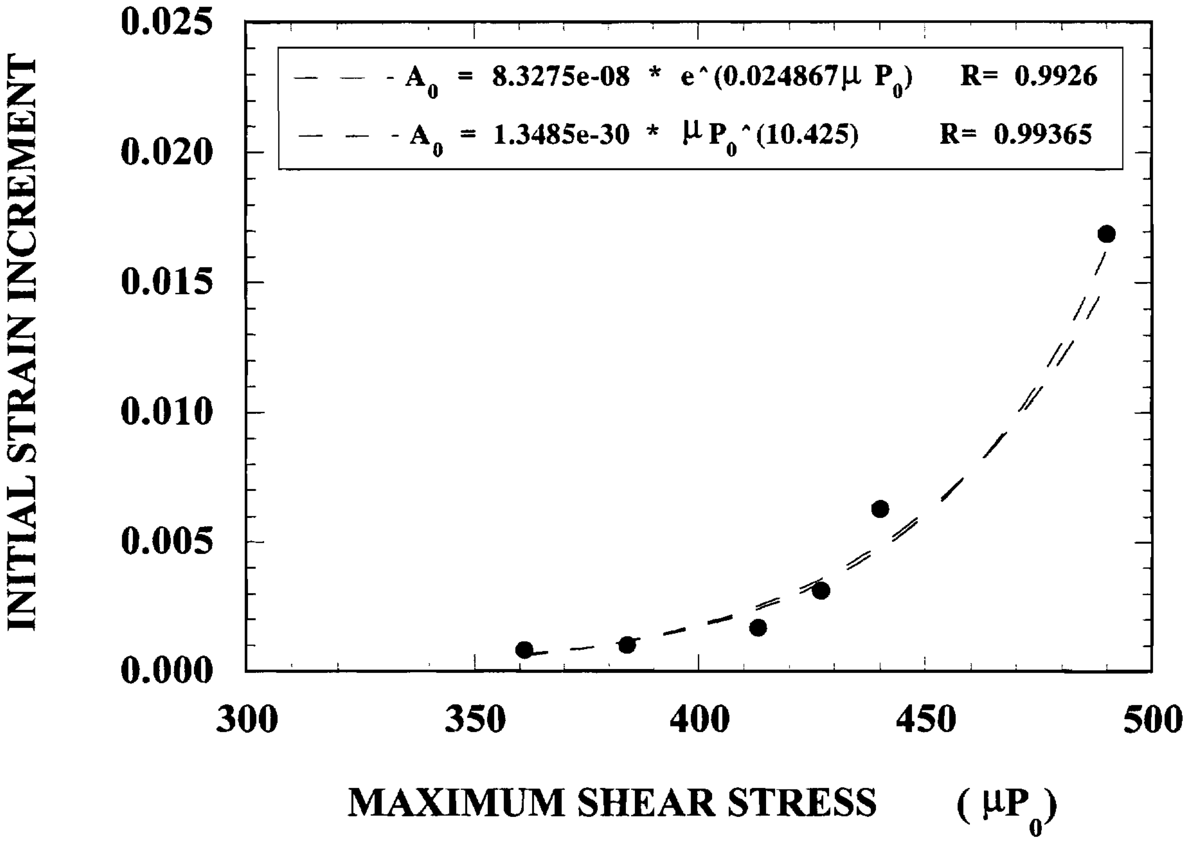

Fig. 4.7. The initial strain increment as a function of the maximum shear stress.

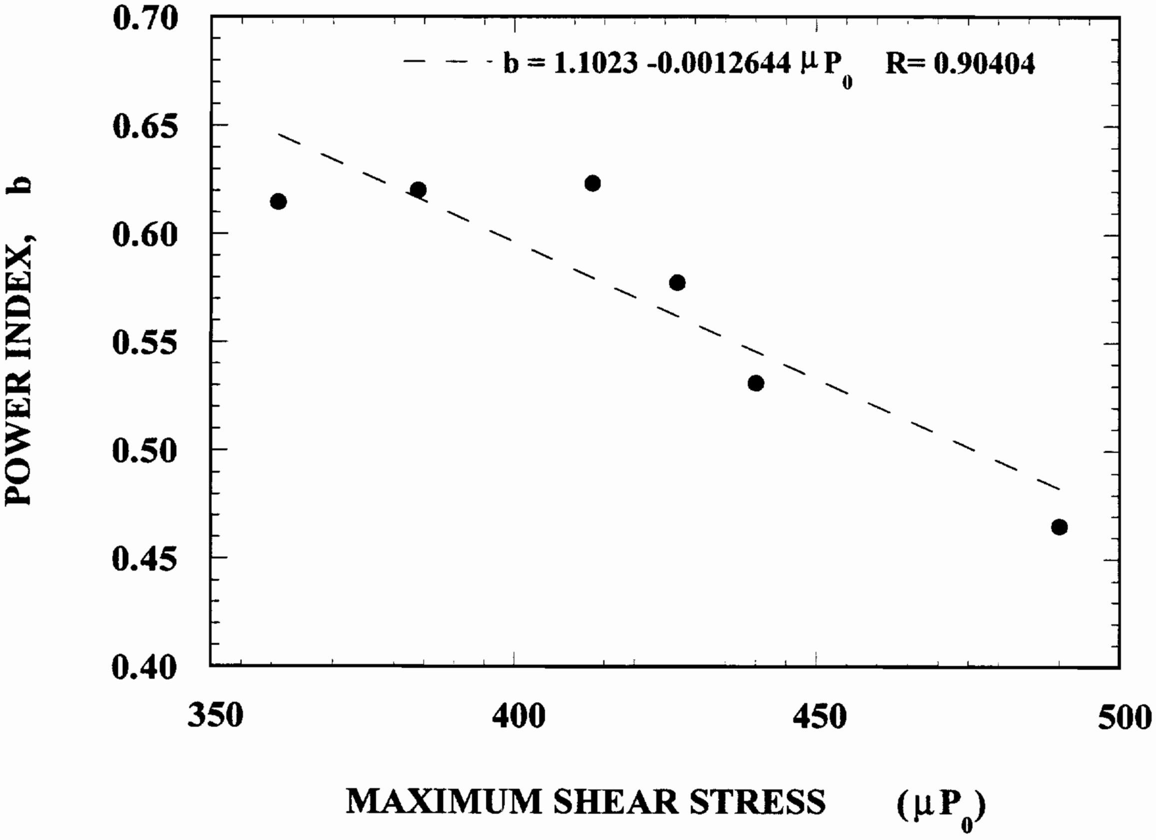

Fig. 4.8. Power index, b, as a function of the maximum shear stress.

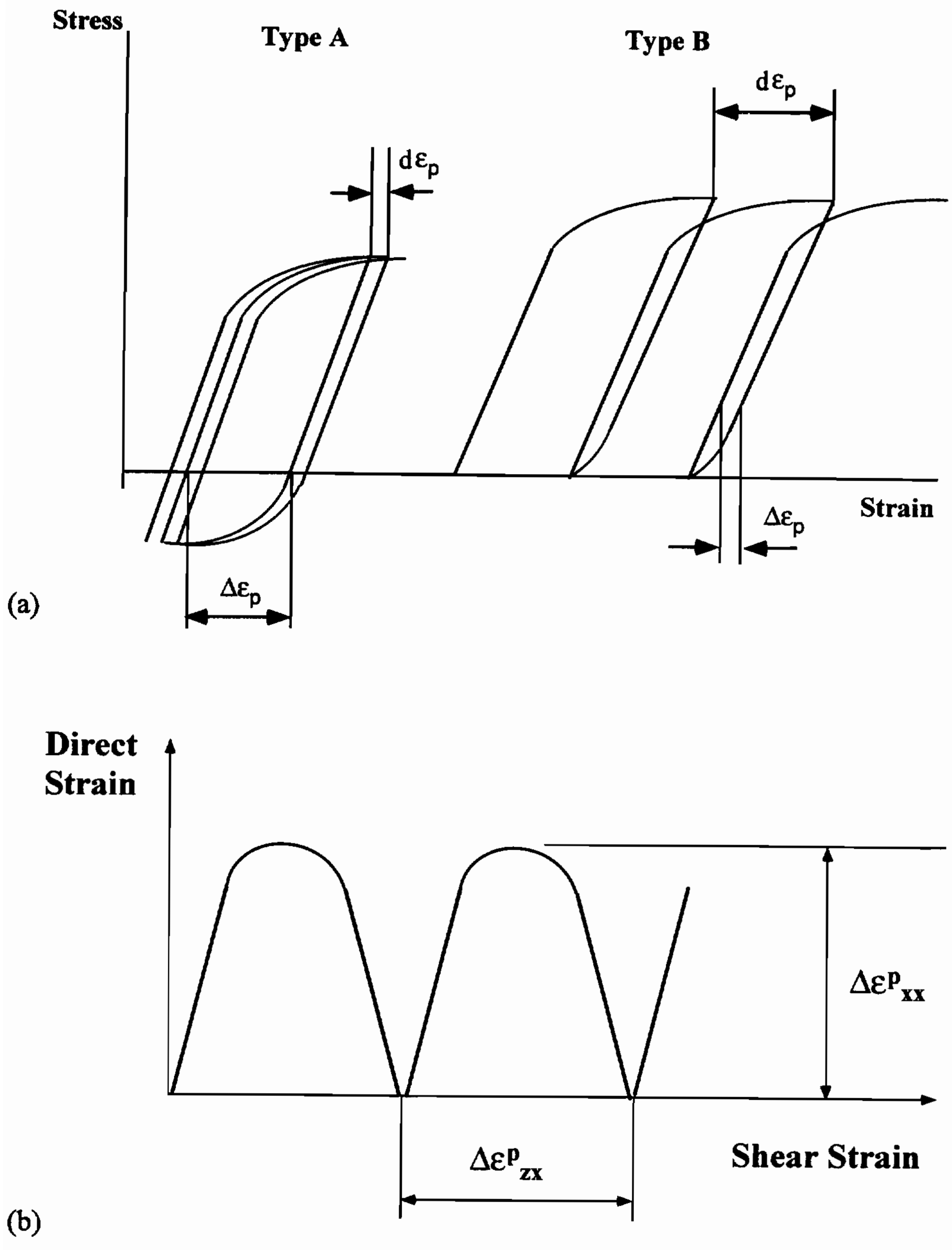

Fig. 4.9. Components of ratchetting strain and cyclic strain (a) uniaxial loading, type A, cyclic > ratchetting and type B, cyclic < ratchetting (b) sliding contact, ratchetting strain $\Delta\varepsilon^{p}_{zx}$ and cyclic strain $\Delta\varepsilon^{p}_{xx}$.

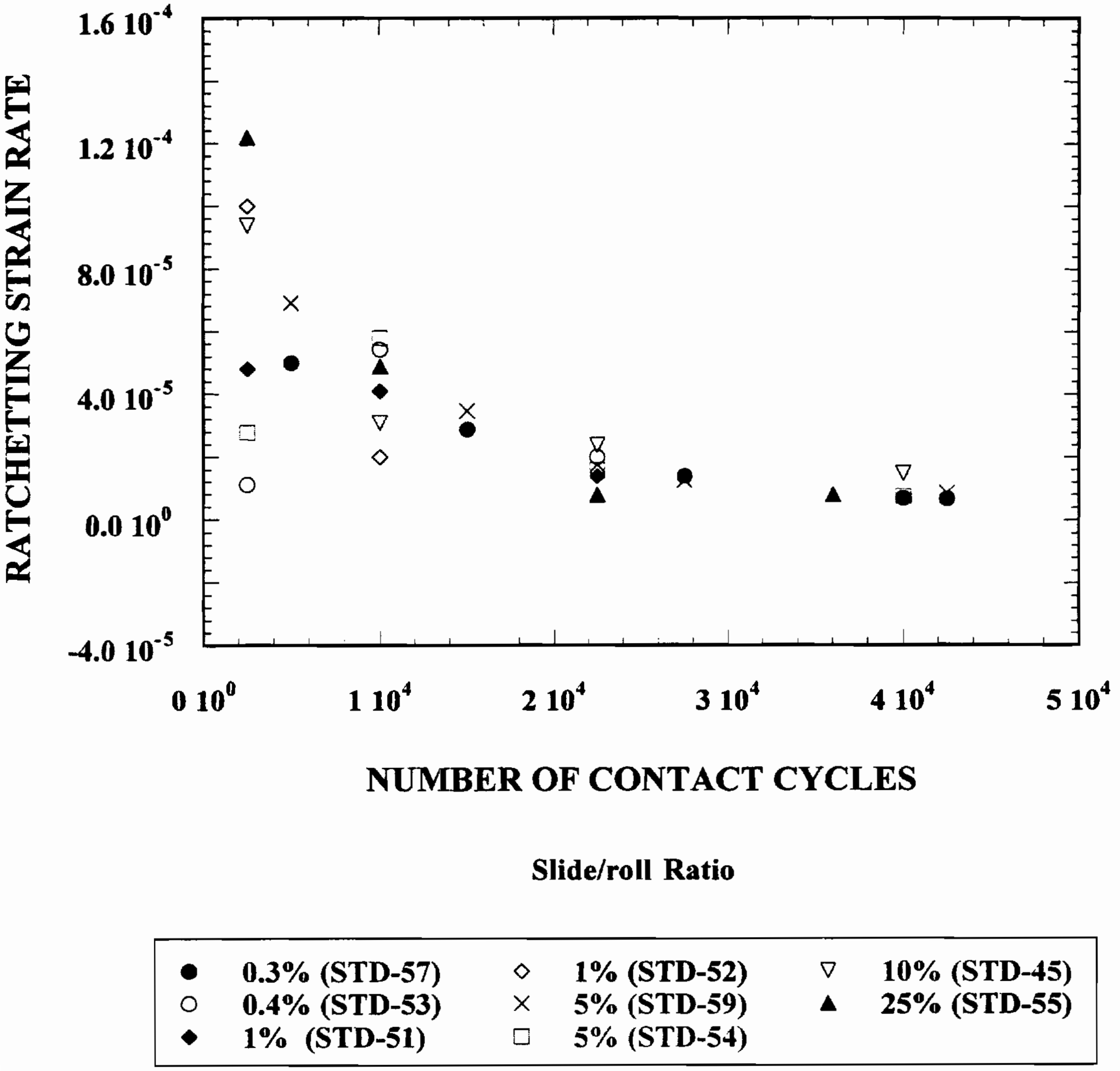

Fig. 4.10. Ratchetting strain rate as a function of contact cycles at different slide/roll ratios, showing a general trend of convergence and an initial increase of the strain rate at slide/roll ratios 1% and 5% consistent with the variations in T/N ratios.

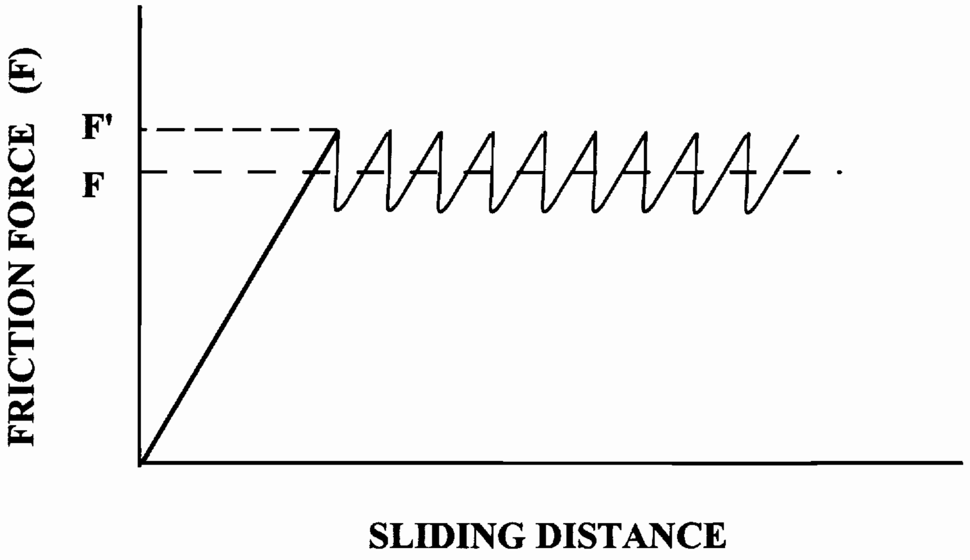

Fig. 4.11. A typical stick-slip phenomenon.[104]

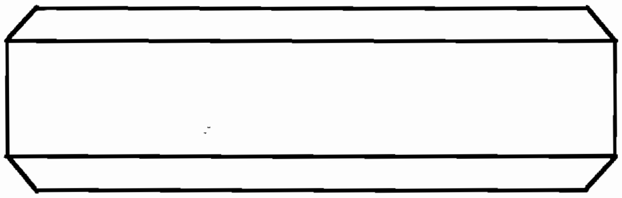

Fig. 4.12. Schematic illustration of alternating bands on the contact surface.

CONCLUSIONS

1 The surface initiated rolling contact fatigue life of low/medium carbon bainitic and eutectoid pearlitic steels is a non-linear function of contact pressure over the range of P_0 from 850 to 2300 MPa for water lubricated contact and a 10% slide/roll ratio.

2 The rolling contact fatigue resistance for any given contact pressure increases with increasing strength irrespective of microstructure. The rank in terms of RCF life versus the maximum contact pressure P_0 from the longest life down is: bainitic steel J6, followed by J1, J2 and HH, then STD and J4.

3 The six steels tested exhibited very similar rolling contact fatigue resistance as a function of normalized contact pressure, P_0/k.

4 Two crack growth modes are involved in surface initiated rolling contact fatigue, characterized by the distinctively different crack morphologies of shear band cracking and branched cracking.

5 The shear band cracking mode dominates when a sufficient surface plastic shear zone layer is formed at conditions above the shakedown limit, i. e. P_0/k greater than 4 in combination with tangential traction to normal pressure ratio of about 0.25, giving rise to fatigue lives that are short and strongly influenced by contact pressure.

6 Branched cracking occurs when the crack propagates below the surface shear zone and dominates at values of P_0/k less than 4, giving rise to longer lives that are far less influenced by contact stress.

7 Even in a situation dominated by branched cracking, the initial cracks can still be produced by shear band cracking.

8 For RCF crack growth, failure by ductile fracture is related to the shear band cracking mode, and failure by cyclic contact fatigue mechanism is related to the branched cracking mode.

9 Liquid lubrication, either by oil or water, exacerbates surface RCF crack growth and shortens RCF life when a prior existing deformation layer containing multiple initiated cracks is present.

10 A specific crack growth mode, either shear or opening, is determined by an interaction of a liquid and the deformation pattern. In the current research, opening mode crack growth was most obvious when water was present.

11 The effectiveness of oil in promoting shear mode cracking is determined by the existence of a shear deformation layer produced during the initial dry rolling/sliding contact. With the presence of the shear deformation layer, oil facilitated shear mode crack growth, but was confined within the boundary of the deformed zone.

12 The function of water in promoting contact fatigue crack growth is less limited to the deformed surface layer. Cracks under water lubrication grew well beyond the boundary of the deformed zone.

13 Ratchetting strain of pearlitic rail steel STD is non-linearly dependent on both contact pressure and contact cycles.

14 The most important feature of the non-linearity in ratchetting strain is its asymptotic nature, showing that decrease in strain rate to reach near saturation is a gradual process, occurring over a large number of contact cycles.

15 Ratchetting strain behavior can be expressed by two major parameters — the initial strain increment, γ_0, and strain accumulation rate, $d\gamma/dN$. Based on the experimental data, the initial strain increment can be expressed as a function of the maximum shear stress, μP_0, and mathematically fitted by the exponential function:

$$\gamma_0 (\mu P_0) = 8.3275\text{x}10^{-8}\, e^{(0.024867\, \mu P_0)}$$

and the ratchetting strain rate is derived as:

$$d\gamma/dN = \gamma_0 b N^{b-1}, \text{ with } b\,(\mu P_0) = -1.1023 - 0.00128\,(\mu P_0)$$

16 The ratchetting strain modulus $K_r = 1/[\gamma_0 b N^{b-1}] = 1/[\gamma_0^{1-1/b}\, b \gamma^{1/b}]$ evolves with contact cycles, or ratchetting strains.

17 For the shear band cracking dominated regime, surface RCF life is controlled by ratchetting strain behavior in terms of a critical strain, γ_c, and the strain rate. The correlation is expressed as

$$N_f = (\gamma_c / \gamma_0)^{1/b}$$

When cumulative strain reaches a critical strain level, the rolling contact surface will fail.

18 The effect of slide/roll ratio on ratchetting strain behavior was most pronounced during the initial contact cycles with a 7 times spread in ratchetting strain at different slide/roll ratios, gradually reducing to 1.4 times with increasing contact cycles.

19 Beyond the initial stage, the general trend is that a higher slide/roll ratio corresponds to higher surface displacement and ratchetting strain.

20 The trend of ratchetting strain with slide/roll ratio is consistent with the trend of the T/N ratios at various slide/roll ratios. A large variation in T/N was generated at slide/roll ratios $\leq 5\%$.

21 The slide/roll ratio effect is partially attributed to the influence of sliding distance on the T/N ratio through building up a stable contact interface, and the stick–slip phenomenon involved at low slide/roll ratios.

RECOMMENDATIONS FOR FUTURE WORK

- Study the effect of microstructural factors, such as prior austenitic grain size and inclusions, on RCF crack growth manifested by spalling in the branched cracking regime.

- Investigate the effect of lubrication as a function of viscosity, focusing on the possibility of the use of lubricants to reduce surface friction but without the detrimental effect of promoting RCF crack growth.

- Investigate the concept of a critical strain for crack initiation. Design an innovative experimental system to determine critical strains to RCF crack initiation for different steels.

- Study the T/N ratio as a function of combined systems of contact pressure, slide/roll ratio, and lubrication conditions.

- Further investigate the slide/roll ratio effect and the stick-slip phenomenon on RCF behavior. Develop a system to quantitatively measure T/N as a function of sliding distance.

- Study the effect of relative top to bottom roller hardness on strain and RCF behavior. Investigate a possible optimal relative hardness range which gives rise to the best RCF performance.

REFERENCES

1. H. A. R. Hanks and J. F. R. Gussow, Planning for traffic growth on rail lines, *Proc. Int. Conf. Heavy Haul Railways*, CO, USA (1982) 82-HH-6.

2. M. D. O'Rourke,Engineering effects of increasing axle load, *Proc. Int. Conf. Heavy Haul Railways*, CO, USA (1982) 82-HH-11.

3. O. Orringer and R. K. Steele, Structural integrity of rail in railroad track in the United States, *ASTM STP* 969 (1988) 260-278.

4. Private conversation with R. K. Steele, formerly with American Association of Railroads (AAR), 1993.

5. UTRECHT Report No. 1, Review of rolling contact fatigue in rails, *Office for Research and Experiments of the International Union of Railways*, April, 1990.

6. G. G. Knupp, W. H. Chidley, J. L. Giove, H. H. Hartman, G. F. Morris, and C. W. Taylor, A review of the manufacture, processing, and use of rail steels in North America - a report of AISI technical subcommittee on rails and accessories, *ASTM STP* 644 (1978) 7-20.

7. M. Sato, *Wear and RCF of Rail Steels*, M.S. Thesis, Ohio State University, 1991.

8. R. K. Steele and D. H. Stone, Developments in railroad rail, *AREA Bulletin 707*, 87 (1986) 311-354.

9. A. W. Worth, J. R. Hornaday, Jr., and P. R. Richards, Prolonging rail life through rail grinding, *Proc. 3rd Int. Conf. Heavy Haul Railways* (1986) IB-9-1.

10. J. Kalousek and A. E. Bethune, Rail wear under heavy traffic conditions, *ASTM STP* 644 (1978) 63-79.

11. P. Clayton and M. B. P. Allery, Metallurgical aspects of surface damage problems in rails, *Canadian Metallurgical Quarterly*, 21, 5 (1982) 31-46.

12. R. K. Steele and T. J. Devine, Wear of rail/wheel systems, *Proc. Int. Symp. Contact Mechanics and Wear of Rail/Wheel Systems*, University of Waterloo Press (1982) 293-312.

13. V. A. Dikshit, *Rolling Contact Fatigue Behavior of Pearlitic Rail Steels*, Ph.D. Thesis, Oregon Graduate Institute of Science and Technology, 1992.

14. B. Paul, A review of rail -wheel contact stress problem, *Proc. Symp. on Railroad Track Mechanics*, Pergamon Press (1975) 323-351.

15. J. O. Smith and C. K. Liu, Stresses due to tangential and normal loads on an elastic solid with application to some contact stress problem, *J. Applied mechanics*, Jume (1953) 157-166.

16. K. L. Johnson, *Contact Mechanics*, Cambridge University Press, 1985.

17. J. J. Kalker, Wheel-rail rolling contact theory, *Wear,* 144 (1991) 243-261.

18. J. A. Greenwood, The contact of real surfaces, *Proc. Int. Symp. Contact Mechanics and Wear of Rail/Wheel Systems,* University of Waterloo Press (1982) 21-35.

19. A. F. Bower and K. L. Johnson, The Influence of strain hardening on cumulative plastic deformation in rolling/sliding line contact, *J. Mech. Physic. Solids*, 37, 4 (1989) 471-493.

20. P. Clayton and D. N. Hill, Rolling contact fatigue of rail steel, *Wear*, 117 (1987) 319-334.

21. J. L. Tevaarwesk, Traction in lubricated contacts, *Proc. Int. Symp. Contact Mechanics and Wear of Rail/Wheel Systems,* University of Waterloo Press (1982) 121.

22. H. Krause and G. Poll, The influence of Real material and system properties on the traction/creep relationship in rolling contact, *Proc. Int. Symp. Contact Mechanics and Wear of Rail/Wheel Systems,* University of Waterloo Press (1982) 353-369.

23. T. G. Pearce and K. A. Rose, Tangential force - creepage relationships in theory and practice, *Proc. Int. Symp. Contact Mechanics and Wear of Rail/Wheel Systems,* University of Waterloo Press (1982) 183-195.

24. A. F. Bower and K. L. Johnson, Plastic flow and shakedown of the rail surface in repeated wheel-rail contact, *Wear,* 144 (1991) 1-18.

25. J. E. Merwin, and K. L. Johnson, An analysis of plastic deformation in rolling contact, *Proc. Inst. of Mechanical Engineers, Symp. on Rolling Contact Fatigue*, 177, 25 (1963) 676-685.

26. D. L. Mcdowell and G. J. Moyar, Effects of non-linear kinematic hardening on plastic deformation and residual stresses in rolling line contact, *Wear*, 144 (1991) 19-37.

27. H. Sehitoglu and Y. Jiang, Residual stress analysis in rolling contact, *FRA/ERRI Int. Conf. Rail Quality and Maintenance for Modern Railway Operations,* Delfer, The Netherlands, June, 1992.

28. G. M. Hamilton, Plastic flow in rollers loaded above the yield point, *Proc. Inst. of Mechanical Engineers, Symp. on Rolling Contact Fatigue*, 177 (1963) 667-675.

29. K. L. Johnson and J. A. Jefferis, Plastic flow and residual stresses in rolling and sliding contact, *Proc. Inst. Mechanical Engineers, Symp. on Rolling Contact Fatigue* (1963) 54-65.

30. G. R. Miller, L. M. Keer and H. S. Cheng, On the mechanics of fatigue crack growth due to contact loading, *Proc. R. Soc. London* A 397 (1985) 197-209.

31. V. Bhargava, G. T. Hahn and C. A. Rubin, An elastic-plastic finite element model of rolling contact, Part two, *Trans. ASME, J. Appl. Mechanics*, 52 (1985) 75.

32. P. H. Dawson, Rolling contact fatigue crack initiation in a 0.3 per cent carbon steel, *Proc. Inst. of Mechanical Engineers*, 183 (1968-69) 1-9.

33. S. Way, Pitting due to rolling contact, *Trans. ASME, J. Appl. Mehcanics*, 2 (1935) A49-A58.

34. P. Clayton, M. B. P. Allery and P. J. Bolton, Surface damage phenomena in rails, *Proc. Int. Symp. Contact Mechanics and Wear of Rail/Wheel Systems,* University of Waterloo Press (1982) 419-441.

35. H. Ghonem and J. Kalousek, Surface crack initiation due to biaxial compression/shear loading, *Proc. Int. Symp. Contact mechanics and Wear in Wheel/rail Systems,* University of Waterloo Press (1986) 339-360.

36. N. P. Suh, The delamination theory of wear, *Wear*, 25 (1973) 111-124.

37. R. E. Mckelvey and C. A. Moyer, The relation between critical maximum compressive stress and fatigue life under rolling contact, *Proc. Fatigue in Rolling Contact*, Inst. of Mech. Engr. (1963) 1-10.

38. S. Kumar, V. Aronov, B. R. Rajkumar and R. Margasahayam, Experimental investigation of plastic flow in rails for a laboratory wheel rail simulation, *Canadian Metallurgical Quarterly,* 21, 1 (1982) 59-66.

39. J. A. Perez-Unzueta and J H. Beynon, Microstructure and wear resistance of pearlitic rail steels, *Wear*, 162-164 (1993) 173-182.

40. Y. C. Chiou and J. R. Hwang, Relationship between the propagation of fatigue cracks and the behavior of plastic flow under rolling/sliding contacts - effect of slip ratio, *Tribo. Int.*, 24, 2 (1991) 101-107.

41. S. Sheppard and M. Comninou, The mechanics of surface fatigue failure, *Proc. Int. Symp. Contact Mechanics and Wear of Rail/Wheel Systems,* University of Waterloo Press (1986) 407-420.

42. A. F. Bower, The influence of crack face friction and trapped fluid on surface initiated rolling contact fatigue cracks, *ASME J. Tribology*, 110 (1988) 704-711.

43. J. Akaoka and K. Hirasawa, Fatigue phenomena under rolling contact accompanied with sliding, *Bulletin of JSME*, 2, 5 (1959) 42-50.

44. M. Sato, P. M. Anderson and D. A. Rigney, Rolling-sliding behavior of rail steels, *Wear*, 162-164 (1993) 159-172.

45. A. R. Rosenfield, A fracture mechanics approach to wear, *Wear*, 61 (1980) 125-132.

46. E. Ollerton and J. W. W. Morey, Fatigue strength of rail steel in rolling contact, *ASTM STP* 644 (1978) 11-22.

47. H. Ichinose, J. Takehara, N. Iwasaki and M. Ueda, An investigation on contact fatigue and wear resistance behavior in rail steels, *Proc. Int. Conf. Heavy Haul Railways*, Australia (1978) Session 307, Paper I.3.

48. A. M. Kumar, G. T. Hahn, V. Bhargava, and C. Rubin, Elasto-plastic finite element analyses of two-dimensional, repeated, rolling-sliding contact deformation of bearing steel, *ASME J. Tribology*, 111 (1989) 309-314.

49. A. F. Bower, K. L. Johnson, and J. Kalousek, A ratchetting limit for plastic deformation of a quarter-space under rolling contact load, *Proc. 2nd Int. Symp. Contact Mechanics and Wear of Rail/Wheel Systems*, Univ. Waterloo Press (1986) 118-131.

50. K. L. Johnson, Plastic flow, residual stress and shakedown in rolling contact, *Proc. 2nd Int. Symp. Contact Mechanics and Wear of Rail/Wheel Systems*, Univ. Waterloo Press (1986) 83-97.

51. V. Bhargava, G. H. Hahn, G. Ham, S. Kulkarni and C. A. Rubin, Influence of kinematic hardening on rolling contact deformation, *Proc. 2nd Int. Symp. Contact Mechanics and Wear of Rail/Wheel Systems*, Univ. Waterloo Press (1986) 134-146.

52. G. L. Ham, G, T, Hahn, C. A. Rubin and V. Bhargava, Finite element analysis of the influence of kinematic hardening in two-dimensional repeated, rolling-sliding contact, *Tribology Transactions*, 32, 3 (1989) 311-316.

53. G. T. Hahn, V. Bhargava,C. A. Rubin, Q. Chen and K. Kim, Analysis of the rolling contact residual stresses and cyclic plastic deformation of SAE 52100 steel ball bearings, *ASME J. Tribology*, 109 (1987) 618-626.

54. A. F. Bower, Cyclic hardening properties of hard-draw copper and rail steel, *J. Mech. Phys. Solids*, 37, 4 (1989) 455-470.

55. D. L. McDowell and G. J. Moyar, A more realistic model of non-linear material response: application to elastic-plastic rolling contact, *Proc.2nd Int. Symp. Contact Mechanics and Wear of Rail/Wheel Systems*, Univ. Waterloo Press (1986) 99-116.

56. A. B. Sadat and M. Y. Reddy, Plastic strain analysis of the machined surface region using fine grid etched by photoresist technique, *Experimental Mechanics*, 29, 3 (1989) 346-349.

57. P. J. Sevenhuijsen, J. S. Sirkis and F. Bremand, Current trends in obtaining deformation data from grids, *Experimental Techniques*, May/June (1993) 22-26.

58. K. Hatanaka, T. Fujimitsu and H. Inoue, A measurement of three-dimensional strains around a creep-crack tip, *Experimental Mechanics*, 32, 3 (1992) 211-217.

59. X. Qiu, Rolling contact fatigue behavior of three eutectoid rail Steels, M.S. Thesis, *Oregon Graduate Institute of Science and Technology*, 1987.

60. B. N. Leis and R. C. Rice, Rail fatigue resistance -- increased tonnage and other factors of consequence, *Proc. Int. Conf. Heavy Haul Railways*, CO, USA (1982) 82-HH-12.

61. K. Morton, D. F. Cannon, P. Clayton and E. G. Jones, The assessment of rail steels, *ASTM STP* 644 (1978) 80-98.

62. K. Sugino, H. Kageyama and H. Masumoto, Development of weldable high-strength steel rails, *Proc. Int. Conf. Heavy Haul Railways*, CO, USA (1982) 82-HH-20.

63. S. Timoshenko and J. N. Goodier, *Theory of Elasticity*, McGraw-Hill Book Company, Inc., 1951.

64. D. H. Stone and R. K. Steele, The effect of mechanical properties upon the performance of railroad rails, *ASTM STP* 644 (1978) 21-62.

65. H. Sunwoo, M. E. Fine, M. Meshii and D. H. Stone, Cyclic deformation of Pearlitic eutectoid rail steel, *Metallurgical Transactions* A, 13A(1982) 2035-2047.

66. Y. J. Park and F. B. Fletcher, Fatigue behavior and fracture toughens of standard carbon and high strength rail steels, *Proc. Int. Conf. Heavy Haul Railways*, CO, USA (1982) 82-HH-21.

67. B. N. Leis, Cyclic inelastic deformation and fatigue resistance characteristics, *ASTM STP* 644 (1978) 449-468.

68. K. M. Kang and J. T. Song, A metallographic study on the subsurface zones of high carbon Cr-Ti alloy steel worn by rolling contact, *Wear*, 140 (1990) 119-134.

69. B. J. Dabell, S. J. Hill and P. Watson, An evaluation of the fatigue performance of conventional British rail steels, *ASTM STP* 644 (1978) 430-448.

70. N. Jin, *Mechanical Properties and Wear Performance of Bainitic Steels*, Ph.D Thesis, Oregon Graduate Institute of Science and Technology, 1995.

71. G. J. Moyar and G. M. Sinclair, Cumulative plastic deformation in rolling contact, *Trans. ASME, J. Basic Engineering* (1963) 105-115.

72. H. Ichinose, J. Takehara and M. Ueda, High strength rails produced by two-stage flame heating and slack heating-quenching, *Proc. Int. Conf. Heavy Haul Railways*, CO, USA (1982) 82-HH-19.

73. V. A. Dikshit and P. Clayton, A simple material model for water lubricated rolling contact fatigue of eutectoid steels, *Proc. STLE/ASME Tribology Conf.* 1991.

74. V. A. Dikshit, P. Clayton and D. Christensen, Investigation of rolling contact fatigue in a head hardened rail, *Wear*, 144 (1991) 89-102.

75. E. E. Laufer, H, Ghonem, J. Kalousek and D. H. Stone, Aspects of plastic deformation and fatigue damage in pearlitic rail steel, *Proc. Int. Conf. Heavy HaulRailways*, CO, USA (1982) 82-HH-31.

76. W. H. Hodgson, R. R. Preston and J. K. Yates, The development of a second generation of alloy steel rails for heavy haul applications, *Proc. Int. Conf. Heavy Haul Railways*, CO, USA (1982) 82-HH-22.

77. H. P. Lieurade, C. Maillard-Salin, R. Y. Deroche and L. Beaujard, Influence of surface conditions on repeated bending behavior of naturally hard rails, *Proc. Int. Conf. Heavy Haul Railways*, CO, USA (1982) 82-HH-27.

78. P. E. Bold, M. W. Brown and R. J. Allen, Shear mode crack growth and rolling contact fatigue, *Wear*, 144 (1991) 307-317.

79. L. M. Keer and M. D. Bryant, A Pitting model for rolling contact fatigue", *Trans. ASME, J. Appl. Mechanics*, 105 (1983) 198-205.

80. M. Dollar, A. W. Thompson, I. M. Bernstein and D. H. Stone, Deformation and wear in rail steels, *Proc. Int. Symp. Contact Mechanics and Wear of Rail/Wheel Systems,* University of Waterloo Press (1986) 315-323.

81. J. Kalousek, D. M. Fegredo and E. E. Laufer, The Wear resistance and worn metallography of pearlitic, bainitic and tempered martensite rail steel microstructures of high hardness, *Wear*, 105, 3 (1985) 199-222.

82. R. Devanathan and P. Clayton, Rolling-sliding wear behavior of three bainitic steels, *Wear*, 151, 2 (1991) 255-267.

83. J. E. Garnham and J. H. Beynon, Dry rolling-sliding wear of bainitic and pearlitic steels, *Wear*, 157 (1992) 81-109.

84. H. Masumoto, K. Sugino, S. Nisida, R. Kurihara and S. Matsuyama, Some features and metallurgical considerations of surface defects in rail due to contact fatigue, *Rail Steels — Developments, Processing and Use*, D. H. Stone and G. G. Knupp eds., *ASTM STP* 644, 1978.

85. T. C. Lindley and K. J. Nix, Metallurgical aspects of fatigue crack growth, Fatigue crack growth, *Proc. Conf. Fatigue Crack Growth,* R. A. Smith Ed., Cambridge, UK (1984) 53-74.

86. S. Suresh, Crack deflection: implications for the growth of long and short fatigue cracks, *Metall. Trans*. A, 14A (1983) 2375-2385A.

87. G. T. Gray III, A. W. Thompson, J. C. Williams and D. H. Stone, Influence of microstructure on fatigue crack growth behavior in fully pearlitic steels, *Fatigue of Metals*, P. G. Forrest, Ed., Pergamon Press (1970) 345-362.

88. P. Kao and J. G. Byrne, Microstructural influences on fatigue crack propagation in pearlitic steels, *Fatigue of Metals*, P. G. Forrest, Ed., Pergamon Press (1970) 313-328.

89. E. A. Starke, Jr., Cyclic plastic deformation and microstructure, Fatigue and Microstructure, *ASM Materials Science Seminar* (1978) 205-243.

90. R. W. Landgraf, Control of fatigue resistance through microstructure — ferrous alloys, *ASM Materials Science Seminar* (1978) 439-466.

91 H. S. Lamba, Nonproportional cyclic plasticity, *T. & A. M. Report* No. 413, University of Illinois, 1976.

92. Y. F. Dafalias, Modeling cyclic plasticity: simplicity versus sophistication, *Mechanics of Engineering Materials*, C. S. Desai and R. H.Gallagher Eds. (1984) 153-178.

93. T. Hassan and S. Kyriakides, Ratchetting in cyclic plasticity, part I: uniaxial behavior, *Int. J. Plasticity*, 8 (1992) 91-116.

94 J. L. Chaboche and D. Nouailhas, Constitutive modeling of ratchetting effects — part I: experimental facts and properties of the classical models, *Trans. ASME J. Engng. Mat. Tech.*, 111 (1989) 384-392

95 J. H. Dautzenberg and J. H. Zaat, Quantitative determination of deformation by sliding wear, *Wear*, 23 (1973) 9-19.

96 W. R. Tyfour, J. H. Beynon, and A. Kapoor, The steady wear behavior of pearlitic rail steel under dry rolling-sliding contact conditions, *Wear*, 180 (1995) 79-89.

97 X. Su and P. Clayton, Surface initiated rolling contact fatigue of pearlitic and low carbon bainitic steels, to be published, *Wear,* 1996

98 A. Kapoor, A re-evaluation of the life to rupture of ductile metals by cyclic plastic strain, *Fatigue Fract. Engng .Mater. Struct.*, 17, 2 (1994) 201-219.

99. B. S. Hockenhull, E. M. Kopalinsky, and P. L. B. Oxley, An investigation of the role of low cycle fatigue in producing surface damage in sliding metallic friction", *Wear*, 148 (1991) 135-146.

100. I. V. Kragelskii, *Friction and Wear*, Butterworth and Co. Ltd., London, 1965.

101. D. G. Teer and R. D. Arnell, Friction theories, *Principles of Tribology*, J. Halling Ed., The MacMillan Press (1979) 72-93.

102. J. Larsen-Basse, Basic theory of solid friction, *ASM handbook*, 18 (1992) 25-38.

103. N. P. Suh and H.-C. Sin, The genesis of friction, *Wear*, 69 (1981) 91-114.

104. Standard guide for measuring and reporting friction coefficients, *ASTM Standard* G115 - 93.

105. A. D. Hearle and K. L. Johnson, Mode II SIF for a crack parallel to the surface of an elastic half-space. *J. Mech. Phys. Solids*, 33 (1985) 61-81.

106. K. L. Johnson, Contact mechanics and the wear of metals, *Wear*, 190 (1995) 162-170.

107. *Handbook of Materials Science*, Charles, T. Lynch, Ed., CRC Press, Inc. 1974.

108. T. Hassan, E. Corona and S. Kyriakides, Ratchetting in cyclic plasticity, part II: multiaxial behavior, *Int. J. Plasticity,* 8 (1992) 117-146.

109. J. L. Chaboche and D. Nouailhas, Constitutive modeling of ratchetting effects, part II, *ASME J. Eng. Mater. Tech.*, 111 (1989) 409-416.

111. D. L. McDowell, An improved algorithm for elastic-plastic rolling/sliding line contact, *Private conversation*, Georgia Institute of Technology, 1995.

113. J. L. Chaboche, On some modifications of kinematic hardening to improve the description of ratchetting effects, *Int. J. Plasticity*, 7 (1991) 661-678.

114.. R. W. K. Honeycombe, *The Plastic Deformation of Metals*, Edward Arnold Ltd. Second edition, 1984.

115. M. Ohnami, *Plasticity and High Temperature Strength of Materials*, Elsevier Applied Science Publishers ltd, 1988

116. P. J. Armstrong and C. O. Frederick, A mathematical representation of the multiaxial Bauschinger effect, *C. E. G. B. report*, RD/B/N 731, 1966.

117. C. Guionnet, Modeling of ratchetting in biaxial experiments, *Trans. ASME J. Engng. Mat. Tech.*, 114 (1992), 56-62.

118. M. Liu and T. N. Farris, Effect of three-dimensional near surface defects on rolling and sliding contact fatigue, *ASME J. Tribology,* 116 (1994) 841- 849.

119. B. J. Lance and F. Sadeghi, The normal approach and stick-slip phenomena at the interface of two rough bodies, *ASME J. Tribology,* 115 (1993) 445- 452.

120. H. Salehizadeh and N. Saka, Crack propagation in rolling line contacts, *ASME J. Tribology,* 114 (1992) 690-697.

121. H. J. Carper, Jr., A. Ertas, J. Issa and O. Cuvalci, Effect of some material, manufacturing, and operating variables on the friction coefficient in OCTG connections, *ASME J. Tribology,* 114 (1992) 698-705.

122. W. Cheng, H. S. Cheng, L. M. Keer and X. Ai, Surface crack initiation under contact fatigue : Experimental observation and contact analysis, *ASME J. Tribology*, 115 (1993) 658-665.

123. M. C. Dubourg and B. Villechaise, Analysis of multiple fatigue cracks-part I: Theory, *ASME J. Tribology*, 114 (1992) 455-461.

124. M. C. Dubourg, M. Godet and B. Villechaise, Analysis of multiple fatigue cracks-part II: results, *ASME J. Tribology*, 114 (1992) 462-468.

125. W. Cheng, H. S. Cheng, T. Mura and L. M. Keer, Micromechanics modeling of crack initiation under contact fatigue, *ASME J. Tribology*, 116 (1994) 2-8.

126. Y. Jiang and H. Sehitoglu, An analytical approach to elastic plastic stress analysis of rolling contact, *ASME J. Tribology*, 116 (1994) 577-587.

127. J. B. Mann, T. N. Farris and S. Chandrasekar, Effects of friction on contact of transverse ground surfaces, *ASME J. Tribology*, 116 (1994) 430-438.

128. U. Bryggman and S. Soderberg, Contact conditions and surface degradation mechanism in low amplitude fretting, *Wear*, 125 (1988) 39-52.

129. G. R. Miller, A preliminary analysis of subsurface crack branching under a surface compressive load, *ASME J. Tribology*, 110 (1988) 292-297.

130. K. Komvopoulos, N. Saka, and N. P. Suh, Plowing friction in dry and lubricated metal sliding, *ASME J. Tribology*, 108 (1986) 301-312.

131. T. E. Tallian, Simplified contact fatigue life prediction model – part I: review of published models. *ASME J. Tribology*, 114 (1992) 207-213.

132. T. E. Tallian, Simplified contact fatigue life prediction model – part I: new model, *ASME J. Tribology*, 114 (1992) 214-222.

133. T. E. Tallian, Spalling life model with relaxed distribution constraints, for rough Hertz line contacts, *ASME J. Tribology*, 115 (1993) 453-459.

134. P. Clayton and D. Christensen, *Burlington Northern Rail Integrity Study, Phase II,* Oregon Graduate Institute of Science and Technology, 1990

135. R. S. Zhou, H. S. Cheng and T. Mura, Micropitting in rolling and sliding contact under mixed lubrication, *ASME J. Tribology*, 111 (1989) 605-613..

136. H. S. Nagaraj, Elastoplastic contact of bodies with friction under normal and tangential loading, *ASME J. Tribology*, 106 (1984) 519-526.

137. D. A. Hills and A. Sackfield, Sliding contact between dissimilar elastic cylinders, *ASME J. Tribology*, 107 (1985) 463-466.

138. B. I. Kostetsky, The structural-energetic concept in the theory of friction and wear (synergism and self-organization), *Wear*, 159 (1992) 1-15.

139. A. T. Alpas, H. Hu and J. Zhang, Plastic deformation and damage accumulation below the worn surfaces, *Wear,* 162-164 (1993) 188-195.

140. D. A. Rigney, The role of hardness in the sliding behavior of materials, *Wear*, 175 (1994) 63-69.

141. J. E. Graham and J. H. Beynon, The early detection of rolling - sliding contact fatigue cracks, *Wear*, 144 (1991) 103-116.

142. E. M. Kopalinsky, Investigation of surface deformation when a hard wedge slides over a soft surface, *ASME J. Tribology*, 114 (1992) 100-106.

143. A. Kapoor and J. A. Williams, Shakedown limits in sliding contacts on a surface-hardened half-space, *Wear*, 172 (1994) 197-206.

144. A. Kapoor, J. A. Williams and K. L. Johnson, The steady state sliding of rough surfaces, *Wear*, 175 (1994) 81-92.

145. Y. Jeng, Experimental study of effects of surface roughness on friction, *Tribology Transaction*, 33, 3 (1990) 402-410.

146. P. Clayton and R. Devanathan, Rolling/sliding wear behavior of a chromium-molybdenum rail steel in pearlitic and bainitic conditions. *Wear*, 156 (1992)121-131.

147. M. Shima, K. Okada, Y. Kimura and T. Yamamoto, Measurements of subsurface plastic flow in rolling contact, *J. JSLE*, 2 (1981) 75-80.

148. R. K. Steele and R. P. Reiff, Rail: its behavior and relationship to total system wear, *Proc. Int. Conf. Heavy HaulRrailways*, CO, USA (1982) 82-HH-24.

149. K. L. Johnson, Contact mechanics and the wear of metals, *Wear*, 190 (1995) 162-170.

150. R. D. Mindlin, Compliance of elastic bodies in contact, *Trans. ASME, J. Appl. Mechanics*, , 71 (1949) 259-268.

151. J. K. Lancaster, A review of the influence of environmental humidity and water on friction, lubrication and wear, *Tribo. Int.*, 23, 6 (1990) 371-389.

VITA

Born in Shanxi Province, north China. Grew up in Inner Mongolian autonomous region and Beijing, China.

Graduated from Beijing 101 highschool in 1968, two years after beginning of the Culture Revolution. Sent to countryside, and worked in factories during the 10 year period of the Culture Revolution. Kept self study in these years and passed national entrance exams after the revolution for colleges and universities.

Received Master's Degree in Mechanical Engineering from Institute of Aeronautical Materials, Beijing, in 1984. Worked as a research engineer at the Institute since then until 1991. During this period, spend three years, from 1985 to 1988, in the United States first as a visiting scholar at the department of Mechanical Engineering, Johns Hopkins University, later as an associated researcher for Materials Lab, Wright-Patterson Air Force Base at the University of Dayton Research Institute.

Moved from China to Canada in December 1991 as an associated researcher at the Department of Mechanical Engineering, University of Toronto. Came to Oregon Graduate Institute for Ph.D. study in the fall of 1992.